

Realizing Directional, Narrowband Thermal Emission through Control of Spectral Dispersion and Strong Coupling

By

J. Ryan Nolen

Dissertation

Submitted to the Faculty of the
Graduate School of Vanderbilt University
in partial fulfillment of the requirements
for the degree of

DOCTOR OF PHILOSOPHY

in

Interdisciplinary Materials Science

May 31, 2021

Nashville, Tennessee

Approved:

Joshua D. Caldwell, Ph.D.

Sharon M. Weiss, Ph.D.

Jason G. Valentine, Ph.D.

Richard F. Haglund Jr., Ph.D.

Justus Ndukaife, Ph.D.

Copyright © 2021 by J. Ryan Nolen
All Rights Reserved

To my mom and dad.

ACKNOWLEDGMENTS

I would first like to thank my advisor, Prof. Josh Caldwell, for his constant support and encouragement throughout my PhD. Thank you for taking a chance on me and giving me the opportunity to join your research group. I am deeply grateful for your mentorship and for the active role that you have played in my development as a scientist and as a person. You have always been available to discuss research and encouraged me to be independent. You are always open to exploring new ideas and forming new collaborations. I feel very fortunate to have ended up in your group and honored to be your first graduate student. Finally, thank you for being such a strong advocate for me as I was searching for a postdoc position. Thank you for all that you have done for me and I hope that we are able to continue working together in the future.

I would also like to thank the other members of my PhD committee, Prof. Jason Valentine, Prof. Sharon Weiss, Prof. Richard Haglund, and Prof. Justus Ndukaife, for their willingness to serve on my committee and provide guidance and advice throughout my graduate school career. I would especially like to thank Prof. Richard Haglund for giving me my first research experience by allowing me to spend the summer in his lab as an undergraduate through the Vanderbilt Institute of Nanoscience and Engineering (VINSE) Research Experience for Undergraduates (REU) program. During that summer, you also arranged for me to visit Oak Ridge National Laboratory and to learn more about the research taking place there. These experiences spurred my interest in optics research and ultimately fueled my decision to pursue a PhD at Vanderbilt.

I have been privileged to work alongside so many talented and incredible people at Vanderbilt. In particular, I would like to recognize the former and current members of the Caldwell Lab, Joseph Matson, Mingze He, Guanyu Lu, Scott Criswell, Ryan Kowalski, Katja Diaz-Granados, Prof. Tom Folland, and Dr. Claire Marvinney. It has been such a joy getting to know all of you and work with you these past few years. To those of you that are still working on your PhDs, I wish you the best of luck with the remainder of your graduate school careers. I would like to extend an enormous thank you to Prof. Tom Folland. Your expertise, work ethic, and consistent positive attitude and willingness to help set a great example for the other members of the group and I hope that I can be even half the postdoc that you were. I would also like to extend a special thanks to Joseph Matson who started in the Caldwell Lab the same time as I did. Over the years we have become very good friends and I hope that we are able to stay in touch. I am grateful for

the experiences that I have been able to share with my lab members while travelling to conferences, such as hiking in Arizona with Tom, Joseph, and Josh, and walking the freedom trail in Boston with Tom and Joseph. These are experiences that I will always look back on fondly. Finally, I would also like to thank the undergraduate students, Alyssa Livingood, Lauren Potechin, and Sebastian Miki-Silva, that worked with me over the past few years.

I would also like to thank the other former and current graduate students that I have gotten to know during my time at Vanderbilt. Special thanks to Dr. You Zhou, who I worked with during a research rotation in the Valentine group my first year. I learned a lot of valuable research skills during my short time working with you. After I joined Josh's lab, it was always nice being able to chat with you about research and I'm excited that I am going to be working with you again very soon. I would also like to thank Dr. Austin Howes, who I have worked with on a couple of different projects. I would also like to thank the other members of the Valentine Lab that I have gotten the chance to know: Chibuzor Fabian Ugwu, Hanyu Zheng, Elena Kovalik, Janna Roethert, Tao Hong, Dr. Zhihua Zhu, and Dr. Zack Coppens. Your comments during group meetings helped me with my research and prepare me for exams. Thank you to Prof. Daniel Mayo and Dr. Claire Marvinney for being such great mentors during my REU in Prof. Richard Haglund's Lab. Thank you also to Sami Halimi from the Weiss Lab, who I have been fortunate to know ever since the beginning undergrad at Lipscomb University. I am so glad that I was able to go to the same graduate school, studying similar research with someone I consider to be such a great friend.

I would also like to thank the VINSE staff for all of their help. Thank you to Kurt Heinrich for leading the development of plasma and physical etching processes I used in my work. Thank you also to Dr. Alice Leach and Dr. Bill Martinez for training me on the equipment in the cleanroom and for all of their support. Thank you to Dr. Anthony Hmelo, Dr. Dmitry Koktysh, and Dr. James McBride for their assistance with the imaging tools. I also owe a special thank you to Alisha McCord and Sarah Ross. Without all of your help, this work would not have been possible. I also want to thank Myrtle Daniels, Chris Lindsey, Sarah Nagy, and Jean Miller from the Mechanical Engineering office for all of their excellent administrative support.

During my PhD, I have been fortunate to form relationships with collaborators outside of Vanderbilt University. I would like to give a special thanks to Prof. Jon-Paul Maria's group at Penn State: Angela Cleri, Josh Nordlander, Dr. Evan Runnerstrom, and Dr. Kyle Kelley. Our

collaboration has not only been very productive, but also very enjoyable. I would also like to thank Dr. Willie Luk at Sandia National Laboratory, Dr. Marko Tadjer at the Naval Research Laboratory, Prof. Nader Engheta at The University of Pennsylvania, Prof. Stephanie Law at the University of Delaware, Prof. Simone De Liberato at the University of Southampton, Prof. Patrick Hopkins at the University of Virginia, Dr. Edward Sachet and Dr. Chris Shelton from Third Floor Materials, Inc., and Prof. Nabil Bassim at McMaster University.

Finally, I want to give an enormous thank you to my family and my girlfriend, Samantha, for their unending love and support. To my parents, thank you for all that you have done to help me succeed. Thank you for setting such a strong example for me when I was growing up. I am so proud to be your son. To my brother, Jacob, thank you for your constant words of encouragement. To Samantha, thank you for your patience, understanding, and constant encouragement. Thank you for putting up with my bad schedule, proofreading my important emails, and listening to my frequent complaints. Most importantly, thank you for believing in me even when I found it difficult at times. I am so lucky to have you in my life and could not have asked for a better partner to accompany me along this arduous journey.

This dissertation is a result of work funded by the Office of Naval Research Grant N00014-18-1-2107 under the direction of Mark Spector.

TABLE OF CONTENTS

	Page
ACKNOWLEDGMENTS.....	iv
LIST OF TABLES	xi
LIST OF FIGURES	xii
LIST OF ABBREVIATIONS	xix
LIST OF PUBLICATIONS.....	xxiii
1. Introduction	1
1.1 Mid- and Long-Wave Infrared Optical Sources.....	1
1.2.1 Surface Plasmon Polaritons and Surface Phonon Polaritons.....	2
1.2.2 Epsilon-Near-Zero Polaritons and Berreman Modes.....	5
1.2.3 – Coupling to Polaritons.....	6
1.3 Engineering Far-Field Thermal Emission.....	8
1.3.1 Spatially Coherent Thermal Emission	9
1.4 Dissertation Overview.....	10
2. Extraction of the Dielectric Functions of n-doped Cadmium Oxide and Hafnium Disulfide using Ellipsometry and FTIR Spectroscopy.....	12
2.1 Interaction of Light with Semiconductor Films.....	12
2.1.1 The Dielectric Tensor	12
2.2 Experimental Techniques for Extracting Semiconductor Dielectric Functions.....	15
2.2.1 Reflection and Transmission Spectra.....	16
2.2.2 Spectroscopic Ellipsometry	18
2.3 Modelling of Common Light-Matter Interactions in Semiconductors.....	19
2.3.1 Tauc-Lorentz Model	20
2.3.2 Free Carrier Absorption	21
2.3.3 Infrared Active Phonons in Polar Semiconductors	22
2.4 Dielectric Function of n-doped CdO Thin Films	24
2.4.1 Fitting Procedure for Ellipsometric and FTIR Data.....	26
2.4.2 Effects of Free Carriers on UV to visible dielectric function of n-CdO.....	30
2.4.3 Effects of Free Carriers on the IR dielectric function of n-CdO.....	32
2.4.4 Influence of Optic Phonons on the FIR dielectric function of n-CdO.....	38
2.4.5 Combined Dielectric Function.....	40
2.4.6 Conclusions	41

2.5 Dielectric Function of HfS ₂ Crystals	41
2.5.1 Extracting HfS ₂ Dielectric Function using FTIR micro-spectroscopy.....	42
2.5.2 Modelling Two-Phonon Absorption in HfS ₂ Crystals	44
2.5.3 Conclusion.....	45
3. Polaritonic Strong Coupling in Multilayer Semiconductor Films	46
3.1 Coupling Between Light and Matter	46
3.1.1 Weak Coupling Regime	47
3.1.2 Strong Coupling Regime.....	47
3.2 SPP-ENZ Strong Coupling in Multilayer CdO Films.....	49
3.2.1 Impact of Coating and Spacer Layer Thickness on the SPP-ENZ Dispersion	53
3.2.2 Impact of Spatial Separation on the SPP-ENZ Dispersion	55
3.2.3 Impact of Spatial Separation on the SPP-ENZ Coupling Strength	56
3.2.4 Electric Field Profiles of SPP-ENZ Modes in Trilayer CdO Films	58
3.2.5 Hopfield Model for SPP-ENZ Coupling in Dispersive Environment.....	59
3.2.6 Effects of Ambient Permittivity on ENZ Modal Absorption	61
3.2.7 Conclusions	62
3.3 Three Mode Strong Coupling in III-V Semiconductor Heterostructures.....	63
3.3.1 Tuning of SPhPs in InAs through LO Phonon-Plasmon Coupling	63
3.3.2 Epsilon-Near-Pole Modes in Polar Dielectrics.....	66
3.3.3 SPhP-ENP and SPP-ENP-ENZ Strong Coupling in InAs-GaSb and InAs-AlSb Films.....	68
3.3.4 InAs Plasma Frequency Dependence	69
3.3.5 AlSb Thickness Dependence	70
3.3.6 Conclusions	72
4. Theoretical Investigation of Monopole – ENZ – ENP Strong Coupling in III-V Heterostructure Resonators for Controlling Spatial Coherence of Thermal Emission	74
4.1 Monopole Resonances.....	74
4.1.1 Monopole Resonances in Si:InAs Resonators	75
4.1.2 Monopole – ENZ – ENP Strong Coupling in Si:InAs-AlSb Resonator Arrays.....	78
4.1.3 Impact of SPP – ENZ Strong Coupling on Angular Dispersion.....	83
4.1.4 Conclusions	85
5. Narrowband Infrared Emitting Metamaterials for Filterless Non-dispersive Gas Sensing .	87
5.1 Introduction	87
5.2 Filterless Non-dispersive Infrared Sensing using CdO NIREM	88
5.2.1 Fabrication of CdO NIREM Device.....	91

5.2.2 Angle – Resolved Thermal Emission of CdO NIREM	91
5.2.3 Patterned Sapphire Substrate Pitch Dependence	97
5.2.4 Polarized Thermal Emission	99
5.2.5 Spectral Bandwidth of CdO NIREM Source	103
5.2.6 Error Analysis of CO ₂ Detection.....	105
5.3 Conclusions	106
6. Design of Wafer-Scale and Lithography-Free Tamm Plasmon Thermal Emitters with Broad Functionality using Gradient Descent Regression Optimization	107
6.1 Introduction to Tamm Plasmons	107
6.1.1 Planar Tamm Plasmon Films for Narrowband Thermal Emission.....	108
6.1.2 Theory of Tamm Plasmons at Metal – 1D Photonic Crystal Interfaces	108
6.1.3 Angular Dispersion of Tamm Plasmons	112
6.2 Designer Tamm Plasmon Films using Gradient Descent Optimization.....	113
6.2.1 Designing Aperiodic Tamm Plasmon Films using Gradient Descent Optimization.....	115
6.2.2 Demonstration of Arbitrary Spectral Control of Tamm Plasmons.....	117
6.2.3 Advantages of CdO in Design of Tamm Plasmon Thermal Emitters	120
6.2.4 NDIR Gas Sensing Using Tamm Plasmons.....	122
6.3 Conclusions	123
7. Spectroscopic Investigation of Hyperbolic Resonances in Monolithic, Homoepitaxial CdO Superlattices	127
7.1 Introduction	127
7.2 CdO Hyperbolic Metamaterials.....	129
7.2.1 Effective Medium Theory – 1D Metamaterials.....	132
7.2.2 Attenuated Total Reflectance Measurements of CdO Hyperbolic Metamaterials.....	134
7.2.3 Role of CdO Hyperbolic Metamaterial Thickness	136
7.2.4 Carrier Density Tunability of CdO Hyperbolic Metamaterials	138
7.2.5 Filling Fraction Tunability of CdO Hyperbolic Metamaterials.....	141
7.2.6 Surface Plasmon Polariton – Hyperbolic Plasmon Polariton Strong Coupling.....	144
7.3 Conclusions	145
8. Conclusions and Future Directions	146
8.1 Conclusions	146
8.2 Future Directions	147
Appendix A.....	149
Parameters of Tamm Plasmon Films Designed Using Inverse Design	149

A.1 Matching the absorption spectra of O ₃ , CH ₄ , and NH ₃	149
A.2 Parameters of Tamm Plasmon Emitters	150
Appendix B.....	152
Angle Resolved Thermal Emission and Gas Cell Measurements	152
B.1 Angle Resolved Thermal Emission Measurements.....	152
B.2 Gas Cell Measurements	153
REFERENCES	155

LIST OF TABLES

Table	Page
Table 2.1: Comparison of optoelectronic properties of TCOs used in MIR plasmonics.....	36
Table 2.2: Fit Parameters from HfS ₂ Extracted from Reflectance Fitting.....	45
Table 6.1: Parameters of designed and as-grown films	117
Table 7.1: Parameters of CdO HMM Films.....	136

LIST OF FIGURES

Figure	Page
<p>Figure 1.1: Dispersion relation for an optically a) thick and b) thin film. As the film thickness is decreased to below the skin depth the surface polariton dispersion splits into upper (blue) and lower (red) branches due to strong coupling. [from ref. ⁶] c) Dispersion relation of three films of varying thicknesses with ENZ frequency at ω_L. The oblique line is the light line in air and horizontal lines are $Re(\epsilon_m) = -1$ and $Re(\epsilon_m) = 0$, as labelled. [from ref. ⁷]</p>	6
<p>Figure 1.2: a) Polaritonic dispersion of polar dielectric semiconductor. The dispersion in a) can be probed using ATR measurements in the b) Kretschmann or c) Otto configuration. Alternatively, a d) grating could also be used to diffractively couple to a propagating surface polariton. e) Localized surface polaritons can also be supported in deeply-subwavelength resonators. [from ref. ¹³].</p>	7
<p>Figure 1.3: a) Thermal emission from Berreman modes in planar multilayer CdO films. [from ref. ²⁵] b) Spatial-coherence of thermal emission realized through out-coupling of thermally-excited SPhP modes on a SiC surface. [from ref. ²¹] c) Schematic of thermal emission focusing from SiC surface using bullseye pattern. [from ref. ²³] d) Strong coupling between a ZFLO and localized and propagating SPhPs for controlling thermal emission. [from ref. ²⁴]</p>	10
<p>Figure 2.1: a) Schematic defining the plane of incidence (P) and polarized wave amplitudes (A_s, A_p, B_s and B_p). [from ref ³⁴] b) Schematic of variable angle reflectance instrument (Pike Technologies) for large-scale FTIR measurements. c) Light path of Cassegrain objective for microscope FTIR measurements. [from ref ¹³]</p>	15
<p>Figure 2.2: a) Real and imaginary permittivity near the optic phonons of undoped-InAs calculated using the TOLO function.[ref ³⁸] b) Contribution of free carriers to the dielectric function of a doped CdO film ($N_d = 3e20 \text{ cm}^{-3}$) calculated using the Drude model. c) Contribution of bandgap absorption to the dielectric function of CdO ($N_d = 1e20 \text{ cm}^{-3}$).</p>	20
<p>Figure 2.3: Representative experimental a) ψ and b) Δ spectra and corresponding least-squares fits for a In:CdO film with a carrier density of $4.1 \times 10^{20} \text{ cm}^{-3}$ at 60° (black) and 70° (red) incident angles. The vertical black dotted line represents the extracted plasma frequency of the film ($\omega_p = 5,218 \text{ cm}^{-1}$).</p>	28
<p>Figure 2.4: a) Plots of absorptivity (α^2) squared vs. photon energy. The optical bandgap is determined by extrapolating the asymptotic region of α^2 to zero. b) Real permittivity (ϵ') as a function of $(E^2 + \gamma^2)$ where γ is the drude damping. The high-frequency permittivity (ϵ_∞) can be determined by fitting the linear region of this relationship and determining the x-intercept.</p>	31
<p>Figure 2.5: a) Real (solid) and imaginary (dashed) parts of the dielectric functions near the bandgap energy of three CdO thin films with differing carrier densities as labeled. Note the blue shift in the bandgap absorption with increasing carrier density. The optical bandgap and high frequency permittivity of In:CdO films as a function of carrier density are shown in b) and c), respectively. The uncertainty in the values, determined from the described fits are provided as error bars. Previously reported values from Liu et. al. ⁸⁰ are also shown in b) and c) for comparison.</p>	32

Figure 2.6: a) Plasma frequency ω_p and b) effective mass m^* of doped CdO films as a function of carrier density. Previously reported values for both ω_p and m^* from Liu et. al.⁸⁰ are also shown for comparison. A fit to the data using Eq. 5 is also provided (red curve)..... 33

Figure 2.7: a) Real and imaginary dielectric function near the plasma frequency of three CdO thin films with differing carrier densities. The dielectric functions were derived from WVASE fitting of spectroscopic ellipsometry data. b) Hall electron mobility and carrier damping (γ) as a function of carrier density in In:CdO films..... 34

Figure 2.8: Quality-factor (eq. 23) calculated at the Fröhlich condition ($Re(\epsilon) = -2$) for several TCOs across a range of ω_p (and therefore N_d). The dielectric function for each material was calculated using the Drude model with the effective mass determined using Eq. 17. Values for m_o^* and C for other TCOs were found in literature.^{88,104} Data points correspond to calculated Q-factor values from the extracted dielectric functions of the films in this study, demonstrating excellent agreement with the values calculated using the Drude model..... 37

Figure 2.9: Low-energy FTIR reflectance of four CdO films with varying levels of doping; unintentionally doped ($1.4 \times 10^{19} \text{ cm}^{-3}$), moderately doped ($6.6 \times 10^{19} \text{ cm}^{-3}$), and highly doped ($1.4 \times 10^{20} \text{ cm}^{-3}$ and $4.1 \times 10^{20} \text{ cm}^{-3}$) measured at an angle of incidence of 60° 39

Figure 2.10: Far-IR dielectric functions for a) three CdO films with varying levels of doping as well as the isolated TOLO contribution (Drude and Tauc-Lorentz oscillators turned off). b) Transfer-Matrix-Method reflectance simulation of a 200 nm CdO film with the TOLO-isolated dielectric function from a) on an MgO substrate..... 40

Figure 2.11: a) Measured and fit b) Transfer-Matrix-Method reflectance simulation of a 200 nm CdO film with the TOLO-isolated dielectric function from a) on an MgO substrate..... 43

Figure 2.12: a) Two fits to measured (red line) transmission. The dashed line shows is a fit ignoring the contribution of two-phonon absorption. The solid black line is a fit that takes the two-phonon absorption into account. b) Dielectric function of HfS₂. c) Contribution of two-phonon absorption in the dielectric function of HfS₂. 44

Figure 3.1: a) Schematic of SPP-ENZ strongly-coupled CdO film with UID CdO layer used as spatial separation between SPP and ENZ layers. b) TMM-calculated dispersion of bilayer ($t_{spacer} = 0 \text{ nm}$) and $t_{spacer} = 50 \text{ nm}$. c) Schematic of SPP-ENZ strongly-coupled CdO film with UID CdO layer deposited as a coating layer. d) TMM-calculated dispersion of bilayer ($t_{coating} = 0 \text{ nm}$) and $t_{coating} = 50 \text{ nm}$. Note that in both cases, the SPP-ENZ anticrossing occurs at the intersection between the uncoupled SPP and ENZ dispersions..... 51

Figure 3.2: a) Hybrid SPP-ENZ polaritonic dispersion for a bilayer CdO film. The polaritonic dispersion of a trilayer film with a 25 nm and 84 nm UID CdO coating layer (see f)) are displayed in b) and c). The polaritonic dispersion of a trilayer film with a 25 nm and 75 nm UID CdO spacer layer (see g)) are displayed in d) and e). The contour plot was calculated using TMM. The dashed blue lines are the uncoupled SPP and ENZ modes and the solid lines are the hybrid dispersion calculated using the Hopfield model. The measured dispersion is included as data points. 55

Figure 3.3: Spectral splitting at SPP-ENZ anti-crossing normalized to the ENZ frequency as a function of a) spacer layer thickness and b) coating layer thickness. c) Linear profile of the z-oriented electric field magnitude $|E_z|^2$ as a function of ambient effective index..... 58

Figure 3.4: Out-of-plane electric field (E_z) calculated at the anticrossing condition for the bilayer film (a, d)), trilayer film with 50 nm spacer layer (b, e)), and trilayer film with 50 nm coating (c, f)). a), b), and c) show E_z in the upper branch and d), e), and f) show the fields in the lower branch. 59

Figure 3.5: (a) Calculated dispersion of 300 nm CdO film ($N_d = 2.5 \times 10^{20} \text{ cm}^{-3}$) coated with a 75 nm UID CdO layer. The strong coupling between the SPP mode and the ENZ mode supported by the UID CdO film ($\omega_{ENZ} \sim 2125 \text{ cm}^{-1}$) results in splitting into upper and lower branches. The upper branch (dashed line) is then used as the uncoupled SPP dispersion $\omega_{k\parallel}^{SPP}$ when calculating the hybrid dispersion in (b). The calculated dispersion of a trilayer film with a 75 nm UID CdO spacer layer is provided in (b)..... 61

Figure 3.6: (a) Geometry of CdO film with UID CdO layer below the ENZ layer. (b) Geometry of CdO film with UID layer above ENZ layer. (c) and (d) contain the TMM-calculated ATR spectra at 60° for the CdO film displayed in (a) and (b), respectively..... 62

Figure 3.7: a) Real permittivity within the Reststrahlen band of undoped InAs and Si:InAs ($\omega_p = 900 \text{ cm}^{-1}$). b) TMM reflectance map of undoped $5 \mu\text{m}$ InAs film on GaAs substrate in Otto configuration (geometry in d)) with an air gap $d_{Gap} = 40 \mu\text{m}$. The dashed lines denote the TO and LO phonon frequencies of InAs and GaAs. c) TMM reflectance map of $5 \mu\text{m}$ Si:InAs film on GaAs substrate. Air gap dependent calculations at a constant incident angle ($k = 1.05k_o$) for undoped InAs and Si:InAs are provided in e) and f). 66

Figure 3.8: a) Real and imaginary permittivity of GaSb and AlSb.³⁸ b) p- and c) s-polarized TMM reflectance map calculated in Otto configuration (geometry in d)) of GaSb thin film on highly doped InAs ($\omega_p = 2500 \text{ cm}^{-1}$) substrate. e) p- and f) s-polarized TMM reflectance map calculated in Otto configuration (geometry in d)) of AlSb thin film on highly doped InAs substrate. 68

Figure 3.9: TMM reflectance showing (a) SPhP-ENP dispersion in undoped InAs-GaSb film and (b) SPP-ENP-ENZ dispersion in Si:InAs-GaSb film in Otto configuration (geometry in (c)) with an air gap $d_{Gap} = 30 \mu\text{m}$. The dashed lines denote the TO and LO phonon frequencies of GaSb. (d) TMM reflectance showing (a) uncoupled dispersion in undoped InAs-AlSb film and (b) SPP-ENP-ENZ dispersion in Si:InAs-AlSb film in Otto configuration (geometry in (f)) with an air gap $d_{Gap} = 20 \mu\text{m}$. The dashed lines denote the TO and LO phonon frequencies of AlSb..... 70

Figure 3.10: (a) Calculated TMM dispersion of SPPs in uncoated Si:InAs ($\omega_p = 1500 \text{ cm}^{-1}$). The calculated dispersion of InAs-AlSb bilayer films with AlSb thicknesses of 250 nm, 500 nm, and 750 nm are provided in (b), (c), and (d). The geometry of the simulations is provided in (e). 72

Figure 4.1: a) Calculated p-polarized reflectance map of doped InAs ($\omega_p = 1500 \text{ cm}^{-1}$) resonator array at angle of incidence of 22° showing the gap-dependent dispersion of the monopole resonance. The geometry of the array is displayed in c). b) s- and p-polarized reflectance of

undoped InAs pillar array with $G = 1.5 \mu m$. The monopole and transverse dipole resonances are labeled. d) Monopole frequency for array with $G = 2.5 \mu m$ as a function of InAs plasma frequency. b) and d) were also calculated at 22° 77

Figure 4.2: a) Angular dispersion of monopole resonance supported by doped InAs at interpillar gap distances of $G = 1.5, 2.5, \text{ and } 3.5 \mu m$. In order to compare the relative shift in the monopole resonance as a function of angle, the resonance frequency was normalized to the extrapolated value at 0° . b) Current density ($J(x)$) extending from InAs resonator (edge of resonator: $x=0$ nm) of monopole resonance at 25 nm below substrate surface. The current density was normalized to the maximum current density (resonator edge). 2D calculation of current density of monopole resonance is provided in c). 78

Figure 4.3: Calculated reflectance maps for the structure shown in c) with AlSb thicknesses of a) $t_{AlSb} = 100 \text{ nm}$ and b) $t_{AlSb} = 200 \text{ nm}$. The plasma frequency of the InAs is $\omega_p = 1500 \text{ cm}^{-1}$. The blue dashed line represents the dispersion of the uncoupled monopole mode ω_G^{MP} , whereas the grey dashed lines are the ENP and ENZ dispersion (labelled on figure). The upper (UB) and middle (MB) branches of the hybrid dispersion are shown as solid blue lines. The coupling strength g_0 is displayed as a function of AlSb thickness in d). 82

Figure 4.4: a) Energy hybridization model of strong coupling between a monopole mode and the ENZ and ENP modes. Strong coupling between the monopole mode, ENZ mode, and ENP mode results in a splitting into three hybrid modes. b) Electric fields oriented along the z-direction for the upper (UB, top panel) and middle (MB, middle panel) branches and the uncoupled monopole resonance (bottom panel). 83

Figure 4.5: a) Calculated reflectance map from Fig. 4a ($t_{AlSb} = 100 \text{ nm}$). b) and c) display the Hopfield components of the middle (MB) and upper (UB) of the hybrid dispersion displayed in a). d) displays the angular dispersion of the UB at three different gap distances $G = 1.5, 2.5, \text{ and } 3.5 \mu m$ (marked in a) as red, grey, and blue dashed lines, respectively). e) displays the angular dispersion of the MB at the same three gap distances. The resonant frequency was normalized to the resonant frequency at normal incidence in order to account for the differences in spectral positions of the modes. 85

Figure 4.6: a) Calculated reflectance map of the structure in b) when $t_{ENZ} = 0 \text{ nm}$ at 22° showing the dispersion of the monopole resonance supported by CdO resonators. Calculated reflectance maps of the structure in b) where $t_{ENZ} = 50 \text{ nm}$ and c) $N_{ENZ} = 6 \times 10^{19} \text{ cm}^{-3}$ and d) $N_{ENZ} = 8 \times 10^{19} \text{ cm}^{-3}$. A clear anticrossing is observed in the gap-dependent dispersion for both carrier densities. 86

Figure 5.1: a) Schematic of conventional NDIR sensor. b) Proposed NIREM-enabled NDIR sensor design. c) Perspective view and cross-section of 120 nm In: CdO film deposited onto 110 nm Au-coated flat sapphire substrate. The same layer thicknesses were deposited onto the PSS substrate sample depicted in d). Here we provide a perspective and top-view of the PSS sample, with geometry labeled. 90

Figure 5.2: a) Schematic of cut of showing cone height and layer thicknesses. b) SEM image of the CdO-coated flat substrate sample. SEM images of coated CdO on PSS samples at d) normal

incidence and e) 22° angle of incidence. In f) we provide an SEM image of a milled CdO film grown on a metal backplane in order to show the columnar growth. 91

Figure 5.3: a) Angle-dependent thermal emission measurements of the flat CdO film sample shown in e). b) Angle-dependent thermal emission measurements of the CdO on PSS sample shown in f). c) and d) display the simulated angle-dependent absorption spectra for the flat CdO and CdO on PSS samples, respectively. The feature seen at 2349 cm⁻¹ in a) and b) is due to absorption from ambient CO₂. 93

Figure 5.4: Polar peak emissivity plots for the a) CdO on PSS and b) CdO flat film samples. The black line represents the measured angle-dependent, unpolarized emissivity and red line is the simulated angle-dependent, unpolarized absorption. Contour plots showing the measured emissivity of the CdO PSS NIREM and CdO Berreman film are displayed in c) and d). 95

Figure 5.5: a) Z-oriented electric field (E_z) and Poynting vector (S) of ENZ mode (2550 cm⁻¹). b) Z-oriented E_z and S of diffractive mode (3000 cm⁻¹). Both field profiles were simulated at a 20° angle of incident. 96

Figure 5.6: Contour plots displaying the simulated angle-dependent p-polarized absorption for a) $p = 2.8 \mu m$, b) $p = 3.02 \mu m$, and c) $p = 3.2 \mu m$. d) Topview of CdO on PSS sample with pitch labeled. e) Spectral dispersion of diffractive mode for three pitches shown in a), b), and c). 98

Figure 5.7: Simulated p-polarized absorption spectra detailing the pitch dependence at normal incidence for the CdO on PSS sample. As the pitch is increased and diffractive mode redshifts through the ENZ mode, the interference effect leads to a reduction in absorption linewidth. 99

Figure 5.8: a) and c) show the s- and p-polarized thermal emission from the CdO on PSS sample depicted in e). b) and d) show the s- and p-polarized thermal emission spectra for the CdO flat film sample depicted in f). 101

Figure 5.9: Absorption spectra at 250°C comparing the performance of our CdO on PSS narrowband emitter to a blackbody at CO₂ concentrations of 400 and 50 ppm. Our narrowband emitter performs comparably to the blackbody sample even at low CO₂ concentrations (50 ppm). 103

Figure 5.10: Normal (0°) incidence thermal emission from CdO on PSS sample, showing spectral overlap with CO₂, N₂O, and CO absorption.¹⁵⁹ 104

Figure 5.11: Absorption spectra illustrating the error analysis performed at CO₂ concentrations of 100 ppm and 200 ppm for our CdO NIREM. The solid lines show the average (\bar{A}) of 10 absorption spectra performed at 250°C. The dashed lines show the average shifted by the standard deviation (σ_A). 105

Figure 6.1: a) Simulated reflectance (solid line) of CdO-on-bottom structure displayed in c). TP modes are supported when $Im(Z_{DBR})$ (red line) is equal to $-Im(Z_{CdO})$ (blue line). Note as well that a dip in DBR reflectance (dashed line) corresponds with the zero-crossing of $Im(Z_{DBR})$. b) Simulated reflectance of the CdO-on-top TP structure displayed in e). The equivalent circuit model representation of the structures in c) and e) are displayed in d) and f), respectively. 110

Figure 6.2: a) Polarized, angle-resolved reflectance calculated (using TMM) for the CdO-on-top structure displayed in figure 6.1e. b) Polarized, angle-resolved reflectance calculated for the CdO-on-bottom structure displayed in figure 1c. 113

Figure 6.3: a) The designable parameters (thickness and carrier density) of the TPP-WS-EMs are randomly initialized, and the spectra of the designed structure (DS) is compared with the target spectrum. The thickness is updated by calculating the gradient over the difference (*error*) through the TMM. b) Following the gradient, the *error* is minimized through iterations, and the structure is optimized. The photo of a fabricated TPP-WS-EM is included to show the scale. The layer thickness of this optimized structure is labeled in the schematic. 116

Figure 6.4: The inverse-design algorithm was employed to realize TMM-EM structures featuring a) single, high Q-factor emission in the MWIR, b) single emission mode in the LWIR, and resonant emission designed for NDIR sensing of c) CO₂ and d) N₂O. The target spectra are plotted as blue dashed lines, while the emissivity experimentally measured at 150°C is plotted as red lines. Blue and red dashed curves are calculated absorption spectra of inversely designed and as-grown thickness, respectively. 120

Figure 6.5: a) TPP-WS-EM designs targeting at DMMP spectra with CdO and gold as metal layers. b) The emissivity (reflectance) of the same DBR on CdO of different carrier densities (sapphire substrate). The plasma frequency of CdO with a carrier density of $7 \times 10^{19} \text{ cm}^{-3}$ ($4.3 \times 10^{20} \text{ cm}^{-3}$) is displayed by the vertical dashed line (above 4000 cm^{-1}). 122

Figure 6.6: Measured absorption spectra of CO₂ at different concentration overlapped with the emission profile of TPP-WS-EM at 250°C. The shadowed region is the absorption band of CO₂, determined from a NIST dataset. 123

Figure 6.7: a) EMs targeting at single frequency with different Q-factors. b) multiple-peak TPP-WS-EM. c) One TPP-WS-EM featuring absorption at LWIR, MWIR and telecommunication simultaneously. d) Matching the absorption spectrum of NO gas for filterless NDIR..... 125

Figure 7.1: Isofrequency contour of a) Type I and b) Type II hyperbolic media. The arrows in the insets indicate the directions of the electric (E) and magnetic (H) fields, the Poynting vector (S), the momentum (k) and the group velocity (v_g) of the HP modes. Reprinted from [ref⁹⁴]. 128

Figure 7.2: EMT-calculated in- ($\epsilon_{x,y}$) and out-of-plane (ϵ_z) real permittivity of CdO HMMs with $f = 0.3$ (red line), $f = 0.5$ (black line), and $f = 0.7$ (blue line) are displayed in a) and b), respectively. The carrier densities of the high and low-doped CdO layers are $N_d = 3 \times 10^{20} \text{ cm}^{-3}$ and $N_d = 3 \times 10^{19} \text{ cm}^{-3}$. c) Phase-diagram of a CdO HMM with the high and low-doped CdO layers of $N_d = 3 \times 10^{20} \text{ cm}^{-3}$ and $N_d = 3 \times 10^{19} \text{ cm}^{-3}$. The dashed lines are the filling fractions of the dielectric functions displayed in a) and b). 133

Figure 7.3: a) Calculated reflectance maps for the structure shown in c) using EMT. b) Calculated reflectance map of the structure in c) where $t = 200 \text{ nm}$ 134

Figure 7.4: a) Kretschmann ATR measurement of the IML with a sapphire (black) and Au (red) backplane b) Diagram of measurement. 135

Figure 7.5: a) Dispersion of film in c) with $t_{HMM} = 1.5 \mu m$. b) Thickness dependence at constant angle ($k_{||}/k_o = 1.37$). The contour plots were calculated using TMM and the data points are from measurements..... 138

Figure 7.6: a) Dispersion relation of sample #2 from table 7.1 ($N = 3e19, 3e20 cm^{-3}$). a) Dispersion relation of sample #1 from table 7.1 ($N = 9e19, 2.4e20 cm^{-3}$). Contour plots are from TMM calculations and the measured values are included as data points overlaying the contour plots..... 140

Figure 7.7: a) s- (black line) and p- (red line) polarized ATR measurements showing resonances supported in the dielectric regime of a CdO HMM with $f = 0.3$. The effective dielectric function of this film is displayed in c). b) p- (red line) polarized ATR measurements showing resonances of a CdO HMM with $f = 0.7$. The response between the Type II and Type I hyperbolic band is featureless (besides the absorption from the IML). The effective dielectric function of this film is displayed in d)..... 143

Figure 7.8: a) Dispersion calculated in face-down geometry (c)). b) Calculated dispersion in the face up geometry (d))..... 145

Figure A1: a) Matching CO. (b-d) Matching the envelope spectra of O₃, CH₄, and NH₄ respectively. 149

Figure B1: a) Experimental setup showing external, angle-dependent thermal emission rig. b) Backport for angular rig as well as external backport thermal emission device used for gas cell measurements. Both diagrams are not drawn to scale. 154

LIST OF ABBREVIATIONS

ENZ	Epsilon Near Zero
SPP	Surface Plasmon Polariton
SPhP	Surface Phonon Polariton
ENP	Epsilon Near Pole
Q-factor	Quality Factor
FOM	Figure of merit
FWHM	Full width at half maximum
VASE	Variable angle spectroscopic ellipsometry
XRR	X-ray reflectometry
SEM	Scanning electron microscopy
HiPIMS	High power impulse magnetron sputtering
FTIR	Fourier transform infrared spectroscopy
ATR	Attenuated total reflectance
MCT	Mercury Cadmium Telluride
DLaTGS	Deuterated L-alanine doped triglycene sulphate
VACNT	Vertically aligned carbon nanotubes

IML	Index matching liquid
GAO	Grazing angle objective
UV	Ultraviolet
NIR	Near-infrared
MIR	Mid-infrared
LWIR	Long-wave infrared
FIR	Far-infrared
CdO	Cadmium Oxide
InAs	Indium Arsenide
AlSb	Aluminum Antimony
GaAs	Gallium Arsenide
GaSb	Gallium Antimony
Ge	Germanium
AlO_x	Aluminum Oxide
r-Al₂O₃	R-plane Sapphire
SiC	Silicon Carbide
HfS₂	Hafnium Disulfide
HfSe₂	Hafnium Diselenide

hBN	Hexagonal Boron Nitride
MgO	Magnesium Oxide
Si	Silicon
Au	Gold
TMDC	Transition metal dichalcogenide
TCO	Transparent Conducting Oxide
TO	Transverse optic
LO	Longitudinal optic
LOPC	LO phonon plasmon coupling
UID	Unintentionally doped
PSS	Patterned sapphire substrate
NDIR	Non-dispersive infrared
CO₂	Carbon Dioxide
N₂O	Nitrous Oxide
CH₄	Methane
N₂	Nitrogen
O₃	Ozone
NH₃	Ammonia

DMMP	dimethyl methylphosphonate
DOS	Density of states
MEMS	Micro-electromechanical system
LED	Light emitting diode
QCL	Quantum cascade laser
NIREM	Narrowband infrared emitting metamaterial
TPP-WS-EM	Tamm plasmon polariton wavelength selective emitter
TP	Tamm plasmon
MQW	Multiple quantum well
EMT	Effective medium theory
TMM	Transfer matrix method
SGD	Stochastic gradient descent
HMM	Hyperbolic metamaterial
VINSE	Vanderbilt Institute of Nanoscience and Engineering

LIST OF PUBLICATIONS

Parts of this dissertation have been adapted with permission from the following publications (*denotes equal contributions):

In Preparation

1. *Designer Tamm Plasmon Films using Gradient Descent Optimization.* M. He*, **J. R. Nolen***, J. Nordlander, A. Cleri, N. S. McIlwaine, G. Lu, T. G. Folland, Y. Tang, B. A. Landman, J. P. Maria, J. D. Caldwell, submitted (2021).
2. *Modifying Hybrid Polariton-Epsilon-Near-Zero in Multilayer Cadmium Oxide Films.* **J. R. Nolen**, A. Cleri, J. Nordlander, T. G. Folland, K. Kelley, E. L. Runnerstrom, J. P. Maria, J. D. Caldwell, in prep. (2021).
3. *Spectroscopic Investigation of Monolithic, Homoepitaxial Hyperbolic Metamaterials.* **J. R. Nolen**, A. Cleri, M. He, E. L. Runnerstrom, K. Kelley, T. G. Folland, J. P. Maria, J. D. Caldwell, in prep. (2021).
4. *Mid- to Far-Infrared Dielectric Functions of HfS_2 and HfSe_2 .* **J. R. Nolen**, S. Miki-Silva, T. G. Folland, S. Law, J. D. Caldwell, in prep. (2021).

Published

1. *Filterless Non-dispersive Infrared Sensing using Narrowband Infrared Emitting Metamaterials.* A. Livingood*, **J. R. Nolen***, T. G. Folland, L. Potechin, G. Lu, S. Criswell, J. P. Maria, C. T. Shelton, E. Sacht, J. D. Caldwell, ACS Photonics 8, 2, 472–480 (2021).
2. *Ultraviolet to far-infrared dielectric function of n-doped Cadmium Oxide thin films.* **J. R. Nolen**, E. L. Runnerstrom, K. P. Kelley, T. S. Luk, T. G. Folland, A. Cleri, J. P. Maria, J. D. Caldwell, Phys. Rev. Materials 4 (2), 025202 (2020).

Chapter 1

1. Introduction

1.1 Mid- and Long-Wave Infrared Optical Sources

The mid-infrared (MIR) and long-wave infrared (LWIR), which together spans from ~ 2.5 – $12 \mu\text{m}$, is home to a large number of fundamental molecular vibrations as well as two atmospheric transmission windows ($\lambda \sim 3\text{--}5$ and $8\text{--}12 \mu\text{m}$) making this spectral range technologically vital for many sensing and communication applications. Despite the potential for technological advancements in the MIR to LWIR, these developments have been hindered by a lack of suitable optical sources that would make these applications realizable. The incoherent emission from a thermal emitter, such as a glo-bar, has been the method of choice for broadband spectroscopic techniques such as Fourier transform infrared (FTIR) spectroscopy. Although FTIR spectroscopy is widely used and generates high-resolution reflectance and transmission spectra, this technique is inherently ill-suited for portable, compact use outside of a lab setting. The broad bandwidth of the incoherent thermal sources used in FTIR poses major drawbacks in other instances where a light-weight, narrow band, light-emitting-diode (LED)-like, source would be more useful, for instance in atmospheric and molecular spectroscopy or for IR beacons for military applications. Further, a narrowband emitter that emits in one of the aforementioned atmospheric windows with a designed directionality and controlled polarization would prove desirable for free space communications.

Currently, these requirements can only be met commercially with gas-phase lasers, such as CO_2 , with emission wavelengths centered at $\lambda = 9\text{--}11 \mu\text{m}^1$, and quantum cascade lasers (QCLs)². However, the large spatial footprint, low wall-to-plug efficiencies, and high costs render these impractical for portable uses as well as in sensing techniques such as nondispersive infrared (NDIR) sensing. Recent work has shown that narrowband, polarized, and directional emission can be realized from a thermal source by controlling the emissive properties of a material. These devices rely on subwavelength structuring of doped and/or polar semiconductor or insulating materials in order to tailor the absorptivity through the excitation of localized surface polariton modes. Further, recently published work has shown that, in some cases, these devices can operate

from waste heat alone³, thereby increasing their utility for low power applications such as search and rescue.

1.2 Polaritonics for Infrared Emissivity Control

1.2.1 Surface Plasmon Polaritons and Surface Phonon Polaritons

Polaritons are hybrid light-matter excitations resulting from the strong coupling between light and a coherently oscillating charge. A wide variety of volume and surface-bound polaritons exist,⁴ however the focus of this dissertation will be on propagating and localized surface plasmon polaritons (SPPs) and surface phonon polaritons (SPhPs) which are supported at the interface between dielectric ($Re(\epsilon_d) > 0$) and metallic ($Re(\epsilon_m) < 0$) materials. Note that the designation of dielectric and metallic materials is solely based on the material's optical response to an incident plane wave and not indicative of the material's electronic properties. Under p -polarization, the following polaritonic dispersion relation can be found as a solution to Maxwell's equations.

$$k_{\parallel} = k_o \sqrt{\frac{\epsilon_m \epsilon_d}{\epsilon_m + \epsilon_d}} \quad (1)$$

where $k_o = \frac{2\pi}{\lambda_o} = \frac{\omega}{c}$ is the light-line in vacuum, and ϵ_m and ϵ_d are the complex dielectric functions of the polaritonic (metallic) and dielectric materials, respectively. Note that as $\sqrt{\epsilon_m \epsilon_d / \epsilon_m + \epsilon_d} > 1$ for $Re(\epsilon_m) < 0$ the in-plane momentum of a surface polariton only exists at in-plane momentum larger than what can be accessed from free space. An example SPhP dispersion plot is provided in fig 1.2a in section 1.2.3 along with multiple methods of overcoming the momentum mismatch between incident light and polariton modes. Upon excitation by one of these techniques, the resulting surface wave is propagative in-plane, along the surface of the metallic interface, with an evanescent field extending out-of-plane into the dielectric medium. As $Re(\epsilon_m)$ approaches $-Re(\epsilon_d)$ the in-plane wavevector increases asymptotically, eventually extending to $k_{\parallel} \rightarrow \infty$ when $Re(\epsilon_m) = -Re(\epsilon_d)$ in the lossless case. Since the polaritonic wavelength relates inversely to the in-plane momentum $k_{\parallel} = \frac{2\pi}{\lambda_{sp}}$, the resultant polaritonic wavelength and mode-volume are compressed to sub-diffractive dimensions. Confining the electric field to sub-diffractive spatial volumes is exciting for several reasons including providing a method for enhancing light-matter interactions as well as a route towards scaling down the size of optical components.

The first, and arguably most-well studied, quasiparticles we will discuss are SPPs which arise from the interaction between light and free carrier oscillations in metals and doped semiconductors. The dielectric function for a plasmonic material can be found by considering the motion and consequent polarization of a free electron gas of carrier density N_d driven by an external AC electric field, known as the Drude-Lorentz model. The resultant complex dielectric function is

$$\varepsilon(\omega) = \varepsilon_\infty - \frac{\omega_p^2}{\omega^2 + i\gamma\omega} \quad (2)$$

where γ is the drude damping constant, ε_∞ is the high-frequency permittivity which correspond to the background polarizability due to interband transitions, and the plasma frequency $\omega_p = \sqrt{N_d e^2 / m^* \varepsilon_0}$ is dictated by the carrier density. When light is incident on a plasmonic material with a frequency below the plasma frequency, the free carriers in the material oscillate coherently in the direction opposite the electric field vector, screening and reflecting the field at the metallic surface. Put in terms of eq. 2, $\varepsilon(\omega) < 0$ for $\omega < \omega_p$ and therefore the incident field is not permitted to propagate in the metal and thus decays exponentially. The elevated carrier densities native to noble metals places the plasma frequency in the NIR-visible-ultraviolet (UV) depending on the metal. Although these materials have formed the foundation for plasmonics in the visible, the low plasma frequency tunability and elevated optical losses at lower frequencies diminishes their utility beyond the NIR. This is more evident when considering the scattering from an idealized metallic sphere. The Fröhlich condition $Re(\varepsilon_m) = -2$ can be used to approximate the absorption cross-section of a plasmonic resonator supporting a localized SPP resonance (LSPR).

Doped semiconductors on the other hand, such as n-CdO, have shown great promise as MIR plasmonic materials due to their lower plasma frequencies which are controllable by doping during film growth that adds a great deal of design flexibility to MIR plasmonic structures. Further, the low optical losses in some high-mobility doped TCOs such as n-doped CdO, which can achieve Hall mobility values exceeding $500 \text{ cm}^2/\text{V}\cdot\text{s}$, can be leveraged to support sharp propagating and localized SPP resonances with Q-factors as high as 24. The optical properties of this material are investigated in chapter 2.

SPhPs behave in a similar way to SPP modes in that they are the manifestation of light coupling to a coherent charge oscillation, with the light-matter wavelength compressing to length scales below the diffraction limit. However, instead of coupling to the oscillation of free carriers as in a plasmonic film, here light couples to the optic phonons of a polar crystal lattice. The two types of optic phonons are transverse (TO) and longitudinal (LO) optic phonons, with the former being IR-active and therefore able to induce the electric field screening seen in plasmonic films. The TO and LO phonon frequency values for a material are dependent on set, material properties such as atomic mass, bond strength, and lattice structure and therefore lack the tunability of shown in plasmonic films of doped semiconductors. For non-polar materials, such as Si, the TO and LO phonons are degenerate at the Γ -point ($k_{\parallel} = 0$) in the phonon dispersion. However, the restoring force of the ionic motion in polar materials increases the LO-phonon frequency, lifting the degeneracy. Using a classical oscillator model, similar to the approach used for free carriers, the displacement of charged ions of the crystal lattice driven by an external AC field and dielectric function can be determined as

$$\varepsilon(\omega) = \varepsilon_{\infty} \left(1 + \frac{\omega_{LO}^2 - \omega_{TO}^2}{\omega_{TO}^2 - \omega^2 - i\Gamma\omega} \right) \quad (3)$$

where ε_{∞} is the permittivity at frequencies much higher than the phonon resonance, Γ is the damping rate and ω_{TO} and ω_{LO} are the TO and LO phonon frequencies, respectively. Due to the strong resonant absorption associated with the TO phonon, the dielectric function increases significantly as the frequency approaches the TO phonon, the sign of the permittivity is then flipped at the TO phonon frequency and remains negative until reaching the LO phonon frequency. In this spectral region between the TO and LO phonon frequencies, known as the Reststrahlen band, the incident field is screened at the polar dielectric interface by the coherent ionic oscillations in a similar way as in plasmonic films below the plasma frequency, resulting in a band of high reflectivity. SPhPs can also be supported in the Reststrahlen band at in-plane wavevectors greater than the free-space light line. Owing to the long scattering lifetimes of optic phonons (on the order of picoseconds) that greatly exceed the lifetime of free carriers (tens of femtoseconds) in plasmonic materials, SPhPs offer exceptionally low optical losses, translating to narrow resonant linewidths.⁵ However, as was stated before, SPhPs lack the tunability of plasmonic films through doping.

Although methods for providing modest perturbations to the optical phonon frequencies in polar materials have been demonstrated, the values are largely set in place.

1.2.2 Epsilon-Near-Zero Polaritons and Berreman Modes

Epsilon-near-zero (ENZ) polaritons can be induced near the zero crossing of the real permittivity $Re(\epsilon_m) \rightarrow 0$ in polaritonic films of deeply sub-wavelength thicknesses ($t \approx \lambda_p/50$).^{6,7} Here, λ_p is either the plasma wavelength in plasmonic media or the wavelength of the LO phonon in polar dielectrics. For polaritonic films with thicknesses greater than the material skin depth, the dispersion (in air) is asymptotic at $Re(\epsilon_m) = -1$, as discussed above (blue line in Fig. 1.1a, red line in Fig. 1.1c). If the film thickness is decreased to below the skin depth strong coupling occurs between polaritons supported on the opposing interfaces of the thin film, which hybridize into high- and low-frequency branches (blue and red lines in Fig. 1.1b), with the former blue-shifting to above the $Re(\epsilon_m) = -1$ condition (blue line in Fig. 1b, green line in Fig. 1.1c). Since surface polaritons can only exist when $Re(\epsilon_m) < 0$, as the thickness is decreased further the mode will become less dispersive and continue to blue shift until becoming asymptotic at $Re(\epsilon_m) \approx 0$ (blue line in Fig. 1.1c). These novel excitations are associated with an extreme enhancement of the electric field, due to conservation of the normal displacement field $\epsilon_{amb}E_{amb} = \epsilon_{ENZ}E_{ENZ}$, enabling control over light-matter interactions such as resonant perfect absorption and strong nonlinear interactions.^{8,9} The Berreman mode is also supported in deeply subwavelength films.⁷ However, unlike the ENZ mode, which requires additional in-plane momentum (see section 1.2.3) in order to be excited, the dispersion of this mode exists inside the free-space light cone (point ‘A’ in Fig. 1.1c) and can therefore couple to free-space. The dispersion relationship of Berreman and ENZ modes supported in a thin films can be calculated by considering a thin film (ϵ_2) separating two semi-infinite dielectric media (ϵ_1 - top, ϵ_3 - bottom) illuminated under p -polarization.⁷

$$1 + \frac{\epsilon_1 k_{z3}}{\epsilon_3 k_{z1}} = i \tan(k_{z2} d) \left(\frac{\epsilon_2 k_{z3}}{\epsilon_3 k_{z2}} + \frac{\epsilon_1 k_{z2}}{\epsilon_2 k_{z1}} \right) \quad (4)$$

Here, ϵ_i is the complex dielectric function, d is the film thickness, and $k_{zi}^2 = \epsilon_i \frac{\omega^2}{c^2} - k_{\parallel}^2$ where $i = 1, 2, 3$

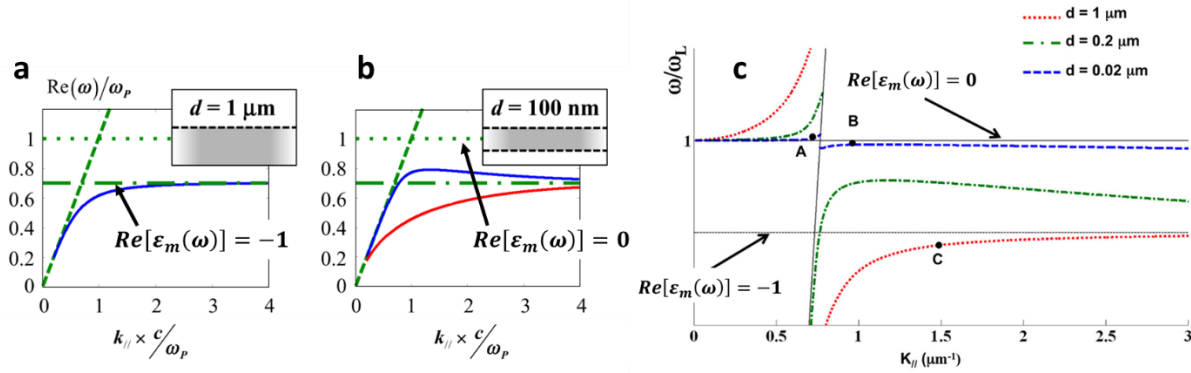


Figure 1.1: Dispersion relation for an optically a) thick and b) thin film. As the film thickness is decreased to below the skin depth the surface polariton dispersion splits into upper (blue) and lower (red) branches due to strong coupling. [from ref. ⁶] c) Dispersion relation of three films of varying thicknesses with ENZ frequency at ω_L . The oblique line is the light line in air and horizontal lines are $Re(\epsilon_m) = -1$ and $Re(\epsilon_m) = 0$, as labelled. [from ref. ⁷]

1.2.3 – Coupling to Polaritons

As stated above, a solution to the SPP and SPhP dispersion relation can only be found outside the light cone in air and therefore these modes cannot be coupled to with a planewave from free space. There are however several techniques of ‘slowing down’ the incident light and overcoming the momentum mismatch. One common method of coupling to polariton modes in films is through prism-coupling, otherwise known as attenuated total reflectance (ATR) measurements. ATR measurements utilize the resultant evanescent wave from total-internal-reflection from the backside of a high refractive index prism. With control over the incident angle, the achievable in-plane momentum range extends to $k_{\parallel} = n_{prism}k_0 \sin \theta$, allowing the polaritonic dispersion to be probed to the light line within the prism (see Fig. 1.2a). There are two configurations of ATR measurements of interest here: the Kretschmann and Otto configurations, which are depicted in Fig. 1.2b and 1.2c, respectively.^{10–12} Kretschmann configuration ATR measurements are performed with the sample in contact with the prism, with the polariton mode being excited on the opposing side of the film (typically into air). In Otto measurements, an air gap separates the prism from the sample and the polariton is excited in the gap between the prism and the sample. Both configurations offer benefits and drawbacks, which have been discussed elsewhere.¹³

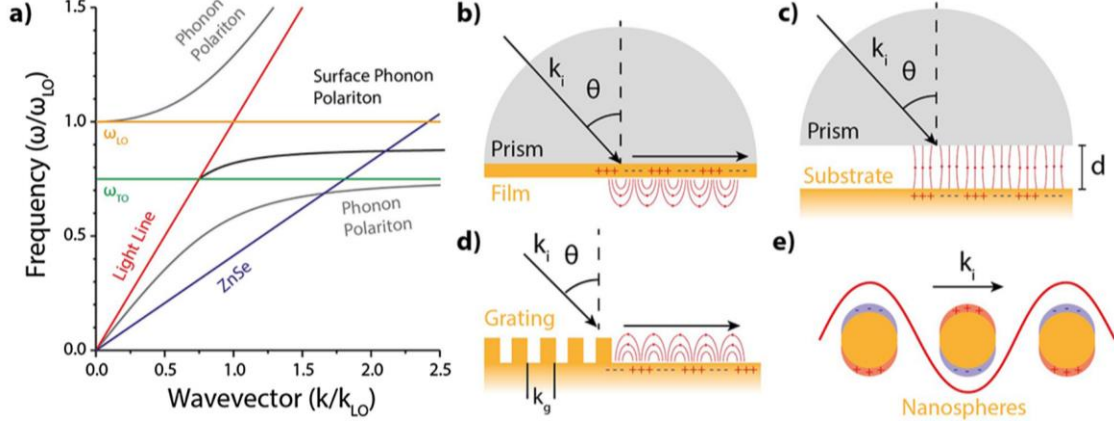


Figure 1.2: a) Polaritonic dispersion of polar dielectric semiconductor. The dispersion in a) can be probed using ATR measurements in the b) Kretschmann or c) Otto configuration. Alternatively, a d) grating could also be used to diffractively couple to a propagating surface polariton. e) Localized surface polaritons can also be supported in deeply-subwavelength resonators. [from ref.¹³].

Another approach of exciting polaritonic modes is through diffractive coupling. Here the periodicity of a grating structure (see Fig. 1.2d) along the film supplies the auxiliary momentum necessary to couple to the propagating polariton mode ($k_{\parallel} = k_0 \sin \theta + \frac{2\pi}{\Lambda} m$) where Λ is the period of the grating and m is an integer. The periodicity of the grating folds the SPP or SPhP dispersion into the first Brillouin zone, therefore permitting coupling from free space. The dispersion relation of SPhPs in SiC using grating coupling is displayed in Fig. 3b in the next section.

The final technique for coupling to surface polaritons from free space is by exciting localized surface polaritons in particles of sub-wavelength dimensions. These can be individual particles, as shown in Fig. 1.2e, such as sharp metal coated atomic-force microscope tips in the context of scattering-type scanning near-field optical microscopy or arrays of resonant antenna structures. Arrays of resonant antennas have been used in a number of applications such as surface enhanced infrared absorption (SEIRA)^{14,15} and for producing narrowband thermal emission.^{16,17} Unlike the other methods described above, here the resonant frequency stays nominally constant with changing incident angle. The resonance is, however, dependent on the size and shape of the structure. Therefore, by plotting the fundamental dipole resonance position as a function of inverse structure size, the polaritonic dispersion can be mapped.

1.3 Engineering Far-Field Thermal Emission

At non-zero temperatures excess thermal energy in a material sets electrons and atomic nuclei into oscillatory motion, generating fluctuating dipole currents. These fluctuating currents produce radiation within the material that can escape into the far-field as thermal emission. The spectral radiance of an ‘ideal’ thermal emitter, referred to as a blackbody, is given by Planck’s law¹⁸:

$$L_{BB}(\omega, T) = \frac{\hbar\omega^3}{4\pi^3 c^2} \frac{1}{e^{\hbar\omega/(k_B T)} - 1} \quad (5)$$

where c is the speed of light in air, \hbar is Planck’s constant, k_B is the Boltzmann constant, ω is the frequency of the emitted light, and T is the temperature of the blackbody. As the temperature of the body increases, the peak of the spectral radiance shifts to higher energy in accordance to Wien’s displacement law, which states $\lambda_{peak} T \approx 2898 \mu m \cdot K$, placing the peak emission wavelength within the MIR for temperatures ranging from ~ 300 to 1400 K.

For a real material the spectral radiance is given as $L(\omega, T, \theta) = \varepsilon(\omega, T, \theta)L_{BB}(\omega, T)$, where $\varepsilon(\omega, T, \theta)$ is the emissivity of the material surface. Conventional thermal emitters, such as glo-bars and filaments, possess high and nominally non-dispersive emissivities. Therefore, the emitted radiation is broadband with low angle sensitivity, making them useful for room lighting and as an incoherent broadband light source, as is required in FTIR. However, the broadband, non-directional emission from these traditional sources is less useful for many applications where either narrow band, polarized and/or spatially coherent light is needed. Narrowband emission can however be achieved by engineering the emissivity of the material surface and/or choosing materials with spectral emissivities that vary strongly with frequency. Kirchhoff’s law states that in thermal equilibrium (and in the absence of scattering) the absorptivity and emissivity of a material are the same $\varepsilon(\omega, T, \theta) = \alpha(\omega, T, \theta)$.¹⁹ Therefore, by modifying the absorptivity ($\alpha(\omega, T, \theta) = 1 - R(\omega, T, \theta) - T(\omega, T, \theta)$) of the surface through nanostructuring the emissive properties can in turn be modified. In the next section we discuss spatial coherence and how it can be engineered in thermal emitters.

1.3.1 Spatially Coherent Thermal Emission

The spatial coherence of a wave is the measure of its ability to interfere with a spatially translated version of itself. For an emitter, the spatial coherence dictates the degree of directionality of the emission. The coherence of a wave with an electric field $E(r)$ at position r can be characterized using a first-order correlation function.²⁰

$$g(r, r + \delta r) = \frac{\langle E^*(r)E(r+\delta r) \rangle}{\sqrt{I(r)I(r+\delta r)}} \quad (6)$$

where $I(r)$ is the intensity and $\langle \dots \rangle$ indicates statistical averaging. From the correlation function, the spatial coherence length $L_c(\omega)$ can then be calculated by determining the position where $g(r, r + \delta r)$ decays by $1/e$. Emitters with low coherence lengths, such as traditional thermal emitters, emit isotropically. On the other hand, those with a high coherence length can produce highly directional radiation. Using the correlation function to determine the coherence length can often be non-trivial, therefore in most cases the coherence length is estimated from the angular dispersion as $L_c(\omega) \propto \Delta\theta^{-1}$. From this expression, a narrow angular resolution for emission at a given frequency is associated with a long coherence length.

The seminal work of Greffet et. al.²¹ demonstrated that by patterning a grating on the surface of SiC, spatial coherence of thermal emission can be achieved by outcoupling thermally excited SPhP modes supported at the SiC interface (Fig. 1.3b).²¹ Since then, there has been plenty of excitement in realizing other platforms for directional thermal emission. Some recent examples include Berreman mode supporting films which exhibit absorption that is highly angular and polarization-dependent (Fig. 1.3a). Another example is thermal emission from tamm plasmon devices which has been shown to exhibit a parabolic angular dispersion.²² Tamm plasmon thermal emitters will be the subject of chapter 6. Fabricating antenna arrays with a non-uniform phase profile on SiC focusing of thermal emission has been proposed theoretically (Fig. 1.3c).²³ Finally, strong coupling between propagating (dispersive) SPhPs and localized (non-dispersive) SPhP modes has been demonstrated as method of controlling the emission profile of a SiC surface (Fig. 1.3d).²⁴

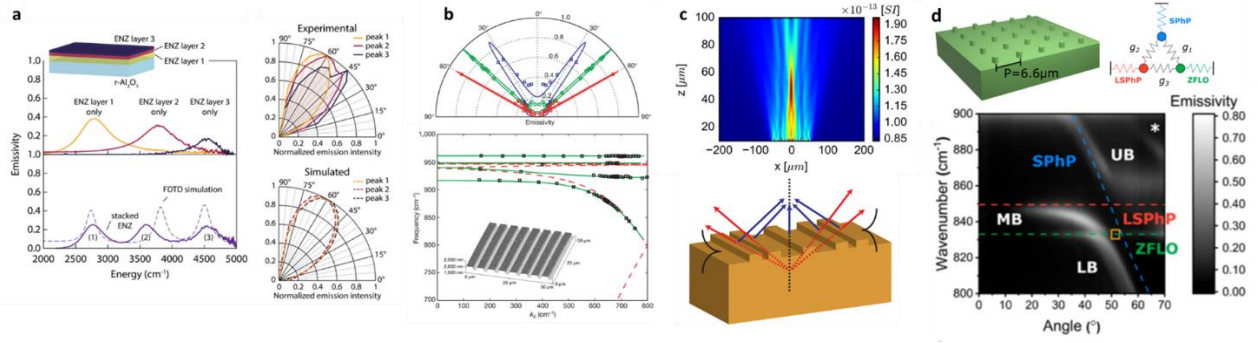


Figure 1.3: a) Thermal emission from Berreman modes in planar multilayer CdO films. [from ref.²⁵] b) Spatial-coherence of thermal emission realized through out-coupling of thermally-excited SPhP modes on a SiC surface. [from ref.²¹] c) Schematic of thermal emission focusing from SiC surface using bullseye pattern. [from ref.²³] d) Strong coupling between a ZFLO and localized and propagating SPhPs for controlling thermal emission. [from ref.²⁴]

1.4 Dissertation Overview

The objective of this dissertation is to realize novel approaches towards achieving spectral and spatial control over thermal emission. In **Chapter 2**, the optical properties of CdO thin films are extracted by a combination of VASE and FTIR techniques. The exciting properties of CdO enable the demonstrations presented in later chapters. We also extract the dielectric function from a HfS₂ crystal using FTIR micro-spectroscopy. This group III TMDC is a promising material for potential applications within the FIR and THz. In **Chapter 3**, the focus is shifted to polaritonic strong coupling in multilayer films. Two systems are investigated in this chapter, first we experimentally investigate SPP-ENZ strong coupling in multilayer CdO films. We then theoretically study SPhP-ENZ and SPP-ENZ-ENZ strong coupling in multilayer III-V semiconductor heterostructures. In **Chapter 4**, we illustrate how strong coupling in multilayer resonators supporting monopole-ENZ hybrid modes can be used to control the spatial coherence of thermal emission. In **Chapter 5**, we characterize a NIREM consisting of an ENZ mode-supporting CdO layer deposited onto a PSS. The PSS allows for the efficient outcoupling of the ENZ mode to free space, therefore enabling high, narrowband emissivity. The device was designed to emit at one of the molecular vibrational frequencies of CO₂. A proof-of-concept CO₂ detection experiment is performed, showing similar performance to conventional detection schemes. In **Chapter 6**, an inverse design technique is employed to design aperiodic Tamm plasmon-supporting films with broadly tunable emissivity. Here we experimentally demonstrate Tamm plasmon thermal emitters featuring single and multiple peak emission with significant control over

the spectral positions and linewidths. Further, we explore more advanced designs which are capable of matching to non-trivial target spectra, such as achieving a strong match to the absorption spectra of a greenhouse gases, and also achieve extremely high Q-factors. In **Chapter 7**, we use ATR measurements to investigate the optical properties of homoepitaxial HMMs consisting of alternating layers of high- and low- doped CdO. Two method of tunability are provided: carrier densities and filling fraction are presented. Finally, in **Chapter 8** a brief conclusion and a discussion of potential future research avenues are provided.

Chapter 2

2. Extraction of the Dielectric Functions of n-doped Cadmium Oxide and Hafnium Disulfide using Ellipsometry and FTIR Spectroscopy

2.1 Interaction of Light with Semiconductor Films

Light can interact with a semiconductor in a number of ways. Most notably, photons of a sufficiently large energy can trigger electronic transitions in the material, resulting in interband absorption. The onset of interband transitions in the absorption spectrum of a material, known as the absorption edge, occurs at the bandgap energy (E_g) which is dictated by the electronic band structure. However, the optical properties of a semiconductor are not governed solely by its electronic band structure. For example, infrared light can interact with the optic phonons of a polar material, resulting in absorptive and reflective features infrared spectra. The phonon dispersion represents the fundamental vibrations of the crystal lattice and is governed by the bond strengths and atomic masses of the constituent atoms. Introducing free carriers, through doping, can also significantly alter the optical properties of a semiconductor, resulting in metallic-like behavior, i.e. high reflectivity, below the plasma frequency and increased optical losses.

Although the underlying physics of these interactions differ, what they have in common is that the incident light is coupling to a charge oscillation within the material. For light with a frequency larger than the bandgap (usually in the visible-ultraviolet), light couples to the bound electron oscillations (electric dipole transitions) within the atoms. Well below the bandgap, the incident oscillating field can excite vibrational oscillations (phonons) in the lattice by displacing ions from their equilibrium positions. Finally, in doped semiconductors (and metals), light can drive free-charge oscillations, a result of the unbound nature of the free electrons (or holes). We will discuss each of these oscillations in greater detail later in this chapter. Although, these represent some of the most common interactions between light and semiconductors this is by no means a comprehensive list.

2.1.1 The Dielectric Tensor

The dielectric tensor of a material contains all information regarding its first-order optical response. As such, determining the dielectric tensor (dielectric functions along a particular

direction) components of a material are of immense interest for optical, polaritonic, and optoelectronic applications. A number of experimental techniques have been employed in order to extract the components of a dielectric function, such as ellipsometry or reflectance/transmission measurements. These methods will be included in the discussion of a later section in this chapter. Here, we provide a brief derivation and discussion of the dielectric tensor and its relationship to the oscillators mentioned above.

A dipolar oscillator (such as the ones mentioned in the previous section) contributes to the linear polarization $\mathbf{P}(\mathbf{k}, \omega)$ of a semiconductor induced due to the presence of an electromagnetic field $\mathbf{E}(\mathbf{k}, \omega)$:

$$\mathbf{P}(\mathbf{k}, \omega) = \varepsilon_0 \vec{\chi}(\mathbf{k}, \omega) \mathbf{E}(\mathbf{k}, \omega) \quad (1)$$

The polarization and applied electric field are linked by the second-rank electric susceptibility tensor $\vec{\chi}(\mathbf{k}, \omega)$, which describes all linear processes of the medium. Here, we assume that the applied field intensity is low and therefore the probability for higher-order (non-linear) effects is insignificant. If non-linear effects were present, the electric susceptibility would be a function of the electric field intensity. In eqn. 1, \mathbf{k} and ω are the wavevector and frequency and ε_0 is the permittivity of free space. It is more typical to consider the electric displacement field which relates to both the electric field and polarization:

$$\mathbf{D}(\mathbf{k}, \omega) = \varepsilon_0 \mathbf{E}(\mathbf{k}, \omega) + \mathbf{P}(\mathbf{k}, \omega) \quad (2)$$

$$= \varepsilon_0 \vec{\varepsilon}(\mathbf{k}, \omega) \mathbf{E}(\mathbf{k}, \omega) \quad (3)$$

where $\vec{\varepsilon}(\mathbf{k}, \omega)$ is the dielectric tensor which relates to the electric susceptibility as:

$$\vec{\varepsilon}(\mathbf{k}, \omega) = \varepsilon_{ij}(\mathbf{k}, \omega) = 1 + \chi_{ij}(\mathbf{k}, \omega) \quad (4)$$

Later in this chapter we describe how the elements of this dielectric tensor can be extracted through ellipsometry and FTIR reflectance measurements. In these studies, the samples we are interested in (CdO thin films and HfS₂ crystals) have relative dimensions (thickness) much larger than the wavelength of the incident light. Therefore, it is reasonable to assume that the interacting photon wavevector \mathbf{k} is zero and non-local effects can be ignored. We will abbreviate the dielectric tensor accordingly to $\vec{\varepsilon}(\omega)$.

In its most general form, the dielectric tensor for a medium can be expressed as a 3x3 matrix where each matrix element contains the dielectric function along a given Cartesian axis in response to an applied field along the same or along a different direction.

$$\varepsilon_{ij}(\omega) = \begin{bmatrix} \varepsilon_{11}(\omega) & \varepsilon_{21}(\omega) & \varepsilon_{31}(\omega) \\ \varepsilon_{12}(\omega) & \varepsilon_{22}(\omega) & \varepsilon_{32}(\omega) \\ \varepsilon_{13}(\omega) & \varepsilon_{23}(\omega) & \varepsilon_{33}(\omega) \end{bmatrix} \quad (5)$$

As an example, the element $\varepsilon_{11}(\omega)$ describes the optical response along direction 1 to an applied field directed along direction 1. Element $\varepsilon_{21}(\omega)$ describes the optical response along direction 1 to an applied field directed along direction 2, and so on. In the majority of cases, however, the dielectric tensor can be simplified to only the terms along the diagonal.

$$\varepsilon_{ij}(\omega) = \begin{bmatrix} \varepsilon_{11}(\omega) & 0 & 0 \\ 0 & \varepsilon_{22}(\omega) & 0 \\ 0 & 0 & \varepsilon_{33}(\omega) \end{bmatrix} \quad (6)$$

The elements $\varepsilon_{11}(\omega)$, $\varepsilon_{22}(\omega)$, and $\varepsilon_{33}(\omega)$ correspond to the dielectric functions along the x, y, and z directions. For materials with highly symmetric crystal structures, such as cubic systems, the optical properties are expected to be isotropic along all crystal axes, and therefore $\varepsilon_{11}(\omega) = \varepsilon_{22}(\omega) = \varepsilon_{33}(\omega)$. Optically isotropic materials are commonly used in infrared optical components (polarizers, prisms, windows, etc.) due to their lack of polarization insensitivity. Some examples include CaF_2 , which has a face-centered cubic structure, or silicon and germanium, which both have a diamond crystal structure. At room temperature CdO has a rocksalt crystal structure, which is symmetric along all crystal directions and therefore is modeled as isotropic in the following sections. The crystal structures of group IV and VI TMDCs, for example MoS_2 ²⁶, HfS_2 ²⁷, and HfSe_2 ²⁷, are hexagonal, resulting in a dielectric tensor that is uniaxial. Materials with uniaxial optical properties have one tensor component that differs from the other two. For example, TMDCs and other 2D materials, such as hBN ²⁸ and graphene, are in-plane isotropic, however, the out-of-plane (along the c-axis) dielectric function differs from the in-plane components $\varepsilon_{11}(\omega) = \varepsilon_{22}(\omega) \neq \varepsilon_{33}(\omega)$. Uniaxial anisotropy is not limited to 2D materials and is observed in numerous bulk crystals, such as several polytypes of SiC .^{24,29,30} Further, uniaxial anisotropy can be engineered in artificial metamaterials by growing films composed of alternating layers each featuring a sub-wavelength thickness.³¹⁻³³ Materials with optical properties that differ along all

crystal directions $\epsilon_{11}(\omega) \neq \epsilon_{22}(\omega) \neq \epsilon_{33}(\omega)$ possess biaxial anisotropy. For example, near- and far-field studies of the biaxial material $\alpha\text{-MoO}_3$ ³⁴, which has an orthorhombic crystal structure, have yielded the exotic properties of phonon-polaritons in this material that result in the in-plane hyperbolicity reported in the natural crystal. Lastly, the dielectric tensors of materials with less symmetric crystal structures, such as the monoclinic $\beta\text{-Ga}_2\text{O}_3$ ³⁵ and triclinic ReS_2 ³⁶ and ReSe_2 ,^{37,38} have non-zero off-diagonal elements. Determining these off-diagonal terms is beyond the scope of this chapter.

2.2 Experimental Techniques for Extracting Semiconductor Dielectric Functions

Several methods have been employed to extract the complex dielectric functions of semiconductor materials. In this section, we provide a short overview of two common techniques and discuss their unique benefits and drawbacks. The first approach is to measure the reflection and/or transmission spectra of the material while the second is to use variable angle spectroscopic ellipsometry (VASE). The post-processing steps following either measurement technique is the same: build a physical oscillator model that describe the absorptive processes and use least-squares fitting to determine the approximate dielectric function of the material. In section 2.3 we will discuss some of the common building blocks (oscillators) of these models. It is not uncommon to either combine these two approaches or to supplement with other analytical techniques, such as Raman spectroscopy, Hall effect measurements, or X-ray diffraction, profilometry, or atomic force microscopy to determine sample thickness. This reduces the degrees of freedom and ultimately the potential correlations between parameters within the model fit.

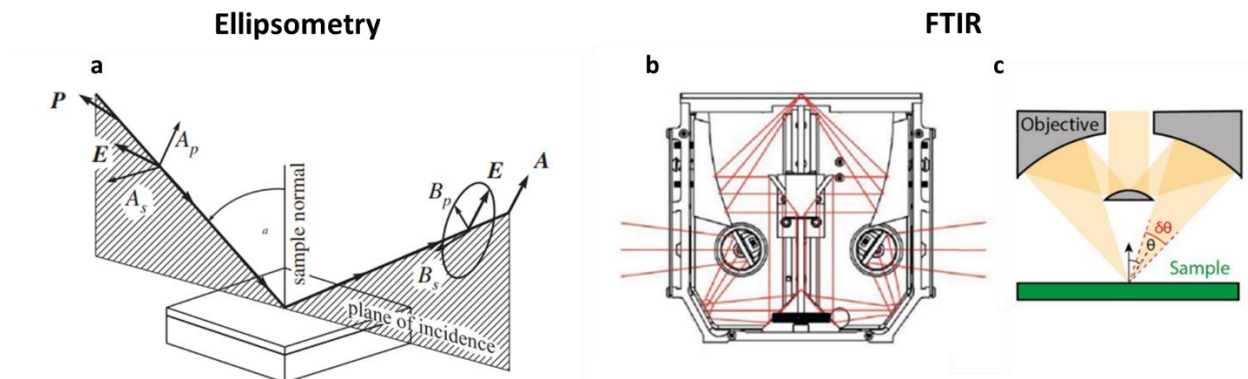


Figure 2.1: a) Schematic defining the plane of incidence (P) and polarized wave amplitudes (A_s , A_p , B_s and B_p). [from ref ³⁹] b) Schematic of variable angle reflectance instrument (Pike Technologies) for large-scale FTIR measurements. c) Light path of Cassegrain objective for microscope FTIR measurements. [from ref ¹³]

2.2.1 Reflection and Transmission Spectra

Perhaps the simplest approach for determining the frequency-dependent optical properties of a material is to collect polarized reflection and/or transmission spectra. In the infrared, these spectra are typically collected using FTIR spectroscopy, whereas in the visible-UV these measurements are performed using UV-Vis spectroscopy. Here we will focus our discussion on measurements performed in the IR. Conventional FTIR utilizes a broadband light source (typically a SiC glowbar) that is highly emissive throughout the IR. Light from the broadband source then passes through a Michelson interferometer and is directed to either the sample compartment located inside of the bench, or to the IR microscope for measuring small-scale samples. The light is then reflected from or transmitted through the sample and collected at the detector. For a more detailed description of FTIR spectroscopy, as well as the trade-offs between different detectors see Folland et. al¹³.

For both reflection and transmission measurements a reference/background spectrum is collected and the sample spectrum is normalized to the reference spectrum by dividing $R, T = \text{sample/reference}$. For reflectance measurements, the reference spectrum is collected from a metal mirror (usually Au) that provides near 100% reflection throughout the IR. The reference spectrum for transmission measurements is performed in air or vacuum. Polarized, angle-resolved reflection and transmission measurements can be performed in the FTIR sample compartment using a variable-angle reflection or transmission rig, such as those available from Pike Technologies. This approach is best for large-scale, uniform films deposited onto a planar substrate.

The collected reflection and/or transmission spectra can then be used to extract the complex dielectric function by comparing to the calculated Fresnel reflection coefficients. Expressed in terms of permittivity the s - and p - polarized complex reflection coefficients of light incident on medium j from medium i are:

$$r_{s,ij} = \frac{k_{z,i} - k_{z,j}}{k_{z,i} + k_{z,j}}, r_{p,ij} = \frac{\frac{k_{z,j}}{\epsilon_{z,j}} - \frac{k_{z,i}}{\epsilon_{z,i}}}{\frac{k_{z,j}}{\epsilon_{z,j}} + \frac{k_{z,i}}{\epsilon_{z,i}}} \quad (7) \text{ and } (8)$$

where $\varepsilon_{(i,j)}$ is the complex dielectric function of the respective layer and $k_{z,(i,j)} = \sqrt{k^2 \varepsilon_{(i,j)} - k_x^2}$.

Note that the angle of incidence is accounted for through k_x . In equations 7 and 8 it is assumed that the $i - j$ interface bisects two half spaces, and therefore film j is assumed to have an infinite thickness. However, for real films a summation over partial waves due to multiple reflections from the backside of the finite-thickness film must be taken into account. This can be calculated through the geometric summation:

$$r_{ijk} = \frac{r_{ij} + r_{jk} \exp(2ik_{z,j}d_j)}{1 + r_{ij}r_{jk} \exp(2ik_{z,j}d_j)} \quad (9)$$

where d_j is the thickness of the film, and r_{ij} and r_{jk} are the Fresnel coefficients for the front and back interfaces, respectively. Equation 9 therefore takes into account the reflection between the film and the substrate (k). Further, the reflectance coefficient for a multilayer stack with an arbitrary number of layers can be calculated by starting at the furthest-most interface and working backwards to the interface at which the light is first incident. The transmission coefficients can then be calculated as $t_{s,p} = 1 + r_{s,p}$ and the reflected and transmitted power calculated as $R_{s,p} = |r_{s,p}|^2$ and $T_{s,p} = 1 - R_{s,p}$, respectively. Knowing the varying contributions to the optical response of the material (i.e. phonons or free-carriers) a model can be built and the dielectric function extracted by using least squares-fitting software such as WVASE, which is frequently used for the fitting of ellipsometric data, to fit to the measured spectra. Note that this method can be used to model both isotropic and anisotropic materials, as the relative influence of the components of the dielectric tensor are dependent on the angle of incidence and polarization.

In addition to the simplicity in collecting these measurements, another advantage of using FTIR spectroscopy is that these measurements are operated under an N_2 atmosphere. Further, some FTIR instruments, such as the Bruker Vertex 70v, can be operated under vacuum, thus eliminating spectral artifacts that arise from fluctuations in atmospheric gases that strongly absorb infrared light, such as H_2O and CO_2 . Therefore, angle-resolved FTIR reflectance measurements can be successfully employed to extract the dielectric function across a wide spectral range, as has been shown in previous literature and in the following sections.⁴⁰

Perhaps the biggest advantage that the FTIR technique has over VASE is that by coupling the FTIR with an IR microscope, the collection area can be reduced significantly. Using an IR

microscope, the collection area is now only restricted by the diffraction limit and therefore the minimum collection area is a function of the spectral range of interest. This adds more flexibility and opens the door to the measurement of small-scale samples such as exfoliated 2D materials.⁴¹ Microscope-based FTIR has been demonstrating as an approach for extracting the dielectric function materials with isotropic, uniaxial, and biaxial optical responses. For example, this is the approach we take in section 2.5 in order to extract the dielectric functions of HfS₂. Further, this is the approach taken to extract the dielectric function of α -MoO₃.³⁴

2.2.2 Spectroscopic Ellipsometry

The polarization state of light incident upon a material is not conserved upon reflection. The change in the polarization of the reflected light is dependent on the optical properties of the material. Ellipsometry measurements determine this shift in the polarization state by relating the ratio of reflected, linearly-polarized electric field amplitudes (B_p/B_s) to the ratio of incident, linearly-polarized electric field amplitudes (A_p/A_s). Figure 2.1a shows a schematic of an ellipsometry measurement where linear p - and s - polarized light with equal magnitudes are incident upon the surface of a sample. Here, p - polarized light and s - polarized are oriented parallel and perpendicular to the plane of incidence, respectively. Upon reflection, the ratio of polarized field amplitudes shifts and the value ρ can be determined as

$$\rho = \frac{\left(\frac{B_p}{B_s}\right)}{\left(\frac{A_p}{A_s}\right)} \quad (10)$$

However, this can be expressed in terms of the p - and s - polarized reflection coefficients $R_p = B_p/A_p$ and $R_s = B_s/A_s$ which are more convenient to determine experimentally. Then ρ can instead be expressed as the ratio of the p - and s - polarized Fresnel reflection coefficients which relate to two ellipsometric parameters, ψ and Δ , through the following expression:

$$\rho = \frac{\left(\frac{B_p}{B_s}\right)}{\left(\frac{A_p}{A_s}\right)} = \frac{R_p}{R_s} = \tan(\psi) e^{i\Delta} \quad (11)$$

In this expression, ψ and Δ represent the amplitude and phase difference between the two polarizations, respectively. Combined, these two quantities enable VASE as a comprehensive approach towards quantifying the optical response of films and substrates featuring isotropic and anisotropic crystal structures.

To this date, instruments have been constructed for performing VASE measurements from the THz^{42,43} through to the UV. Infrared (IR)-VASE utilized an FTIR source and IR detector, usually a DLaTGs for mid- to near-IR or helium-cooled bolometer for far-IR, to study optical properties throughout the IR. One of the benefits of ellipsometry is that this technique is not reliant on references or background measurements, such as an Au-coated substrate for FTIR reflection measurements. This reduces the number of potential non-idealities associated with slight differences in experimental conditions between measurements and also reference standards that are non-ideal. However, VASE is limited in utility to large-scale samples. Therefore, at this point, VASE is not suitable for determining the dielectric function of materials that require a small collection area, such as 2D materials. For these materials, it is more appropriate to utilize polarized, microscope measurements as is described in the previous section and as we perform in section 2.5. Here, we have only provided a brief discussion of ellipsometry. There are, however, more in-depth discussions provided elsewhere.³⁹

2.3 Modelling of Common Light-Matter Interactions in Semiconductors

In this section we provide some of the common oscillators employed to model the dielectric function of a material. These sections will be referenced in sections 2.4 and 2.5, wherein we discuss the various interactions comprising the dielectric functions of n-doped CdO and HfS₂, respectively. It is convenient to view the overall dielectric response of a material as a linear summation of the frequency-dependent contributions from individual oscillators. For example, as we demonstrate in section 2.4, the dielectric function spanning the FIR-UV for n-doped CdO is a combination of phonon, free carrier, and interband absorption processes.

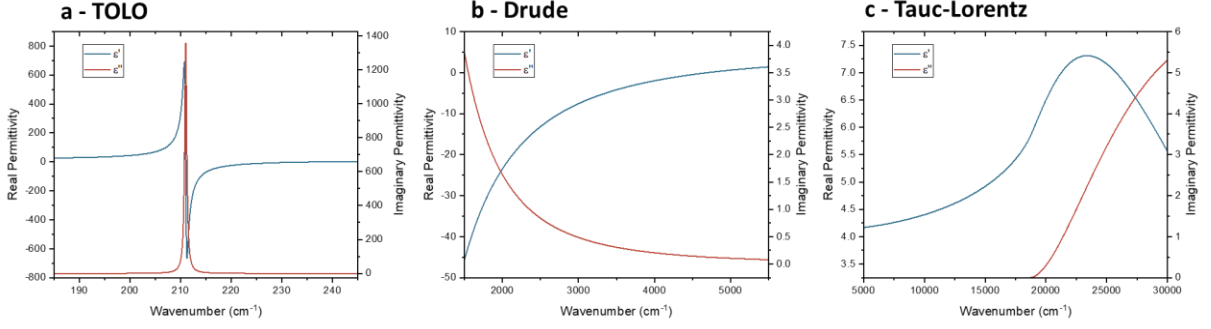


Figure 2.2: a) Real and imaginary permittivity near the optic phonons of undoped-InAs calculated using the TOLO function.[ref ⁴⁴] b) Contribution of free carriers to the dielectric function of a doped CdO film ($N_d = 3e20 \text{ cm}^{-3}$) calculated using the Drude model. c) Contribution of bandgap absorption to the dielectric function of CdO ($N_d = 1e20 \text{ cm}^{-3}$).

2.3.1 Tauc-Lorentz Model

The Tauc-Lorentz model has been used to account for absorption due to interband transitions and extract the optical constants of several doped semiconductors including n-doped CdO films and nanoparticles. This parameterized model, developed by Jellison and Modine^{45,46}, combines the 3D Tauc joint density of states for a direct bandgap semiconductor with the imaginary part of the Lorentz model for a collection of non-interacting atoms.

$$\varepsilon_{TL}(\omega) = \varepsilon'_{TL}(\omega) + i[\varepsilon''_T(\omega)\varepsilon''_L(\omega)] \quad (12)$$

The Tauc contribution to the imaginary permittivity above the bandgap is given by:

$$\varepsilon''_T(\omega) = A_T \left(\frac{\omega - \omega_T}{\omega} \right)^2 \Theta(\omega - \omega_T) \quad (13)$$

Here, A_T is the Tauc amplitude and ω_T is the optical bandgap. ω is the photon frequency and the Heavyside function ($\Theta(\omega - \omega_T)$) is equal to zero for $\omega < \omega_T$ and one for $\omega > \omega_T$. This ensures that the imaginary permittivity below the bandgap is zero. The imaginary part from the Lorentz oscillator model is expressed as:

$$\varepsilon''_L(\omega) = A_L \frac{\omega_o \omega C}{(\omega^2 - \omega_o^2)^2 + \omega^2 C^2} \quad (14)$$

where A_L is the amplitude of the Lorentzian, C is the broadening, and ω_o is the center frequency. The product of $\varepsilon''_T(\omega)$ and $\varepsilon''_L(\omega)$ results in the Tauc-Lorentz imaginary permittivity:

$$\varepsilon_{TL}''(\omega) = \frac{A_{TL}\omega_o C(\omega-\omega_T)^2}{(\omega^2-\omega_o^2)^2+\omega^2 C^2} \frac{\Theta(\omega-\omega_T)}{\omega} \quad (15)$$

Here, A_{TL} is the total Tauc-Lorentz amplitude ($A_{TL} = A_T A_L$). Note again that due to the Heavyside function the imaginary permittivity from the Tauc-Lorentz model is zero below the bandgap. Therefore, absorption within the bandgap and intraband absorption cannot be accounted for using the Tauc-Lorentz model alone. Knowing the imaginary dielectric function, the real part can be calculated using the Kramers-Kronig relation:

$$\varepsilon_{TL}'(\omega) = \varepsilon_{\infty,TL} + \frac{2}{\pi} P \int_{\omega_T}^{\infty} \frac{\xi \varepsilon_{TL}''(\xi)}{\xi^2 - \omega^2} d\xi \quad (16)$$

The high-frequency permittivity ($\varepsilon_{\infty,TL}$) describes the contribution to the real dielectric function well above the bandgap and P indicates that the Cauchy principal value of the integral is to be taken. The full expression for the real part of the permittivity has been calculated and can be found elsewhere. For a single Tauc-Lorentz oscillator there are a total of five fit parameters: $\varepsilon_{\infty,TL}$, A_{TL} , C , ω_o , and ω_T . In several cases, a single Tauc-Lorentz oscillator is sufficient for reproducing the absorption above the bandgap. However, to model the interband absorption of materials with more complicated band structures additional oscillators may need to be employed. The values of $\varepsilon_{\infty,TL}$ and ω_T will be the same for all oscillators, therefore each new oscillator requires three additional fit parameters: $A_{TL,n}$, C_n , and $\omega_{o,n}$, where n refers to the n^{th} oscillator. Figure 2.2c displays the resultant real and imaginary parts of a single Tauc-Lorentz oscillator.

2.3.2 Free Carrier Absorption

The Drude model has been employed in the past to model the near-IR – mid-IR complex dielectric functions of highly-doped semiconductors,⁴⁷ as well as most metals.⁴⁸ While the residual polarizability from interband transitions dictates the scaling of the real part of the dielectric function within the IR, for doped semiconductors, such as CdO, this spectral range is dominated by free-carrier effects. The influence of free-carriers can be modelled using the Drude formalism:

$$\varepsilon_{Drude}(\omega) = -\frac{A_D}{\omega^2 + i\gamma\omega} \quad (17)$$

In this equation, A_D is expressed as $A_D = \varepsilon_\infty \omega_p^2$. As is stated above, ε_∞ is the real permittivity at frequencies far above the plasma frequency. The magnitude of ε_∞ is a result of the background polarizability of the lattice due to interband transitions at much higher frequencies. Therefore, if the spectral range of interest were truncated to below the band edge absorption, such that interband absorption were not considered in the model, ε_∞ would represent the contribution from interband absorption to the real part of the permittivity. The imaginary part is driven by the free-carrier damping (γ), which is inversely related to the corresponding scattering lifetime. Alternatively, the free-carrier damping can be expressed as being inversely related to the optical mobility $\gamma = \frac{e}{\mu_{opt} m^*}$, therefore a large mobility translates to low optical losses. The plasma frequency $\omega_p = \sqrt{N_d e^2 / m^* \varepsilon_\infty \varepsilon_0}$ increases with the square root of the electron carrier density $\sqrt{N_d}$, with ε_0 and m^* representing the permittivity of free space and effective mass, respectively. Note, that below the plasma frequency the real permittivity is negative and therefore an incident electric field would be ‘screened’ at the interface resulting in high reflectivity.

Due to the correlation between N_d and m^* in calculating the plasma frequency, these values cannot be determined from least-squares fitting simultaneously. However, the carrier density can be determined through alternative techniques, such as Hall effect measurements, in order to decrease the number of fit parameters.

2.3.3 Infrared Active Phonons in Polar Semiconductors

Phonons, the collective excitation of the atoms in a crystal lattice, fall into two general categories: acoustic and optical phonons. Optical phonons, as opposed to acoustic phonons, intersect the Γ -point ($k = 0$) in the phonon dispersion and therefore (in some cases) can be excited with light. Whether an optical phonon mode can interact directly with light, referred to as an infrared (IR)-active mode, is governed by the ionicity of the bonds in the crystal and the selection rules which can be derived from group theory. However, a discussion of these selection rules is beyond the scope of this section.

In a polar dielectric, the bonds are ionic in character. The restoring force of the ionic charge motion associated with the LO phonon lifts the degeneracy with the TO modes at the Γ point.⁴⁹ This increases the LO phonon frequency, resulting in a spectral band between these two optical phonon energies that is referred to as the Reststrahlen band. The frequencies at which these phonon

modes fall is related to the masses of the atoms in the crystal. Polar crystals with heavier elements tend to have phonon frequencies at lower frequencies, whereas lighter elements tend to have higher frequency phonon modes. Again, the TO-LO splitting is governed by the ionicity of the bonds. Therefore, for covalent crystals, such as Si and Ge, the TO and LO phonons are not IR-active and the TO-LO degeneracy is not lifted.

Within the Reststrahlen band, polar materials are highly reflective, resulting from the charge screening of the oscillating polar crystal lattice. Just as light can couple to free charge oscillations in metals and doped semiconductors (SPPs), light can also couple to optic phonons in polar lattices. These excitations, known as surface phonon polaritons (SPhPs) are also of keen interest for IR nanophotonics.^{5,49-51} This results from the real part of the permittivity becoming negative between the TO and LO phonon frequencies. In contrast to Drude response, for this so-called ‘TOLO oscillator model’ the real part of the permittivity disperses rapidly, becoming progressively more positive with increasing frequency until the TO phonon frequency, resulting in ultra-high refractive indices due to the strong resonant absorption associated with the TO phonon.^{29,52-54} For perspective, near the TO phonon in SiC, the index of refraction can exceed 20 (Highest reported $n = 21.84$).^{16,54-57} At the TO-phonon frequency, the sign of the permittivity is flipped and remains negative (and highly dispersive) until the LO-phonon frequency. For a single IR-active phonon, the permittivity can be derived from a simple harmonic oscillator model resulting in the so-called ‘TOLO’ oscillator:

$$\epsilon_{TOLO}(\omega) = \epsilon_{\infty,TOLO} \left(\frac{\omega_{LO}^2 - \omega_{TO}^2}{\omega_{TO}^2 - \omega^2 - i\gamma\omega} \right) \quad (18)$$

where ω_{LO} and ω_{TO} correspond to the LO and TO phonon frequencies, respectively. The high frequency permittivity $\epsilon_{\infty,TOLO}$ defines the real part of the dielectric function at frequencies above the LO phonon frequency. Note that in the case where the Drude and TOLO terms must be taken into account that the high-frequency term for both oscillators would be the same.

Although equation 18 has been successfully utilized to model the permittivity of several polar materials, such as hBN and SiC, this approximation fails when anharmonic phonon coupling must be taken into effect. In this case the TO ($\gamma_{TO,i}$) and LO ($\gamma_{LO,i}$) phonon damping for the same phonon branch (i) would not be assumed to be the same, as in equation 18. This is true of materials

with multiple phonon modes that are close in frequency, such as in perovskites and alkali halides.^{58,59} A more general representation of the TOLO oscillator that allows for independent TO and LO damping has been derived as

$$\varepsilon(\omega) = \varepsilon_{\infty,TOLO} \prod_i^n \frac{\omega_{LO,i}^2 - \omega^2 - i\omega\gamma_{LO,i}}{\omega_{TO,i}^2 - \omega^2 - i\omega\gamma_{TO,i}} \quad (19)$$

Note that when $\gamma_{TO,i} = \gamma_{LO,i}$, this reduces to the simple harmonic oscillator model. In order for this model to be physical it is necessary that the condition $\sum_i^n (\gamma_{LO,i} - \gamma_{TO,i}) > 0$ be met, otherwise the imaginary permittivity well above the LO phonon frequency would become negative. In addition to modelling multiple phonon materials, equation 19 has been used to model the absorption due to two-phonon processes in MnO, MgO, and NiO.⁶⁰ In section 2.5 we will also demonstrate how this model can be used to reproduce TOLO and two-phonon absorption features in HfS₂.

2.4 Dielectric Function of n-doped CdO Thin Films

Transparent conducting oxides (TCOs) are most commonly utilized in applications requiring high optical transmittance and low electrical resistivity. This unique combination of optoelectronic properties is achieved by semiconductor materials possessing visible to UV bandgaps and high defect and/or extrinsic dopant concentrations, with the associated impurity close to the conduction band edge.^{61,62} In recent years, TCOs have also found utility as potential alternative plasmonic materials for nanophotonic applications within the NIR to MIR, due to the lower optical losses in reference to gold and most doped semiconductors in this spectral range.^{63,64}

Although CdO has been known as a TCO for over a century⁶⁵, recent work has demonstrated *n*-doped CdO as a unique plasmonic material with broad spectral tunability and exceptionally low optical losses, surpassed only by graphene.⁶³ These properties result due to the low effective mass (m^* ranging from 0.12 – 0.26 in epitaxially-grown films with carrier densities ranging from $N_d \approx 10^{19} - 10^{20} \text{ cm}^{-3}$) and high electron mobilities ($\mu > 300 \text{ cm}^2/\text{V-s}$ between $N_d \approx 10^{19} - 10^{21} \text{ cm}^{-3}$).⁶³ Interestingly, it has been demonstrated that μ actually increases with increasing carrier density over a broad range of accessible doping levels, reaching a maximum value of almost $500 \text{ cm}^2/\text{V-s}$ at $N_d \approx 5 \times 10^{19} \text{ cm}^{-3}$.⁶³ Multiple aliovalent dopants have been employed to exhibit this novel behavior including Dy³⁺⁶³, In³⁺⁶⁶, Y³⁺⁶⁷, and F⁶⁸, each of which

have atomic radii similar in size to either Cd^{2+} or O^{2-} . This allows for substitutional, aliovalent cation (e.g., Dy^{3+} for Cd^{2+}) or anion (e.g., F^- for O^{2-}) doping while minimizing lattice strain, and thus, carrier scattering. Very high-quality CdO film growth has recently been demonstrated using high-power impulse magnetron sputtering (HiPIMS).⁶⁷ This technique uses a pulsed (1-10 μs short pulses) DC plasma in order to attain extremely large power densities ($\geq \text{kW}/\text{cm}^2$) and therefore high sputter rates and high density films, all while maintaining low surface roughness.^{69,70} Surprisingly, HiPIMS deposition offers comparable doping precision, carrier mobility, and even improved material quality in comparison to CdO grown via molecular beam epitaxy (MBE), while allowing for potential scalability.

While traditional approaches for plasmonic applications in the near-IR have utilized noble metals, with applications realized in surface plasmon resonance (SPR) biosensing⁷¹⁻⁷³, enhanced vibrational spectroscopies such as surface enhanced Raman scattering (SERS)⁷⁴⁻⁷⁶, SEIRA^{14,15,77}, and optical metasurfaces such as planar lenses,⁷⁸⁻⁸⁰ there are significant drawbacks to using metals for MIR plasmonics.⁸¹ First, metals have large, fixed carrier densities resulting in static plasma frequencies that fall within the visible to ultraviolet regime, complicating their applications to longer wavelengths. Further, fast electron-electron scattering at these large carrier densities brings about high Drude losses, which are exacerbated in the MIR. These losses, combined with extremely large negative permittivity values in this spectral range, render noble metals impractical for applications requiring narrow resonant features such as chemical sensing⁸² or narrow-band IR sources.¹⁷ In contrast, CdO films are capable of supporting relatively sharp (Q-factors calculated here from the dielectric function to be as high as 24, 5 – 10x larger than gold in the MIR^{83,84}), frequency tunable resonances in the MIR, including highly-absorptive SPP and ENZ modes, all without the need for nanostructuring. Careful *in-situ* control over N_d during film growth has also opened the door to monolithic, multilayered films that exhibit metamaterial-like optical properties such as multi-frequency thermal emission. Similar multilayer films have also been used to demonstrate the potential for strongly coupled polaritonic systems, as will be explained in chapter 3.

Before CdO can be adopted for advanced applications, it is imperative that an accurate dielectric function be established and a full understanding of the various contributions controlling this function. This is especially pertinent for CdO, as the carrier density-driven modifications of

the bandgap, effective mass and high-frequency permittivity ensure that the dielectric function employed must be extracted from a film with similar doping levels, unless appropriate trends can be identified. While prior work examined the NIR dielectric function of non-epitaxial, polycrystalline CdO films⁸⁵, accurate experimental MIR dielectric functions for high-quality/extreme-mobility (i.e., grown by MBE or HiPIMS), CdO films have yet to be reported. Here, we experimentally measure the UV to FIR optical properties of epitaxial In:CdO thin films on MgO substrates (grown via HiPIMS) as a function of free-carrier density ($1.1 \times 10^{19} \text{ cm}^{-3}$ – $4.1 \times 10^{20} \text{ cm}^{-3}$) and extract their corresponding dielectric functions. We utilize both V-VASE and IR-VASE to measure the optical response and utilize these measurements to extract the complex dielectric function. Through this effort, we extend the focus beyond the NIR to include the UV and visible as well as the MIR to FIR, thereby accommodating the optical properties within the various IR atmospheric windows. In past work, high carrier densities ($N_d > 5 \times 10^{20} \text{ cm}^{-3}$) were achieved by using dopant densities as high as 10 mol%, potentially leading to the formation of secondary phases.⁸⁶ In comparison, the carrier densities of the films in this study remain below the dopant solubility limit. All films are epitaxial, phase pure, with consistently narrow x-ray linewidths and low surface roughness values.^{63,67,68} In addition to extracting the complex dielectric functions, we also compare the optical properties of these high-quality, In:CdO films with values reported in past work for polycrystalline, non-epitaxial In:CdO films. Finally, to supplement visible- and IR-VASE measurements, which provide ellipsometric data above 333 cm^{-1} , we utilized FTIR spectroscopy to extend the measured range to 150 cm^{-1} , allowing us to also determine the effects of low-energy phonons on the FIR dielectric function. Combined, these techniques allow for a complete characterization of the polarization-dependent reflection and transmission coefficients, and thus the tunable carrier density-dependent factors comprising the dielectric response of In:CdO from the UV to the FIR.

2.4.1 Fitting Procedure for Ellipsometric and FTIR Data

In this section we discuss our approach of extracting the complex dielectric function of n-CdO films from ellipsometric and FTIR measurements. We initiated the dielectric function fitting by focusing on the VASE measurements (Figure 2.3) in the MIR spectral range, which is dominated by free-carrier effects that can be modeled by the Drude oscillator model and at the focus of the high potential of this material for nanophotonic experiments and applications. Within

the Drude model, we initially set the effective mass to be a value falling in the range of those reported in the literature. for such highly doped CdO films. This allowed us to fit the corresponding ellipsometry spectra using only the high-frequency permittivity, carrier density and mobility as fitting parameters. The former was initially set to previously reported values and was restricted to the range between 4.5-5.5, and the carrier density and mobilities were allowed to vary within the prior reported ranges for this material. While the film thickness can be determined from ellipsometric measurements, in order to reduce the number of free fitting parameters, we implemented X-Ray reflectivity (XRR) which provides film thickness measurements with accuracy on the order of the X-ray wavelength (Cu K α : 1.54 Å). It is important to note that the film thicknesses were chosen such that they were significantly larger (> 150 nm) than the threshold for supporting ENZ polaritons. This was done in order to ensure that the extracted dielectric function was representative of the bulk behavior and to avoid the additional thickness dependence of such ENZ modes upon the dielectric function, as was recently reported for tin-doped indium oxide.⁸⁷ The CdO films were modelled in WVASE using two CdO layers, a thin carrier depletion/accumulation layer on top of a bulk layer, on an MgO substrate. In the fit the total thickness (thin layer + bulk layer) of the film was initially set to the value determined from XRR. To account for the thickness of the thin layer, which is not certain, each layer thickness was allowed to vary by $\pm 5\%$.

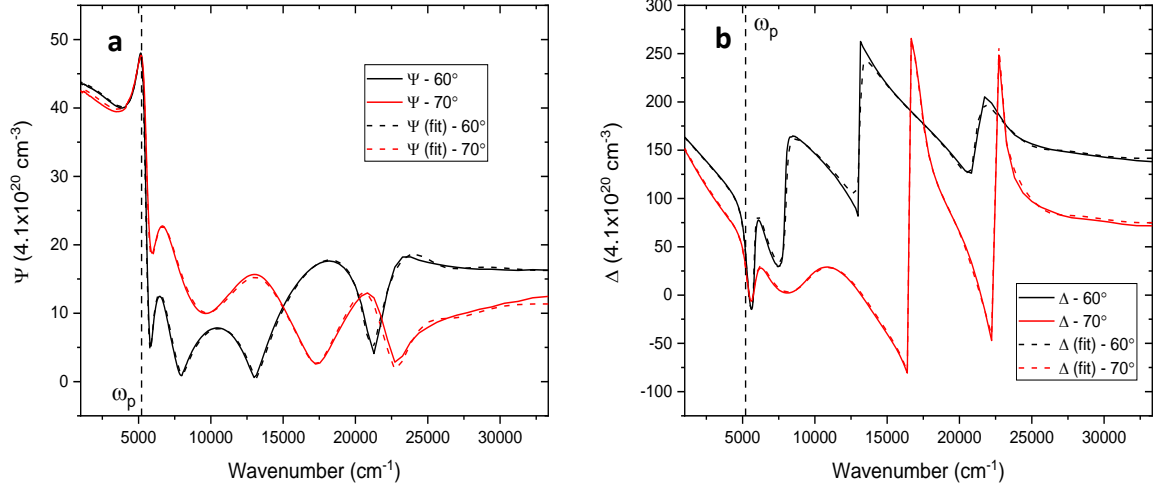


Figure 2.3: Representative experimental a) ψ and b) Δ spectra and corresponding least-squares fits for a In: CdO film with a carrier density of $4.1 \times 10^{20} \text{ cm}^{-3}$ at 60° (black) and 70° (red) incident angles. The vertical black dotted line represents the extracted plasma frequency of the film ($\omega_p = 5,218 \text{ cm}^{-1}$).

As the plasma frequency and plasma damping constants are only dependent upon the ratio of carrier density to effective mass ($\omega_p \propto \sqrt{\frac{N_d}{m_{eff}^*}}$) and the product of effective mass and optical mobility ($\gamma \propto (m_{eff}^* \mu_{opt})^{-1}$), respectively, this ratio and product were then treated as fixed parameters. Following the preliminary fitting procedure, we used the carrier density extracted from Hall effect measurements and input this into the ratio to extract the effective mass at this carrier density.

$$\omega_{p,Hall} = \omega_{p,fit} \rightarrow \frac{N_{Hall}}{m_{eff}^*} = \frac{N_{fit}}{m_{fit}^*} \quad (20)$$

Here, m_{fit}^* is the effective mass value set for MIR ellipsometric fitting and N_{fit} is the resultant fit value for carrier density. N_{Hall} is the carrier density measured using Hall effect measurements and m_{eff}^* is the true effective mass. We then used the calculated effective mass from this ratio as the known in the product dictating the damping constant to extract the optical mobility value.

$$\gamma_{fit} = \gamma_d \rightarrow m_{fit}^* \mu_{fit} = m_{eff}^* \mu_{opt} \quad (21)$$

Optical mobility values were compared with prior literature as well as to the values extracted from our Hall effect measurements to verify they were in reasonable agreement. Following this, the fit was performed once more using these newly extracted values to validate that the fit remained in agreement. The surface accumulation/depletion layer was determined to have a negligible effect on the MIR optical properties. Thus, in order to cut down on the number of fit parameters, the Drude oscillator was not included for this thin surface layer within this spectral range.

Following the fit of the ellipsometric data in the MIR, we then turned our focus to the FIR spectral range. Here, we utilized FTIR spectroscopy in order to supplement our VASE measurements, which provide ellipsometric data above 333 cm^{-1} . Polarized reflectance of the CdO films were measured at two angles (60° and 70°) from 150 cm^{-1} to 5000 cm^{-1} , spanning both the FIR and MIR, thereby providing spectral overlap with the ellipsometric data. A Drude oscillator equipped with the carrier density extracted from Hall effect measurements (N_{Hall}) and those extracted from our MIR ellipsometric fitting (m_{eff}^*, μ_{opt}) was included along with a TOLO oscillator term for fitting the impact of the polar ionic lattice. The spectral positions for the CdO TO and LO phonon frequencies were initially set to 262 cm^{-1} and 523 cm^{-1} , which correspond to previously-reported values, and were only allowed to vary within the fit over a narrow range ($\pm 2\text{ cm}^{-1}$). The TO and LO phonon damping constants were then determined by fitting the reflectance data fitting. The TOLO fit parameters are set to be identical for both the bulk and the surface charge CdO layers. We then take the TOLO fit values from the reflectance measurements and incorporated them back into the ellipsometric fits. Thus, this resulted in a combined model incorporating both the TOLO and Drude oscillators in our ellipsometric fit, thereby allowing for the NIR-FIR CdO dielectric function to be finalized.

Following the finalization of the near-, mid- to far-IR fitting, we added a Tauc-Lorentz oscillator to both the bulk and surface charge CdO layers in order to model the band-edge absorption in the UV-VIS. Here, we restricted the fitting range to above $10,000\text{ cm}^{-1}$ (UV-VIS spectral range). The Tauc-Lorentz function took the place of the high frequency permittivity value we were using for the MIR and FIR fitting, so in order to avoid correlation between the Tauc-Lorentz fitting parameters and the TOLO amplitude (high-frequency permittivity), the TOLO oscillator was disabled while modeling the UV-VIS. The four fitting parameters in the Tauc-Lorentz function are the optical bandgap (E_g), center energy (E_n), broadening (C), and amplitude

(A). The optical bandgap value was first approximated using the Burstein-Moss⁸⁸ relation along with previously reported values, and was allowed to vary by ± 0.3 eV.

2.4.2 Effects of Free Carriers on UV to visible dielectric function of n-CdO

From the finalized ellipsometric fits (Fig. 2.3) it is possible to extract the real and imaginary parts of the dielectric function. This procedure was performed for three films featuring carrier densities (Hall mobilities) of $6.6 \times 10^{19} \text{ cm}^{-3}$ ($426 \text{ cm}^2/\text{V}\cdot\text{s}$), $1.4 \times 10^{20} \text{ cm}^{-3}$ ($389 \text{ cm}^2/\text{V}\cdot\text{s}$), and $4.1 \times 10^{20} \text{ cm}^{-3}$ ($312 \text{ cm}^2/\text{V}\cdot\text{s}$). The corresponding real and imaginary parts of the dielectric functions from 15,000 to 30,000 cm^{-1} (0.667 to $0.333 \mu\text{m}$) are provided in Fig. 2.5a. The central energy of the absorption features corresponds to the CdO conduction band edge, which is observed to blueshift with increased carrier density due to the donor behavior of In dopants in CdO. As the carrier density increases, the conduction band electron population is elevated, which subsequently raises the Fermi energy, consistent with the Moss-Burstein effect.^{88,89} The resultant E_g values of the CdO films are shown in Fig. 2b along with the previously reported values by Liu *et al.*⁸⁵ provided for comparison, illustrating that this observed effect is general to CdO films independent of growth method. The optical bandgap values were determined by first calculating the extinction coefficient (κ) from the extracted dielectric functions. The absorption coefficient ($\alpha = \frac{4\pi\kappa}{\lambda}$) can then be calculated and E_g approximated by extrapolating α^2 to zero (Fig. 2.4a). Plots of α^2 vs. photon energy are provided in Fig. 2.4b. The peak amplitude and broadening of the real dielectric function also follow a similar trend, implying increased absorption and loss around the band edge energy as the carrier density is increased.

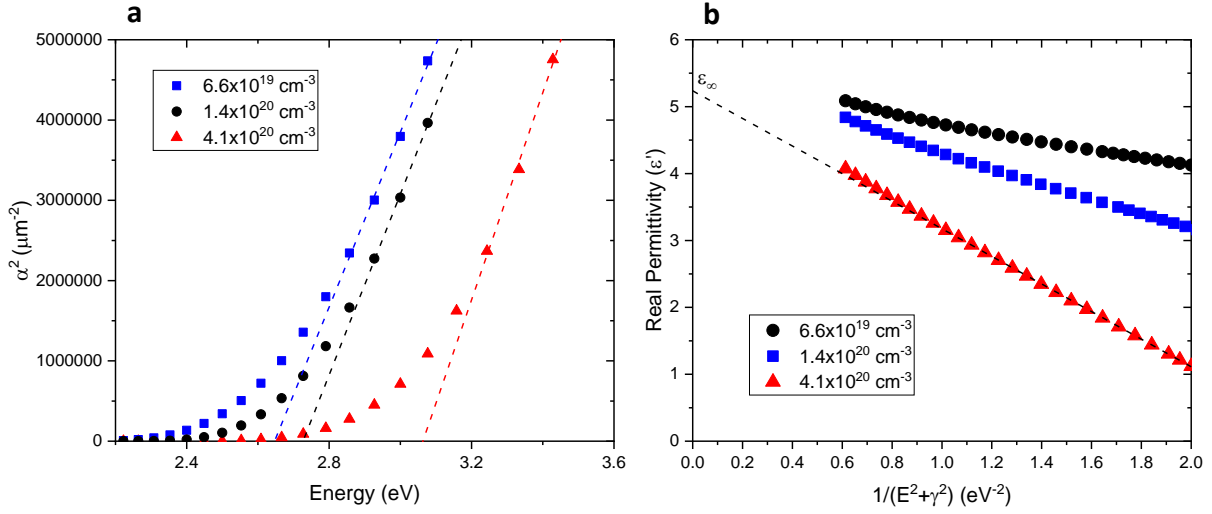


Figure 2.4: a) Plots of absorptivity (α^2) squared vs. photon energy. The optical bandgap is determined by extrapolating the asymptotic region of α^2 to zero. b) Real permittivity (ϵ') as a function of $1/(E^2 + \gamma^2)$ where γ is the drude damping. The high-frequency permittivity (ϵ_∞) can be determined by fitting the linear region of this relationship and determining the x-intercept.

These shifts in band edge energy and absorption impact the background polarizability of the lattice and therefore the extracted high frequency permittivity (ϵ_∞) of the Drude function which describes the dielectric function in the MIR. At low enough energies, sufficiently below the optical bandgap, $\epsilon'_{TL}(\omega)$ takes the constant value of ϵ_∞ . As the band edge absorption shifts to higher energy with increasing N_d , the high frequency permittivity is observed to decrease from 5.5 to 5.1 in our films (Fig. 2.5c). This inverse relationship between the high frequency permittivity and lowest-energy interband transition, known as Moss's rule, has been well-documented across many semiconductors.⁹⁰ High-frequency permittivity values were obtained by plotting real permittivity as a function of $(E^2 + \gamma^2)^{-1}$, where $E = \hbar\omega$ is photon energy and γ is Drude damping which will be discussed in the following section, and determining the x-intercept (Fig. 2.4a).

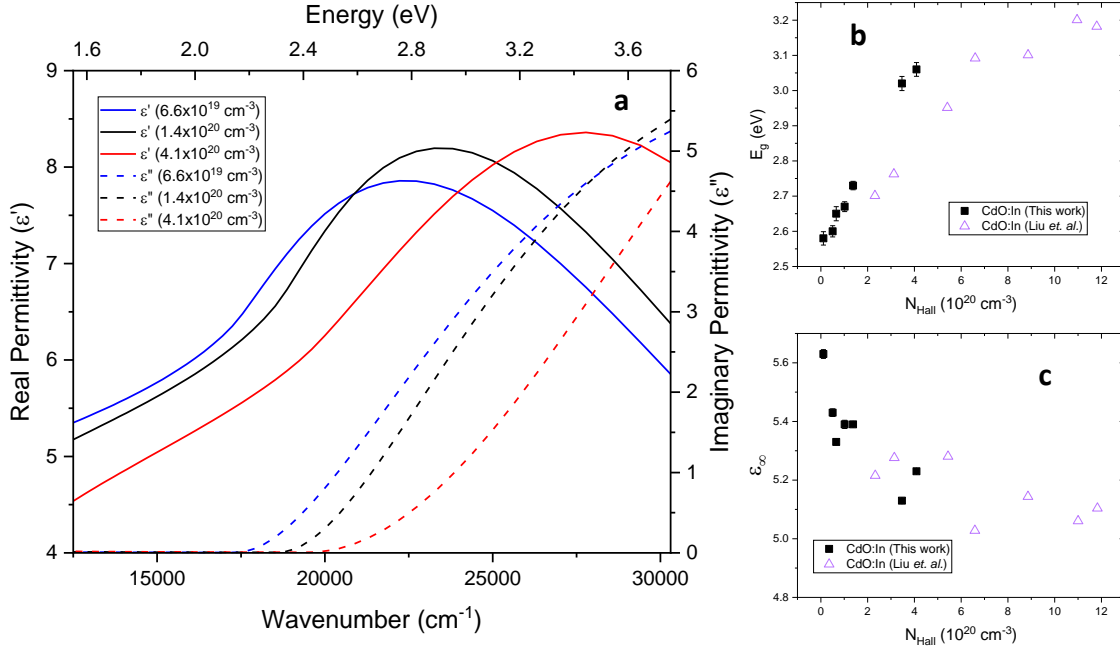


Figure 2.5: a) Real (solid) and imaginary (dashed) parts of the dielectric functions near the bandgap energy of three CdO thin films with differing carrier densities as labeled. Note the blue shift in the bandgap absorption with increasing carrier density. The optical bandgap and high frequency permittivity of In: CdO films as a function of carrier density are shown in b) and c), respectively. The uncertainty in the values, determined from the described fits are provided as error bars. Previously reported values from Liu et. al.⁸⁵ are also shown in b) and c) for comparison.

2.4.3 Effects of Free Carriers on the IR dielectric function of n-CdO

As was stated in our discussion of the Drude model in section 2.3.2, the plasma frequency $\omega_p = \sqrt{N_d e^2 / m^* \epsilon_\infty \epsilon_0}$ increases with the square root of the electron carrier density $\sqrt{N_d}$, with ϵ_0 and m^* representing the permittivity of free space and effective mass, respectively. The $\sqrt{N_d}$ scaling of ω_p can be discerned from the experimentally obtained values of ω_p in Figure 2.6a. From the dielectric functions provided in Fig. 4a, we extracted corresponding ω_p of 2584 cm^{-1} ($6.6 \times 10^{19} \text{ cm}^{-3}$), 3680 cm^{-1} ($1.4 \times 10^{20} \text{ cm}^{-3}$), and 5215 cm^{-1} ($4.1 \times 10^{20} \text{ cm}^{-3}$), respectively. The values of ω_p for the other CdO films in this study are reported in Fig. 2.6a. The relative rate of this scaling is dictated by the effective mass (m^*) which, for In: CdO, ranges from $0.11 - 0.26 m_0$ for $N_d \sim 1 \times 10^{19} - 4 \times 10^{20} \text{ cm}^{-3}$, consistent with the non-parabolic conduction band model.^{91,92}

$$m^* = m_o^* \sqrt{1 + 2C \frac{\hbar^2}{m_o^*} (3\pi^2 N_d)^{2/3}} \quad (22)$$

Here m_o^* is the effective mass at the base of the conduction band, C is a nonparabolicity fitting parameter, and N_d is assumed to be the carrier density measured in Hall effect measurements, N_{Hall} . Electron mobility was also determined through Hall effect measurements (μ_{Hall}). These values differ from optical mobility (μ_{opt}) values that were extracted through ellipsometric fitting. Note that Fig. 2.6b includes the effective mass values for two sample sets: high-quality HiPIMS CdO films (black squares) and highly-doped, polycrystalline films grown using MBE (purple triangles). Interestingly, our reported values of m^* in Fig. 2.6b demonstrate excellent continuity with these samples reported in previous work⁸⁵, illustrating that the growth quality appears to have little to no effect on the carrier-density-dependent effective mass of In:CdO. Effective mass has also been shown to be independent of crystallinity in other high-mobility TCOs, such as H:In₂O₃.⁹³ We provide a fit to the combined m^* data, resulting in fitting parameter values of $C = 0.69 \pm 0.08 \text{ eV}^{-1}$ and $m_o^* = 0.10 \pm 0.01 m_o$. The excellent agreement across sample sets and two orders of magnitude in carrier density justifies the use of this fit for approximating the effective mass of In:CdO with great accuracy. This can be compared to the fit provided in Liu *et. al.*, which resulted in $C = 0.49 \pm 0.19 \text{ eV}^{-1}$ and $m_o^* = 0.13 \pm 0.03 m_o$ for highly-doped films alone ($N_d > 5 \times 10^{20} \text{ cm}^{-3}$).^{85,94}

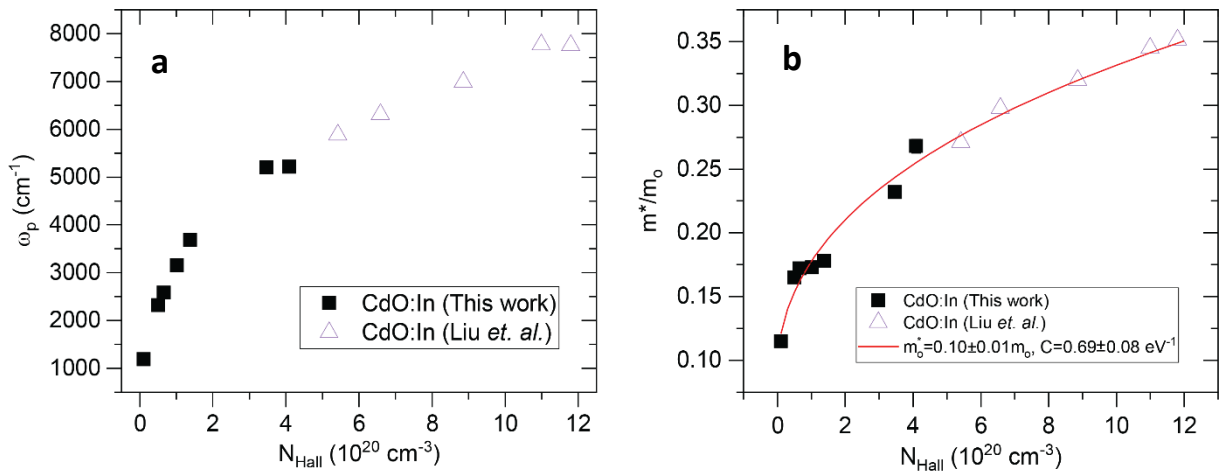


Figure 2.6: a) Plasma frequency ω_p and b) effective mass m^* of doped CdO films as a function of carrier density. Previously reported values for both ω_p and m^* from Liu *et. al.*⁸⁵ are also shown for comparison. A fit to the data using Eq. 5 is also provided (red curve).

From Eq. 17 in section 2.3.2, it is clear that the free carrier damping rate, defined as $\gamma = \frac{e}{\mu_{opt}m^*}$, is directly related to the imaginary part of the permittivity and therefore provides a convenient figure of merit for determining loss in polaritonic materials.^{54,95,96} Using the extracted values of m^* and optical mobility (μ_{opt}), the damping rate was calculated for each film as a function of carrier density and is reported in Fig. 2.7b. As was stated previously, μ (both optical and Hall values) is observed to increase in CdO up to $N_d \sim 5 \times 10^{19} \text{ cm}^{-3}$, however CdO maintains consistently high electron mobilities even at carrier densities exceeding this value. Thus, the resulting low damping rates are shown to decrease over a broad range of carrier densities (and therefore, plasma frequencies), even in the region of decreasing electron mobility.

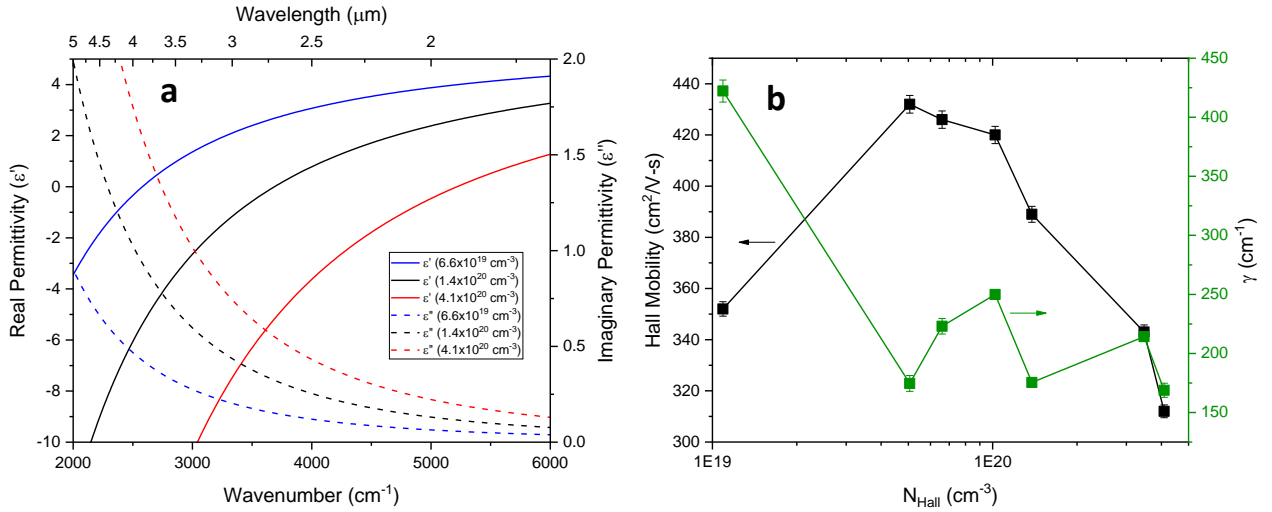


Figure 2.7: a) Real and imaginary dielectric function near the plasma frequency of three CdO thin films with differing carrier densities. The dielectric functions were derived from WVASE fitting of spectroscopic ellipsometry data. b) Hall electron mobility and carrier damping (γ) as a function of carrier density in In:CdO films.

As these excellent CdO transport properties are widely beneficial for a variety of nanophotonic applications including chemical sensing^{82,97}, narrow-band thermal emitters²⁵, and non-linear optics⁸, quantifying the loss and comparing to state-of-the-art polaritonic materials is of distinct interest. A more insightful FOM can be found in the modal Q-factor, which is widely implemented in photonic resonators and can be predicted from the extracted dielectric function as:⁹⁵

$$Q = \frac{\omega \frac{d\varepsilon'}{d\omega}}{2\varepsilon''} \quad (23)$$

From this expression it can be seen that the Q-factor for a localized SPP is inversely proportional to the imaginary part of the dielectric function, while it is directly proportional to the frequency dispersion of the real part. Thus, to achieve high Q, the material losses must be low and/or the rate of change in the dielectric constants must be high. While Q-factors in excess of 100 are routinely observed in SPhP resonators^{41,54,82,98,99}, the much slower dispersion of plasmonic materials, coupled with the faster scattering of free carriers with respect to optical phonons^{5,51}, naturally limits plasmonic cavities to values below 44, with typical values falling below 20.⁴⁸ However, as the rate of dispersion doesn't vary significantly between plasmonic materials (thanks to the Drude model), it is the imaginary part of the dielectric function that predominantly determines Q for such materials. Therefore, considering a spherical resonator allows for an insightful comparison between materials: an analytical solution exists for the Mie scattering from such a structure, with resonance occurring at the Fröhlich condition $[Re(\varepsilon) = -2\varepsilon_a]$.¹⁰⁰ Here, ε_a is the real part of the permittivity for the ambient environment, which for air will result in the polaritonic resonance condition occurring at $Re(\varepsilon) = -2$. To our knowledge the highest reported Q-factor for noble metal resonators in the MIR is 20-25, as demonstrated with hollow silver nanotubes on a silver backplane.¹⁰¹ Thus, the Q-factor for In:CdO at the Fröhlich condition, calculated here from the dielectric function to reach up to 24, is on par with that of noble metal resonators in the MIR and ~3-4 times higher than other TCOs, such as AZO¹⁰², ITO¹⁰³, and GZO¹⁰⁴. This is demonstrated in Table 2.1, which compares the optoelectronic properties of CdO to other TCOs for films doped to achieve $\lambda_p = 1.55 \mu m$. Note, the carrier mobility of CdO is an order of magnitude larger than that of other TCOs, resulting in significantly lower $Im(\varepsilon)$ and enhanced Q-factors.

Table 2.1: Comparison of optoelectronic properties of TCOs used in MIR plasmonics.

Material	Effective Mass [m^*/m_o]	N_d for $\lambda_p = 1.55 \mu\text{m}$ [$\times 10^{20} \text{ cm}^{-3}$]	Carrier Mobility [$\text{cm}^2/\text{V} - \text{s}$]	$Im(\epsilon)$ at [Re(ϵ) = -2] for Film of N_d in Column 3	Q (eq. 23) at [Re(ϵ) = -2] for Film of N_d in Column 3	Propagation FOM (FOM $\approx \frac{\omega_p}{\gamma}$) for Film of N_d in Column 3
ITO ¹⁰⁵	0.38	6.76	36	0.88	6.5	8.5
Ga:ZnO ¹⁰⁶	0.38	6.79	30.96	0.79	7.3	7.3
Al:ZnO ¹⁰⁷	0.38	6.75	47.6	0.59	9.5	11.2
H:In ₂ O ₃ ⁹³	0.28	5.46	118	0.37	18	22
In:CdO	0.27	5.36	285	0.20	24	48

While Eq. 23 provides the means to compare plasmonic materials over a broad spectral range, it is typically more instructive to normalize the spectral dispersion in Q to the real part of the permittivity to eliminate the inherent spectral shifts in ω_p between materials as a function of carrier density. This has been provided in Fig. 2.8, which shows the range of Q -factor values at the Fröhlich condition for In:CdO along with the corresponding values for three other TCOs: ITO (red)¹⁰⁵, Al-doped (AZO, purple)¹⁰⁷, and Ga-doped (GZO, light blue) zinc oxide¹⁰⁶ as a function of ω_p (from $1500 - 4500 \text{ cm}^{-1}$). The dielectric functions for each TCO were calculated using Eq. 17. For AZO, GZO, and ITO the effective mass was calculated using eq. 23 and the corresponding values of m_o^* and C ,¹⁰⁸ whereas the value listed in Table 2.1 was used for H:In₂O₃. A constant value for the carrier mobility (provided in Table 2.1) was assumed for ITO, AZO, GZO, and H:In₂O₃ however for CdO the mobility values were interpolated using the data provided in Fig. 2.7b. From Fig. 2.8, it is clear that consistent with the analysis of spherical particles, In:CdO is anticipated to exhibit Q -factors that are at least ~ 4 times higher than other common TCOs across a broad range of permittivity values and thus nanostructure shapes and sizes. In practice, the assumption of constant mobilities with increasing carrier densities in the other TCOs is not realistic and presumably overestimates the Q factors possible at high carrier density values. Further, the values for In:CdO actually compare favorably to measured values for silver ($Q \sim 20 - 25$ in MIR),

which still represents the highest quality noble metal for plasmonic applications. In addition, due to the consistently high carrier mobility and rapidly increasing effective mass, the Q-factor is actually found to increase at a much faster rate in CdO than for other TCOs at elevated doping levels. Increasing Q-factors with doping density have been reported previously in LSPRs supported by In: CdO nanoparticles within the near-infrared.¹⁰⁹ As was mentioned above, the increase in Q-factor is a result of the value of $Im(\epsilon)$ at the Fröhlich condition, which diminishes with increased N_d . Note, the imaginary permittivities at the condition $Re(\epsilon) = -2$ for the CdO films with carrier densities of $6.6 \times 10^{19} \text{ cm}^{-3}$, $1.4 \times 10^{20} \text{ cm}^{-3}$, and $4.1 \times 10^{20} \text{ cm}^{-3}$ films (Fig. 2.7a) were determined to be $Im(\epsilon) = 0.67, 0.45,$ and $0.31,$ respectively. The measured Q-factor values are also provided in Fig. 2.8 for the films in this study, verifying this trend.

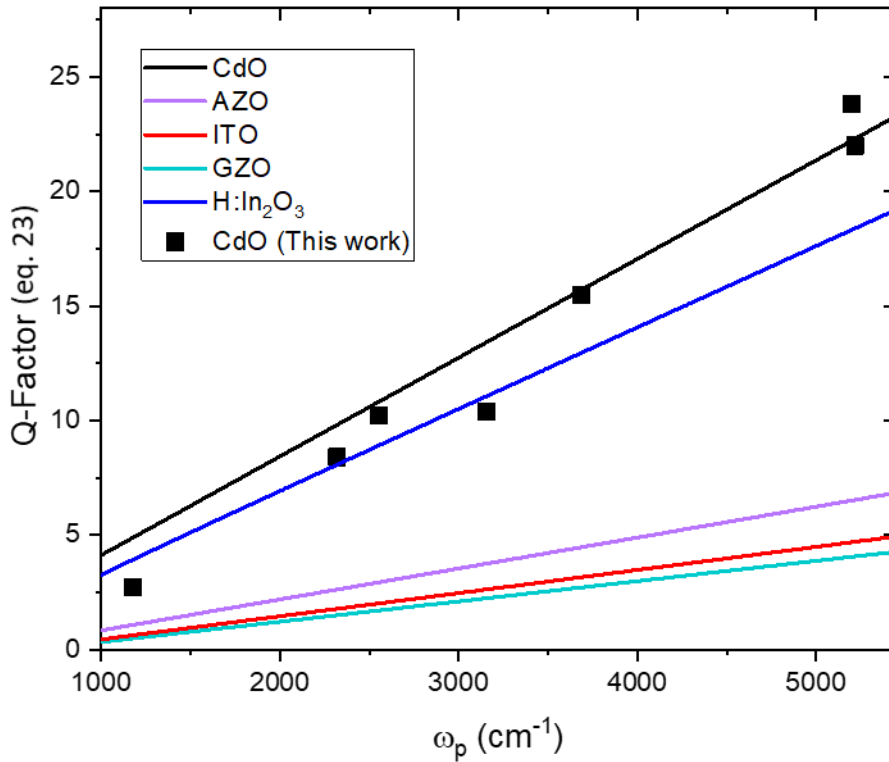


Figure 2.8: Quality-factor (eq. 23) calculated at the Fröhlich condition ($Re(\epsilon) = -2$) for several TCOs across a range of ω_p (and therefore N_d). The dielectric function for each material was calculated using the Drude model with the effective mass determined using Eq. 17. Values for m_o^* and C for other TCOs were found in literature.^{93,108} Data points correspond to calculated Q-factor values from the extracted dielectric functions of the films in this study, demonstrating excellent agreement with the values calculated using the Drude model.

2.4.4 Influence of Optic Phonons on the FIR dielectric function of n-CdO

As with other polar dielectric materials, the TO-phonon of CdO is associated with a net dipole moment and is IR active. In undoped polar semiconductors and dielectrics, the TO phonon induces strong dispersion in the real part of the permittivity that dominates the IR dielectric function.¹¹⁰ To examine the polar phonon contribution to the IR dielectric function, FIR reflectance measurements were performed at 60° angle of incidence on all three CdO films using a Bruker Vertex 70v FTIR spectrometer in tandem with a DLaTGS detector. This was required as the optic phonons of CdO occur at frequencies beyond those sampled by the IR-VASE system ($>333\text{ cm}^{-1}$). The strong absorptive nature of the TO phonon, which occurs at 266 cm^{-1} , is distinct in the reflectance spectra for the unintentionally doped CdO (Figure 2.9, red curve). The center frequency of this absorptive resonance agrees well with previously reported values for the CdO TO phonon using other measurement techniques.¹¹¹ However, the relative intensity, with respect to the baseline reflectance, decreases as carrier density increases. This is demonstrated in the reflectance spectra in Fig. 2.9. Here the absorption resonance caused by the TO phonon is easily discernable in the unintentionally doped ($1.4 \times 10^{19}\text{ cm}^{-3}$) and low-doped ($6.6 \times 10^{19}\text{ cm}^{-3}$) CdO films, but is not observable in the higher carrier density ($1.4 \times 10^{20}\text{ cm}^{-3}$ and $4.1 \times 10^{20}\text{ cm}^{-3}$) films. This is consistent with the concept of the free-carrier contribution dominating the dielectric function with increased carrier density, where the higher carrier densities result in the real part of the dielectric function exhibiting larger negative values at the TO phonon frequency, thereby screening out the otherwise strong phonon absorption. This results in the reflection spectra flattening in the spectral region near the TO phonon, as shown in Fig. 2.9. The high reflectance above $\sim 400\text{ cm}^{-1}$ is induced by optic phonons in the MgO substrate. Modeling the Lorentzian lineshape of the TO phonon absorption observed in Fig. 2.9 using the TOLO formalism for a single TO-LO pair (Eq. 18) enables the extraction of the spectral position and damping (phonon scattering rate) of the TO phonon within the various films. However, to perform this fitting, three of the four key values dictating the Lyddane-Sachs-Teller relationship must be known, with the fourth derived from this relation.⁴⁹ As for even the unintentionally doped CdO films there exists sufficient free-carriers to preclude the observation of a distinct, highly reflective Reststrahlen band, a previously-reported value for the LO phonon frequency from IR absorption measurements was employed as a starting value in the fitting process,¹¹² while the TO phonon and damping were derived from the reflectance spectra, and the high-frequency permittivity extracted from the prior Drude fits.

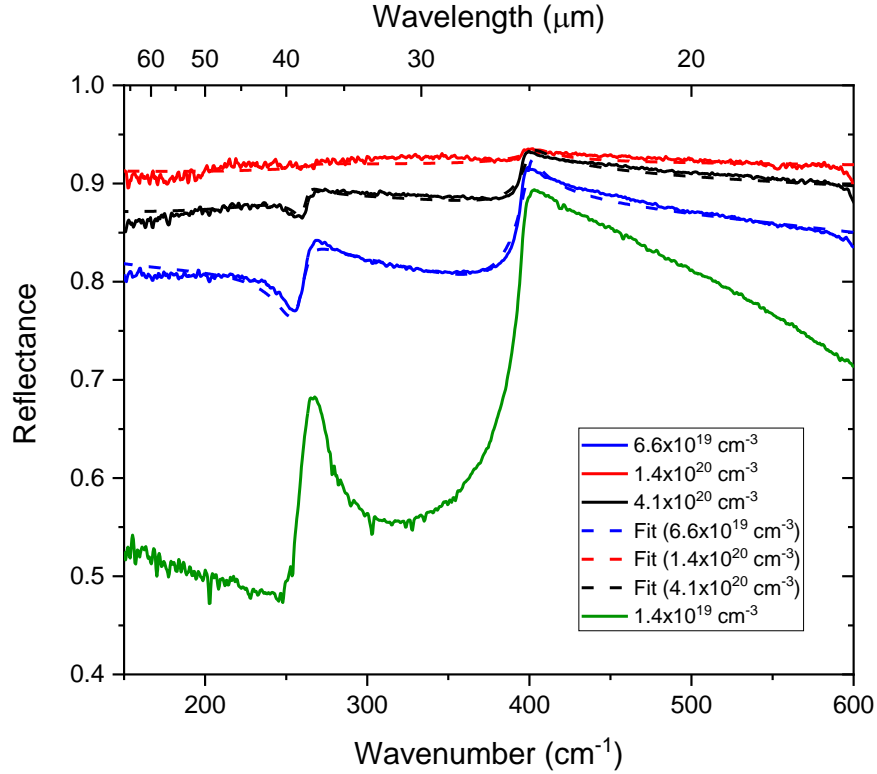


Figure 2.9: Low-energy FTIR reflectance of four CdO films with varying levels of doping; unintentionally doped ($1.4 \times 10^{19} \text{ cm}^{-3}$), moderately doped ($6.6 \times 10^{19} \text{ cm}^{-3}$), and highly doped ($1.4 \times 10^{20} \text{ cm}^{-3}$ and $4.1 \times 10^{20} \text{ cm}^{-3}$) measured at an angle of incidence of 60° .

From the above referenced data, the phonon contribution to the FIR dielectric function can be derived, which are provided in Fig. 2.10a for the three films originally introduced in Fig. 2.5a and 2.7a. A Lorentzian lineshape can clearly be observed in the imaginary part of the dielectric function for all samples, regardless of N_d . However, the scaling of the ω_p due to free carriers is evident in the FIR, resulting in a more negative real part and larger imaginary part of the permittivity with increased carrier density. The TOLO contribution to the dielectric function in the absence of free-carrier and bandgap effects is also displayed in Fig. 2.10a. A Transfer-Matrix-Method (TMM)¹¹³ calculation of the reflectance for a 200 nm CdO film using this TOLO-only dielectric function grown on a MgO substrate is presented in Fig. 2.10b and compares well with the FIR FTIR measurement of the unintentionally doped ($1.4 \times 10^{19} \text{ cm}^{-3}$) film shown in Fig. 2.9.

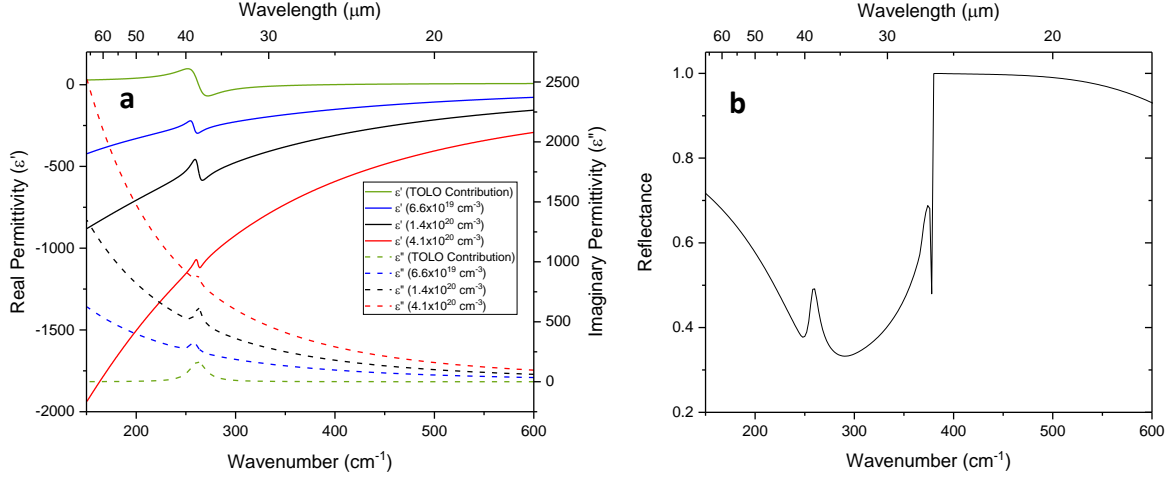


Figure 2.10: Far-IR dielectric functions for a) three CdO films with varying levels of doping as well as the isolated TOLO contribution (Drude and Tauc-Lorentz oscillators turned off). b) Transfer-Matrix-Method reflectance simulation of a 200 nm CdO film with the TOLO-isolated dielectric function from a) on an MgO substrate.

2.4.5 Combined Dielectric Function

While we have presented the various contributions to the dielectric function of CdO within three distinct spectral ranges and described the salient features governing these effects separately, the combined spectral response is of course the primary goal of this work. Taking the three key contributions from Eq. 15 and 16 (Tauc-Lorentz), 17 (Drude) and 18 (TOLO) together, the unified dielectric function can be described as follows:

$$\varepsilon(\omega) = \varepsilon_{TOLO} + \varepsilon_{Drude} + \varepsilon_{TL} = \left(\varepsilon_{\infty,TL} + \frac{2}{\pi} P \int_{\omega_T}^{\infty} \frac{\xi \varepsilon''(\xi)}{\xi^2 - \omega^2} d\xi + i \frac{A\omega_n C(\omega - \omega_T)^2}{(\omega^2 - \omega_n^2)^2 + \omega^2 C^2} \frac{\Theta(\omega - \omega_T)}{\omega} - \frac{A_D}{\omega^2 + i\gamma\omega} \right) \left[\left(\frac{\omega_{LO}^2 - \omega_{TO}^2}{\omega_{TO}^2 - \omega^2 - i\gamma\omega} \right) \right] \quad (24)$$

Using the above relations, with interpolated values derived from the films discussed here, the dielectric function of In:CdO extending from the visible to the FIR spectral range may be derived for arbitrary carrier density and mobility, which we expect will prove useful for accurate nanophotonic simulations that use In:CdO building blocks.

2.4.6 Conclusions

With the ever-expanding interest into realizing advanced nanophotonic and optoelectronic concepts within the MIR spectral regime, the low optical losses and broad spectral tunability associated with CdO and other TCOs is of increasing interest. However, for the true potential of CdO for a variety of applications to be validated, predictive modeling of advanced optical or electrooptic components must be undertaken. This requires an accurate dielectric function, which we have provided here over the spectral range from $150 - 33,333 \text{ cm}^{-1}$ ($66 - 0.3 \text{ }\mu\text{m}$). A multi-oscillator model describing the near-UV-FIR complex dielectric function for doped CdO was extracted using spectroscopic ellipsometry, FIR FTIR spectroscopy, and dielectric function modeling using the WVASE program, implementing a least-squares fitting routine. Seven HiPIMS CdO films with varying levels of doping were characterized, giving insight into the role of free carriers not only upon the Drude term (through spectral shifting of the plasma frequency and effective mass and changes to carrier mobility), but also upon the bandgap related interband transitions and in determining the relative role of the optic phonons at FIR frequencies. Using our extracted permittivity values, the prior assertions of CdO as one of the lowest loss MIR plasmonic materials for the 3-5 μm and 8-12 μm atmospheric windows were validated. This has implications for next generation IR sources¹⁷, hot-carrier-based detectors and waveguides. Although the Drude term is the dominant feature of the extended CdO dielectric function, it is useful to include optic phonons and interband transitions into the model to further explain the ellipsometric line shapes at low and high frequencies, respectively, and to provide context as to the origin of the background permittivity outside of the spectral range of these resonant modes. The model of the VASE data resulted in highly accurate fits, with the analysis presented here aiding in the demonstration of CdO-enabled next-generation nanophotonic and optoelectronic devices, while also providing an underlying physical description of the key properties dictating the dielectric response.

2.5 Dielectric Function of HfS₂ Crystals

HfS₂ is a group IV TMDC with a hexagonal unit cell. IR and Raman demonstrations have revealed that the in-plane TO and LO phonon frequencies of HfS₂ are 166 cm^{-1} and 318 cm^{-1} , respectively.^{27,114} Past studies utilizing second-order Raman¹¹⁵ and absorption¹¹⁶ measurements

have been used to gain more information about the out-of-plane phonon frequencies. However, to our knowledge, the out-of-plane dielectric function has yet to be reported. In this section, we provide a brief description of the process of extracting the in- and out-of-plane components of the dielectric function of HfS₂ using FTIR micro-spectroscopy measurements.

2.5.1 Extracting HfS₂ Dielectric Function using FTIR micro-spectroscopy

The HfS₂ sample is a free-standing layered crystal (pictured in Figure 2.11c), making it not ideal for large-scale measurement techniques such as bench FTIR measurements and ellipsometry. The large collection area of these techniques results in significant thickness non-uniformity that is difficult to model. Here, FTIR micro-spectroscopy was used as this allows for the collection area to be decreased significantly, therefore reducing the non-idealities associated with the other methods. Two spots on the sample were measured and the fitting parameters are provided in Table 2.2. We modelled the optical response of HfS₂ using a uniaxial dielectric tensor with single TOLO functions being used to model the dielectric function along the in- and out-of-plane axes. Reflectance spectra were collected using a Hyperion 2000 microscope equipped with a long working distance IR objective (Pike, 10x, 0.28NA) and grazing angle objective (GAO) (Bruker, 55°). Therefore, reflectance spectra were collected at normal incidence and at a steep angle of incidence (55°), allowing for the in- and out-of-plane components of the HfS₂ dielectric function to be determined.

We began the fitting procedure by collecting a reflectance spectrum well above the Reststrahlen band using the 10x objective (Figure 2.11a). The microscope apertures were set to 300 x 300 μm, significantly decreasing the collection area for these measurements. From these measurements we were able to determine the in-plane high-frequency permittivity and the thickness of the sample in that area. In this fit, a previously reported value of the high-frequency permittivity was used as an initial value ($\epsilon_{\infty} = 6.2$). Note that although we were able to significantly decrease the thickness non-uniformity, there is still some slight non-uniformity present. This is evident in the collected spectrum. The reflectance of a HfS₂ crystal with a constant thickness would exhibit Fabry-Perot fringing. However, when the thickness of the crystal is slightly non-uniform, the amplitude of the Fabry-Perot fringing will decrease as the frequency increases (as is seen in Figure 2.11a). This non-ideality can however be accounted for in the model using WVASE.

Knowing the thickness and in-plane high-frequency permittivity we then measured the s -polarized reflectance in the FIR using the GAO objective (Figure 2.11b). From these measurements we were able to extract the remaining values of the in-plane permittivity: $\omega_{TO,(x,y)}$, $\omega_{LO,(x,y)}$, $\gamma_{TO,(x,y)}$, and $\gamma_{LO,(x,y)}$. These values are provided in Table 2.2. Finally, we measure the p -polarized reflectance at the same location using the GAO objective (Figure 2.11d). The previously extracted values for the in-plane dielectric function are incorporated into our model, allowing us to focus on the out-of-plane contribution. Note, although our model is successful in matching the overall shape of the reflectance measurements, there are additional absorptive features that are not accounted for in our model. We attribute this to two-phonon absorption, which will be discussed in the next section.

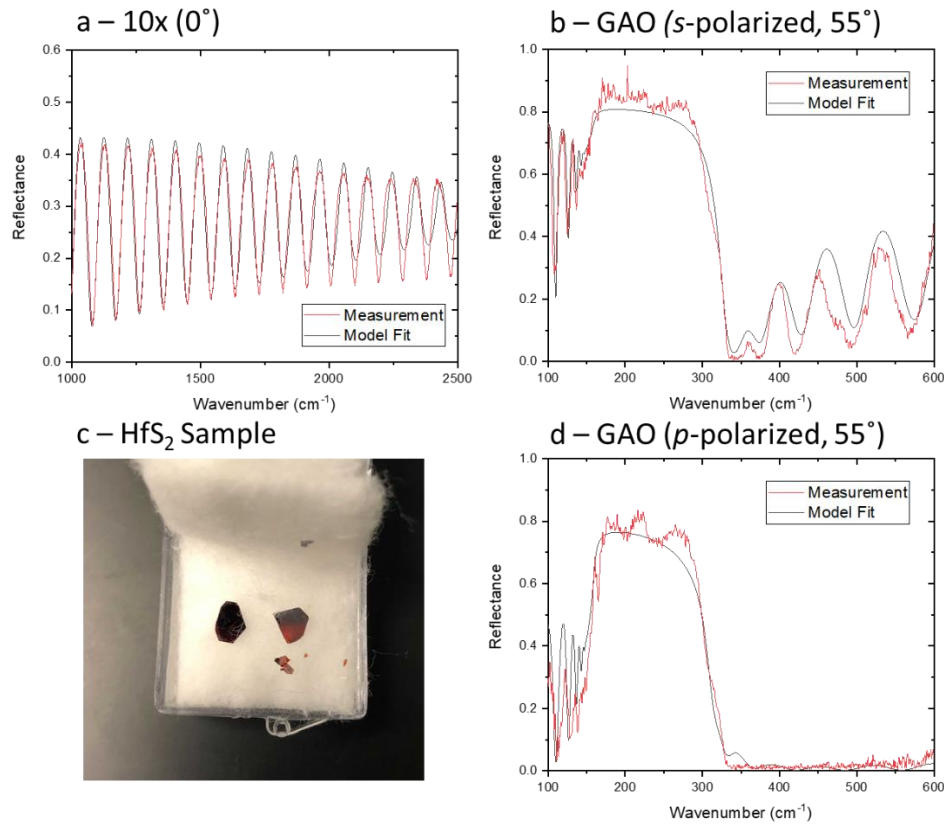


Figure 2.11: a) Measured and fit b) Transfer-Matrix-Method reflectance simulation of a 200 nm CdO film with the TOLO-isolated dielectric function from a) on an MgO substrate.

2.5.2 Modelling Two-Phonon Absorption in HfS₂ Crystals

As was stated in the previous section, additional absorptive features are observed in the polarized reflectance spectra that are not attributed to the first-order optic phonon response. In order to understand the origin of these features we performed transmission measurements at normal incidence using a very thin, relatively flat sample ($t = 9.9 \mu\text{m}$), which are provided in figure 2.12a. Here, we are measuring at normal incidence and therefore only the in-plane contribution to the dielectric function is considered. In these measurements, we see additional features at 350 cm^{-1} , 470 cm^{-1} , 505 cm^{-1} , and 550 cm^{-1} that cannot be accounted for by a single TOLO model (Figure 2.12a, dashed line). Similar features have been observed at these frequencies in two-phonon absorption measurements of HfS₂ crystals. We then modelled each of the two-phonon absorption peaks using the anharmonic TOLO function, as has been used in prior work (Figure 2.12a, black solid line). Although the two-phonon absorption features are prominent in the transmission spectrum, their resultant contribution to the dielectric function very weak in comparison to first-order optic phonons (Figure 2.12b and 2.12c).

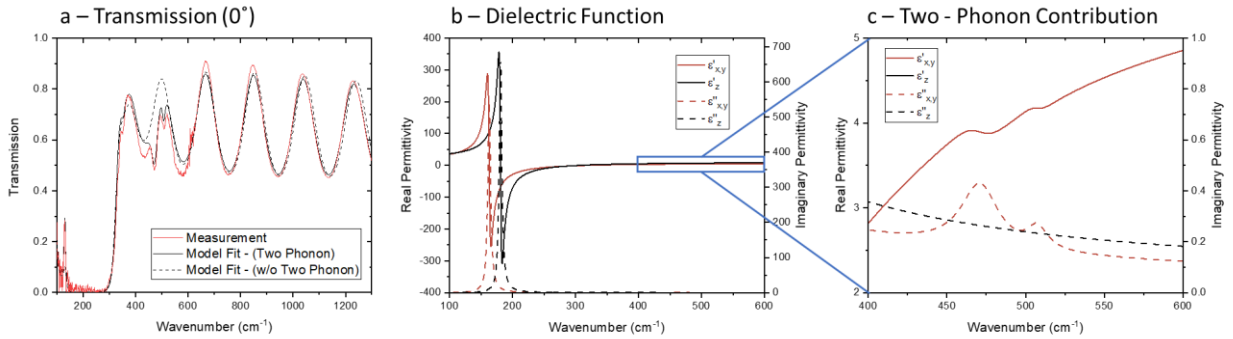


Figure 2.12: a) Two fits to measured (red line) transmission. The dashed line shows a fit ignoring the contribution of two-phonon absorption. The solid black line is a fit that takes the two-phonon absorption into account. b) Dielectric function of HfS₂. c) Contribution of two-phonon absorption in the dielectric function of HfS₂.

Table 2.2: Fit Parameters from HfS₂ Extracted from Reflectance Fitting

Spot	s1	s2
Thickness (nm)	21700 ± 302	23302 ± 496
ω_{TO} (cm ⁻¹) (x,y)	160 ± 0.22	159.5 ± 0.18
ω_{LO} (cm ⁻¹) (x,y)	314.48 ± 0.67	317.17 ± 7.4
γ_{TO} (cm ⁻¹) (x,y)	5.35 ± 0.5	7.26 ± 0.5
γ_{LO} (cm ⁻¹) (x,y)	15 ± 0.92	18.2 ± 1.1
ϵ_{∞} (x,y)	6.2 ± 0.16	6.13 ± 0.3
ω_{TO} (cm ⁻¹) (z)	183 ± 6.2	179 ± 8.2
ω_{LO} (cm ⁻¹) (z)	307.35 ± 0.78	305.8 ± 0.82
γ_{TO} (cm ⁻¹) (z)	4 ± 2.2	4 ± 2
γ_{LO} (cm ⁻¹) (z)	13.3 ± 1.35	16.9 ± 2.2
ϵ_{∞} (z)	9.59 ± 0.97	10.5 ± 1.2
Thickness Non-uniformity (%)	3.07 ± 0.05	1.23 ± 0.45
First Reflection (%)	83 ± 0.5	86.45 ± 0.6

2.5.3 Conclusion

In this section we have outlined how FTIR micro-spectroscopy can be used to extract the dielectric function of non-ideal samples, such as HfS₂ crystals. Using the dielectric function that we have extracted here, calculations seeking to determine HfS₂ resonator geometries for supporting confined SPhPs are currently underway. These structures will be fabricated at Vanderbilt and measured using far-field and near-field techniques. In the future we will also employ the same approach in order to determine the dielectric function of other group IV TMDCs, such as HfSe₂.

Chapter 3

3. Polaritonic Strong Coupling in Multilayer Semiconductor Films

3.1 Coupling Between Light and Matter

It is well-established that the radiative properties of an emitter are heavily influenced by the environment in which it is embedded. This was first outlined in the seminal work of Purcell in 1946 that demonstrated that the spontaneous emission rate of an emitter can be engineered by altering the access to photonic states, i.e. enhancing the local density of states (LDOS).¹¹⁷ In the decades that followed there was a lot of research focused in enhancing the interaction between light and matter to the point where the coupling strength (g) exceeds the losses within the system, placing the system in the strong coupling regime. This was first demonstrated by Haroche et. al. in 1983, where Rabi oscillations were observed between a concentration of Rydberg atoms and a microwave cavity.¹¹⁸ Since then, there have been numerous demonstrations of strong coupling within a variety of optical systems, for example exciton-cavity coupling resulting in exciton-polariton condensates¹¹⁹, polaritonic strong coupling in films and nanostructures^{12,24,120,121}, superconducting circuits¹²², and optomechanical systems¹²³.

As a simple example, we consider the coupling between a single emitter and a cavity. The coupling strength between the emitter and a single cavity mode can be found through the expression

$$g(\mathbf{r}, \omega) = \boldsymbol{\mu} \cdot \mathbf{E}(\mathbf{r}, \omega) \quad (1)$$

Where $\boldsymbol{\mu}$ is the dipole moment of the emitter and $\mathbf{E}(\mathbf{r}, \omega)$ is the local electric field. The coupling strength is directly related to the rate of energy transfer between the emitter and the cavity, referred to as the Rabi frequency $\Omega = 2g$. This value is critically important since, when compared against the losses and/or fundamental frequency of the system, it determines the coupling regime of the system. In this chapter, we first give a brief review of the most commonly explored coupling regimes: weak and strong coupling. More in-depth reviews of light-matter coupling can be found elsewhere.^{124,125} We then detail strong coupling within two planar, multilayer systems: SPP-ENZ coupling in multilayer CdO films and SPhP/SPP-ENP-ENZ coupling in III-V heterostructures.

3.1.1 Weak Coupling Regime

Within the weak coupling regime, the linewidths of the resonances are larger than the coupling strength. The dispersion of coupled oscillators within the weak coupling regime would intersect in $\omega - k$ as opposed to spectrally splitting into hybrid eigenstates and therefore the individual oscillators would remain separate entities. If we again consider the cavity-emitter example from the previous section, in the weak coupling regime the emitter will radiate into the cavity mode which will subsequently radiate preferentially to free space due to the low Q-factor. The energy in this system is therefore not reversible as the cavity will emit to free space at a greater rate than will be transferred back to the emitter. This makes the weak coupling regime advantageous for a number of applications such as enhancing the emission rate of a single-photon emitter or the output from low-threshold lasers. However, the application space is not limited to enhancing the emission output of a quantum emitter, other instances of weak coupling include SEIRA^{14,77,126}, SERS^{74,127}, and Fano interference.^{126,128}

3.1.2 Strong Coupling Regime

When the coupling strength between two modes is sufficiently high, exceeding the linewidth of the individual resonances, the modes enter the regime of strong coupling. The resultant dispersive behavior manifests as a spectral splitting into two hybrid eigenstates (ω^+ and ω^-), with the amplitude of the splitting being directly related to the coupling strength ($\Omega = 2g = \omega^+ - \omega^-$).¹²⁵ The two modes can no longer be described discretely but as a single hybrid system with energy being exchanged coherently and reversibly between the two eigenstates. Methods of exploiting and controlling this extreme light-matter interaction has been the interest of a host of prior works. Some previous demonstrations include J-aggregates and dye-molecules strongly-coupled with propagating polaritons¹²⁹, ENZ modes coupled with propagating and localized SPPs and SPhPs^{12,120}, and strong coupling between localized and propagating SPhP modes in SiC resonators on a SiC substrate.¹²¹ Further, 3-mode polariton strong coupling has recently been demonstrated by Lu et. al. between the zone-folded LO-phonon and propagating and localized SPhP modes supported by 4H-SiC pillars patterned into a 4H-SiC substrate.²⁴ Surface polaritons (SPPs and SPhPs) are also the result of strong light-matter coupling; for SPPs the matter component is the oscillation of free charge whereas for SPhP the matter components are the optic phonons. Other examples include coupling between cavity photons and excitons and the

vibrational^{130–132} and electronic states^{133–135} of molecules, strong coupling between light and superconducting qubits¹³⁶, and intersubband transitions within cavities^{137,138}. Strong coupling between cavity photons and exciton states has led to the formation of exciton-polariton condensates which is an attractive potential platform for realizing coherent emission.¹¹⁹ A more comprehensive list of strong coupling demonstrations can be found in literature.

Several models have been used to describe the coupling between light and matter, the first being the Rabi model which is a simple model describing the interaction between a single mode of a cavity and a single two-level system (quantum emitter). The Dicke model extends the Rabi model to multiple emitters. Other examples include the Jaynes-Cummings and the Tavis-Cummings models, which apply the rotating wave approximation to the case of a single and multiple emitters, respectively.¹²⁵ A discussion of when this approximation is appropriate is beyond the scope of this section. Another powerful model is the Hopfield model which is a generalized version of the Rabi model that can be used to describe the interaction between two coupled harmonic oscillators. The broad generalizability of this model has made it useful for describing the coupling between light and collective excitations in a number of different quantum and classical systems. In this dissertation we use the Hopfield model to analyze the strong coupling within multiple systems. First, later in this chapter we use the Hopfield model to calculate the hybrid dispersion of SPP-ENZ modes supported in multilayer CdO films. Then in the next chapter the Hopfield model is used to study strong coupling between localized SPP resonances supported by InAs nanostructures and the ENZ mode supported by a polar material. Hamiltonian for a coupled two-oscillator system is

$$\mathcal{H} = \mathcal{H}_a + \mathcal{H}_b + \mathcal{H}_{int} \quad (2)$$

$$\mathcal{H} = \hbar \sum_{\mathbf{k}_{\parallel}} \omega_{\mathbf{k}_{\parallel}}^a \hat{a}_{\mathbf{k}_{\parallel}}^{\dagger} \hat{a}_{\mathbf{k}_{\parallel}} + \omega_{\mathbf{k}_{\parallel}}^b \hat{b}_{\mathbf{k}_{\parallel}}^{\dagger} \hat{b}_{\mathbf{k}_{\parallel}} + g \left(\hat{a}_{\mathbf{k}_{\parallel}}^{\dagger} \hat{b}_{\mathbf{k}_{\parallel}} + \hat{a}_{\mathbf{k}_{\parallel}} \hat{b}_{\mathbf{k}_{\parallel}}^{\dagger} \right) \quad (3)$$

where $\omega_{\mathbf{k}_{\parallel}}^a$ and $\omega_{\mathbf{k}_{\parallel}}^b$ are the energies of oscillators a and b , respectively, and $\hat{a}_{\mathbf{k}_{\parallel}}$ and $\hat{a}_{\mathbf{k}_{\parallel}}^{\dagger}$ are annihilation and creation operators. Here we have ignored the diamagnetic term (\mathcal{H}_{dia}) of the Hamiltonian as it is negligible in the strong coupling regime. However, this approximation breaks down when the coupling strength exceeds the fundamental energy of the system ($\eta > g/\omega_o$), a coupling regime referred to as the ultrastrong coupling regime. The Hamiltonian can be diagonalized using the Hopfield-Bugoliubov procedure¹³⁹ resulting in the Hopfield matrix

$$\mathcal{M}_{k_{\parallel}} = \begin{bmatrix} \omega_{k_{\parallel}}^a & g \\ g & \omega_{k_{\parallel}}^b \end{bmatrix} \quad (4)$$

The subscript k_{\parallel} denotes that the Hopfield matrix is calculated at each value of in-plane momentum. Then, the eigenvalues and eigenvectors of the Hopfield matrix yield the hybrid dispersion $\omega_{k_{\parallel}}^i$ and Hopfield coefficients $a_{k_{\parallel}}^i$ and $b_{k_{\parallel}}^i$.

$$[\mathcal{M}_{k_{\parallel}} - \omega_{k_{\parallel}}^i] \begin{pmatrix} a_{k_{\parallel}}^i \\ b_{k_{\parallel}}^i \end{pmatrix} = 0 \quad (5)$$

The Hopfield coefficients act as a relative mixing fraction of constituent modes in each branch of the hybrid dispersion. Here, we have focused on the simplest case: two coupled harmonic oscillators within the strong coupling regime. However, the Hopfield model can be expanded to an arbitrary number of coupled oscillators by expanding the Hopfield matrix.

3.2 SPP-ENZ Strong Coupling in Multilayer CdO Films

Optical fields can be concentrated to length scales far below the diffraction limit through the excitation of propagating and localized surface polariton modes. Establishing methods of controlling the polaritonic dispersion of these light-matter excitations has been of great interest recently as the non-zero group velocity ($v_g = \frac{\partial\omega}{\partial k}$) and high confinement make surface polaritons useful for a broad range of nanophotonic applications including thermal emissivity control and sensing, as well as in-plane nano-scale waveguiding and information transfer.

One promising platform for realizing control over the polaritonic dispersion is multilayer CdO films. Control over the carrier density during film growth has opened the door to realizing multilayer, homoepitaxial CdO heterostructures capable of exhibiting a wide range of exciting behaviors such as multifrequency narrowband thermal emission from multilayer CdO stacks²⁵ and modal strong coupling between SPP and ENZ modes. Despite the homogeneity of the crystal structure, the elevated carrier densities and carrier density driven changes to the Fermi energy and effective mass confines carriers to their constitutive layers.^{40,140} SPP-ENZ strong coupling has been realized in bilayer CdO films wherein an ENZ-supporting CdO film is grown on top of a thicker SPP supporting CdO film featuring a larger carrier density. Here, hybrid SPP-ENZ modes are observed with spatial and dispersive characteristics of the individual modes. Notably, these

hybrid states inherit the strong spatial confinement of the ENZ mode and extended propagation length of the SPP modes, overcoming the challenges associated with the discrete modes.

Past studies were successful in outlining the degree to which the SPP-ENZ strong coupling in these bilayer CdO films is influenced by the constitutive modal properties. For example, Runnerstrom et. al.¹²⁰ provided two tuning knobs for modifying the SPP-ENZ coupling (and thus the SPP-ENZ hybrid dispersion): the oscillator strength of the ENZ mode and spectral overlap of the SPP and ENZ modes. The former is tunable by controlling the ENZ layer thickness, while the latter through the control of the carrier density of one or both layers. However, an accounting of the dielectric environment and modal separation and their effect on the polaritonic coupling conditions have yet to be considered. In the following, we outline the effects of the dielectric environment and spatial separation on the coupling strength and k-space tuning of the SPP-ENZ anti-crossing position in multilayer CdO films. Namely, we explore the effects of incorporating an unintentionally-doped (UID, $N_d \approx 4 \times 10^{19} \text{ cm}^{-3}$) CdO layer as both a spacer layer between the SPP and ENZ layers, as well as a top coating layer on the bilayer films (see Figures 3.1a and 3.1c). These results are compared to simulated results using both TMM and a Hopfield model.

In this study the thickness and carrier density of the SPP and ENZ layers are kept nominally constant across all samples (SPP layer: 300 nm, $N_d \approx 2.5 \times 10^{20} \text{ cm}^{-3}$ and ENZ layer: 50 nm, $N_d \approx 1 \times 10^{20} \text{ cm}^{-3}$). Carrier density and electron mobility values were extracted using Hall effect measurements and layer thicknesses were determined using X-ray reflection measurements between each layer growth. Knowing these values, the MIR dielectric function was calculated for each layer using the Drude formulism equipped with a non-parabolicity effective mass model.⁴⁰ Knowing the dielectric function for all layers, the corresponding dispersion relationship for a multilayer CdO film can be calculated using TMM as we do later.

For an SPP mode supported at the interface of a single CdO film with a thickness larger than the evanescent skin depth, the dispersion relation can be calculated (dashed red line in figures 3.1c and 3.1d) simply as

$$k_{\parallel} = k_o \sqrt{\frac{\epsilon_{SPP} \epsilon_{amb}}{\epsilon_{SPP} + \epsilon_{amb}}} \quad (6)$$

Here, ϵ_{SPP} is the dielectric function of the SPP-supporting CdO layer ($N_d \approx 2.5 \times 10^{20} \text{ cm}^{-3}$), ϵ_{amb} is the permittivity of the ambient dielectric environment above the film. The in-plane wavevector and wavenumber in vacuum are represented by k_{\parallel} and k_o , respectively. However, if the thickness of the CdO film is far lower than the evanescent skin depth ($d_{ENZ} < \frac{\lambda_p}{50}$) the film is capable of supporting an ENZ mode. As is discussed in chapter 1, these ENZ modes are associated with a large enhancement and localization of the electric field magnitude to the film volume, which is sub-diffraction in scale. This high-degree of spatial localization corresponds with a spectral dispersion that is nominally flat (see dashed black line in Figures 3.1c and 3.1d) and group velocity which is nearly zero.

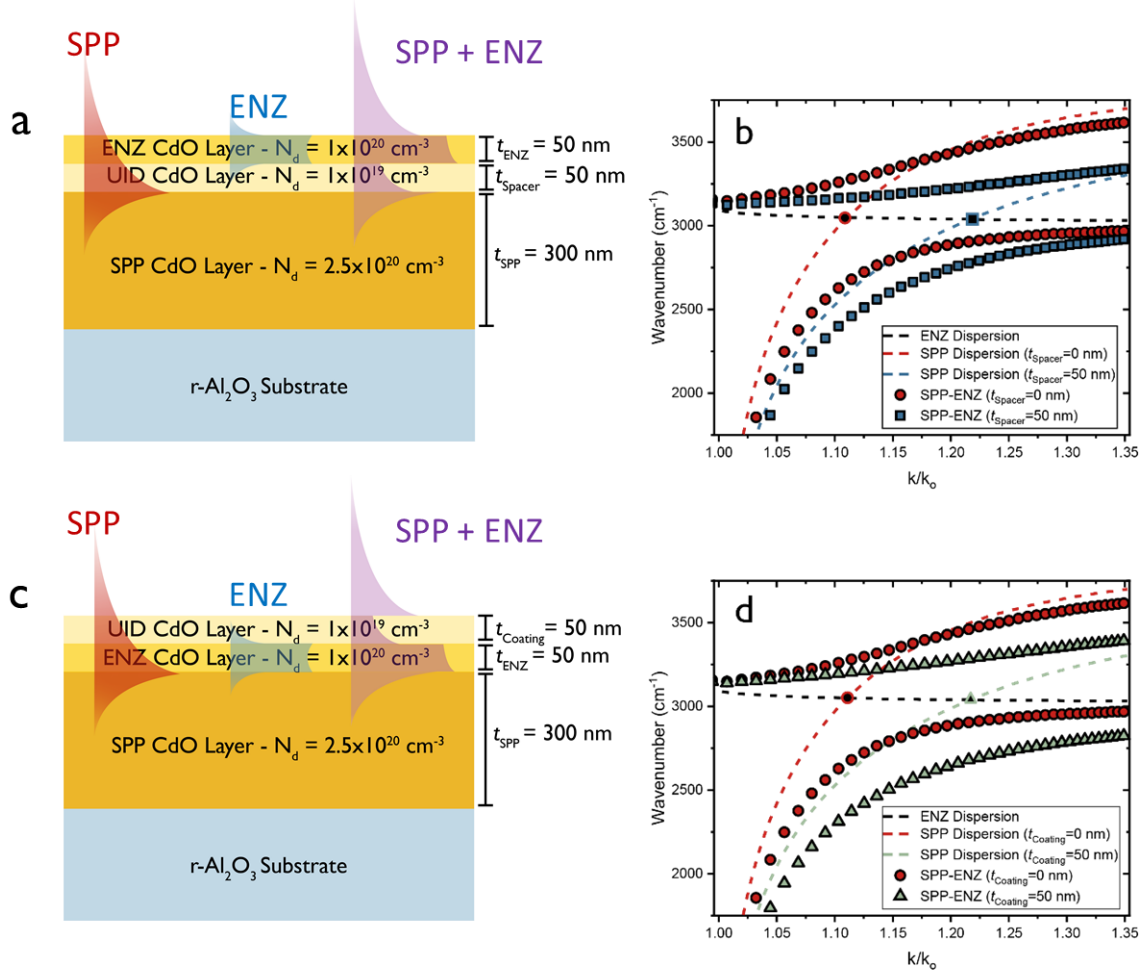


Figure 3.1: a) Schematic of SPP-ENZ strongly-coupled CdO film with UID CdO layer used as spatial separation between SPP and ENZ layers. b) TMM-calculated dispersion of bilayer ($t_{spacer} = 0 \text{ nm}$) and $t_{spacer} = 50 \text{ nm}$. c) Schematic of SPP-ENZ strongly-coupled CdO film with UID CdO layer deposited as a coating layer. d) TMM-calculated dispersion of bilayer ($t_{coating} = 0 \text{ nm}$) and $t_{coating} = 50 \text{ nm}$. Note that in both cases, the SPP-ENZ anticrossing occurs at the intersection between the uncoupled SPP and ENZ dispersions.

As was stated above the carrier density of CdO can be varied during HIPIMS deposition allowing for the realization of multilayer, homoepitaxial CdO films. By growing an ENZ-supporting CdO film on top of an SPP-supporting CdO film, placing the ENZ layer within the evanescent extent of the SPP mode, a distinct modification to the modal dispersion can be achieved. Namely, if the ENZ dispersion spectrally overlaps with the SPP dispersion, an anti-crossing emerges at the (k_{\parallel}, ω) position that the uncoupled modes would otherwise intersect (red circles in Fig. 3.1c and 3.1d), signifying strong coupling between the two modes. As was stated above, the spectral splitting can be altered in these bilayer CdO films by controlling the carrier density and/or thickness of the ENZ CdO film.

The dielectric environment also plays a critical role in the behavior of polaritonic modes. From eq. 6 it is evident that for SPP modes the in-plane wavenumber becomes asymptotic when approaching the $\epsilon_{SPP} = -\epsilon_{amb}$ condition. Therefore, an increase in the real part of the ambient permittivity results in a redshift of this asymptotic condition (blue and green dashed lines in Figures 3.1b and 3.1d, respectively). Further, the increased ambient refractive index reduces the slope of the free-space light line ($\frac{\omega}{k} = \frac{c}{n_{amb}}$) leading to a decrease in the phase velocity of the SPP mode. As the evanescent decay of the SPP mode $E_z \propto e^{-k_z z}$ where $k_z = \sqrt{k_0^2 \epsilon_{amb} - k_{\parallel}^2}$ is heavily dependent on the in- and out-of-plane momentum, the modified dispersion ‘squeezes’ the electromagnetic energy into smaller mode volumes. A simple method of perturbing the local dielectric environment above a polaritonic film is to coat the surface with a thin (with respect to the evanescent decay), high-index dielectric layer, resulting in an elevated effective ambient permittivity ($\epsilon_{amb} = \epsilon_{eff}$) which takes into account the contribution from the coating and air. This approach was previously employed by Li et. al. to alter the dispersion of SPhPs supported by a quartz film coated in $\text{Ge}_3\text{Sb}_2\text{Te}_6$ (GST).¹⁴¹

Similarly, by coating the surface of a bilayer CdO film with a thin layer ($t_{coating} = 50 \text{ nm}$) of UID CdO the SPP-ENZ hybrid dispersion can be tailored, as is displayed in Figure 3.1d. The carrier density of the ‘coating’ layer is $N_d \approx 4 \times 10^{19} \text{ cm}^{-3}$, placing the plasma frequency well below the energies at which the SPP and ENZ modes are supported. Thus, the permittivity of the coating layer is positive and approaching the magnitude of ϵ_{∞} at frequencies around the SPP-ENZ anti-crossing. Note that this film is slightly dispersive, however this is easily accounted for in our

TMM calculations by incorporating the full frequency-dependent dielectric function for all layers across the entire spectral range.⁴⁰ The shift in the SPP-ENZ dispersion is a result of the hybrid nature of the SPP-ENZ modes but can be best understood by considering the uncoupled SPP and ENZ modes separately. Adding a 50 nm coating layer induces a slight spectral shift to the uncoupled ENZ mode however this shift is very small with respect to the ENZ modal linewidth ($\Delta\omega_{ENZ}/\gamma_{ENZ} \ll 1$) due to the high volume confinement/low evanescent extent of the ENZ mode⁶ (see section 3.2.6). In contrast, the dispersion of the SPP mode is heavily influenced by the 50 nm coating layer (green dashed line in Fig. 3.1d), as was discussed above, becoming asymptotic at lower frequencies. Now the uncoupled SPP and ENZ modes intersect at higher momentum, shifting the anti-crossing in the SPP-ENZ hybrid dispersion from $k_{\parallel}/k_o \approx 1.12$ for the bilayer film to $k_{\parallel}/k_o \approx 1.22$ for the coated film. The 50 nm coating layer does not significantly alter the spectral splitting of the bilayer film, with simulation results showing an increase from $\Omega = 516 \text{ cm}^{-1}$ for the bilayer film to $\Omega = 517 \text{ cm}^{-1}$ for the coated film. This is due to the decreased mode volume and increased ENZ absorption with increased coating layer thickness, which will be discussed later.

Alternatively, the UID CdO layer can be grown in-between the SPP and ENZ CdO layers, providing spatial separation between the two modes instead of being used as a coating layer for the bilayer CdO film. For a given ‘spacer’ thickness (for example, $t_{spacer} = 50 \text{ nm}$ as is shown in figure 3.1a) the ambient dielectric environment above the SPP layer is identical to that of a coated-bilayer film with the same coating thickness ($t_{Coating} = 50 \text{ nm}$). Therefore, the spacer layer induces the same redshift to the uncoupled SPP mode and shifts the SPP-ENZ anti-crossing to the same position in k-space ($k/k_o \approx 1.22$) that is shown for the coating layer sample (Fig. 3.1b). Note that as with the coating layer, the spacer layer has very little effect on the spectral position of the ENZ mode (Section 3.2.6). However, the spatial separation of the SPP and ENZ layers reduces the modal overlap and hence the coupling strength. For example, from the calculated dispersion provided in figure 3.1b the spectral splitting reduces from $\Omega = 516 \text{ cm}^{-1}$ for the bilayer film to $\Omega = 403 \text{ cm}^{-1}$ for when a 50 nm spacer layer is introduced.

3.2.1 Impact of Coating and Spacer Layer Thickness on the SPP-ENZ Dispersion

In order to explore the dependence of the CdO coating layer thickness on the SPP-ENZ dispersion, we grew four CdO bilayer films and coated three with a thin layer of UID CdO

($t_{\text{coating}} = 25, 50, \text{ and } 84 \text{ nm}$). We left one of the bilayer films uncoated ($t_{\text{coating}} = 0 \text{ nm}$) to use as a control sample. All films were grown epitaxially on r-Al₂O₃ substrates and, as is stated above, maintain epitaxy throughout the multilayer stack. An illustration of the sample geometry is displayed in Fig. 3.2f. Although the targeted thickness and carrier densities of the SPP and ENZ layers are constant across all samples, there are minor differences in SPP and ENZ carrier densities between samples ($\pm 1 \times 10^{19} \text{ cm}^{-3}$). Further, the bilayer CdO film is Y-doped, whereas the three coated samples are In-doped which will result in small differences in the effective mass.⁶⁷ We account for these slight variances and discuss the effects on the coupling strength in section 3.2.3. We then performed ATR measurements in the Kretschmann configuration in order to extract the SPP-ENZ dispersion of each film and compared these results with TMM-calculated $R(k_{\parallel}, \omega)$ (contour plots in Figure 3.2f) maps and the eigenfrequencies ($\omega_{k_{\parallel}}^{\pm}$) calculated using the Hopfield model (solid lines).

The measured SPP-ENZ dispersion of the bilayer CdO film (figure 3.2a) displays a splitting into upper and lower branches, with the upper (lower) branch exhibiting a large (small) group velocity v_g . With the introduction of a 25 nm CdO coating layer (figure 3.2d) the group velocity in both the upper and lower branches is reduced, a result of the perturbed ambient permittivity above the film. The group velocity is reduced even further when the coating thickness is increased to 84 nm. In all cases, the measured dispersion agrees favorably with the calculated dispersion using TMM and the Hopfield model. In addition, the intersection of the uncoupled modes (dashed lines in figure 3.2) shifts to higher in-plane momentum as the coating layer thickness increases, resulting in the anti-crossing in the hybrid dispersion shifting as well. Finally, although the coating layer induces spectral detuning of the SPP mode, shifting the $\epsilon_{\text{SPP}} = -\epsilon_{\text{amb}}$ condition to a lower frequency and reducing the spectral overlap of the SPP and ENZ modes, the decrease in SPP mode volume and increase in ENZ absorption results in an increase in the coupling strength, and therefore spectral splitting, as the coating layer thickness increases.

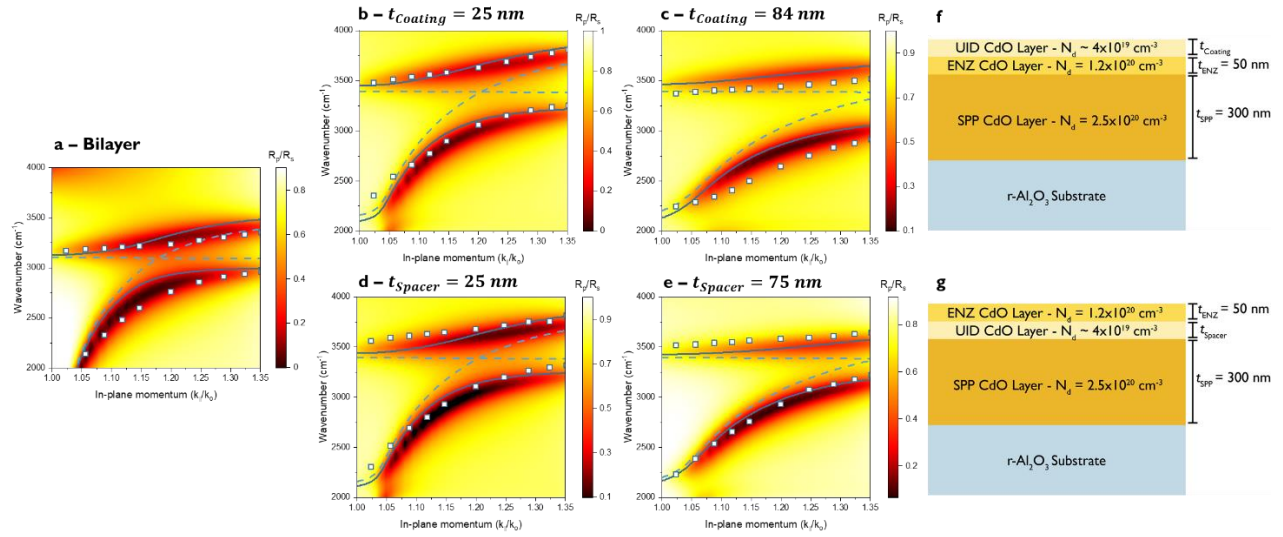


Figure 3.2: a) Hybrid SPP-ENZ polaritonic dispersion for a bilayer CdO film. The polaritonic dispersion of a trilayer film with a 25 nm and 84 nm UID CdO coating layer (see f) are displayed in b) and c). The polaritonic dispersion of a trilayer film with a 25 nm and 75 nm UID CdO spacer layer (see g)) are displayed in d) and e). The contour plot was calculated using TMM. The dashed blue lines are the uncoupled SPP and ENZ modes and the solid lines are the hybrid dispersion calculated using the Hopfield model. The measured dispersion is included as data points.

3.2.2 Impact of Spatial Separation on the SPP-ENZ Dispersion

In order to determine the impact of spatial separation on the SPP-ENZ dispersion, ATR measurements were performed on three additional samples that were grown with UID CdO ‘spacer’ layers (geometry is shown in figure 3.2.g) of varying thicknesses ($t_{spacer} = 25, 50,$ and 75 nm). Similar to what was observed for the coating layer samples, the introduction of a 25 nm spacer layer (Fig. 3.2.d) results in a reduction in the group velocity of both branches in the SPP-ENZ dispersion and decreased even further as t_{spacer} increases to 75 nm (Fig. 3.2.e). Further, the SPP-ENZ anti-crossing shifts to higher in-plane momentum as the spacer layer thickness is increased. However, the spectral splitting between the SPP and ENZ modes decreases as the spacer layer thickness increases to 25 and 75 nm, a result of the reduced spectral and spatial overlap as the SPP mode decays exponentially in the spacer layer. Note that for the thick spacer/coating samples in Fig. 3.2.c and 3.2.e there is a clear inflection in the polaritonic dispersion at low frequencies and in-plane momentum, which is due to dispersion in the UID CdO layer. As the carrier density of the UID CdO layer is $N_d \approx 4 \times 10^{19} \text{ cm}^{-3}$ and the thickness is deeply subwavelength, this layer also exhibits ENZ behavior, however, at a frequency far below

($\omega_{ENZ(UID)} \approx 2125 \text{ cm}^{-1}$) the ENZ mode supported in the ‘ENZ layer’. This is discussed further in the section 3.2.5, where we outline our approach for calculating the dispersion using the Hopfield model.

3.2.3 Impact of Spatial Separation on the SPP-ENZ Coupling Strength

From the dispersion relation provided in Fig. 3.2 it is evident that the placement of the ENZ layer within the multilayer CdO stack is a critical factor in controlling the SPP-ENZ coupling strength. In order to track how the coupling strength changes across samples we calculated the spectral splitting ($\Omega_{splitting}$) at the anti-crossing position from the measured polaritonic dispersion for each of the films. As was stated above, there is a slight variance in the ENZ and SPP layer carrier densities across samples. Since the coupling strength is dependent on the SPP-ENZ spectral overlap, we have accounted for these slight differences by first normalizing the spectral splitting to the ENZ frequency ($\frac{\Omega_{splitting}}{\omega_{ENZ}}$) of each film. We then compared the measured coupling strength to calculated values using the TMM for multilayer films with an SPP layer carrier density of $N_d = 1.9 \times 10^{20} \text{ cm}^{-3}$ (Fig. 3.3a and 3.3b, red line) and $N_d = 2.5 \times 10^{20} \text{ cm}^{-3}$ (Fig. 3.3a and 3.3b, blue line), respectively. For these calculations the ENZ and UID CdO layer carrier densities were kept constant at $N_d = 1.1 \times 10^{20} \text{ cm}^{-3}$ and $N_d = 4 \times 10^{19} \text{ cm}^{-3}$, respectively.

When the UID CdO layer is used as a coating layer, the normalized spectral splitting is shown to increase from 0.125 to 0.17 as the coating layer thickness is increased to 100 nm (Fig. 3.3b). This increase can be attributed to the aforementioned decrease in SPP mode volume as well as an increase in ENZ modal absorption. The rate at which the evanescent electric field decays above the SPP layer is dictated by the ambient effective permittivity as $E_z \propto e^{-k_z z}$ where $k_z = \sqrt{k_0^2 \epsilon_{eff} - k_{\parallel}^2}$. For the bilayer sample, the ENZ layer is adjacent to the SPP layer and therefore spatially overlaps with the exponentially-decaying SPP field at the field maximum. The same is true for the coating layer samples, however the thickness of the coating layer leads to an increase in ϵ_{eff} above the SPP film and therefore shorter exponential decay of E_z . Alternatively, if the film is viewed as a 1-D open cavity with out-of-plane field confinement, the shift of the anti-crossing to higher in-plane momentum observed in the SPP-ENZ dispersion is analogous to a compression of the SPP mode volume. For the coated samples the ENZ layer is in direct contact with the SPP

layer, therefore the spatial overlap of the SPP and ENZ modes remains high even as the SPP mode volume diminishes.

The increase in ε_{eff} is a hindrance on the coupling strength for the spacer layer samples. The spacer layer spatially separates the ENZ mode from the SPP film, placing it further out in the evanescent extent of the SPP mode. Therefore, the rate at which the evanescent field decays within the spacer plays a significant role in decreasing the coupling strength with increased spacer layer thickness. Indeed, the normalized spectral splitting was shown to decrease from ~ 0.14 to ~ 0.1 for increased spacer layer thicknesses out to 100 nm. Note that the coupling strength does not increase (decrease) linearly with coating (spacer) layer thickness, which is due in part to the relationship between the ambient permittivity and UID CdO layer thickness and the nonlinear dispersion of the SPP mode. For both the spacer and coating layer samples the data extracted from our measurements agrees well with values from TMM calculations of the SPP-ENZ dispersion. Further, the SPP layers for the bilayer and 50 nm spacer samples are from the same growth and therefore have identical carrier density ($N_d \approx 1.9 \times 10^{20} \text{ cm}^{-3}$) and thickness values. The same is true for the remaining samples ($N_d \approx 2.5 \times 10^{20} \text{ cm}^{-3}$). Due to the lower carrier density in the bilayer and 50 nm spacer samples, the spectral overlap between the SPP and ENZ modes within these films¹²⁰, and thus the coupling strength, is expected to be lower as is shown in Fig. 3.3.

Another significant factor driving the SPP-ENZ coupling strength is the ENZ modal absorption. Although the electric field of an ENZ mode is volume-confined, the magnitude of the electric field and modal absorption is largely dependent on the dielectric environment above the ENZ-supporting film ($\varepsilon_{ENZ} E_{ENZ} = \varepsilon_{amb} E_{amb}$). Therefore, an increase in the ENZ absorption is expected with the introduction of the coating layer but not the spacer layer (See section 3.2.6). This can be viewed, equivalently, as an increase in the oscillator strength of the ENZ mode with increased ambient permittivity, similar to what was observed in bilayer SPP-ENZ films as the thickness of the ENZ layer was increased. This is also illustrated in Fig. 3.3c, which shows a 1-D profile of the electric field magnitude for a 50 nm ENZ film as a function of the ambient permittivity above the film. These field profiles were calculated using CST Studio Suite at an incident angle of 60° with a purely real ambient permittivity ($\varepsilon_{imag} = 0$).

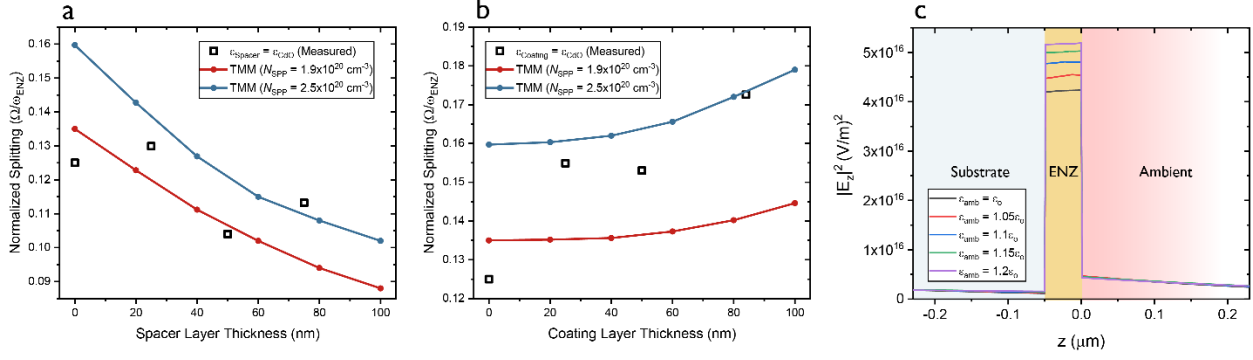


Figure 3.3: Spectral splitting at SPP-ENZ anti-crossing normalized to the ENZ frequency as a function of a) spacer layer thickness and b) coating layer thickness. c) Linear profile of the z -oriented electric field magnitude $|E_z|^2$ as a function of ambient effective index.

3.2.4 Electric Field Profiles of SPP-ENZ Modes in Trilayer CdO Films

In order to further understand the behavior of SPP-ENZ hybrid modes in these multilayer films we calculated (using CST Studio Suite) the upper and lower branch electric fields (E_z) oriented out-of-plane for the bilayer, 50 nm spacer and 50 nm coating samples at the anti-crossing positions ($k/k_0 \approx 1.12, 1.22,$ and $1.22,$ respectively). The SPP and ENZ layer carrier densities ($N_d = 2.5 \times 10^{20} \text{ cm}^{-3}$ and $1.1 \times 10^{20} \text{ cm}^{-3}$, respectively) and thicknesses (300 and 50 nm, respectively) were consistent across all simulations. Note that the modal behavior exhibited in the bilayer film remains consistent with the introduction of the spacer or coating layer, meaning that E_z in the upper (Fig. 3.4a, 3.4b, and 3.4c) and lower branch (Fig. 3.4d, 3.4e, and 3.4f) retains its symmetric and anti-symmetric character, respectively. As was mentioned above, the SPP-ENZ anti-crossing is pushed to higher in-plane momentum with the introduction of the UID layer, however occurring at the same position for the spacer and coating layer samples due to the identical dielectric environment leading to a compression of the in-plane polaritonic wavelength. In the lower band the polaritonic wavelength decreases by 9.2% and 5.9% for the spacer and coating layers, respectively, when compared with the bilayer sample. For the upper band the polaritonic wavelength decreases by 5.6% and 7.2% for the spacer and coating layers, respectively. The slight disparity in polaritonic wavelengths is due to the difference in coupling strength between the spacer and coating samples, resulting in resonant positions that differ in energy. The penetration depth is also shown to decrease between the bilayer and trilayer samples, concentrating the electric field to reduced spatial regions. For the lower (upper) branch the penetration depth is 833 nm (703

nm) for the bilayer sample, this however decreases by 20% (18%) and 19% (22%) for the spacer and coating layer samples, respectively.

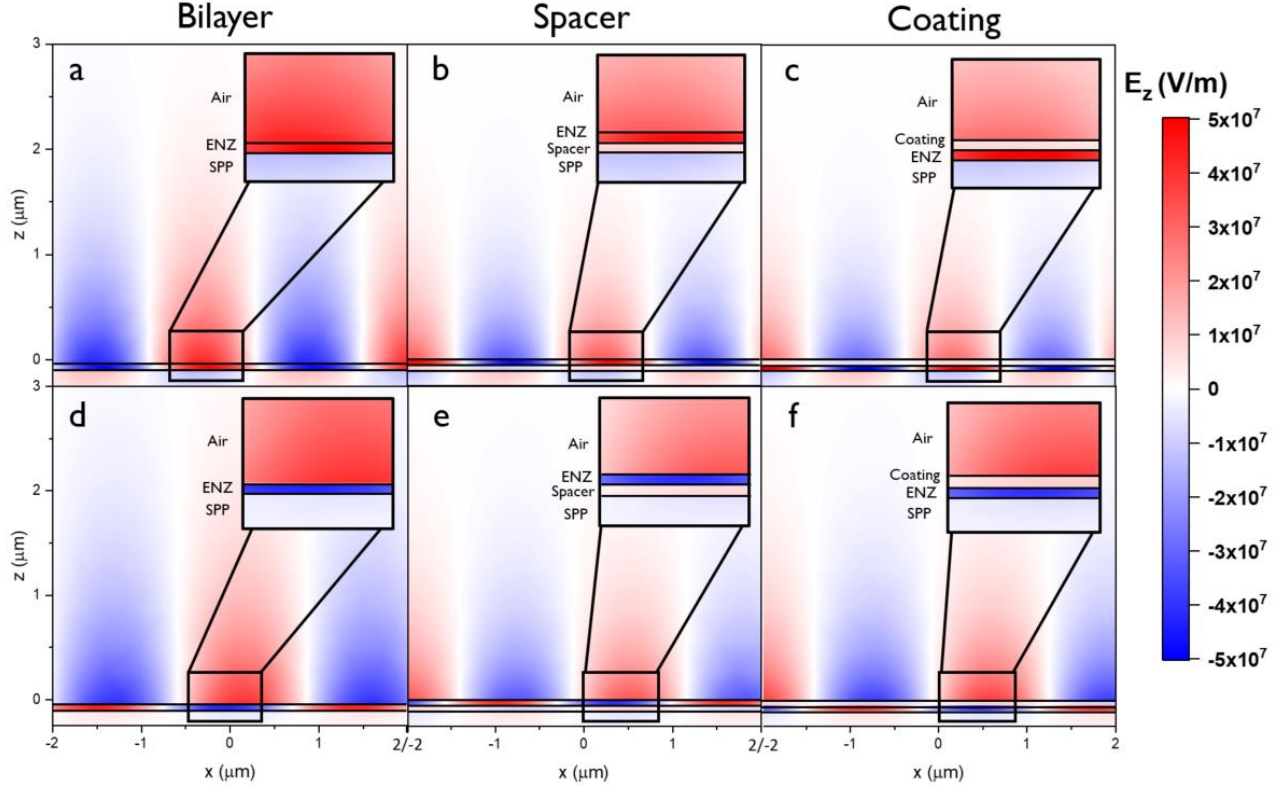


Figure 3.4: Out-of-plane electric field (E_z) calculated at the anticrossing condition for the bilayer film (a, d)), trilayer film with 50 nm spacer layer (b, e)), and trilayer film with 50 nm coating (c, f)). a), b), and c) show E_z in the upper branch and d), e), and f) show the fields in the lower branch.

3.2.5 Hopfield Model for SPP-ENZ Coupling in Dispersive Environment

The SPP-ENZ coupled system can also be described using the Hopfield model. This approach has been used to calculate the hybrid dispersion in previous studies of polaritonic strong coupling.^{12,24} For our purposes, we are interested in a simple two-mode coupled system with eigenfrequencies ω_q^\pm given by

$$\omega_{k_{\parallel}}^{\pm} = \frac{\omega_{k_{\parallel}}^{SPP} + \omega_{k_{\parallel}}^{ENZ} \pm \sqrt{(\omega_{k_{\parallel}}^{ENZ} - \omega_{k_{\parallel}}^{SPP})^2 + 4g^2}}{2} \quad (7)$$

Here $\omega_{k_{\parallel}}^{SPP}$ and $\omega_{k_{\parallel}}^{ENZ}$ are the frequencies of the uncoupled SPP and ENZ modes, respectively. The coupling strength g is determined phenomenologically whereas the dispersion relations of the

uncoupled modes were calculated. The dispersion of the ENZ mode can be approximated using the expression

$$\omega_{k_{\parallel}}^{ENZ} = \omega_p \left[1 - \frac{k_{\parallel}d}{4} \right] - i \frac{\gamma}{2} \quad (8)$$

Where ω_p and γ are the plasma frequency and Drude damping of the ENZ layer, respectively, and d is the thickness. In calculating the hybrid mode dispersion, we are only concerned with the real part of $\omega_{k_{\parallel}}^{ENZ}$. For the bilayer CdO film, the SPP dispersion $\omega_{k_{\parallel}}^{SPP}$ can be calculated using equation 6 or TMM. However, for the trilayer films the SPP dispersion needs to take into account the dispersion in the effective ambient environment above the film. Therefore, we have used TMM to calculate the uncoupled SPP dispersion for all of the films.

For the bilayer film, the reflectance map was calculated in the Kretschmann ATR configuration for a single 300 nm CdO film with a carrier density of $N_d = 2.5 \times 10^{20} \text{ cm}^{-3}$. Then, $\omega_{k_{\parallel}}^{SPP}$ was extracted by tracking the reflectance minima as a function of in-plane momentum. For the trilayer films, the dispersive dielectric environment above the SPP layer is accounted for by adding a UID layer on top of the SPP layer. An anticrossing is observed in the resultant dispersion (figure 3.5a) at the plasma frequency of the UID layer (2125 cm^{-1}), with the dispersion splitting into upper and lower branches. The upper branch was then used as $\omega_{k_{\parallel}}^{SPP}$ in equation 7 to calculate the SPP-ENZ eigenfrequencies $\omega_{k_{\parallel}}^{\pm}$ of the trilayer film. The dispersion of the uncoupled SPP and ENZ modes used to calculate the hybrid dispersion in figure 3.5b are displayed as dashed lines. Since all that changes between the spacer and coated samples is the stacking order of the ENZ and UID layers, the dielectric environment above the SPP layer in the spacer and coating samples with identical UID layer thicknesses is assumed to be the same.

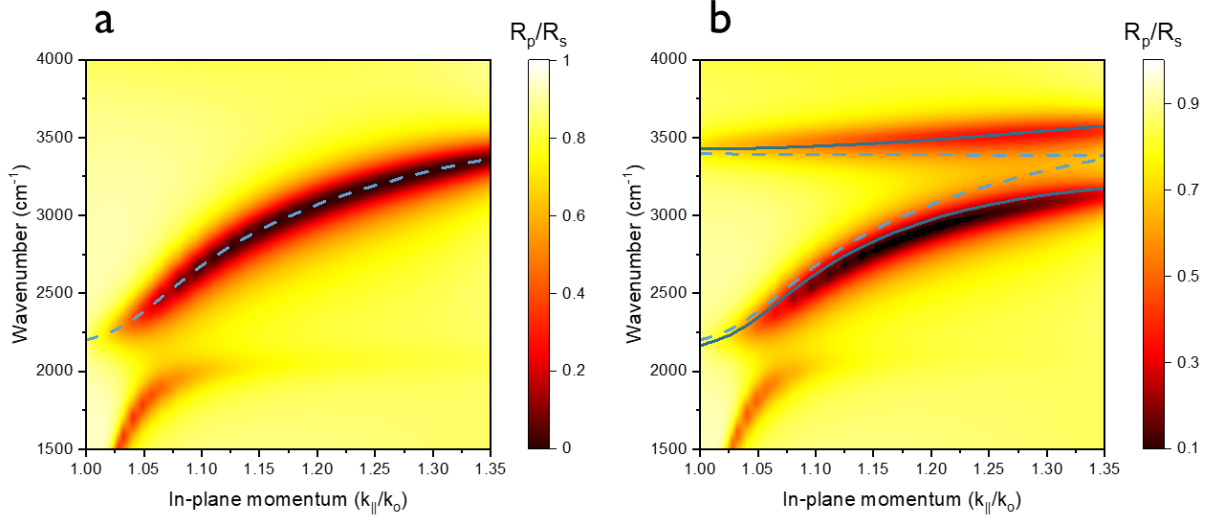


Figure 3.5: (a) Calculated dispersion of 300 nm CdO film ($N_d = 2.5 \times 10^{20} \text{ cm}^{-3}$) coated with a 75 nm UID CdO layer. The strong coupling between the SPP mode and the ENZ mode supported by the UID CdO film ($\omega_{ENZ} \sim 2125 \text{ cm}^{-1}$) results in splitting into upper and lower branches. The upper branch (dashed line) is then used as the uncoupled SPP dispersion $\omega_{k_{||}}^{SPP}$ when calculating the hybrid dispersion in (b). The calculated dispersion of a trilayer film with a 75 nm UID CdO spacer layer is provided in (b).

3.2.6 Effects of Ambient Permittivity on ENZ Modal Absorption

Although the ENZ electric field is volume-confined, the magnitude is directly related to the real permittivity of the ambient dielectric environment ($\epsilon_{ENZ} E_{ENZ} = \epsilon_{amb} E_{amb}$). Therefore, the incorporation of the UID CdO layer on top of an ENZ-supporting CdO layer results in an increase in the ENZ absorption (Figure 3.6a) at a constant angle. There is a slight spectral shift with increased UID CdO layer thickness, however this shift is very small with respect to the ENZ linewidth ($\Delta\omega_{ENZ}/\gamma_{ENZ} \ll 1$). If the same calculation were performed with the UID CdO layer below the ENZ layer, the ENZ absorption and frequency would remain nominally the same (Figure 3.6b).

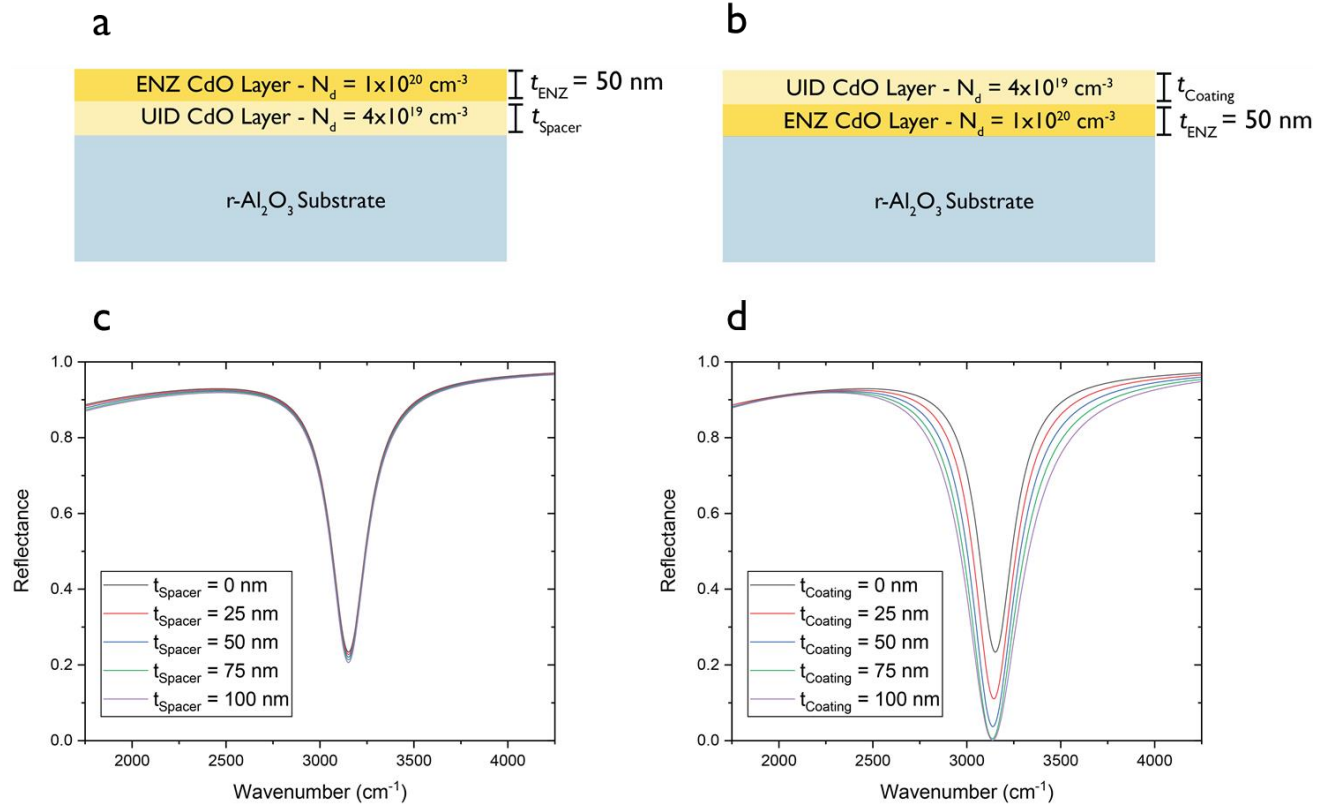


Figure 3.6: (a) Geometry of CdO film with UID CdO layer below the ENZ layer. (b) Geometry of CdO film with UID layer above ENZ layer. (c) and (d) contain the TMM-calculated ATR spectra at 60° for the CdO film displayed in (a) and (b), respectively.

3.2.7 Conclusions

Here we have exploited the high carrier confinement and exceptionally low losses in n-doped CdO films in order to illustrate the effects that introducing UID CdO as a dielectric spacer or coating layer has on the SPP-ENZ dispersion. Namely, how the dielectric environment and modal separation dictates the in-plane momentum of the anticrossing position and coupling strength. Although we rely on UID CdO as a ‘dielectric’ layer, this analysis could potentially be extended by incorporating other dielectric materials. Further, by leveraging the dynamic permittivity of phase change (VO_2 or GST) or ferroelectric materials as a spacer or coating layer dynamic tunability over the polaritonic dispersion could potentially be realized. The platform we’ve studied is purely plasmonic, however the analysis provided is still of interest and translates intuitively to a much wider set of planar and non-planar coupled systems making the work

presented here of great utility in the realization of a number of novel applications of strongly-coupled systems.

3.3 Three Mode Strong Coupling in III-V Semiconductor Heterostructures

III-V semiconductors are a widely studied class of materials that have been utilized in quantum well structures¹⁴², plasmonics⁴⁷, and hyperbolic metamaterials¹⁴³. Due to their polar lattices, these materials support SPhP modes between the TO and LO phonon frequencies (within the Reststrahlen band). Further, at film thicknesses far below the polariton wavelength, these films support volume-confined epsilon-near-pole (ENP) and ENZ modes near the TO and LO phonon frequencies, respectively. In this section we demonstrate that SPhP-ENP and SPP-ENP-ENZ strong coupling can be achieved in bilayer InAs-GaSb and InAs-AlSb films. Further, we provide multiple methods of tuning the hybrid dispersion within these III-V heterostructures.

3.3.1 Tuning of SPhPs in InAs through LO Phonon-Plasmon Coupling

Introducing dopants into a polar dielectric crystal results in coupling between the LO phonon and free carrier plasma.^{144,145} This effect is referred to as the LO phonon-plasmon coupling (LOPC) effect and has been observed in several material systems including GaN, SiC, and InP. The LOPC effect results in a change to the effective polarizability of the crystal, and therefore the dielectric function, that can be modeled by using a combined Drude-Lorentz term.¹⁴⁶

$$\varepsilon(\omega, N_j) = \varepsilon_\infty \left(1 + \frac{\omega_{LO}^2 - \omega_{TO}^2}{\omega_{TO}^2 - \omega^2 - i\omega\gamma} \right) - \sum_{j=e,h} \frac{\omega_{p,j}^2}{\omega^2 + i\omega\Gamma} \quad (9)$$

Here, $\omega_{p,j}^2 = \frac{N_j e^2}{\varepsilon_0 m_j^* m_0}$ and $j = e$ and $j = h$ refer to contributions from electrons and holes, respectively. At low doping levels the Reststrahlen band is effectively extended by blue shifting the zero-crossing of the real permittivity while introducing a slight increase in damping Γ due to carrier-carrier scattering. However, at high carrier densities the Drude component dominates the optical response, as was seen near the optic phonons of CdO in section 2.4.4, resulting in $Re[\varepsilon(\omega, N_j)] < 0$ and an elevated $Im[\varepsilon(\omega, N_j)]$ across the entire spectral range. In this section we demonstrate how the SPhP mode dispersion can be modified in InAs by introducing Si-dopants.

In section 3.3.4, the carrier tunability of the SPhP dispersion will be employed to demonstrate strong coupling between SPhPs, ENZ, and ENP modes (discussed in the following section) modes within InAs-GaSb and InAs-AlSb films.

Propagating SPhP modes are supported at the interface of undoped InAs films between the TO (211 cm^{-1}) and LO (237 cm^{-1}) phonon frequencies. These modes can be observed in Otto configuration ATR measurements, as is shown in the calculated reflectance maps in Figure 3.7. Kretschmann configuration measurements could also potentially be employed if the appropriate substrate material were used, however in order to reduce strain at the InAs-substrate interface the substrate must be lattice matched with the InAs. It is common to use GaAs as a substrate, as we have implemented here. However, GaAs is very dispersive within the spectral range of interest making Kretschmann configuration measurements challenging and even impossible within the GaAs Reststrahlen band which spans from $\omega = 268 - 292 \text{ cm}^{-1}$. In Otto configuration, since the SPhPs are excited in the air-gap separating the film and prism, with a sufficiently thick InAs layer ($t_{\text{InAs}} = 6 \mu\text{m}$) the influence of the substrate can be substantially decreased within the InAs Reststrahlen band.

Using TMM, a p -polarized reflectance map showing the SPhP dispersion of a $6 \mu\text{m}$ undoped InAs film on a GaAs substrate was calculated (Figure 3.7a). This calculation was performed in the Otto configuration (geometry in Figure 3.7d) using a diamond prism ($n \sim 2.4$) which is highly transmissive throughout the FIR. The dispersion follows the relation expressed in equation 6, becoming asymptotic at $\text{Re}[\epsilon_{\text{InAs}}(\omega, N_j)] = -1$. In addition to the SPhP mode supported at the InAs interface, an SPhP mode is also present within the GaAs Reststrahlen band. This is due to $\text{Re}[\epsilon_{\text{InAs}}(\omega, N_j)] > 0$ in this spectral range when dopants are not present and therefore, an SPhP mode is also supported at the InAs-GaAs interface. If Si-dopants are introduced during the InAs film growth such that the plasma frequency $\omega_p = 900 \text{ cm}^{-1}$, the zero-crossing of the real dielectric function blue shifts. This shifts the asymptotic condition ($\text{Re}[\epsilon_{\text{InAs}}(\omega, N_j)] = -1$) to higher frequency, allowing SPP modes to be supported at higher frequencies. Further, the negative real permittivity of InAs within the GaAs Reststrahlen band forbids the SPhP at the InAs-GaAs interface from being supported (Figures 3.7b and 3.7f).

Due to the long wavelength within the FIR ($250 \text{ cm}^{-1} = 40 \text{ }\mu\text{m}$), the evanescent fields from the prism and SPhP extend 10s of microns. Therefore, in order to achieve near-critical coupling to the SPhPs (and therefore efficient SPhP absorption) at the InAs-air interface the gap between the prism and the InAs in Figures 3.7b and 3.7c was set to $40 \text{ }\mu\text{m}$. Critical coupling to an SPhP mode in Otto configuration is dependent on several factors such as the resonant frequency, incident angle, and Q-factor of the SPhP mode. When $d_{\text{Gap}} < d_{\text{critical}}$ the evanescent SPhP field would leak out through the prism leading to a reduction in the absorption and Q-factor. Conversely, when $d_{\text{Gap}} > d_{\text{critical}}$ the overlap of the evanescent field from the prism would not sufficiently overlap with the SPhP field, decreasing the absorption and increasing the Q-factor. This is demonstrated in the reflectance maps provided in figures 3.7e and 3.7f, showing the gap dependence at a single incident angle ($k = 1.05k_o$) for undoped and Si-doped InAs, respectively. At low gap distances, the SPhP linewidth for both films are broad, however the linewidth decreases significantly as the gap distance increases. Finally, the evanescent extent of both the prism and SPhP fields compresses as the in-plane momentum is increased. Therefore, d_{critical} decreases as the dispersion moves away from the free-space light line.

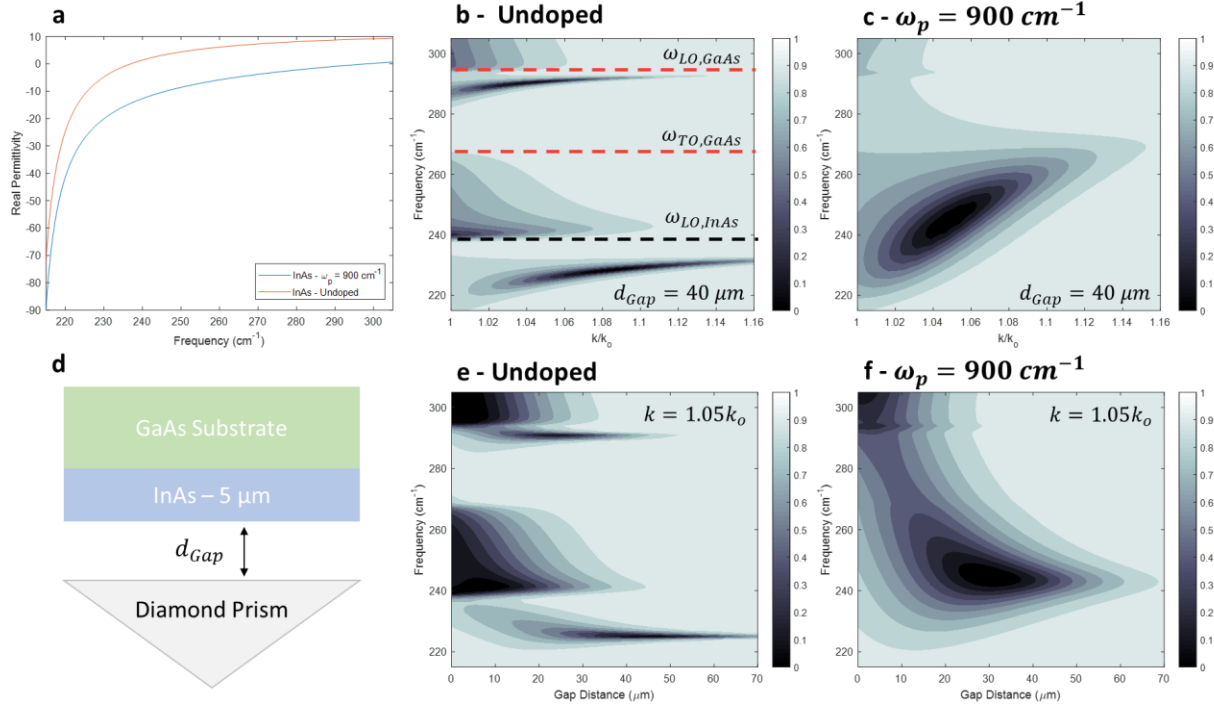


Figure 3.7: a) Real permittivity within the Reststrahlen band of undoped InAs and Si:InAs ($\omega_p = 900$ cm⁻¹). b) TMM reflectance map of undoped 5 μ m InAs film on GaAs substrate in Otto configuration (geometry in d)) with an air gap $d_{gap} = 40$ μ m. The dashed lines denote the TO and LO phonon frequencies of InAs and GaAs. c) TMM reflectance map of 5 μ m Si:InAs film on GaAs substrate. Air gap dependent calculations at a constant incident angle ($k = 1.05k_0$) for undoped InAs and Si:InAs are provided in e) and f).

3.3.2 Epsilon-Near-Pole Modes in Polar Dielectrics

From the Lorentz term in equation 9, it is clear that in the absence of optical losses ($\gamma \rightarrow 0$) there is a singularity in the real permittivity at the TO phonon frequency $Re[\epsilon(\omega)] \rightarrow \infty$. In real materials, the optical losses set a finite upper limit on $Re[\epsilon(\omega)]$, however in polar dielectrics where optical losses are low this upper limit is often very large. For example, $Re[\epsilon(\omega)]$ in undoped InAs exceeds 675 at the TO phonon frequency. Therefore, the real and imaginary permittivity becomes extremely dispersive at frequencies around the TO phonon.

In addition to supporting an ENZ mode at the LO phonon frequency, subwavelength thickness polar dielectric films also support an additional absorptive mode that coincides with the peak in $Im[\epsilon(\omega)]$ known as the ENP mode. Previous studies of ENP modes supported by metamaterials, which can be engineered to have an effective dielectric function with a similar Lorentzian lineshape to polar dielectrics, have shown that these modes exhibit extremely high,

omnidirectional, polarization-insensitive absorption within the free-space light cone making them an exciting potential platform for narrowband thermal emitters.¹⁴⁷ This is in contrast to natural and artificial media that support the Berreman mode which is polarization-sensitive and angle-sensitive (within the free-space light cone).

Similar to SPhP modes supported at the surface of polar dielectrics, the subject of the previous section, both the ENP and ENZ modes of a polar dielectric can be observed in Otto configuration ATR measurements. To demonstrate this, we calculated the reflectance maps of two thin (250 nm) III-V polar dielectric layers, GaSb and AlSb, on top of a 5 μm thick, highly doped ($\omega_p = 2500 \text{ cm}^{-1}$) InAs layer. We used a GaAs substrate, just as we did in the calculations in the previous section. Not only are GaSb and AlSb epitaxially-matched to InAs, the phonon frequencies of these materials are only slightly higher than the phonon frequencies of InAs. Therefore, through the LOPC effect, the zero-crossing of InAs can be blue-shifted by introducing Si-dopants. This opens the door to realizing strong coupling between the InAs SPhP modes and the ENP and ENZ modes of GaSb and AlSb. In the calculations provided in figure 3.8, a highly-doped InAs layer was used in order to provide a reflective backplane for the GaSb and AlSb layers (geometry in figure 3.8d) and prevent interactions with the SPhPs.

The electric field associated with ENP and ENZ modes is concentrated within the film volume and the evanescent field does not extend nearly as far as SPhP modes. So, in order to efficiently couple to these modes, the film needs to be much closer to the prism (5 μm in the calculations here). Outside of the free-space light cone, the ENP and ENZ modes maintain their polarization insensitivity and sensitivity, respectively. Therefore, the ENZ mode is observed only in p -polarization whereas the ENP mode is observed in both s - and p -polarizations. This is confirmed in the p -polarized reflectance map (Figure 3.8b) of the GaSb film which shows two absorptive features at $\sim 230 \text{ cm}^{-1}$ and $\sim 241 \text{ cm}^{-1}$ corresponding with the ENP and ENZ modes, respectively. In s -polarization, however, only the feature at $\sim 230 \text{ cm}^{-1}$ is observed. Similarly, the p -polarized reflectance map of the AlSb film shows ENP and ENZ modes at $\sim 316 \text{ cm}^{-1}$ and $\sim 340 \text{ cm}^{-1}$, respectively, with only the ENP being observed in s -polarization.

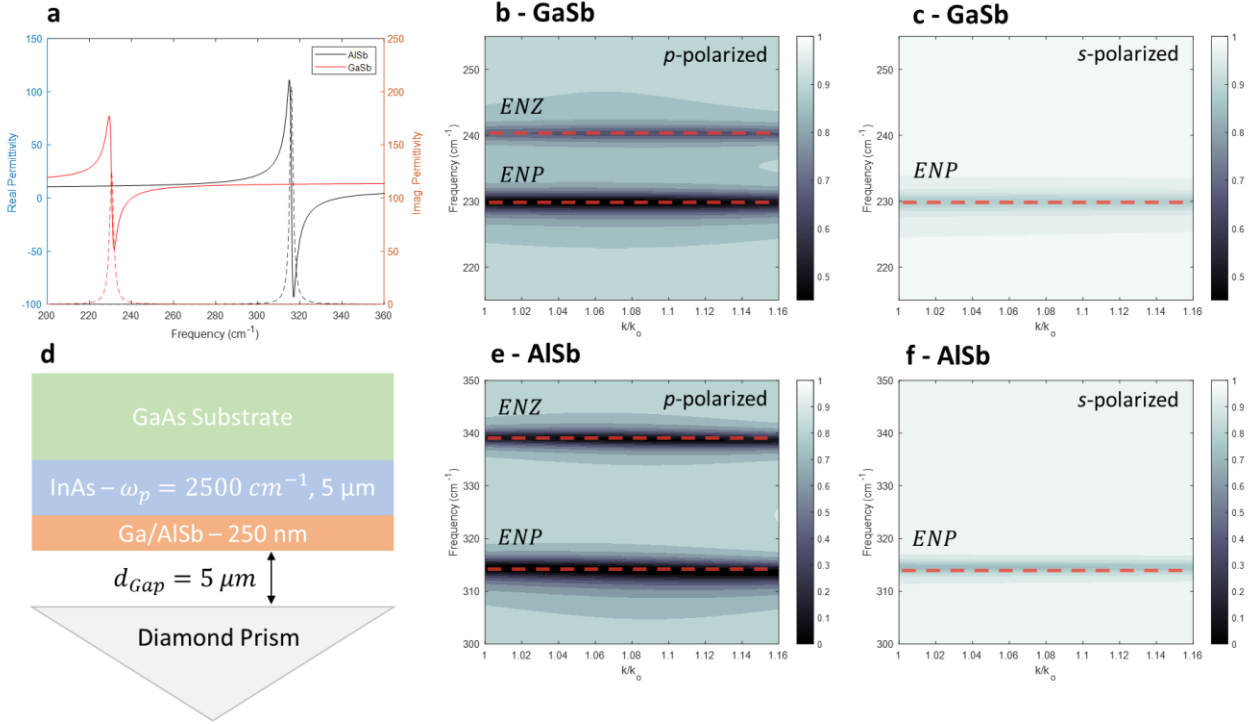


Figure 3.8: a) Real and imaginary permittivity of GaSb and AlSb.⁴⁴ b) *p*- and c) *s*-polarized TMM reflectance map calculated in Otto configuration (geometry in d)) of GaSb thin film on highly doped InAs ($\omega_p = 2500 \text{ cm}^{-1}$) substrate. e) *p*- and f) *s*-polarized TMM reflectance map calculated in Otto configuration (geometry in d)) of AlSb thin film on highly doped InAs substrate.

3.3.3 SPhP-ENP and SPP-ENP-ENZ Strong Coupling in InAs-GaSb and InAs-AlSb Films

In the previous two sections we have discussed tunable SPhP modes in InAs and ENP and ENZ modes in GaSb and AlSb independently. Here, we combine these two systems by including a thin GaSb or AlSb layer adjacent to the InAs layer (geometry in Figure 3.9c and 3.9f). Due to the spatial and spectral overlap of the ENP and ENZ modes in the GaSb or AlSb layers and the SPhP modes supported by the InAs, strong coupling is achieved between all three modes. This system offers large tunability over the resultant dispersion through changes to the InAs plasma frequency and the GaSb/AlSb layer thicknesses. Finally, since the dressed states of the hybrid system are linear combinations of the constituent modes (see section 3.1.2), the evanescent extent of each mode can be related to the modal fraction. Therefore, in Otto configuration the critical coupling distance can be related to the Hopfield coefficients of the hybrid modes. Although we provide a cursory example of the changes in critical coupling lengths in section 3.3.1, a full analysis employing the Hopfield model will be the subject of future work.

3.3.4 InAs Plasma Frequency Dependence

The ENP and ENZ modes occur at the TO and LO phonon frequencies of a polar dielectric, respectively. Therefore, in order to achieve strong coupling between SPhPs supported by the InAs and the ENP and/or ENZ modes of GaSb or AlSb the phonon frequencies must overlap with the Reststrahlen band of the undoped InAs or the extended negative permittivity region of Si:InAs. The TO phonon of GaSb falls within the Reststrahlen band of undoped InAs whereas the LO phonon frequency falls just above it. Therefore, the SPhP supported by the undoped InAs is expected to couple to the ENP mode but not the ENZ mode of GaSb in the InAs-bilayer system. Indeed, in the calculated reflectance map displayed in figure 3.9a, an anticrossing is observed near the GaSb TO phonon, signifying SPhP-ENP strong coupling, whereas the ENZ mode remains uncoupled. However, if the plasma frequency of the InAs is increased to a point that the zero-crossing of the InAs permittivity is higher than the ENZ mode frequency (Figure 3.9b), an additional anticrossing emerges in the dispersion near the GaSb LO phonon frequency, signifying strong coupling between the SPP, ENP, and ENZ modes.

The TO and LO phonons of AlSb are both at frequencies above the InAs Reststrahlen band. Therefore, the SPhP-ENP-ENZ interaction would be minimal due to the lack of spectral overlap between the SPhPs supported by the undoped InAs and the ENP and ENZ modes supported by the AlSb. However, increasing the plasma frequency of the InAs to 1500 cm^{-1} , and therefore placing the real permittivity zero-crossing above the AlSb LO phonon frequency, results in a splitting into three SPP-ENP-ENZ hybrid states with two anticrossings emerging at the AlSb TO and LO phonon frequencies. In the next section we will discuss the effects that changes to the GaSb/AlSb layer has on the polaritonic dispersion.

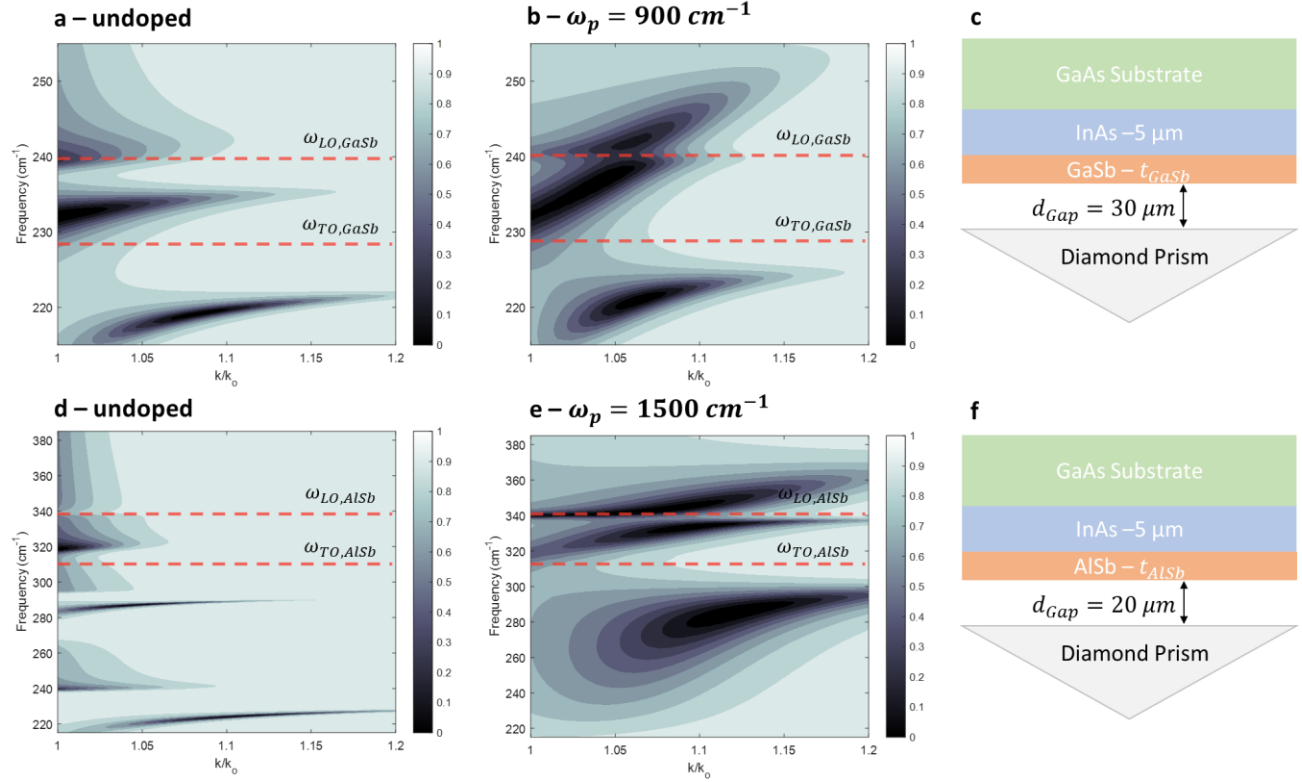


Figure 3.9: TMM reflectance showing (a) SPhP-ENP dispersion in undoped InAs-GaSb film and (b) SPP-ENP-ENZ dispersion in Si:InAs-GaSb film in Otto configuration (geometry in (c)) with an air gap $d_{Gap} = 30 \mu\text{m}$. The dashed lines denote the TO and LO phonon frequencies of GaSb. (d) TMM reflectance showing (a) uncoupled dispersion in undoped InAs-ALSb film and (b) SPP-ENP-ENZ dispersion in Si:InAs-ALSb film in Otto configuration (geometry in (f)) with an air gap $d_{Gap} = 20 \mu\text{m}$. The dashed lines denote the TO and LO phonon frequencies of ALSb.

3.3.5 ALSb Thickness Dependence

In the previous section we demonstrated the broad tunability of the SPhP-ENP-ENZ dispersion of InAs-GaSb and InAs-ALSb heterostructures that is afforded through changes to the InAs plasma frequency. Here we focus on the role that the top layer thickness plays in the hybrid dispersion. In previous studies of SPP-ENZ coupling in bilayer CdO films and SPhP-ENZ coupling in SiC-AlN heterostructures, it was reported that the Rabi splitting scales with the square root of the ENZ layer thickness $\sqrt{d_{ENZ}}$. This is analogous to strong coupling demonstrations of involving multiple emitters wherein the Rabi splitting scales with the concentration of the emitter (J-aggregates, quantum dots, atoms) as $\Omega \propto \sqrt{N}$.¹⁴⁸ Here, we note a similar relationship between the Rabi splitting and the thickness of the ENZ and ENP supporting layer, however in a system where three-mode strong coupling is observed as opposed to two-mode strong coupling.

Using TMM, we calculated the SPP-ENP-ENZ dispersion of InAs-ALSb bilayers where the ALSb thickness was varied from 0 to 750 nm. Although we focus only on InAs-ALSb bilayer films here, these results are readily translatable to the InAs-GaSb system. The plasma frequency of the InAs was set such that the zero-crossing in the InAs dielectric function occurs above the ALSb LO phonon. Therefore, the uncoupled SPP dispersion (Figure 3.10a) will overlap with both the uncoupled ENP and ENZ dispersions (Figure 3.10a) resulting in a splitting into lower, middle, and upper polariton branches (Figures 3.10b, c, and d). From observation of the calculated reflectance maps, it can be inferred that as the ALSb thickness is increased the spectral splitting between all three modes is increased. This is most evident in the lower polariton dispersion which is shown to redshift away from the ALSb TO phonon frequency as the ALSb thickness is increased. A decrease in the linewidths of the middle and upper branches is also observed, which is most likely a result of a decrease in the SPP contribution in these two modes. Note again that the critical coupling condition changes throughout the polaritonic dispersion. Since the dispersion was calculated at a constant gap distance ($d_{Gap} = 15 \mu m$), this would result in additional linewidth broadening in some regions of the polaritonic dispersion. Due to the strong coupling, the three hybrid states exhibit characteristics of the constituent, uncoupled modes with the weighting of each of the contributions (Hopfield coefficients) of each mode changing at different points along the dispersion. Implementing a Hopfield model in order to gain further understanding of the SPP-ENP-ENZ hybrid system and provide quantitative changes in Rabi splitting will be the subject of future work.

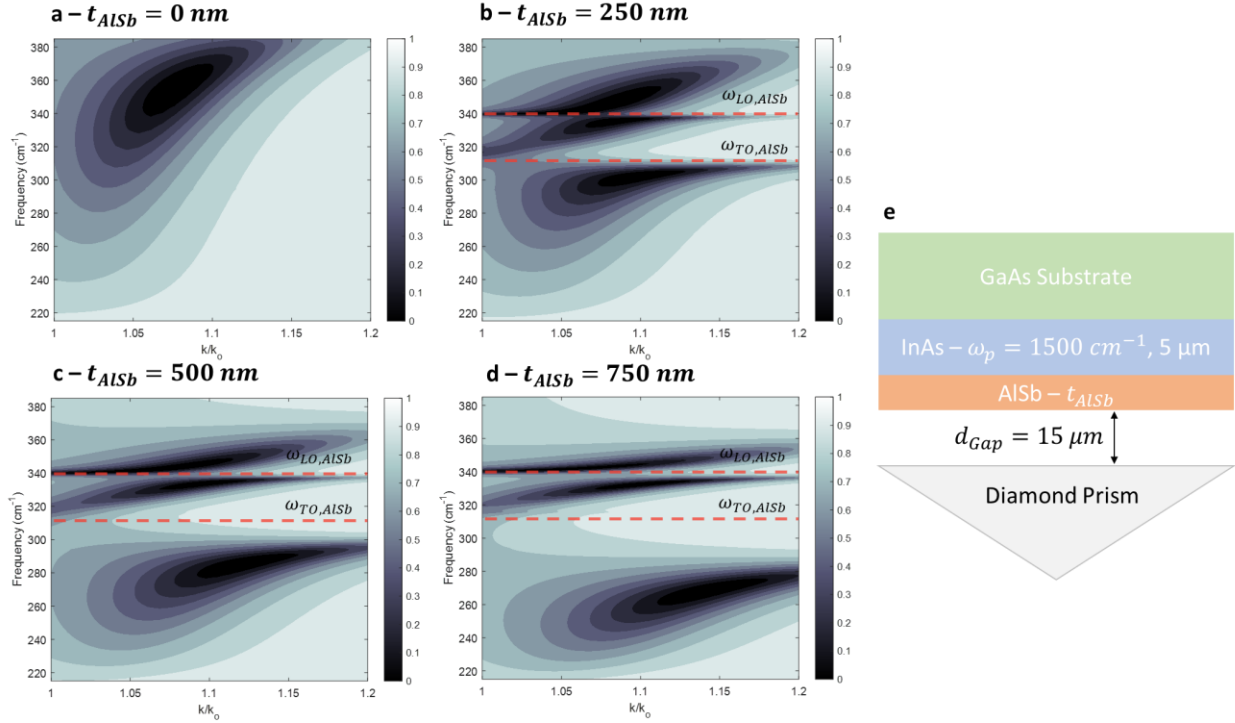


Figure 3.10: (a) Calculated TMM dispersion of SPPs in uncoated Si:InAs ($\omega_p = 1500 \text{ cm}^{-1}$). The calculated dispersion of InAs-AlSb bilayer films with AlSb thicknesses of 250 nm, 500 nm, and 750 nm are provided in (b), (c), and (d). The geometry of the simulations is provided in (e).

3.3.6 Conclusions

Here, we provided an initial study of SPhP-ENP and SPP-ENP-ENZ strong coupling in III-V polar semiconductor heterostructures. The tunability of the plasma frequency allows for the SPhP or SPPs supported by the InAs to be tuned throughout the Reststrahlen bands of both GaSb and AlSb. Due to the strong coupling between the modes, the hybrid modes take on characteristics of the constituent modes. As was stated in the previous section, future theoretical work will be placed on incorporating a Hopfield model in order to provide a quantitative analysis of the coupling strengths and modal weightings (Hopfield coefficients). As the relative weighting of each of the polariton branches results in varying evanescent extents (and therefore critical coupling conditions) we will then perform gap-dependent calculations at several angles in order to relate the coupling condition to the Hopfield coefficients. These simulation results will be compared against measurement results from InAs-GaSb and InAs-AlSb films grown using MBE. Finally, by incorporating a low-index dielectric as a dielectric coating, these films can be grown in the so-called ‘pseudo-Otto’ configuration. Here, instead of an air-gap providing the separation between

the prism and film, a dielectric layer is grown on top of the samples and placed directly in contact with the prism. As, with this method we will have precise control over the dielectric film thickness, this may prove to be a more controlled and promising route towards studying the nature of the hybrid modes in these structures.

Chapter 4

4. Theoretical Investigation of Monopole – ENZ – ENP Strong Coupling in III-V Heterostructure Resonators for Controlling Spatial Coherence of Thermal Emission

4.1 Monopole Resonances

Monopole antennas have been utilized in radio communications for over a century. Recent work has shown that these antennas can be scaled down to sub-diffractive length scales by coupling light to charge oscillations at the surface of polaritonic resonators. Monopole resonances are supported in resonators on a substrate with a negative real permittivity (typically the same material as the antenna) and derive their name from the mirror symmetry of the electric field across the resonator. Due to the lack of charge neutrality within the resonator, these modes are dark at normal incidence. However, at off-normal angles of incidence an image charge forms within the substrate that mirrors the ‘point – like’ charge distribution of the antenna, satisfying charge neutrality. Therefore, isolated monopole antennas are often modeled as a dipole resonator with a length that is twice the height of the antenna. Monopole modes have been investigated in localized SPP and SPhP – supporting structures, exhibiting large local electric field enhancements and Q-factors.^{98,149,150}

When monopole-supporting resonators are brought within close proximity (in resonator arrays with modest fill-fractions $f = \frac{\text{Resonator top surface area}}{\text{Unit cell area}}$), the negative-permittivity substrate facilitates substantial interpillar coupling by mediating charge transfer between adjacent pillars. This results in several interesting effects. For instance, an enhancement in the monopole absorption is observed up until the interpillar gap is reduced to some critical separation, implying that this may correspond to a critical coupling condition. At gap distances below this critical coupling condition, the absorption and Q-factor diminish significantly due to quenching of the fields. Further, due to the alignment of the dipoles along the longitudinal axis of the pillars, the monopole resonance blue shifts as the interpillar gap decreases.^{98,150} This is in contrast with transverse dipole resonances that are also supported in these structures, which red-shift as the interpillar gap decreases. Transverse dipole resonances are also more localized and therefore exhibit far less interpillar coupling than their longitudinal counterparts. Finally, the interpillar coupling relaxes the locality of the monopole mode resulting in long-range correlations across the

resonator array. In the previous section we discussed how long-range order is necessary for achieving spatially coherent thermal emission. Indeed, previous theoretical studies of localized SPhPs supported by SiC resonators on a SiC substrate have shown that the monopole resonance disperses with increased in-plane momentum (incident angle).¹⁵⁰

Prior works have realized spatially coherent thermal emission by momentum matching to propagating surface modes through diffractive coupling.^{21,24} In these cases, although the thermal emission is highly directional, the emitted power at the desired wavelength/angle is diminished due to light being emitted across a rainbow of wavelengths. For example, in polar materials like SiC, this results in the device thermally emitting throughout the Reststrahlen band, with the wavelength of emission being linked to the angle of emission through the grating equation: $k \sin \theta = k_{\parallel} + n \frac{2\pi}{\Lambda}$. Here, k_{\parallel} is the in-plane momentum of the propagating mode, n is the diffractive order, and Λ is the grating period. The angular dispersion of the monopole resonance is instead due to near-field coupling between individual resonators supporting localized resonances.¹⁵¹ Therefore, the angular dispersion is constricted in comparison to the grating-coupled devices and tunable through changing the electric field overlap of adjacent pillars.

In the following section, we investigate the angular dispersion of monopole resonances supported by Si:InAs resonators on a Si:InAs backplane. We used Si:InAs as this material has a widely tunable plasma frequency and relatively low optical losses throughout the FIR and MIR. Further, Si:InAs is a III-V material with a zinc-blende crystal structure and can therefore be grown epitaxially adjacent to other III-V materials such as AlSb and GaSb, allowing for more advanced resonator designs and design freedom. We take advantage of this later in the chapter, where we observe SPP monopole-ENZ strong coupling in multilayer InAs-AlSb and InAs-GaSb resonators. We then demonstrate how this strong coupling can be utilized to control the spatial coherence of thermal emission.

4.1.1 Monopole Resonances in Si:InAs Resonators

Localized SPhP modes are supported by sub-diffractive, undoped InAs resonators within the corresponding Reststrahlen band, the spectral range of negative real permittivity between the TO and LO phonon frequencies. These localized modes include transverse dipole resonances that can be excited at normal incidence and longitudinal resonances, such as the monopole mode, which

require that the electric field be oriented out-of-plane in order to be excited. Monopole modes are therefore polarization sensitive and forbidden by symmetry at normal incidence. Introducing Si-dopants to the InAs during film growth results in coupling between the LO phonon and free charge plasma through the so-called LOPC effect, effectively extending the region where the material exhibits a negative real part of the permittivity in accordance with the Drude-Lorentz model. More details are provided in section 3.3.1 of chapter 3. Consequently, as the plasma frequency of the InAs is increased, the spectral range where localized polaritonic resonances are supported is expanded. However, with the introduction of free charge carriers the resonances become plasmonic, as opposed to being phononic in character. The change in the real permittivity of the pillar and substrate also shifts the frequencies of the localized resonances. Therefore, a monopole mode supported by an InAs pillar on an InAs substrate blueshifts as the plasma frequency is increased (Figure 4.1d), even though the geometry of the unit cell remains constant (geometry in Figure 4.1c). Finally, as was mentioned in the previous section, the monopole resonance is highly dispersive with changes to the interpillar gap. This is confirmed in the calculated p -polarized reflectance map provided in Figure 4.1a, which shows that the monopole resonance blue shifts from 375 cm^{-1} to 312 cm^{-1} as the gap is decreased from 1 to $4 \mu\text{m}$. Note that in previous works that employed the monopole resonance as a non-dispersive localized mode, the gap distance was sufficiently large as to limit the interpillar coupling ($P \approx 6 - 7 \mu\text{m}$)^{24,121}, resulting in significantly reduced angular dispersion. This is in contrast with the transverse dipole resonances supported by these structures, which are nominally non-dispersive over most ranges of gap sizes.¹⁵¹

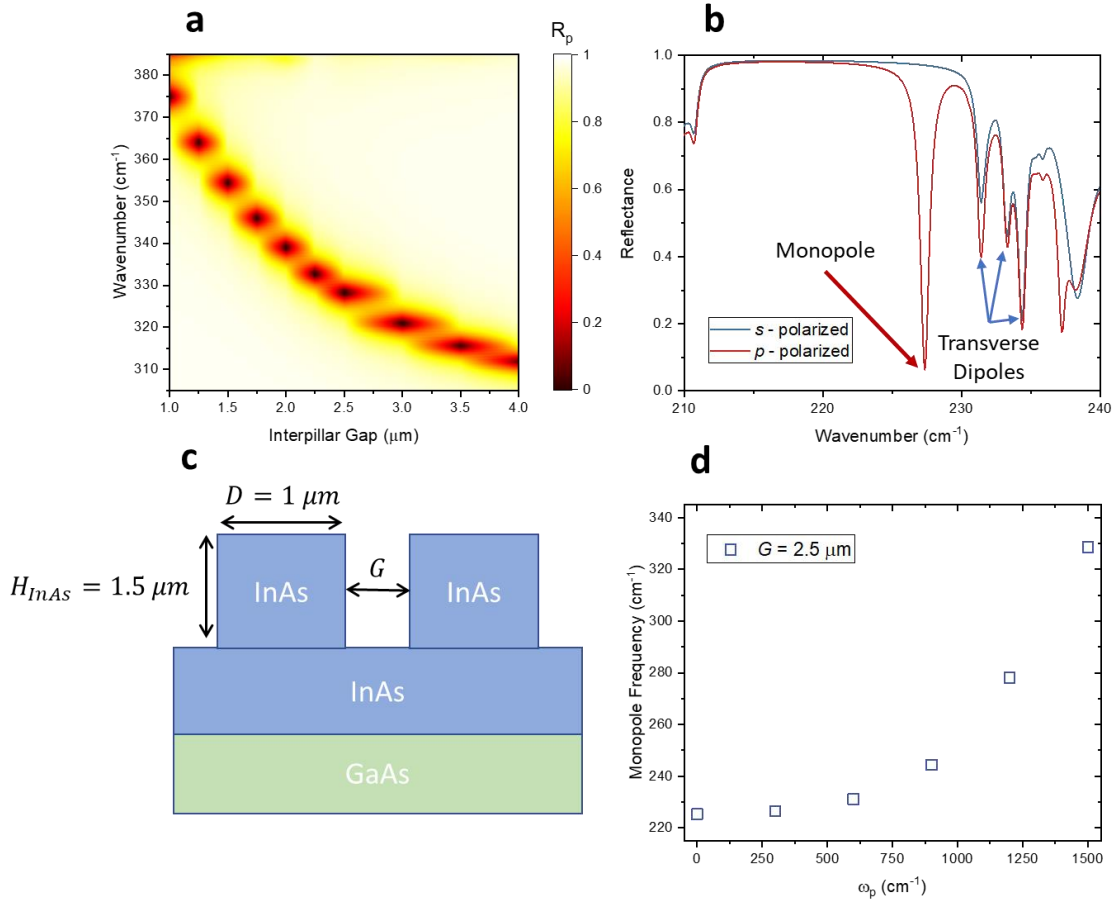


Figure 4.1: a) Calculated p -polarized reflectance map of doped InAs ($\omega_p = 1500 \text{ cm}^{-1}$) resonator array at angle of incidence of 22° showing the gap-dependent dispersion of the monopole resonance. The geometry of the array is displayed in c). b) s - and p -polarized reflectance of undoped InAs pillar array with $G = 1.5 \mu\text{m}$. The monopole and transverse dipole resonances are labeled. d) Monopole frequency for array with $G = 2.5 \mu\text{m}$ as a function of InAs plasma frequency. b) and d) were also calculated at 22° .

In the previous section it was stated that the angular dispersion of the monopole resonance is a result of near-field coupling between adjacent resonators. In order to determine the relationship between the interpillar coupling and the angular dispersion, calculations of the angle-dependent reflectance of doped InAs ($\omega_p = 1500 \text{ cm}^{-1}$) resonators were performed for arrays with three interpillar gaps: $G = 1.5, 2.5,$ and $3.5 \mu\text{m}$. Since the interpillar gap also governs the monopole mode frequency, the dispersion for each gap distance was normalized to the extrapolated monopole frequency at $k_{\parallel} = 0$. The monopole absorption for the $G = 3.5 \mu\text{m}$ array exhibits an angular dispersion that is parabolic in shape (Figure 4.2a), blue shifting at high incident angles. The angular dispersion of the $G = 2.5 \mu\text{m}$ and $G = 1.5 \mu\text{m}$ arrays share a similar dependence on incident angle

as the $G = 3.5 \mu\text{m}$ array, however dispersing faster as the interpillar gap is reduced (Figure 4.2a). The increased slope of the angular dispersion is attributed to the increased interpillar coupling mediated by the metallic substrate. Note that at high incident angles there is a slight inflection in the $G = 1.5 \mu\text{m}$ array angular dispersion which is due to coupling between the monopole and higher-order resonances. In the absence of these higher-order resonances the dispersion would follow the same shape as the $G = 2.5 \mu\text{m}$ and $G = 3.5 \mu\text{m}$ dispersion. For validation, we calculated the current density at the base of the InAs pillar for all three gap distances (Figure 4.2b). These current density distributions were normalized to the current density at the edge of the InAs pillar (similar to the calculations performed by Chen et. al.⁹⁸). For all three interpillar gaps, the normalized current density is shown to decay exponentially from the edge of the pillar. However, the rate of decay and saturation point (minimum in the current density distribution) shows a strong dependence on the interpillar gap distance.

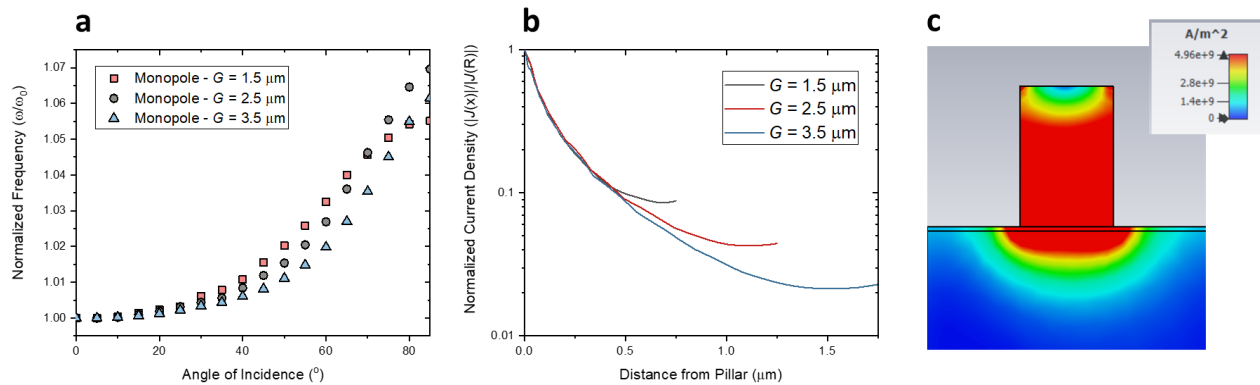


Figure 4.2: a) Angular dispersion of monopole resonance supported by doped InAs at interpillar gap distances of $G = 1.5, 2.5,$ and $3.5 \mu\text{m}$. In order to compare the relative shift in the monopole resonance as a function of angle, the resonance frequency was normalized to the extrapolated value at 0° . b) Current density ($J(x)$) extending from InAs resonator (edge of resonator: $x=0 \text{ nm}$) of monopole resonance at 25 nm below substrate surface. The current density was normalized to the maximum current density (resonator edge). 2D calculation of current density of monopole resonance is provided in c).

4.1.2 Monopole – ENZ – ENP Strong Coupling in Si:InAs-AlSb Resonator Arrays

The large electric field enhancement, small mode volumes, and high Q-factors associated with the monopole mode result in large Purcell enhancement making these modes potentially useful for a number of spectroscopic applications, such as SERS^{74,127} and SEIRA^{14,15}. When an absorber with a large oscillator strength, such as an ENZ supporting film or a MQW structure

supporting ISB transitions, is placed within the local electric field, strong coupling between the monopole and the oscillator can be realized. Here, we achieve such strong polaritonic coupling between the monopole mode supported by the InAs structure and the ENZ and ENP modes supported by a thin AlSb film. III-V polar materials, such as AlSb, are lattice matched to InAs and can therefore be grown adjacent to InAs to form multilayer heterostructures with minimal interface strain. This has been used in the past to realize tunable, MIR hyperbolic metamaterials consisting of alternating layers of Si:InAs and GaSb and Si:InAs and AlSb. At thicknesses far below the polariton wavelength, AlSb films support highly absorptive, non-dispersive ENP and ENZ modes near the TO and LO phonon frequencies, respectively.

In section 3.3, it was demonstrated that by growing a thin AlSb or GaSb layer adjacent to an SPP-supporting, Si-doped InAs layer, and therefore within the evanescent decay of the SPP mode, strong coupling can be achieved between the SPP supported by the Si:InAs layer and the ENP and ENZ modes supported by the AlSb or GaSb. We take a similar strategy here in order to achieve strong coupling between a localized SPP resonance and the ENZ mode of AlSb. On resonance, the monopole mode exhibits a large, electric field aligned along the length of the pillar. By placing a thin (100 – 200 nm) AlSb layer at the base of the InAs pillar, strong overlap of the monopole electric field and the AlSb layer is achieved. Note, from the discussion of ENZ modes provided in chapter 1, that the orientation of the local electric field is critical in exciting the ENZ mode. Since the orientation of the electric field associated with the monopole mode is aligned along the pillar, and therefore normal to the AlSb interface, the monopole mode couples efficiently to the ENZ mode. The plasma frequency of the Si:InAs can be judiciously tuned such that the entire AlSb Reststrahlen band fits within the spectral range of negative permittivity of the Si:InAs. Therefore, the monopole resonance can be tuned through the entire AlSb Reststrahlen band by changing the interpillar gap, interacting with both the ENZ and ENP modes. The absorption of the ENP mode is angular and polarization insensitive, therefore it is observed in both *s*- and *p*-polarization. However, strong coupling is only observed in *p*-polarizations due to the polarization sensitivity of the monopole resonance. The coupling between the monopole and ENZ resonances results in a splitting in the gap-dependent reflectance map at the AlSb LO phonon frequency (Figures 4.3a and 4.3b). The InAs plasma frequency was also chosen such that the uncoupled monopole absorption is large throughout the AlSb Reststrahlen band. If the plasma frequency were

set too high, the interpillar gap would need to be large near the AlSb Reststrahlen band resulting in a reduction in the monopole and ENZ absorption (and therefore coupling strength).

Prior studies of SPP-ENZ coupling in CdO bilayer films and SPhP-ENZ coupling in SiC-AlN films have shown that the coupling strength g increases with the ENZ layer thickness as $\sqrt{d_{ENZ}}$. This is similar to cavity – emitter/absorber strong coupling demonstrations where the coupling strength is proportional to the concentration of the emitter.¹⁴⁸ In order to determine whether a similar relationship would be expected in these InAs-AlSb bilayer resonators, we calculated the p -polarized reflectance for resonator arrays across a range of interpillar gaps ($G = 1 - 4 \mu\text{m}$). These calculations were performed at an angle of incidence of 22° ($k_{\parallel}/k_o \sim 0.37$) and the resonator diameter and height were set at 1 and 1.5 μm , respectively. Here, we set the resonator height and plasma frequency such that the uncoupled monopole dispersion only slightly overlaps with the TO phonon in order to minimize the impact of the ENP mode. However, in order to accurately describe the behavior of the hybrid modes it is necessary that all three modes are considered. If the height of the pillar were increased, the monopole dispersion would redshift resulting in increased spectral overlap with the ENP mode. We then fit to these numerical results using a three-mode Hopfield model in order to extract the coupling strengths. A similar approach has been taken to model the interaction between multiple electronic or vibrational states of molecules or MQW structures placed in a cavity.^{131,133} The Hopfield matrix of the three-mode system is

$$\mathcal{M}_G = \begin{bmatrix} \omega_G^{MP} & g_0 & g_1 \\ g_0 & \omega_G^{ENZ} & 0 \\ g_1 & 0 & \omega_G^{ENP} \end{bmatrix} \quad (1)$$

where G denotes that \mathcal{M}_G pertains to the gap-dependent dispersion. The gap-dependent dispersion of the monopole, ENZ, and ENP modes are denoted as ω_G^{MP} , ω_G^{ENZ} , and ω_G^{ENP} , respectively. The coupling strength between the monopole and ENZ is g_0 and the coupling strength between the monopole and ENP modes is g_1 . It was assumed that the ENP and ENZ modes would couple to the monopole resonance but not with each other due to the spectral separation of the uncoupled modes. The coupling strengths are then determined phenomenologically from a fit to numerical calculations. The bare monopole dispersion ω_G^{MP} was calculated numerically for the InAs pillar on an InAs substrate without the AlSb layer. It was also assumed that ω_G^{ENP} and ω_G^{ENZ} occurs near the

TO and LO phonon frequency and exhibited little gap-dependence. The dispersion of the hybrid polariton states can then be calculated from the eigenproblem

$$[\mathcal{M}_G - \omega_G^i] \begin{pmatrix} \alpha_G^i \\ \beta_G^i \\ \gamma_G^i \end{pmatrix} = 0 \quad (2)$$

where α_G^i , β_G^i and γ_G^i are the Hopfield coefficients denoting the relative weighting of the monopole, ENZ, and ENP modes, respectively. Three hybrid eigenmodes ω_G^i are expected to emerge as a result of the monopole-ENZ-ENP coupling, splitting into upper (UB), middle (MB), and lower (LB) branches. Here it is assumed that the dispersion of the bare and hybrid modes are real.

Using the three-mode Hopfield model we then extracted the coupling strengths by comparing to numerically-calculated reflectance maps. In Figure 4.3, we only plot the UB and MB as the LB is not observed within this range of gap sizes. For AlSb thicknesses of 100 and 200 nm (Figures 4.3a and 4.3b, respectively), the analytically calculated dispersion agrees very well with the numerical calculations, validating the three-oscillator model used here. The extracted coupling strength is shown to increase from 14 cm^{-1} for the 100 nm AlSb film to 18 cm^{-1} for the 200 nm AlSb film. It is clear that although the coupling strength increases with increased AlSb layer thickness, it deviates from the $\sqrt{d_{ENZ}}$ dependence (dashed gray line in Figure 4.3d) that was observed in SPhP-ENZ and SPP-ENZ films. We attribute this to the interaction with the interaction between the hybrid monopole-ENZ modes with the ENP mode. Finally, we would like to note that although here we are interested in studying hybrid modes in InAs-AlSb heterostructure resonators, due to the tunability of the plasma frequency of InAs, this analysis can easily be transferred to systems featuring other III-V materials, such as GaSb taking the place of AlSb, provided epitaxial growth or deposition of high quality films is possible.

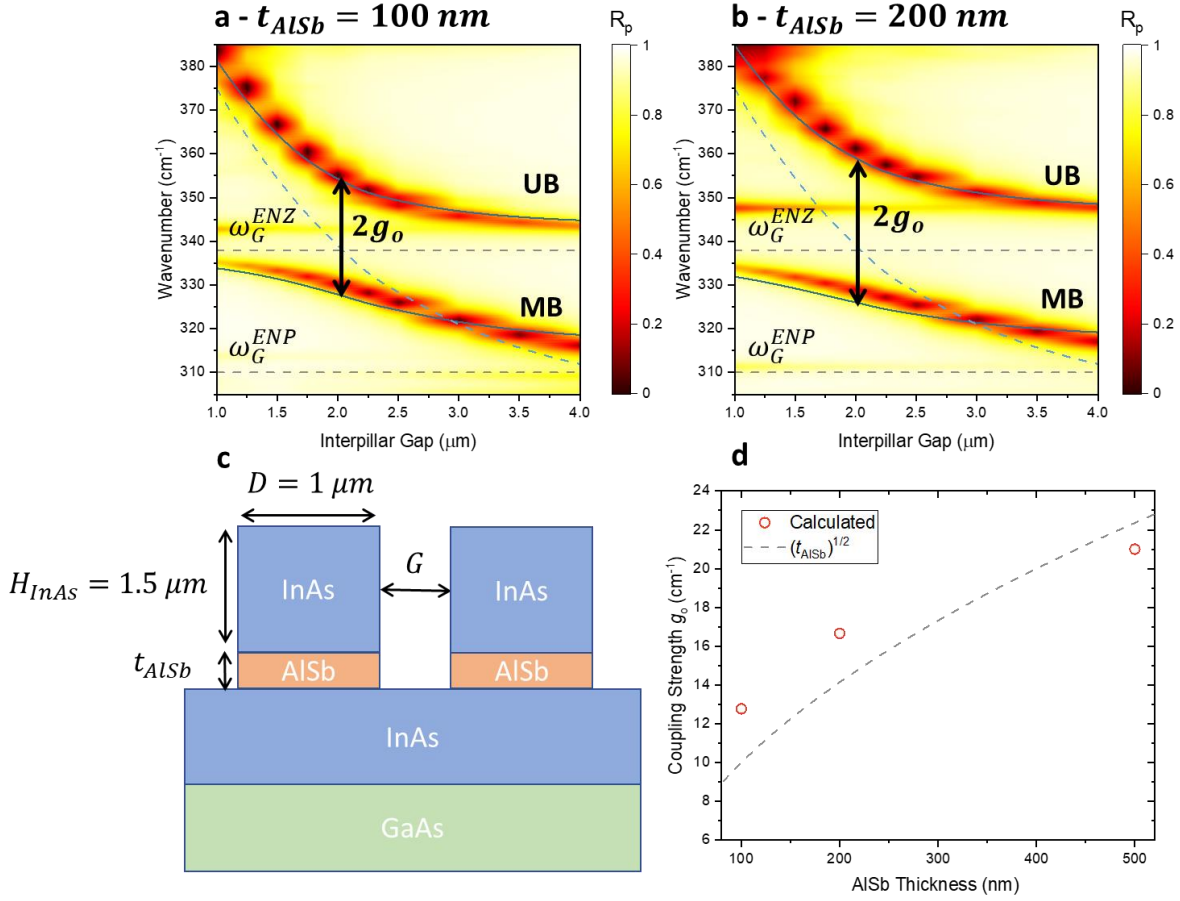


Figure 4.3: Calculated reflectance maps for the structure shown in c) with ALSb thicknesses of a) $t_{ALSb} = 100$ nm and b) $t_{ALSb} = 200$ nm. The plasma frequency of the InAs is $\omega_p = 1500$ cm⁻¹. The blue dashed line represents the dispersion of the uncoupled monopole mode ω_G^{MP} , whereas the grey dashed lines are the ENP and ENZ dispersion (labelled on figure). The upper (UB) and middle (MB) branches of the hybrid dispersion are shown as solid blue lines. The coupling strength g_0 is displayed as a function of ALSb thickness in d).

The mode hybridization is further confirmed by observing the electric field profiles of the hybrid modes. As is described in the previous section, the electric field associated with the monopole resonance is mirror symmetric across the InAs resonator (Figure 4.4b, bottom panel). The ENZ modes, exhibits an extremely large enhancement of the electric field within the ultrathin film bulk. Strong coupling results in a splitting into upper (symmetric, Figure 4.4b, top panel) and lower (anti-symmetric, Figure 4.4b, middle panel) states, with both modes exhibiting characteristics of the constituent modes. For example, the field profiles of both hybrid modes are mirror symmetric across the resonator (monopole mode) and exhibit extremely high field concentration within the ALSb layer (ENZ mode). However, the electric field associated with the

upper (lower) branch is in-phase (out-of-phase) with the electric field within the ENZ layer, owing to the symmetric (anti-symmetric) nature of the modes.

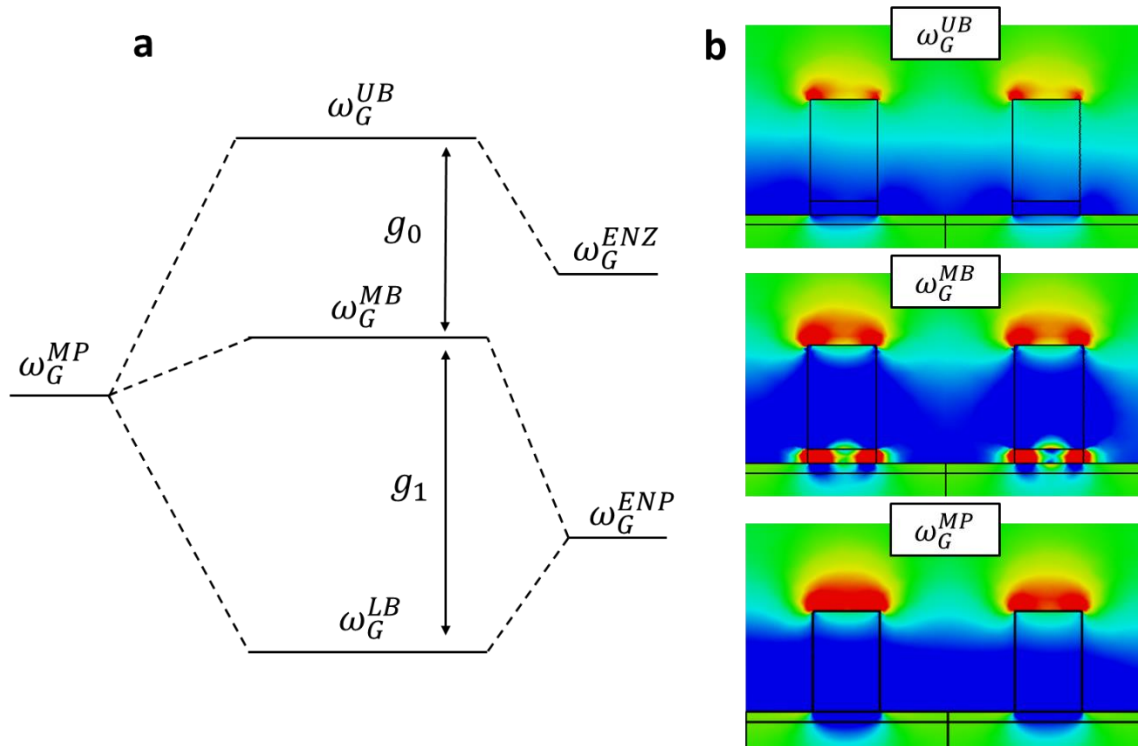


Figure 4.4: a) Energy hybridization model of strong coupling between a monopole mode and the ENZ and ENP modes. Strong coupling between the monopole mode, ENZ mode, and ENP mode results in a splitting into three hybrid modes. b) Electric fields oriented along the z-direction for the upper (UB, top panel) and middle (MB, middle panel) branches and the uncoupled monopole resonance (bottom panel).

4.1.3 Impact of SPP – ENZ Strong Coupling on Angular Dispersion

The hybrid modes of a strongly coupled system take on the properties of the constituent modes. For a given branch of the hybrid dispersion, the relative mixing of the constituent modes can be found by taking the absolute value of the Hopfield coefficients. In the monopole-ENZ-ENP system we are studying here, the value of these coefficients is a function of the geometry of the unit cell and the angle of incidence (k_{\parallel}). Therefore, assuming that the pillar height and diameter are kept constant, the Hopfield coefficients of the monopole-ENZ-ENP dispersion are expected to change as the gap between pillars changes (Figures 4.5b and 4.5c). As was stated in section 4.1.1, the monopole mode is angularly dispersive as a result of near-field coupling between pillars whereas the ENZ and ENP modes are non-dispersive. Therefore, the angular dispersion of the

monopole-ENZ-ENP hybrid modes is expected to be related to the mixing fractions of the discrete modes.

In order to determine the effect of monopole-ENZ-ENP strong coupling on the angular dispersion, we calculated the angle-dependent reflectance of the InAs-AlSb structure from Figure 4.3c with $t_{AlSb} = 100 \text{ nm}$ at three gap distances $G = 1.5, 2.5, \text{ and } 3.5 \mu\text{m}$. Here, we again only focus on the UB and MB of the hybrid dispersion. We then normalized the absorption frequencies of the UB and MB modes to the extrapolated absorption frequency at normal incidence (Figures 4.5d and 4.5e). From these calculations we observed a distinct difference in the behavior of each band as the gap distance, and therefore the Hopfield coefficients at $\theta = 22^\circ$, was modified. At small interpillar gaps, the mixing fraction of the UB is dominated by the contribution of the monopole resonance $|\alpha_G^{UB}|^2$ (See Figure 4.5c). However, as the gap distance is increased, the monopole contribution decreases and the ENZ contribution $|\beta_G^{UB}|^2$ increases, crossing at $G \approx 2.1 \mu\text{m}$. In the angular dispersion, this translates to a decrease in the angular dispersion of the UB with increased gap distance (Figure 4.5d). Note that for the $G = 1.5 \mu\text{m}$ mode in the UB, that there is a slight inflection at high angles of incidence, which is due to strong coupling between the UB and the high-frequency, higher-order modes (See Figure 4.1b above). However, in the absence of the coupling with higher-order resonances, the slope of the $G = 1.5 \mu\text{m}$ dispersion exceeds that of the larger gap sizes. Contrarily, the behavior of the MB in the dispersion is more ENZ-like at low gap distances, with $|\beta_G^{MB}|^2$ being significantly higher than the contribution from the monopole $|\alpha_G^{MB}|^2$ and ENP contribution $|\gamma_G^{MB}|^2$. However, as the gap distance increases, $|\beta_G^{MB}|^2$ decreases as the gap distance increases, which is in stark contrast to the behavior of the UB. Indeed, the calculated angle-dependent absorption of the MB at varying gap distances verifies that as the gap distance increases, so does the angular dispersion (Figure 4.5e).

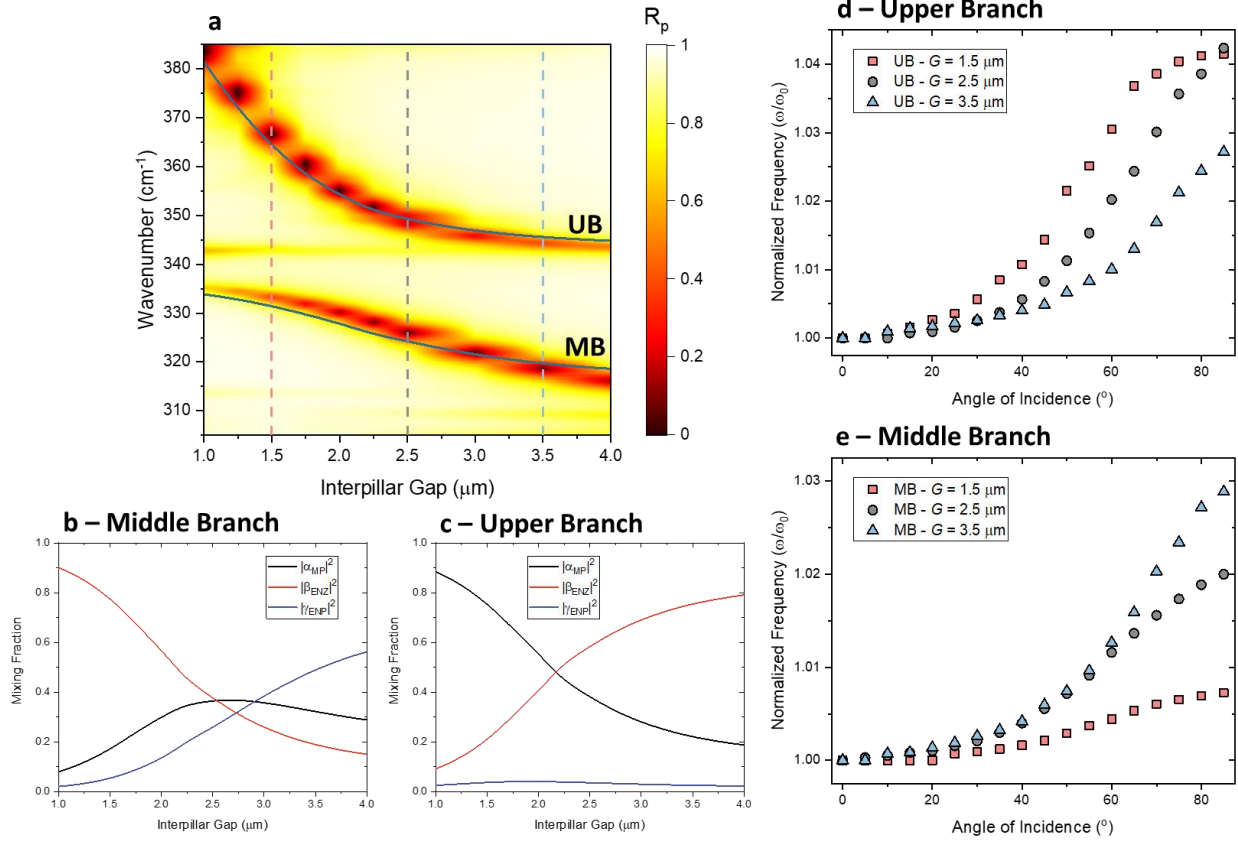


Figure 4.5: a) Calculated reflectance map from Fig. 4a ($t_{\text{AlSb}} = 100 \text{ nm}$). b) and c) display the Hopfield components of the middle (MB) and upper (UB) of the hybrid dispersion displayed in a). d) displays the angular dispersion of the UB at three different gap distances $G = 1.5, 2.5,$ and $3.5 \mu\text{m}$ (marked in a) as red, grey, and blue dashed lines, respectively). e) displays the angular dispersion of the MB at the same three gap distances. The resonant frequency was normalized to the resonant frequency at normal incidence in order to account for the differences in spectral positions of the modes.

4.1.4 Conclusions

In this chapter, we demonstrated that tunable monopole – ENZ – ENP coupling can be realized in bilayer doped InAs-AlSb pillars on an InAs backplane. Although we do not explore the carrier density dependence of the InAs on the coupling strength here, this would also have a significant impact on the hybrid dispersion. This, along with changes to the pillar geometry such as increasing the pillar height, can result an increase in the spectral overlap of the monopole and ENP mode, allowing for the role of the ENP mode in the three-mode dispersion to be better understood. It would also be interesting to investigate methods of enhancing the near-field coupling between resonators, potentially increasing in the angular dispersion of the uncoupled

monopole resonance. Finally, the analysis provided here can be extended to other material systems. For example, by decreasing the InAs plasma frequency and replacing the AlSb with GaSb, which has lower frequency optic phonons, similar behavior would be expected. Another example would be multilayer CdO structures where a thin, ENZ-supporting CdO layer is placed between a high-doped CdO pillar and backplane (Figure 4.6b). Initial simulations reveal that these bilayer CdO structures exhibit strong coupling between the monopole supported by the high-doped pillar and the ENZ mode supported by the ENZ layer (Figure 4.6c and 4.6d). Here, an ENP mode would not be supported due to the Drude dielectric function of CdO, however the ENZ mode frequency is tunable throughout the MIR by changing the ENZ layer carrier density.

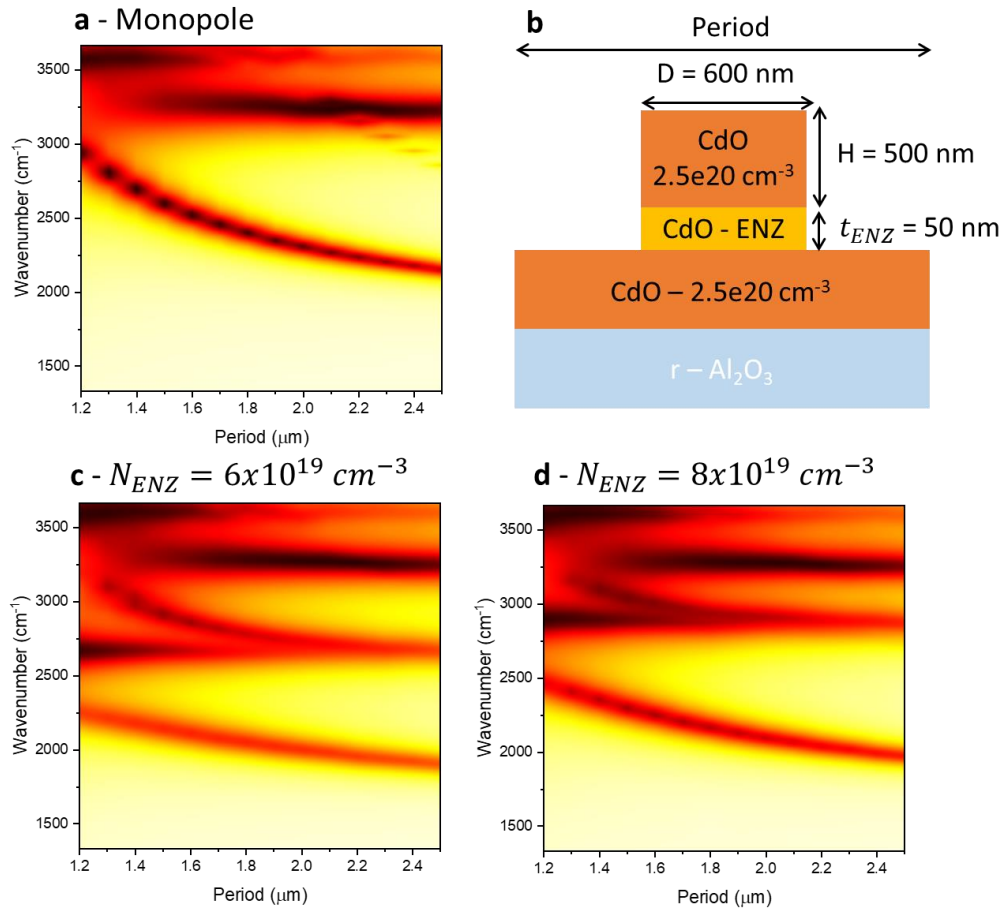


Figure 4.6: a) Calculated reflectance map of the structure in b) when $t_{ENZ} = 0 \text{ nm}$ at 22° showing the dispersion of the monopole resonance supported by CdO resonators. Calculated reflectance maps of the structure in b) where $t_{ENZ} = 50 \text{ nm}$ and c) $N_{ENZ} = 6 \times 10^{19} \text{ cm}^{-3}$ and d) $N_{ENZ} = 8 \times 10^{19} \text{ cm}^{-3}$. A clear anticrossing is observed in the gap-dependent dispersion for both carrier densities.

Chapter 5

5. Narrowband Infrared Emitting Metamaterials for Filterless Non-dispersive Gas Sensing

5.1 Introduction

For many industrial and manufacturing applications detecting and identifying low concentrations of harmful gases and byproducts are performed using NDIR sensors. These simple devices utilize a broadband IR emitter, thermopile detector and a spectrally narrow bandpass filter tuned to a vibrational resonance of the analyte of interest. However, such filters are expensive to fabricate and limit the NDIR to operation at only a single frequency, unless filter wheels are employed, which expand the size and complexity of the device considerably. Here, we create a nanophotonic infrared emitting metamaterial (NIREM) fabricated from thin films of doped CdO grown on patterned sapphire substrates (PSS) that exhibit narrowband thermal emission. By coupling a sufficiently narrow linewidth emitter with a simple broadband detector such as a thermopile, the functionality of the NDIR sensor can be replicated without the need for the narrow bandpass filter. Unlike many metamaterial-based emitters, our device emits both *p*- and *s*-polarized light with near-unity emissivity at angles ranging from 0° to 40° off the surface normal without complicated and expensive lithography steps. As a proof of concept, we implement this NIREM for CO₂ gas detection within an FTIR spectrometer, demonstrating performance comparable with a conventional blackbody/filter combination. This demonstrates that the NIREM concept can provide a suitable plug-and-play replacement for NDIR devices as they can be implemented in a form-factor commensurate or significantly reduced in comparison to the current state of the art. In principle, by incorporating multiple NIREM dies tuned to emit at different frequencies, multiple vibrational modes could be sequentially detected, making the approach amenable to identification and quantification of complicated molecules within a single NDIR configuration.

Molecular sensing plays a critical role in a variety of applications such as chemical and industrial manufacturing, oil and gas exploration and extraction, defense and security, as well as environmental safety. Many schemes exist for the detection of chemical species, and for gases with characteristic absorption bands within the infrared, optical spectroscopy is commonly used and has advantages over other techniques.¹⁵² Typically, this is achieved through exploitation of the Beer-Lambert law; a reduction in the transmission of IR light resonant with a molecular vibrational

absorption over a defined cross-sectional area and path length is directly proportional to the concentration of that molecule. This inherently implies that for infrared detection there is a need for either a spectroscopic solution, such as FTIR spectroscopy, or a single frequency excitation/detection scheme. In the case of the latter, a number of potential solutions arise: 1) implementation of a broadband light source and detector pair, with a narrow bandpass filter (see Fig. 5.1a), 2) implementation of a narrow band detector with a broadband source^{153,154}, or 3) use a narrow band source with a broadband detector (Fig 5.1b). The first solution is the basis for NDIR gas sensors that are widely implemented in industry due to their device simplicity.¹⁵⁵ A platform supporting both a narrow band source and detector pair, such as the MEMS-based sensor designed by Lochbaum et. al.¹⁵⁶, is another potential solution. However, these come with the inherent limitation of only operating at a single fixed frequency, and the inclusion of sufficiently narrow bandpass filters results in significant increases in cost. Multiple frequencies can be measured via NDIR through the incorporation of a filter wheel featuring multiple bandpass filters, however, this significantly increases the cost, size and complexity of the device. In such dual narrow bandwidth approaches the signal-to-noise ratio is enhanced resulting in similar sensitivity and selectivity to conventional methods in a significantly smaller device. However, the single narrow bandwidth resonance supported by the emitter and detector precludes multifrequency operation and typically comes with significant increases in design complexity and expense. Thus, ideally, an NDIR approach would implement a simple, inexpensive, narrowband source or detector to eliminate these challenges, while still maintaining the standard form factor and sensitivity of commercial NDIR systems.

5.2 Filterless Non-dispersive Infrared Sensing using CdO NIREM

One obvious solution to eliminate the need for a narrow bandpass filter within NDIR designs is to integrate a similarly narrow bandwidth detector. Such systems have been demonstrated using a broad range of materials, for instance graphene resonator designs and plasmonic resonant structures.^{153,157} However, this requires extensive nanoscale lithographic fabrication, resulting in increases in cost and complexity, while in many cases also limiting the absorptivity of the device. A similar, but arguably more powerful approach is to integrate Bragg mirrors in order to resonantly enhance detection, but this requires the accurate growth of thick

mirror layers.¹⁵³ Alternatively, one could utilize a narrow band source, for example by incorporating an IR laser, however, within the molecular fingerprint window ($500\text{-}3500\text{ cm}^{-1}$) this requires QCLs or gas lasers¹³, both of which have large electrical power requirements. While it is possible to make extremely sensitive gas sensors using these devices, such solutions are less palatable for most industrial settings where low cost and compact solutions are absolutely required for commercial viability. Mid-infrared LEDs have become increasingly more appealing for such applications; however, these devices still have low output power and relatively broadband emission, which results in a high probability of cross-talk with other absorbing gases. Recently, photonic crystals¹⁵⁸⁻¹⁶⁰, polaritonic^{3,16,17,21} and metamaterial^{161,162} designs have been employed to control thermal emissivity and realize narrow-band IR sources.¹⁶³ These NIREMs have been designed to exhibit linewidths approaching that of the molecular vibrations themselves^{17,151}, illustrating the potential for targeted and sensitive measurements. Recently, such metamaterials implementing the so-called perfect absorber geometry^{164,165} were demonstrated for an advanced NDIR approach, illustrating similar sensitivity to CO_2 as commercial devices, without the requirement of the aforementioned bandpass filter.¹⁶⁶ Yet, in that work electron beam lithography was required to fabricate the metallic nanostructures necessary to stimulate the localized SPP resonances within the MIR, the spectral range for which this device was designed.

Here we demonstrate that our NIREM concept overcomes each of the previously mentioned challenges, enabling a potential plug-and-play platform for direct replacements of current NDIR devices. This is realized through the narrowband, near-unity absorption of both p - and s -polarized light (>0.95 from $0\text{-}40^\circ$ off the surface normal) facilitated via epsilon-near-zero (ENZ) modes^{6,7} within thin films ($<150\text{ nm}$) of n -type, In-doped CdO (In:CdO) grown on patterned sapphire substrates (PSS). A side and top-view schematic of the coated PSS structure is shown in Fig. 1d. These modes can be spectrally tuned from approximately $2\text{-}10\text{ }\mu\text{m}$ free-space wavelengths ($5,000\text{ - }1,000\text{ cm}^{-1}$) in CdO via doping^{9,40,67}, allowing these devices to target essentially the full fingerprint region. Similarly, narrowband single and multifrequency thermal emission has been demonstrated in ultrathin, Berreman-mode-supporting CdO films and multilayer stacks, respectively.²⁵ However, in flat films these Berreman excitations couple only to p -polarized light and exhibit highly off-normal emission angles, with the emissivity peaking near the Brewster condition ($\sim 65^\circ$). By growing the ENZ CdO film upon a PSS, the thermal emission is no longer restricted to angles around the Brewster angle, instead resulting in ENZ-polariton modes that emit

over a hemisphere, with the strongest emission occurring around the surface normal. If illuminated at normal incidence, scattering from the conical structures of the PSS results in the excitation of the ENZ mode in the CdO film. Reciprocally, through Kirchhoff's law, the cylindrical symmetry of the PSS cones allows for the out-coupling of both *s*- and *p*-polarized emission from the thermal excitation of the ENZ mode. While the periodicity of the PSS structuring does induce some angular dispersion in the spectra, this is primarily observed at the steepest angles, and thus induces minimal influence upon the NDIR response normal to the surface. Finally, we provide a proof-of-principle experiment illustrating the detection of CO₂ using the NIREM device demonstrating similar sensitivity to that of a broadband emitter used in a standard NDIR detector. These experiments illustrate the potential for the NIREM devices as a direct IR source replacement for the broadband emitter in conventional NDIR devices. This enables the elimination of the bandpass filter as well as offering the opportunity to realize next generation devices offering multi-frequency detection (through depositing multiple films on the same sample, or multiple die combined into a single NDIR architecture) within the same gas cell.

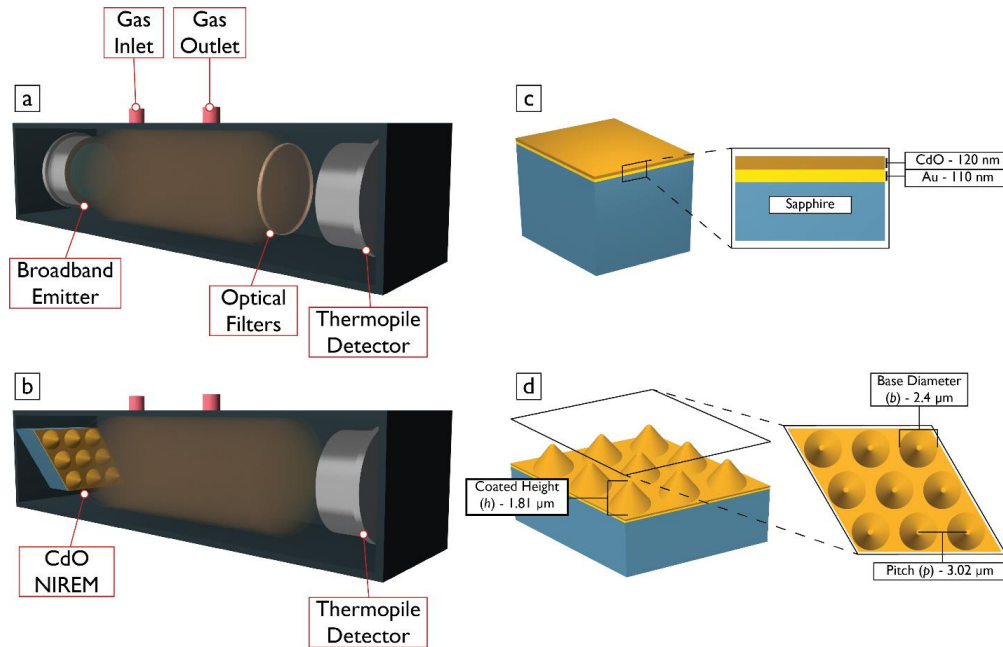


Figure 5.1: a) Schematic of conventional NDIR sensor. b) Proposed NIREM-enabled NDIR sensor design. c) Perspective view and cross-section of 120 nm In:CdO film deposited onto 110 nm Au-coated flat sapphire substrate. The same layer thicknesses were deposited onto the PSS substrate sample depicted in d). Here we provide a perspective and top-view of the PSS sample, with geometry labeled.

5.2.1 Fabrication of CdO NIREM Device

In:CdO was deposited using reactive high power impulse magnetron sputtering (R-HiPIMS) from a metallic cadmium target. Doping was achieved through RF co-sputtering from a metallic indium target. After deposition, samples were annealed at 700°C in an O₂ atmosphere. PSS substrates were sourced from Precision Micro-Optics Inc. We then collected SEM images of the CdO PSS emitter using a Zeiss Merlin SEM in order to determine the geometry of the hexagonal lattice and conical structures (Fig. 5.2a). This also allowed us to determine the alignment of the hexagonal lattice with respect to the overall sample in order to align the polar angle along the $[11\bar{2}0]$ axis during angle-dependent thermal emission measurements.

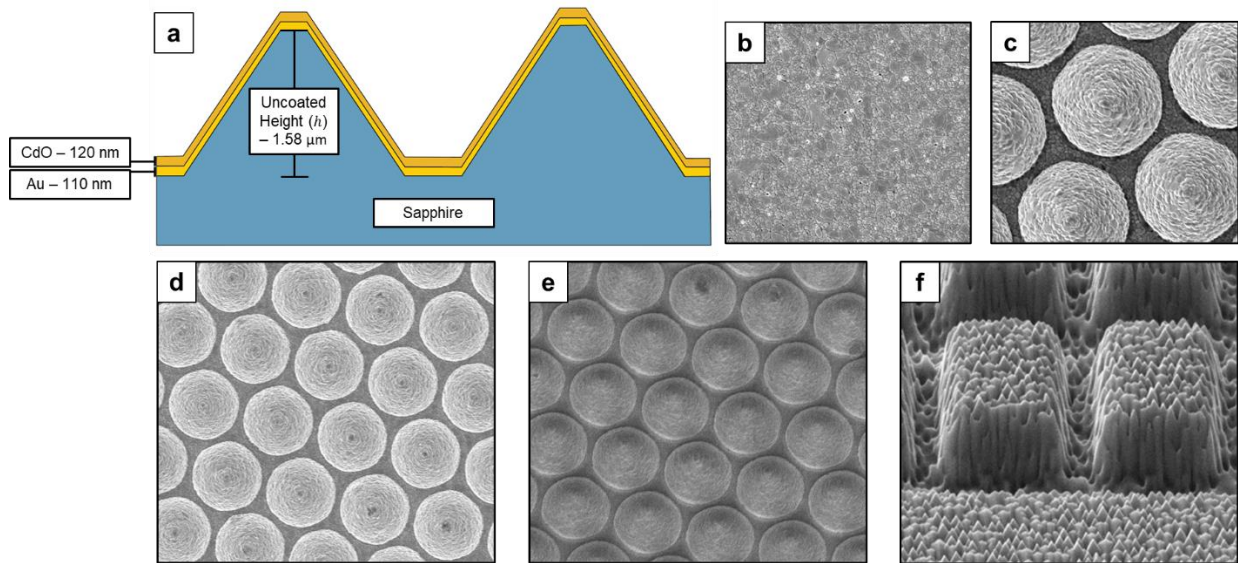


Figure 5.2: a) Schematic of cut of showing cone height and layer thicknesses. b) SEM image of the CdO-coated flat substrate sample. SEM images of coated CdO on PSS samples at d) normal incidence and e) 22° angle of incidence. In f) we provide an SEM image of a milled CdO film grown on a metal backplane in order to show the columnar growth.

5.2.2 Angle – Resolved Thermal Emission of CdO NIREM

Our NIREM device is based on the strong absorption of the Berreman and ENZ-polariton modes within thin films of polaritonic media. The Berreman mode, along with the ENZ polariton mode that is its sub-diffractive counterpart, are the result of strong coupling between surface polaritons supported on the opposing interfaces of a thin film.⁷ Thin films of In:CdO on the order of 120-nm thick (Figure 5.1c) support both Berreman and ENZ modes, with the former being accessible from free-space and providing near-unity absorption of p -polarized light at angles near

the Brewster angle.²⁵ The ENZ dispersion exists outside of the free-space light cone, requiring auxiliary momentum in order to be accessed. The Berreman/ENZ modal dispersion is discussed and calculated in chapter 1. In our work we observe strong emission from such a 120-nm thick $N_d = 5.8 \times 10^{19} \text{ cm}^{-3}$ In:CdO film that is derived from this dispersion relation, as discussed below. The experimentally measured and numerically calculated emission from our thin film CdO are shown in Figures 5.3a and 5.3c, respectively. As the emission spectra provided in Figure 5.2a is unpolarized, an emissivity at close to 0.5 implies near-unity absorption of p -polarized light through Kirchhoff's law, at an angle of approximately 70° (see polarized thermal emission spectra in section 5.2.4). However, such steep emission angles are non-ideal for NDIR applications, as the majority of the light will be emitted towards the gas cell wall, rather than being directed towards the detector. Adjustments could be made to account for this off-normal emission from the flat film, such as the incorporation of a wedge to direct the emission towards the detector, yet this would inherently reduce the collected power and/or require high numerical aperture collection optics to overcome. Furthermore, the possible collected power is still limited to below 50% as the Berreman mode only couples to p -polarized light. Thus, for the NDIR application an alternative device design is required if such challenges are to be overcome.

To enable strong thermal emission of both p - and s -polarized light, designs exploiting different types of physics have been employed. One method broadly implemented in the perfect absorber geometry is to utilize a cross-shaped polaritonic resonator, whereby each arm of the cross can couple to the orthogonal polarization states. When combined with a dielectric spacer and metallic back plane, perfect absorption can be realized.^{164,165} Indeed, this was the geometry utilized by Lochbaum et al.^{156,166} for demonstrating a narrowband emitter and detector for an advanced NDIR scheme. However, as noted above, for such structures to provide polaritonic resonances in the mid-IR, advanced lithographic tools and typically costly plasmonic metals are required. Alternatively, one could envision realizing nanostructures through growth of a polaritonic medium on a periodically textured surface. However, this approach has not been employed for such a device due to the challenges associated with epitaxy on such a non-planar surface. This would inherently result in an increase in defect density and a propensity to form polycrystalline, rather than single crystal epitaxial films, which in turn result in increases in optical loss. As was discussed in chapter 2, CdO offers substantial benefits as it has been previously demonstrated that for highly doped CdO maintains high electron mobilities ($\mu > 300 \text{ cm}^2/V - s$) at plasma frequencies throughout

the IR.⁶³ Furthermore, this material offers a propensity for high-quality growth via HiPIMS on non-planar structures and metal films while maintaining the low loss tangents that highlight the promise of this material.^{9,67}

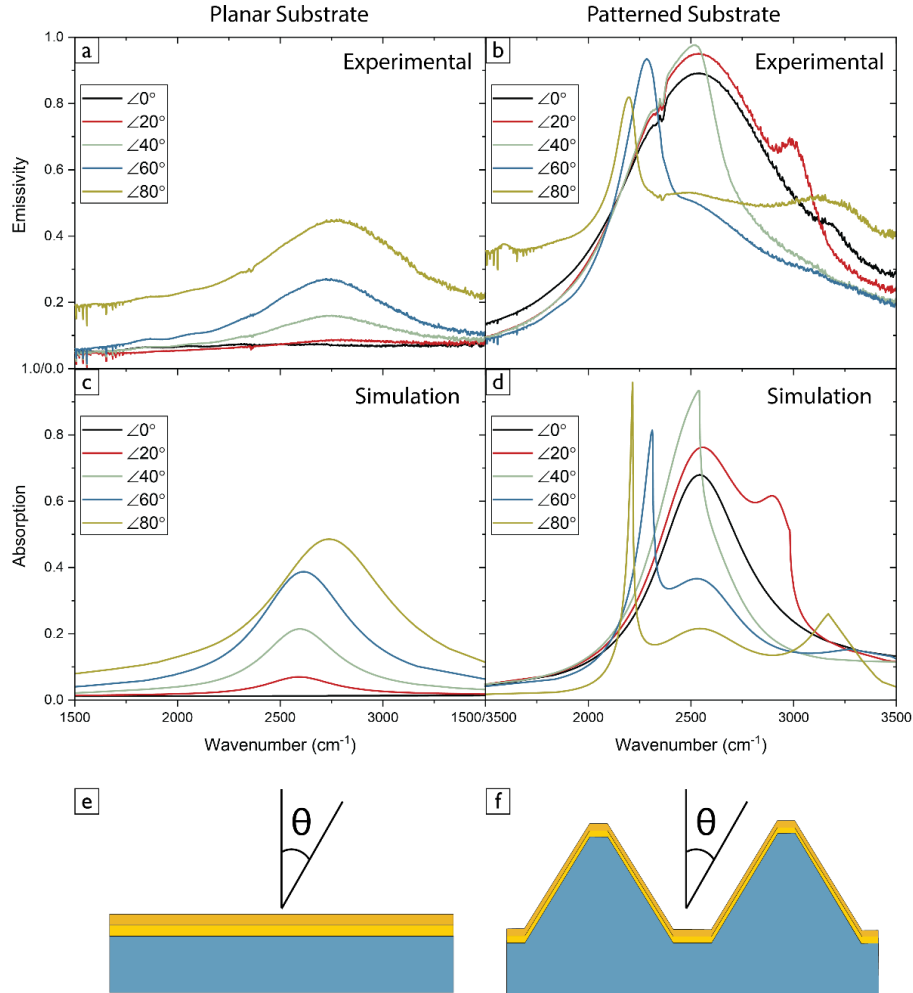


Figure 5.3: a) Angle-dependent thermal emission measurements of the flat CdO film sample shown in e). b) Angle-dependent thermal emission measurements of the CdO on PSS sample shown in f). c) and d) display the simulated angle-dependent absorption spectra for the flat CdO and CdO on PSS samples, respectively. The feature seen at 2349 cm⁻¹ in a) and b) is due to absorption from ambient CO₂.

Due to the requirement of NDIR sensors to be inexpensive, any structured surface must be one that can be realized via scalable, low-cost methods on large-area substrates. Patterned sapphire substrates offer such a template as the structured surface is the result of wet chemical treatment in H₂SO₄ at elevated temperatures (~240 °C) or plasma-based dry etching techniques¹⁶⁷, and are commercially available at up to 8-inch wafers at low cost. For the purpose of testing the spectral and spatial emissivity of an ENZ CdO film when grown on such a PSS substrate, a 120-nm thick

n-type In:CdO film was grown via HiPIMS on a PSS substrate that had first been coated with a 110-nm thick sputtered gold layer. A schematic of the PSS cone cross-section along with scanning electron microscope (SEM) images of the coated structure are provided in Fig. 5.2 of section 5.2.1. Note that the layer thicknesses and material stacking order are identical for the CdO flat film and PSS samples. The PSS substrates used consisted of a periodic array (pitch $p = 3.02 \mu\text{m}$) of circular-base ($b = 2.4 \mu\text{m}$) conical structures with an uncoated height of $1.58 \mu\text{m}$. A top-view schematic of the gold/CdO-coated structure is depicted in Fig 5.1d. Note, in contrast to the flat Berreman-supporting film (Fig. 5.3a and 5.3c), when the same film is grown on the PSS, several significant modifications are realized (Fig. 5.3b and 5.3d, respectively). First, as noted above, the structuring of the film results in near-unity emissivity (absorptivity) at near-normal incidence up to approximately 40° off-normal (Fig. 5.4a). The symmetric, conical shape of the structures also enables out-coupling of both p - and s -polarized light on resonance with high efficiencies. Further, the emission along the sidewalls of the cones is partially directed back towards the substrate and adjacent cones, resulting in reabsorption into the ENZ mode and emission enhancement at near-normal emission angles. As the angle is increased away from the surface normal, a significant narrowing of the resonant mode is observed due to interference between the dispersive diffractive and non-dispersive ENZ resonant modes as can be seen in Fig. 5.3b, as well as in the contour plot presented in Fig. 5.4c. The slight difference in emission frequencies between the flat film and PSS sample is a result of the Berreman/ENZ origin of these modes. Due to the anti-crossing at the intersection⁷ of the plasma frequency and light line in air the Berreman mode is excited slightly above and ENZ-polariton just below the plasma frequency in polaritonic films, with the magnitude of this shift being dependent upon the film thickness. The resonant frequencies are therefore slightly offset from the plasma frequency, but in opposite directions spectrally. Also, note that the measured emission and simulated absorption (Figs. 5.3a and 5.3c, respectively) of the planar film exhibits a slight blue shift at high emission angles. This is due to the corresponding blue shift of the Berreman mode as the dispersion approaches the light line from the left ($k/k_o < 1$). This is in contrast to the non-dispersive thermal emission from the PSS sample, which is the result of the excitation of the ENZ-polariton mode described above. These angle-dependent thermal emission measurements were performed using a motorized, angle-resolved thermal emission rig that was built in-house and coupled to the existing Bruker Vertex 70v FTIR spectrometer. The measured baseline emissivity is slightly elevated at high emission angles (80°), which is due to the collection

of the emission from the hot plate behind the sample. At these large emission angles the spot size (5 mm) was slightly larger than the projection of the sample. A detailed description of the FTIR thermal emission measurements are provided in the methods section and a schematic of the thermal emission setup is provided in the supporting information.

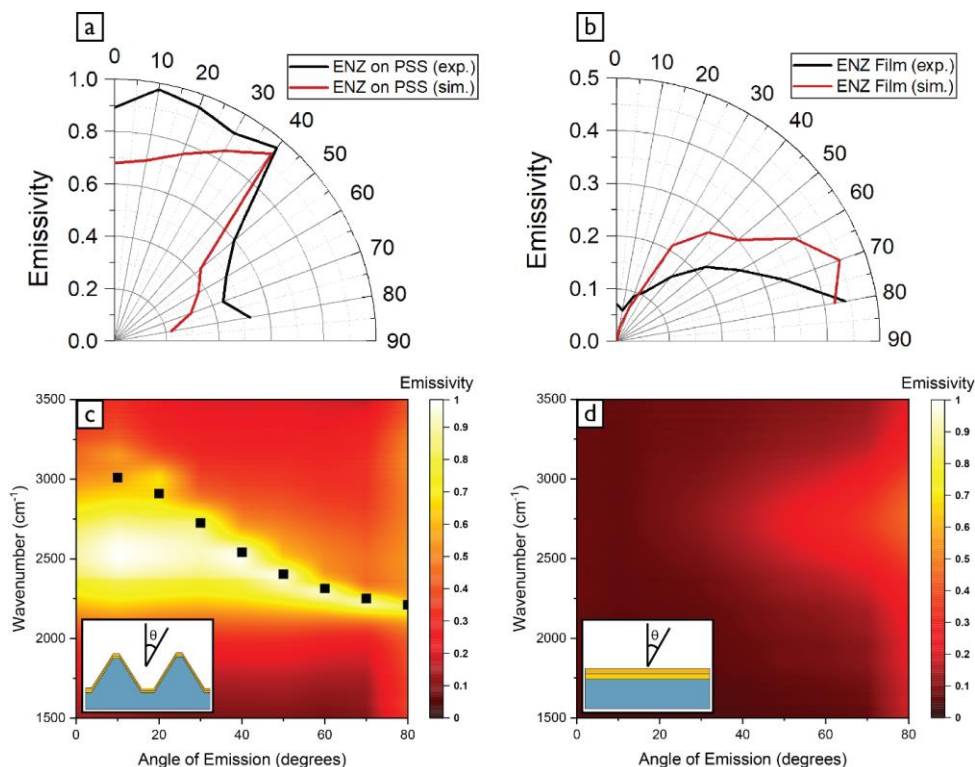


Figure 5.4: Polar peak emissivity plots for the a) CdO on PSS and b) CdO flat film samples. The black line represents the measured angle-dependent, unpolarized emissivity and red line is the simulated angle-dependent, unpolarized absorption. Contour plots showing the measured emissivity of the CdO PSS NIREM and CdO Berreman film are displayed in c) and d).

The origin of the spectral narrowing is indicative of interference between the ENZ-polariton and the diffractive mode resulting from the periodic patterning^{101,168,169} of the PSS template. Indeed, such Fano-like interactions have been reported in a broad range of periodic arrays of polaritonic resonators.^{14,126,170,171} To validate this claim, three-dimensional, finite-element-method electromagnetic simulations of the ENZ CdO layer on a PSS substrate were performed using CST Studio Suite. Here a dielectric function model previously reported by our group⁴⁰ and the sample geometry presented in Fig. 5.1d were implemented in order to determine the angle-dependent absorption spectra displayed in Fig. 5.3d. Calculations of the angle-dependent absorption of the structure (Fig. 5.3d) agree well with our experiments (Fig. 5.3c). However, there

are very slight differences between the measured emission and simulated absorption peak positions for both the planar film (Figs. 5.3a and 5.3c) and PSS film (Figs. 5.3b and 5.3d), which is due to the dielectric function employed for simulations not exactly matching that of this specific CdO film. From Fig. 5.3b and 5.3d it can be seen that the dispersive, diffractive mode effectively tunes through the ENZ polariton resonance, which maintains a nominally constant frequency, granting no indication of strong modal coupling. Note again that due to Kirchoff's law that these absorption spectra can be compared directly to the measured angle-dependent emissivity spectra. The simulated spectral position of the diffractive mode is included as black squares overlaying the measured emissivity contour plot (Fig. 5.4c) showing excellent agreement between measured and simulated values.

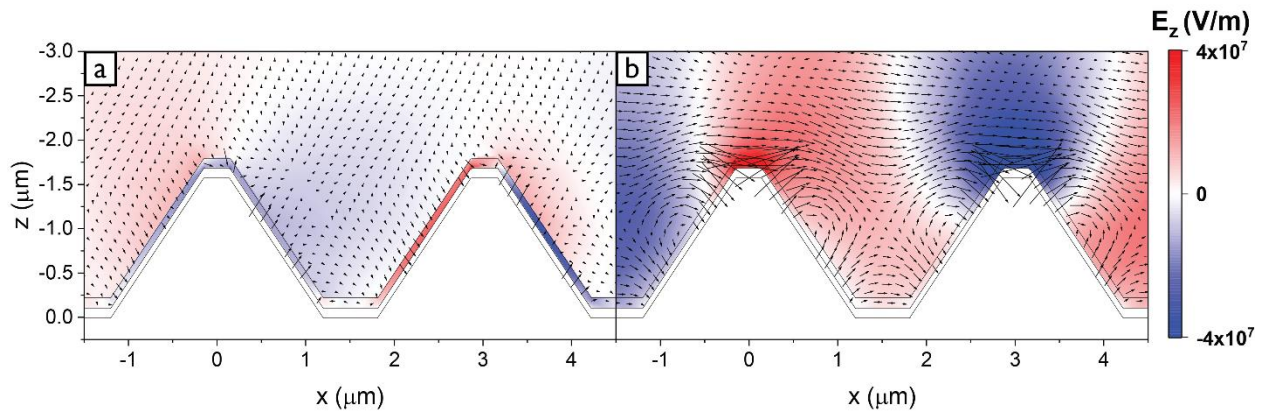


Figure 5.5: a) Z-oriented electric field (E_z) and Poynting vector (\vec{S}) of ENZ mode (2550 cm^{-1}). b) Z-oriented E_z and \vec{S} of diffractive mode (3000 cm^{-1}). Both field profiles were simulated at a 20° angle of incident.

The origin of these resonant features as diffractive in nature is confirmed through comparison of the spectral dispersion at different grating pitches, with the diffractive mode shown to red shift as the pitch is increased (Fig. 5.5 in section 5.2.3). Additionally, cross-sectional field profiles of the z-oriented electric field (E_z) as well as the Poynting vector (\vec{S}) at the ENZ condition (2550 cm^{-1}) and at the peak of the diffractive order for angles of 20° (3000 cm^{-1}) are provided in Figs. 5.5a and 5.5b, respectively, showing distinctly different resonant behavior. At the ENZ resonance (Fig. 5.5a), a strong confinement of the electromagnetic fields are observed within the ENZ layer, with a clear dipolar character in the phase across the resonant structure. Further, the magnitude of \vec{S} is relatively small ($|\mathcal{S}_{max,ENZ}| = 3.3 \times 10^{12} \text{ W/m}^2$) both inside and outside of the CdO layer, with an orientation matching that of the incident wave. However, at the diffractive

resonance, the mode is identified as having a strong in-plane momentum, as indicated by the alignment and magnitude of \vec{S} ($|S_{max,Diff}| = 7.0 \times 10^{13} \text{ W/m}^2$) above the sample, and fields coupled between adjacent resonators consistent with a diffractive mode. However, while the presence of the diffractive modes induces some angular dispersion in the spectral emissivity, this is predominantly at steep angles in the spectral region of interest ($\omega \approx 2550 \text{ cm}^{-1}$), and thus, at angles within $\pm 40^\circ$ off normal the emission spectra is still peaked at the ENZ condition with near-unity emissivity (Fig. 5.4a and Fig. 5.4c). This diffractive order can be tuned spectrally by depositing an identical CdO film on a PSS featuring a different pitch. Thus, it is possible to design a CdO on PSS structure in which the grating resonance is non-interacting with the ENZ emission at larger off-normal angles or one featuring a strong overlap with the ENZ resonance at normal incidence as is shown in Fig. 5.7.

5.2.3 Patterned Sapphire Substrate Pitch Dependence

Due to the wavelength-scale pitch ($p = 3.02 \mu\text{m}$) of the PSS structure, the thermal emission spectra exhibit a highly dispersive mode that we attribute to the excitation of a diffractive order. We justify this by examining the E_z and \vec{S} profiles, which are provided in Fig. 5.5 in section 5.2.2. Here we provide additional justification through simulation results illustrating the pitch-dependence of the spectral position for this dispersive mode. Due to the hexagonal pattern of the PSS, approximating the system as a simple 1D grating does not fully reproduce the spectral position of the diffractive mode. Instead, the PSS must be viewed as a 2D photonic crystal with the diffractive order corresponding to the lowest energy mode lying within the free-space light cone of the photonic dispersion.

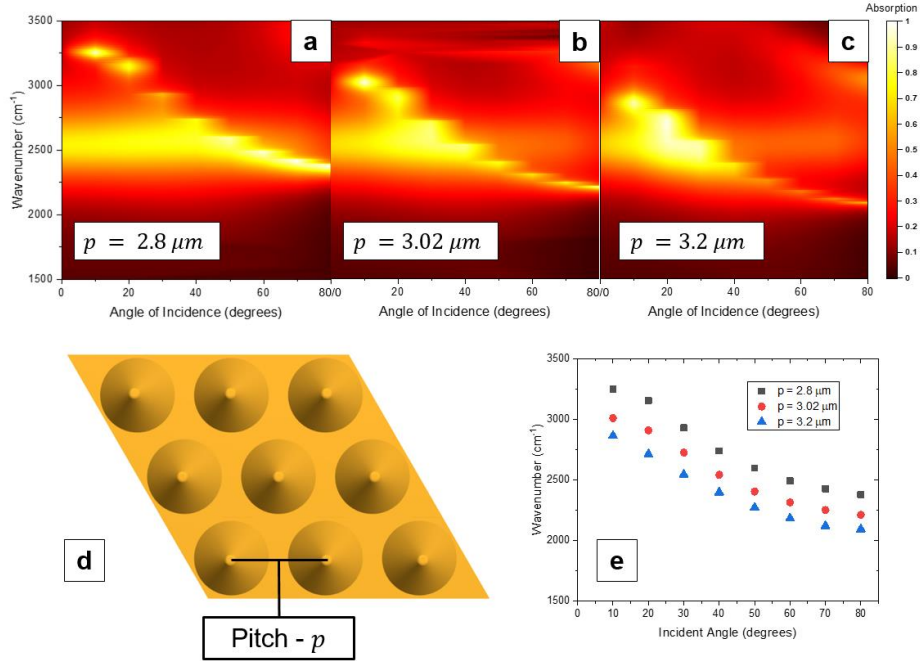


Figure 5.6: Contour plots displaying the simulated angle-dependent p -polarized absorption for a) $p = 2.8 \mu\text{m}$, b) $p = 3.02 \mu\text{m}$, and c) $p = 3.2 \mu\text{m}$. d) Topview of CdO on PSS sample with pitch labeled. e) Spectral dispersion of diffractive mode for three pitches shown in a), b), and c).

Using CST studio suite, we performed numerical calculations (Fig. 5.6) of the p -polarized, angle-dependent absorption for CdO on PSS structures featuring three pitches ($p = 2.8, 3.02$ and $3.2 \mu\text{m}$). In these simulations, the base diameter ($b = 2.4 \mu\text{m}$) and height of the cones ($h = 1.58 \mu\text{m}$), as well as the Au and CdO layer thicknesses remained constant. Additional details about these simulations are provided in the methods section. For all three pitches, in addition to the ENZ absorption centered at $\omega_{ENZ} \approx 2550 \text{ cm}^{-1}$, there is a diffractive resonance that tunes towards lower frequencies with increased angle of incidence. For clarity, we provide the spectral position of this diffractive mode alone, in Fig. 5.6e, revealing a clear spectral dependence on the PSS pitch. Namely, a decrease (increase) in the PSS pitch results in a blueshift (redshift) in the spectral location of the diffractive mode. Alternatively, at the same frequency (ω) the diffractive mode is shifted to higher in-plane momentum (larger incident angle) as the pitch decreases. This is consistent with diffractive coupling using a grating, wherein the additional in-plane momentum provided by the grating is inversely dependent on the pitch ($G = 2\pi/p$).

The measured, angle-dependent thermal emission of the fabricated CdO PSS (Fig. 5.3 and 5.4) shows that the diffractive mode for $p = 3.02 \mu\text{m}$ originates (Γ -point, 0°) at a frequency greater

than the ENZ frequency and tunes through the ENZ mode at higher emission angles. The spectral overlap of the modes results in an interference effect that significantly decreases the emission linewidth. From the simulation results provided in Fig. 5.6, we have determined that the spectral position at a given angle redshifts as the pitch increases. Therefore, it is conceivable that by increasing the PSS pitch such that the diffractive mode at the Γ -point overlaps with the ENZ emission, that this interference effect and spectral narrowing could in principle be realized at 0° . Indeed, simulation results reveal (Fig. 5.7) that a significant narrowing of the absorption linewidth can potentially be achieved at normal incidence by increasing the PSS pitch to $p = 5 \mu\text{m}$.

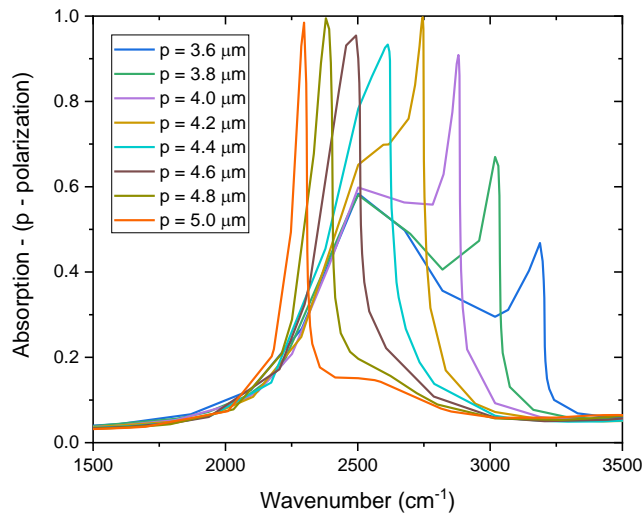


Figure 5.7: Simulated p -polarized absorption spectra detailing the pitch dependence at normal incidence for the CdO on PSS sample. As the pitch is increased and diffractive mode redshifts through the ENZ mode, the interference effect leads to a reduction in absorption linewidth.

5.2.4 Polarized Thermal Emission

As was stated in the main text, CdO films of deeply subwavelength thicknesses support both Berreman and ENZ modes where $Re[\epsilon_{CdO}(\omega)] \approx 0$. In planar films on an unstructured substrate (Fig. 5.8e) Berreman and ENZ modes can only be supported in p -polarization, with the former being accessible from free space. Reciprocally, through Kirchhoff's law, only p -polarized thermal emission is expected to be generated from CdO planar films through the thermal excitation of the Berreman mode. Since the Berreman mode is unable to couple to s -polarized emission, the maximum unpolarized thermal emission that can be harnessed from the sample is limited to 50%. However, by depositing an identical CdO film on a PSS, as we have done here (Fig. 5.8f), the

momentum mismatch between free space light and the ENZ polariton mode can be bridged, enabling both *s*- and *p*-polarizations to be absorbed/emitted. It is important to reiterate that in the flat CdO film that only the Berreman mode can be accessed from free space, whereas the ENZ mode can be coupled from free space only if the wavevector of the incident light can be increased as is observed in the CdO films grown on the PSS, giving rise to our nanophotonic infrared emitting metamaterial (NIREM) samples. The dispersion relation for these excitations is discussed later in section III of the supporting information. Therefore, the total emissivity of the PSS sample can in principle reach a value of 1, in contrast to the 0.5 limit appropriate for the flat film.

In order to confirm the polarization response of the flat and PSS CdO emitters, we performed polarized, angle-dependent thermal emission measurements of a 120 nm CdO film ($N_d = 5.8 \times 10^{19} \text{ cm}^{-3}$) deposited onto a flat, Au-coated (110 nm) sapphire substrate (Fig. 5.8a and 5.8c) and a PSS also featuring the same thickness Au film (Fig. 5.8b and 5.8d). These measurements are detailed in the methods section and a schematic of the beam path is provided in Fig. 5.12. The unpolarized thermal emission from these samples are provided in Fig. 5.3 and 5.4 of the main text. The thermal emission from the flat film exhibits a significant polarization dependence as expected. In *p*-polarization (Fig. 5.8c), the thermal emissivity climbs from $\epsilon \approx 0$ to nearly $\epsilon \approx 0.8$ ($\epsilon \approx 0.4$ for unpolarized measurements) at the plasma frequency as the angle of emission is increased from 0° to 80° , with the strongest emission occurring near 70° . However, in *s*-polarization (Fig. 5.8a) the emissivity remains consistently-low and featureless, even as the emission angle is increased. In contrast, the CdO-coated PSS sample is strongly emissive for both polarizations, with the emission peaking at the ENZ frequency ($\omega_{ENZ} \approx 2550 \text{ cm}^{-1}$) in both in both *s*- and *p*-polarization. Further, the radiation pattern is completely changed, with the thermal emission most strongly observed at angles between 0° (normal to sample surface) and 40° . This is due to the symmetry of the PSS pattern, which allows the ENZ mode to be out-coupled in both polarizations. Further, the dispersive, diffractive resonance present in the unpolarized measurements (Fig. 5.3 and 5.4) is evident in both polarizations as well.

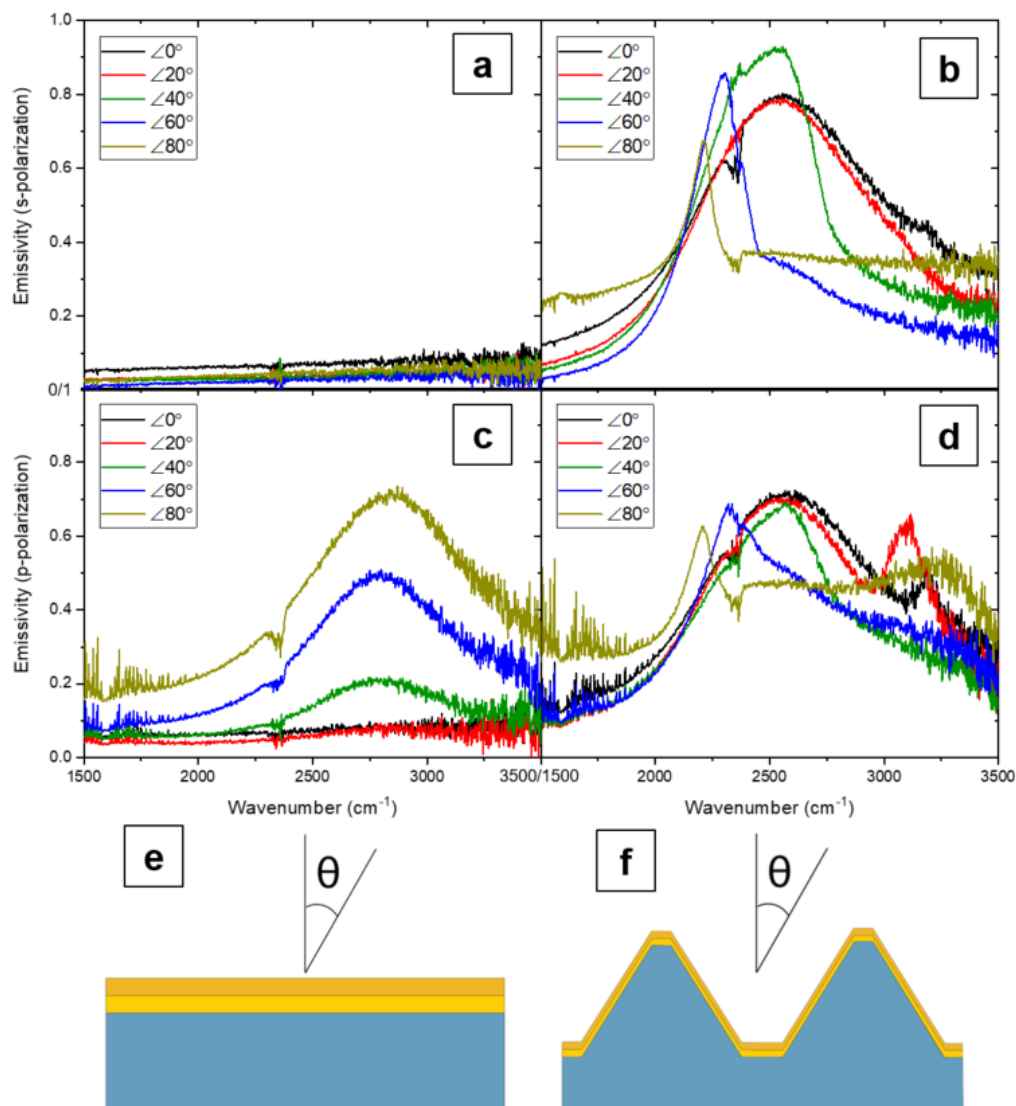


Figure 5.8: a) and c) show the *s*- and *p*-polarized thermal emission from the CdO on PSS sample depicted in e). b) and d) show the *s*- and *p*-polarized thermal emission spectra for the CdO flat film sample depicted in f).

Based on the near-unity, narrow bandwidth thermal emission resulting from the CdO PSS structure, and the redirection of both *p*- and *s*-polarized light within a radiation pattern directed at angles within 40° of the surface normal, it is clear that there is a high potential for this CdO-based NIREM device for advanced NDIR approaches. To validate this supposition, we implemented the external thermal emission input of our Bruker Vertex 70v FTIR spectrometer, integrating the thermal emission (250°C) from the CdO-PSS device at the surface normal as the source. This was passed through the interferometer and a short-path gas cell from Pike Technologies and detected using an MCT detector. The sample compartment, which housed the gas cell, as well as the rest of

the FTIR were kept under N₂ purge. Once the gas cell was adequately purged, CO₂ gas was passed through the cell using calibrated gas cylinders with 400 or 50 ppm of CO₂ in N₂. To enable direct comparison with a more traditional blackbody-based NDIR approach, these results were compared with similar measurements performed using a vertically-aligned carbon nanotube (VACNT) array blackbody (NanoTechLabs, Inc.) reference as the source. For more details about the gas cell measurements, see the methods section.

The mid-infrared spectrum of CO₂ consists of two molecular vibrational modes corresponding to the anti-symmetric stretching modes at 2349 cm⁻¹ and 3756 cm⁻¹.¹⁷² As the collected spectra from the NIREM device is peaked at 2550 cm⁻¹, with a radiation pattern suitable for directing the light towards the detector, it is anticipated that this device would be well suited for sensitive detection of CO₂, targeting the absorption at 2349 cm⁻¹. In a conventional CO₂ NDIR gas sensor the presence of CO₂ results in a drop in the transmitted power through the chamber at this 2349 cm⁻¹ absorption. Although we are not measuring this drop in integrated power from the broadband detector directly, FTIR allows us to determine the change in absorption at 2349 cm⁻¹ when CO₂ is introduced into the gas cell. Using the experimental setup outlined in the previous paragraph and detailed in the methods section, we were able to validate this hypothesis as the NIREM device demonstrated similar sensitivity to CO₂ gas at both 50 and 400 ppm (Fig. 5.9) as the blackbody source. It should be noted that even at the lowest concentration of the CO₂ calibration gas that was commercially available (50 ppm), we still detected over 1.5% absorption. This would imply that with this non-optimized geometry that over an order of magnitude further reduction in CO₂ concentration should still be detectable in such a 15-cm cell as used here. From this comparison it is clear that although the CO₂ absorption at 400 ppm is roughly equivalent for both sources, at 50 ppm it is slightly suppressed for the NIREM source, differing by just under 0.6% from the VACNT, however, such a difference is within the error of our measurements. Details regarding our error analysis can be found in the section 5.2.6. Although these measurements were performed under a N₂ purge, there is still the possibility of background CO₂ fluctuations, which can cause slight deviations in the absorption magnitude. We would like to also note the aforementioned ~200 cm⁻¹ spectral detuning of the NIREM emission center frequency from the CO₂ absorption. Thus, with further optimization of the ENZ emission center frequency with respect to the CO₂, a potential increase in sensitivity could be anticipated. Another point that should be raised is that the spectral linewidth of the NIREM emitter highlighted here is sufficiently

broad that some spectral overlap would occur with other gases of interest featuring vibrational modes in the spectral vicinity of CO₂, for instance N₂O. However, it is critical to point out that the device featured here by no means is representative of the narrowest CdO-based ENZ emitter/absorber linewidths reported, as values as narrow as 307 cm⁻¹ having been detailed previously.²⁵ For such narrower emission devices, this spectral overlap would be absent and thus the concept of filterless NDIR with our simple, low-cost NIREM emitter accessible. Furthermore, by implementing more advanced detection schemes, such as differential or modulated spectroscopies, or by further optimizing the ENZ resonance to the center frequency of the CO₂ absorption and increasing the PSS pitch to induce a narrowing of the emission linewidths, increased selectivity, and potentially sensitivity, can be realized. We discuss potential routes towards achieving further reductions in the emission linewidth from our NIREM source in section 5.2.5.

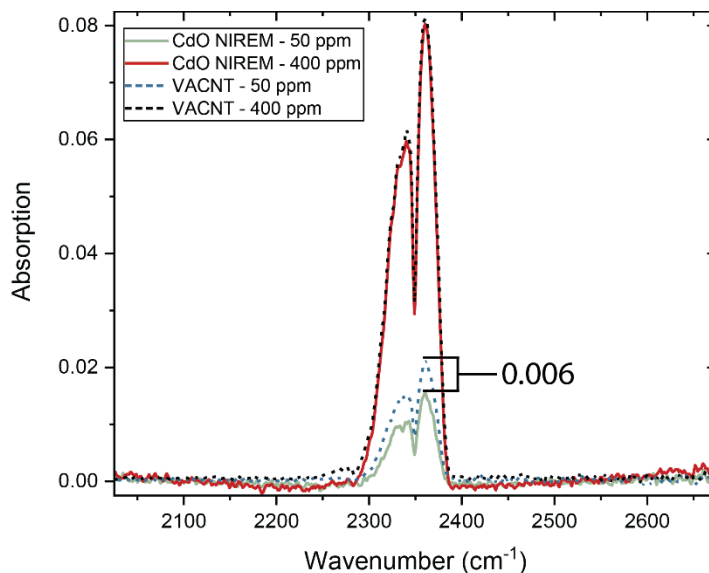


Figure 5.9: Absorption spectra at 250° C comparing the performance of our CdO on PSS narrowband emitter to a blackbody at CO₂ concentrations of 400 and 50 ppm. Our narrowband emitter performs comparably to the blackbody sample even at low CO₂ concentrations (50 ppm).

5.2.5 Spectral Bandwidth of CdO NIREM Source

Although our device is successful in detecting trace concentrations of CO₂, we would like to point out that the emission linewidth of the CdO NIREM does not only overlap with this molecular absorption, but also with absorption peaks associated with other common gasses, such

as CO and N₂O (Fig. 5.10). As was state in the text, CdO ENZ absorber/emitter linewidths have been reported to be as low as 307 cm⁻¹²⁵ so the device reported here does not represent the narrowest possible absorption/emission linewidth. From the SEM images collected of the CdO NIREM on PSS devices, the top surface of the films appears rough, presumably resulting in significant increases in scattering-based losses, thereby broadening the linewidth with respect to prior state-of-the-art. Similar surface roughness is also observed in CdO grown on metallic films such as Au (Fig. 5.2b), as this results in a columnar growth (Fig. 5.2f). Thus, one alternative approach would be to replace the metallic film with a CdO layer with carrier density well in excess of the CdO ENZ emitting layer. As the plasma frequency of such a highly doped layer will be well in excess of the emitting layer, this would serve the same highly reflective role that the metal layer currently serves. As such columnar growth is not observed in growth on sapphire or CdO, the losses would be anticipated to be significantly reduced. Another approach is through optimizing the PSS periodicity, as is described in section 5.2.3, whereby further narrowing of the emission linewidth at normal incidence could also be potentially achieved. In this optimized geometry the spectral overlap with non-targeted molecular absorption bands would no longer be present.

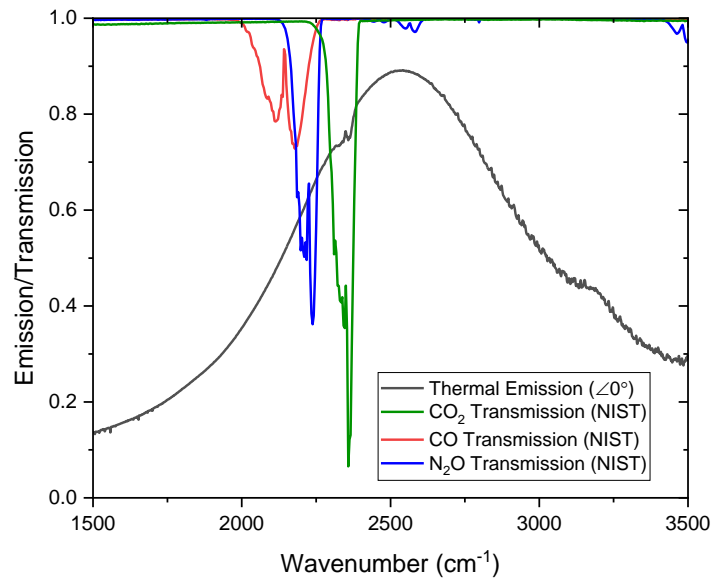


Figure 5.10: Normal (0°) incidence thermal emission from CdO on PSS sample, showing spectral overlap with CO₂, N₂O, and CO absorption.¹⁷²

5.2.6 Error Analysis of CO₂ Detection

Using the procedure provided in the methods section, ten CO₂ transmission measurements were performed in succession using our CdO NIREM at CO₂ concentrations of 100 ppm and 200 ppm. From each set of measurements, we were then able to calculate the average CO₂ absorption and standard deviation at each concentration. This allowed us to determine the influence of ambient CO₂ and temperature fluctuations on the CO₂ transmission measurements. The average in the standard deviation within the CO₂ absorption band ($\sim 2325 - 2375 \text{ cm}^{-1}$) was calculated to be 0.09 and 0.11 for 100 ppm and 200 ppm, respectively. Therefore, the noise floor due to temperature and CO₂ fluctuations remains consistent for both concentrations. If we were to increase the number of measurements used in our error analysis, we believe that the average standard deviation values for each concentration would converge.

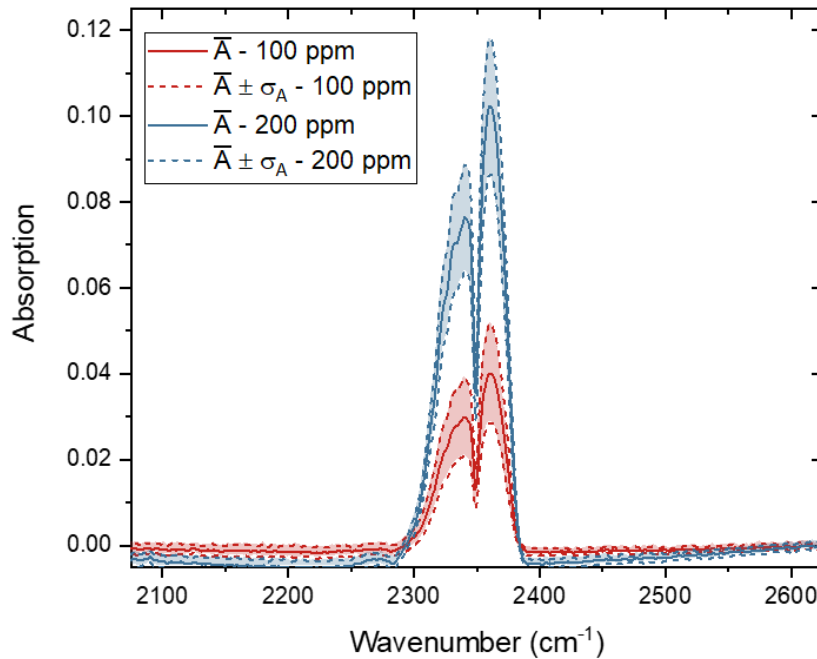


Figure 5.11: Absorption spectra illustrating the error analysis performed at CO₂ concentrations of 100 ppm and 200 ppm for our CdO NIREM. The solid lines show the average (\bar{A}) of 10 absorption spectra performed at 250°C. The dashed lines show the average shifted by the standard deviation (σ_A).

5.3 Conclusions

Here we have demonstrated the use of n-type In:CdO thin films grown on a PSS template offers several key advantages as mid-IR thermal emitter sources over thin flat CdO films discussed previously.²⁵ This results from the structured surface enabling near-unity emissivity of both *p*- and *s*-polarized light from the Berreman/ENZ-polariton modes, while redirecting the light from the Brewster angle ($\sim 65^\circ$) observed for flat films into a radiation pattern featuring >0.9 emissivity throughout the solid angle defined by $\pm 40^\circ$ off-normal. This NIREM device therefore offers a narrowband, near-perfect absorber with directional emission suitable for replacement of a broadband blackbody source and bandpass filter pair typically employed within NDIR sensor platforms. The periodicity of the PSS template was observed to induce a strong diffractive mode that results in a large spectral narrowing at highly off-normal emission angles ($>40^\circ$), however, this was demonstrated to have minimal impact upon the emission peak at the Berreman condition at shallower angles and thus negligible impact upon the performance within an NDIR configuration. However, in advanced designs this diffractive coupling could be employed for reducing the radiated power at off-normal angles, further improving the spatial coherence and efficiency of the thermal emission. We further validate the performance of our NIREM device for such an NDIR application, observing similar sensitivity to trace level concentrations (50 ppm) of CO₂ gas as a blackbody currently employed in NDIR technologies. Our results therefore imply that such NIREM devices could provide a designer IR source for plug-and-play replacement of the blackbody/bandpass filter combo, thereby reducing NDIR device cost, complexity and potentially extending its functionality. The elimination of the bandpass filter offers the potential for realizing multiple NIREM devices within a single die, enabling serial detection of several molecules within the same gas cell, without requiring the inclusion of a bulky and expensive filter wheel or multiple NDIR devices. Furthermore, by using this approach, one could also envision advanced NDIR concepts whereby multiple vibrational resonances of more complicated analytes could be detected, thereby extending the NDIR concept from the current state of the art that is limited to simple molecules such as CO₂, CO and CH₄, to one compatible with more complicated gases such as biological and chemical warfare agents, chemical byproducts, or environmental contaminants.

Chapter 6

6. Design of Wafer-Scale and Lithography-Free Tamm Plasmon Thermal Emitters with Broad Functionality using Gradient Descent Regression Optimization

6.1 Introduction to Tamm Plasmons

It is well known that the electron and phonon band structures of a material are a result of the translational symmetry of the crystal lattice. The band structures are split into regions of allowed and forbidden transitions, with the forbidden regions referred to as the band gap. Recent advancements in material growth methods and fabrication techniques have made it possible to engineer translational symmetry in multilayered and/or periodically structured materials. For example, MBE can deliver precise multilayer film growth that is useful for growing multi-quantum well structures. Other examples include one-dimensional (1D) photonic and phononic crystals that can be realized through wavelength-scale periodic modulation of the refractive index and bulk density, respectively. Just as with natural crystals, these artificial crystals possess a bandgap in their respective dispersion where light (photonic crystal) or acoustic (phononic crystal) waves are not allowed to propagate.

A break in the translational symmetry of a crystal gives rise to bound states within the bandgap. Finite crystals break translational symmetry at the crystal interface, resulting in the formation of surface states. One example of these surface states is referred to as a Tamm state which was first predicted by Igor Tamm in relation to electronic states bound to the surface of a crystal. They have since been investigated in other natural and artificial crystals such as electron plasmas, electronic, vibrational, and optical systems. Optical Tamm states, referred to as Tamm plasmons (TPs), have received significant attention recently as a promising platform for infrared photonic applications, such as narrowband absorbers and thermal emitters.^{173,174} For one, the TP dispersion falls within the light cone in air and therefore can readily couple to free space, bypassing the need for expensive and time-consuming lithographic and etching steps. Further, TP excitations generally exhibit much narrower resonance linewidths (and therefore higher Q-factors) than conventional plasmonic devices. By incorporating quantum wells into TP-supporting films, strong coupling has been achieved between TPs and intersubband transitions, which has been proposed as a promising platform for lasing. In this chapter, we outline an approach towards achieving

narrowband thermal emission with arbitrary spectral control through the inverse design of aperiodic TP films. First, however, in the following section we provide an intuitive model for understanding how these novel excitations arise in simple TP-supporting film.

6.1.1 Planar Tamm Plasmon Films for Narrowband Thermal Emission

As has been mentioned throughout this thesis, nano and microstructuring materials has been a popular method of altering the thermal photonic DOS and therefore the emissivity of a polaritonic surface. For this application, SPhPs and SPPs have seemingly contrasting benefits and drawbacks. For one, due to the long scattering lifetimes (on the order of ~ 1 ps) of optic phonons, SPhPs are associated with narrow resonant linewidths and therefore high Q-factors. However, SPhPs are bound to the spectral range of negative real permittivity spanning between the TO and LO phonons which are dictated by the crystal structure and therefore exhibit little-to-no tunability. SPPs, on the other hand, exhibit wide spectral tunability through carrier density-driven changes to the dielectric function. However, plasmonic materials are notoriously plagued with elevated optical losses, as electron-electron scattering rates are on the order of 1 fs. Therefore, the prospect of achieving absorption/emission features of sufficiently narrow linewidths for sensing applications is inherently low without invoking complicated resonator designs.

There are two additional shortcomings of using patterned surfaces to control thermal emission that diminish the utility of this approach: (i) fabricating devices consisting of resonator arrays is oftentimes a multi-stage process requiring expensive and time-consuming lithographic, etching and film deposition steps limiting the scalability of a potential device and (ii) as the quasi-normal mode frequencies are governed by the geometry of the repeating unit cell, achieving arbitrary multi-resonant absorption/emission spectra is not trivial without resorting to complicated resonator geometries which can be computationally expensive to design. In this chapter, we outline an alternative approach towards achieving narrowband thermal emitters which overcomes all of the aforementioned challenges through the inverse design of aperiodic TP films.

6.1.2 Theory of Tamm Plasmons at Metal – 1D Photonic Crystal Interfaces

TP modes can form between two dissimilar distributed Bragg reflectors (DBRs) or between a DBR and a metal film so long as phase matched condition is met at interface.^{22,175,176} In other words, in order for a TP state to exist within the bandgap of the DBR, the reflection phase of the

two mirrors (along opposing directions) must be equivalent but differ in sign ($\varphi_1 + \varphi_2 = 0$). From this condition it is clear that a metal-metal interface would not support a TP mode due to $sgn(\varphi_{Metal}) = -\pi$ at both interfaces.

There are two geometries for supporting TPs at a metal-DBR interface: the metal-on-top geometry (Fig. 6.1e) and metal-on-bottom geometry (Fig. 6.1c). In our work, we utilized the metal-on-bottom DBR-metal geometry where alternating layers of AlO_x and Ge are grown on top of a doped CdO film. As was previously mentioned, TPs are supported at the phase-matched condition between the metal and the DBR. Therefore, one could determine whether or not a TP mode would be supported at a metal-DBR interface by calculating the Fresnel reflection coefficients directed toward the DBR and toward the metal (see Fig. 6.1d and 6.1f). There are several techniques for calculating the reflection coefficients of a multilayer structure, such as the TMM which we use in our inverse design calculation. However, for this simple explanation I will rely on an impedance model as this method is conceptually more intuitive due to its connection to circuit theory. Further, through the lumped element model approach this analysis can be easily extended to TP-supporting films featuring a metasurface in place of the un-structured metal film.

The characteristic p -polarized wave impedance in a material with a complex dielectric function ϵ_n is given as

$$Z_n = \frac{k_{z,n}}{\omega \epsilon_o \epsilon_n} \quad (1)$$

where $k_{z,n} = \sqrt{k_o^2 \epsilon_n - k_x^2}$ is the propagation constant along the z -direction, ω is the frequency, and ϵ_o is the permittivity of free space. From equation 1 it is evident that utilizing a doped semiconductor as opposed to noble metals as the metal layer results in additional design flexibility due to the tunability of the optical impedance. Noble metals possess a high, fixed carrier density and therefore the dielectric functions of these materials are also fixed. Alternatively, as was shown in chapter 2, the plasma frequency of n -doped CdO is widely tunable throughout the IR granting additional flexibility to the design of TP-supporting films. This is demonstrated further in section 6.2.3.

Now that we have calculated the characteristic impedances of each material, we can now calculate the total lumped impedances of the DBR and metal films. Figures 6.1d and 6.1f show the

equivalent circuit model representation of a TP film in the metal-on-bottom and metal-on-top geometries. To calculate the lumped impedance of the DBR, starting at the dielectric layer furthest away from the CdO-DBR interface (CdO-on-top: bottom layer; CdO-on-bottom: top layer) the impedance of each layer can be calculated using a recursive method. The impedance of an individual layer with a finite thickness is given as

$$Z_{n,n+1} = Z_n \frac{Z_{n+1} + iZ_n \tan(k_{z,n}d_n)}{Z_n + iZ_{n+1} \tan(k_{z,n}d_n)} \quad (2)$$

where d_n is the layer thickness and n is an index denoting the layer number in the stack. Z_{n+1} is the total impedance behind the layer, so when calculating the impedance of the first layer of the DBR in the CdO-on-bottom geometry $Z_{n+1} = Z_{air}$. In the CdO-on-top geometry, $Z_{n+1} = Z_{substrate}$ for the first layer in the DBR. The total impedance of the DBR (Z_{DBR}) is then solved for by progressing through the remaining layers in the stack. The impedance of the CdO layer (Z_{CdO}) is calculated the same way, however only for one layer.

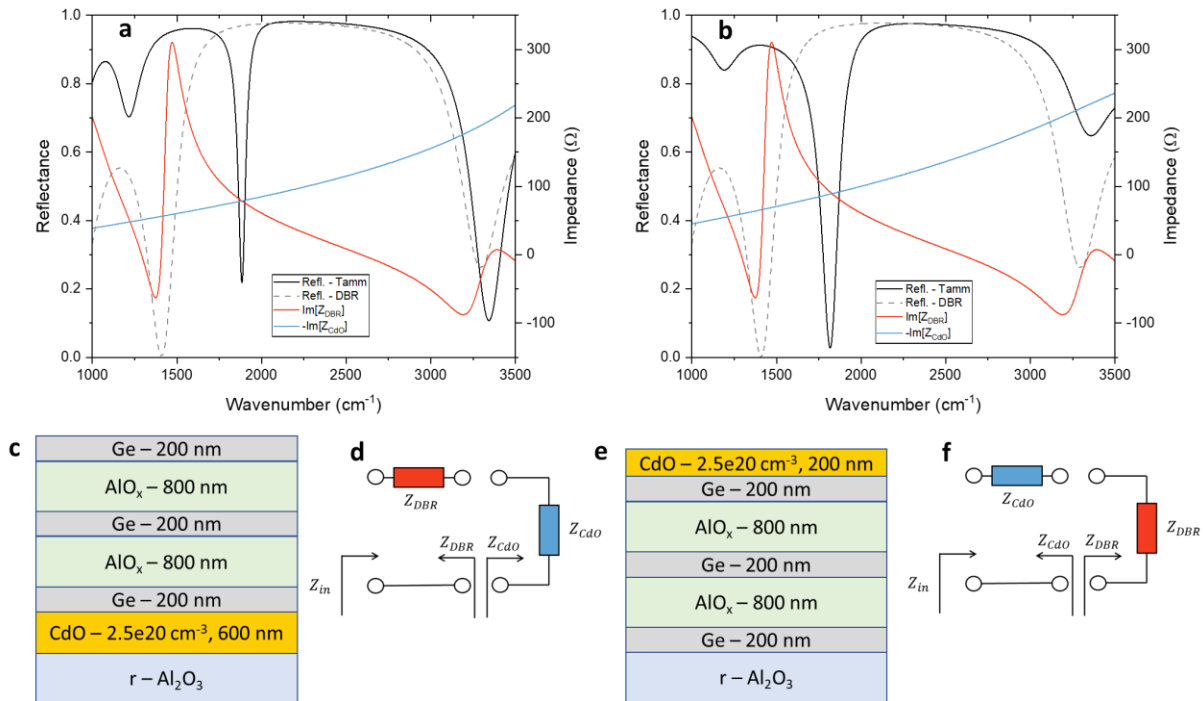


Figure 6.1: a) Simulated reflectance (solid line) of CdO-on-bottom structure displayed in c). TP modes are supported when $\text{Im}[Z_{DBR}]$ (red line) is equal to $-\text{Im}[Z_{CdO}]$ (blue line). Note as well that a dip in DBR reflectance (dashed line) corresponds with the zero-crossing of $\text{Im}[Z_{DBR}]$. b) Simulated reflectance of the CdO-on-top TP structure displayed in e). The equivalent circuit model representation of the structures in c) and e) are displayed in d) and f), respectively.

With the calculated lumped impedances Z_{DBR} and Z_{CdO} seen from the DBR-CdO interface looking in opposing directions (See arrows in Figures 6.1d and 6.1e) we can now model the TP films as simple AC equivalent circuit (Figures 6.1d and 6.1e) with source and load impedances. Note that the designation of source or load is dependent on the geometry. For example, Z_{CdO} takes the role of the load (source) impedance in the CdO-on-bottom (CdO-on-top) geometry. From circuit theory, the maximum active power is dissipated by the load at the conjugate impedance matched condition $Z_{DBR} + Z_{CdO}^* = 0$. In TP films, this translates to a TP mode being supported when $Im[Z_{DBR}] = -Im[Z_{CdO}]$, and absorption maximized when also $Re[Z_{DBR}] = Re[Z_{CdO}]$. Alternatively, this reduces to the phase-matched condition mentioned above $\varphi_{DBR} + \varphi_{CdO} = 0$, which can be calculated from the complex Fresnel coefficients $\varphi_{DBR/CdO} = Arg(r_{DBR/CdO})$, where $r_{DBR/CdO} = (Z_{DBR/CdO} - Z_{air}) / (Z_{DBR/CdO} + Z_{air})$.

The total simulated reflectance of the CdO-on-bottom TP film ($|r_{Tamm}|^2$) at normal incidence is displayed as a black line in figure 6.1a. The optical bandgap of the DBR (gray dashed line) manifests as a region of high, uniform reflectance, spanning from 1410 cm^{-1} to 3295 cm^{-1} . This TP film supports two TP modes, one at 1210 cm^{-1} and the other at 1884 cm^{-1} , corresponding with the intersections of $Im[Z_{DBR}]$ (red line in figure 6.1a) and $-Im[Z_{CdO}]$ (blue line in figure 6.1a). The CdO thickness (600 nm) is above the evanescent skin depth and therefore the CdO layer impedance is close to that of the characteristic impedance. This, along with the high carrier density (and therefore high plasma frequency) results in low transmission through the film. Thus, the large dip in reflectance at the TP mode frequency is associated with an equivalently large peak in absorption ($A = 1 - T - R$). Further, as was discussed in section 6.1.1, these modes are associated with a high Q-factor in comparison to traditional plasmonic devices. For the metal-on-bottom film in figure 6.1c, which is not an optimized system but simply used as an example, the simulated Q-factor is 34. The absorption and Q-factor can both be further optimized by tuning the parameters of the TP system. For example, in section 6.2.2 we experimentally realize a CdO-based TP films that achieves Q-factors as high as 135. Further, in section 6.3 we demonstrate that Q-factors as high as 10,000 can potentially be achieved by including more dielectric layers and using low loss dielectric materials in the DBR.

A TP structure in the CdO-on-top geometry with an identical DBR and CdO carrier density supports two TP modes at similar frequencies (1187 cm^{-1} and 1816 cm^{-1} in figure 6.1b) to those in

the CdO-on-bottom film. In this geometry there is an optimum thickness for maximizing the TP absorption, too thin and the light would transmit through the CdO upon back-reflection, reducing absorption and increasing radiative losses (and therefore lowering the Q-factor). On the other hand, if the CdO layer is too thick, the incident light would not be able to transmit through the CdO, therefore severely limiting the absorption. Previous studies have reported on how perfect absorption in metal-on-top TP films can be achieved through the balancing of radiative and non-radiative losses.¹⁷⁷ Another thing to note is that since the spectral positions of the TP modes occur at the impedance matched condition, and the impedance of the CdO layer is impacted by the CdO layer thickness, the spectral position of the TP modes within a single photonic bandgap can be tuned by changing the CdO layer thickness.

6.1.3 Angular Dispersion of Tamm Plasmons

The angular dispersion of TP modes is parabolic in shape, with the resonant frequency blue-shifting as the incident/emission angle is increased away from the Γ -point (0°). Figures 6.2a and 6.2b show the polarized reflectance maps, calculated using TMM, of the metal-on-top and metal-on-bottom structures from figures 6.1e and 6.1c, respectively. In both geometries and polarizations, the TP mode dispersion follows the characteristic parabolic distribution. However, the *s*- and *p*- polarized dispersion differ slightly from one another, with the *p*- polarized absorption being slightly more dispersive at higher incident angles than the *s*- polarized absorption.

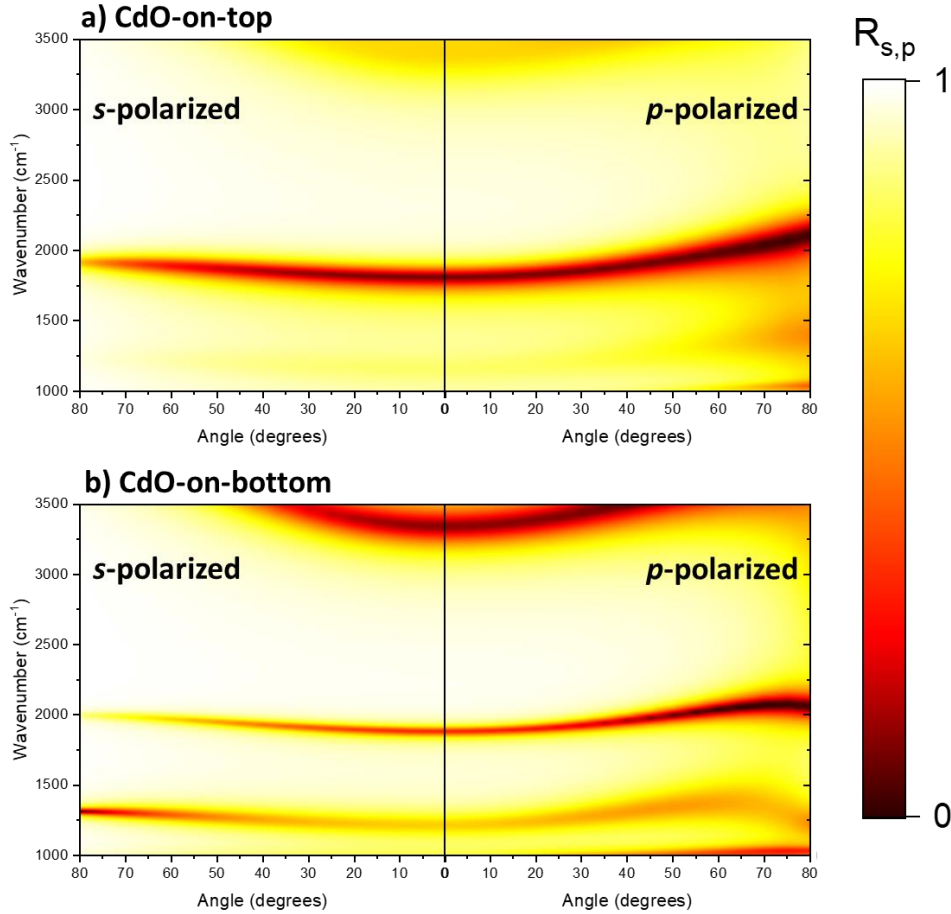


Figure 6.2: a) Polarized, angle-resolved reflectance calculated (using TMM) for the CdO-on-top structure displayed in figure 6.1e. b) Polarized, angle-resolved reflectance calculated for the CdO-on-bottom structure displayed in figure 1c.

6.2 Designer Tamm Plasmon Films using Gradient Descent Optimization

Despite the advantages offered by Tamm plasmon polariton-wavelength-selective emitters (TPP-WS-EMs), realizing designs for novel applications is hampered due to challenging design requirements. The traditional brute-force design strategy, i.e., performing a sweep of the device parameters, cannot be employed because of the extremely large parameter space. As an example, optimizing a 9-layer-aperiodic-DBR would require at least 10^9 separate calculations, costing a total of 2,700 hours assuming 10 simulations per second, and this time would grow exponentially with the addition of more layers to the DBR. For this reason, there has been substantial recent research focused on using inverse design techniques, such as Bayesian optimization¹⁷⁸, to design narrowband TPP-WS-EMs at desired wavelengths and linewidths (Q-factors). Yet, the

optimization efficiency in these demonstrations is still poor, requiring 24-day simulation times on a cluster even for one single structure while also restricting the design flexibility. Additionally, these demonstrations were limited to single wavelength operation. However, for some applications having an emitter that produced thermal radiation at multiple desired wavelengths would be advantageous. To our knowledge, designing thermal emitters targeting multiple, arbitrary wavelengths at high Q-factors has yet to be reported. In this chapter, we demonstrate an inverse design algorithm based on stochastic gradient descent (SGD) that overcomes all of these challenges. The optimized Tamm plasmon thermal emitter consisted of an aperiodic DBR deposited onto an n-doped CdO film. The DBR consisted of alternating layers of Ge and AlO_x . Using the SGD algorithm, the layer thicknesses of the DBR and the carrier density of the CdO were determined independently and efficiently, with the total optimization time taking only minutes on a consumer-grade desktop. The SGD algorithm is described in more detail in the following section.

Experimentally, we demonstrate inversely designed TPP-WS-EMs targeting frequencies of interest for various applications, such as filterless NDIR. For example, we design and characterize a TPP-WS-EM with a single emission peak that is spectrally collocated with one of the principal absorption peaks of CO_2 . Further, we realize a TPP-WS-EM that exhibits multi-peak thermal emission wherein the peaks in emissivity match with two principal absorption features of N_2O . In addition, we demonstrate broad control over the emission frequency and linewidth, with single-peak, high-Q emission being supported in the LWIR and MIR. In section 6.3, we illustrate the power of the TPP-WS-EM platform and our SGD algorithm by providing designs suitable for a wide range of applications. Some examples include single peak emission from the LWIR to telecommunication ($1.55 \mu\text{m}$), ultra-high Q-factors (over 10,000), multi-peak (>2 peaks) designs for free-space communication, and near exact matches to the absorption spectra of molecules with non-trivial absorption spectra, such as dimethyl methylphosphonate (DMMP). Our design takes full advantage of the broad tunability of the CdO plasma frequency through doping, which greatly increases the design flexibility. Further, the use of CdO also makes the fabrication CMOS compatible.¹⁷⁹ The combination of our algorithm and material advancements enables cost-effective, wafer-scale, and lithography-free TPP-WS-EMs for numerous applications, including NDIR, sensing, free-space communications and IR beacons desired for search and rescue.

6.2.1 Designing Aperiodic Tamm Plasmon Films using Gradient Descent Optimization

As stated in the previous section, this work employs an SGD-based inverse design technique to determine individual layer thicknesses and CdO carrier density for a TPP-supporting heterostructure consisting of a CdO base layer capped with a DBR of alternating Ge and AlO_x layers. The SGD optimization process is initiated by assigning the maximum number of layers to the DBR, with the thicknesses of each layer and the carrier concentration for the CdO film being randomly initialized. Using the TMM, the absorption spectrum of the designed structure (DS) is calculated and compared to the input target spectra (TS), resulting in a scalar *error*. The error is expressed as a combination of mean-squared difference (MSE, the first term) and mean absolute difference (MAE, the second term) terms:

$$error = mean \left\{ ratio1 \cdot (\overrightarrow{DS} - \overrightarrow{TS})^2 + ratio2 \cdot |(\overrightarrow{DS} - \overrightarrow{TS})| \right\} \quad (3)$$

where *ratio1* and *ratio2* are hyperparameters that can be modified for different targets. While the MSE regulates the algorithm to focus on spectral ranges where the difference between DS and TS is greatest, MAE weighs the difference at every frequency equally. Note that the such a combination of error is commonly employed in deep learning field, and some techniques to modify the *error* can be very powerful for designing TPP-WS-EMs, such as the weighted sampling technique. During each iteration, the *error* will be back-propagated to find the gradient over the vector (\vec{t}) via SGD, which represents the fit parameters of the system so here the thicknesses of each layer and the carrier concentration of CdO. The gradient will be used to update \vec{t} upon each iteration in the inverse design protocol:

$$\vec{t}^n = \vec{t}^{n-1} - step \frac{\partial error^{n-1}(\vec{t}^{n-1})}{\partial \vec{t}^{n-1}} \quad (4)$$

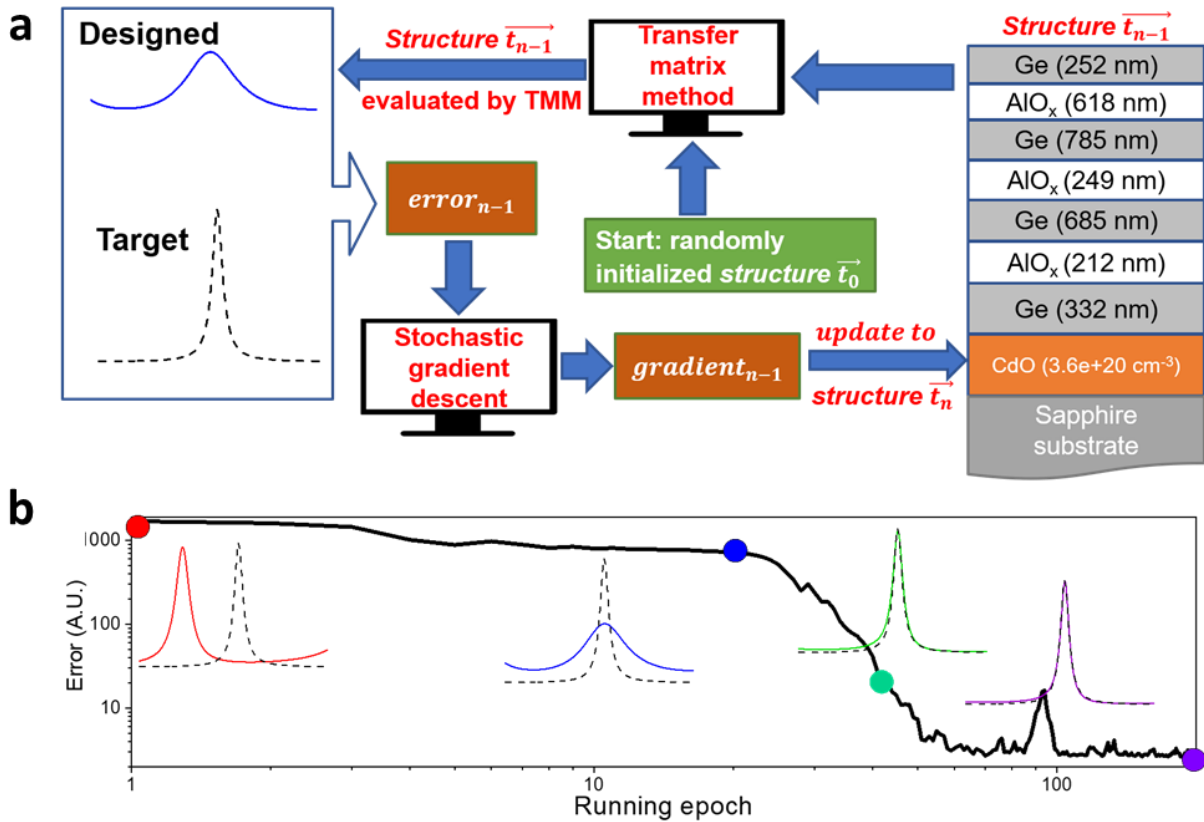


Figure 6.3: a) The designable parameters (thickness and carrier density) of the TPP-WS-EMs are randomly initialized, and the spectra of the designed structure (DS) is compared with the target spectrum. The thickness is updated by calculating the gradient over the difference (error) through the TMM. b) Following the gradient, the error is minimized through iterations, and the structure is optimized. The photo of a fabricated TPP-WS-EM is included to show the scale. The layer thickness of this optimized structure is labeled in the schematic.

Initially, the absorption spectrum of the randomly initialized structure (red solid line Figure 6.3b) differs significantly from the target spectrum. After several iterations, the error decreases and the structure is optimized as the designed spectrum converges towards the target (solid red \rightarrow blue \rightarrow green \rightarrow purple lines in Figure 6.3b). Unlike traditional gradient descent calculations employed in commercial software, and previous publications, the SGD used here reduces the possibility of getting trapped at a local minimum and improves the optimization performance.^{180–182}

6.2.2 Demonstration of Arbitrary Spectral Control of Tamm Plasmons

In this section we experimentally demonstrate the power of our SGD optimization technique by designing and characterizing TPP-WS-EMs that exhibit a wide range of unique spectral features. The designed and as-grown DBR layer thicknesses and CdO carrier densities of every TPP films are tabulated below.

Table 6.1: Parameters of designed and as-grown films

	7 layer (Fig. 6.4a) High-Q MIR		3 layer Fig. (6.4d) LWIR		3 layer (Fig. 6.4c) CO ₂ NDIR		5 layer (Fig. 6.4d) N ₂ O NDIR	
	Designed [nm]	As-grown [nm]	Designed [nm]	As-grown [nm]	Designed [nm]	As-grown [nm]	Designed [nm]	As-grown [nm]
Ge	264	228	Air		Air		Air	
AlO_x	356	540						
Ge	671	755					468	560
AlO_x	293	200					559	290
Ge	598	627	499	540	270	250	525	450
AlO_x	178	198	829	440	430	590	585	268
Ge	304	208	315	400	656	641	412	644
CdO N_d [cm⁻³]	3.5e+20		0.7e+20		3.6e+20		1.7e+20	

First, we demonstrate an inversely designed TPP-WS-EM that exhibits a single, high-Q emission peak (Figure 6.4a) targeting 2650 cm⁻¹, placing this emission peak within one of the atmospheric transmission windows (2000 – 3300 cm⁻¹) which is important for free-space communications. We model the target spectrum as a flat line with a single, sharp absorption peak at 2650 cm⁻¹ which the resultant spectrum of the designed structure matched very well (Figure 6.4a). The

experimentally measured resonance is centered at 2721 cm^{-1} with a Q-factor of 128 because of the difference between designed and fabricated layer thicknesses, which agrees well with the calculation based on as-grown thicknesses. Such a Q-factor (128) is on-par with surface phonon polariton resonators ($\sim 100\text{-}400$)^{41,54,99}. Although our experimental Q-factor was limited to 128 in this work, this is not a fundamental limitation of but due to the reduced number of DBR layers (7 total layers) and the material loss of evaporated AlO_x . In section 6.3 we demonstrate that Q-factors over 10,000 are achievable by exchanging AlO_x for a material with lower losses (such as ZnSe) and increasing the number of dielectric layers.

There are two atmospheric transmission windows within the IR, the previously mentioned window spanning from $2000 - 3300\text{ cm}^{-1}$ and another found in the LWIR ($800 - 1250\text{ cm}^{-1}$). To demonstrate the broad spectral tunability of our CdO-based TMM-EMs, we also inversely designed a TPP-WS-EM with a single, near-unity emission peak at 1250 cm^{-1} using the same strategy mentioned above (Q-factor = 16). The target spectrum, the calculated spectra based on the designed and as-grown thicknesses, and the experimentally measured emission spectrum show extraordinary agreement (Figure 6.4b). Additionally, despite differences between the as-grown and designed thicknesses, the discrepancy in the spectra is minimal, indicating the robustness to certain range of fabrication error.

Beyond free-space communications, the MIR is of great interest for the unique absorption fingerprint spectra of molecules. Thus, one application of WS-EMs is filterless NDIR gas sensing^{156,166,183} which was described in the previous chapter. To demonstrate the potential of our inversely designed TPP-WS-EMs for NDIR applications, we designed a sample that supports a single peak in emissivity that spectrally overlaps with one of the anti-symmetric stretching modes of CO_2 (2349 cm^{-1}) with a minimal number of dielectric layers (only 3 here) to reduce the fabrication complexity. While the designed TPP-WS-EM exhibits a peak in emissivity centered at 2350 cm^{-1} with a Q-factor of 40, the actual measured emissivity is centered at 2360 cm^{-1} with a Q-factor of 21 (Figure 6.4c), again showing great agreement.

So far, we have demonstrated designs of TPP-WS-EMs with only a single, tunable peak in emissivity. However, there most gases feature multiple spectral vibrational modes that define the molecular fingerprint. For example, N_2O exhibits two primary absorption peaks at 1280 and 2230 cm^{-1} . In the filterless NDIR configuration, it is ideal that the gas of interest absorbs all light at

these, and only these frequencies. Thus, the light emitted by the WS-EM must be tailored to match both the vibrational frequencies and linewidths. Yet, to our knowledge WS-EMs matching more than one vibrational bands of a molecule have yet to be demonstrated. Owing to the flexibility of our inverse design approach, we are able to use the absorption spectrum of N₂O as the target spectrum in order to design a TPP-WS-EM that reproduces the absorptive features. Here, we use five dielectric layers for our design, yielding two absorption peaks centered at 1300 and 2200 cm⁻¹ (Figure 6.4d), closely matching the amplitude, frequencies, and FWHMs of both the molecular resonances. However, due to the thicknesses of the DBR dielectric layers not matching the design exactly, the experimentally measured emissivity are slightly shifted (1361 and 2361 cm⁻¹) from the target spectra (Figure 6.4d). We would like to stress that the limitation of growth in our demonstration is caused by differential heating between the substrate stage and quartz crystal microbalance (QCM) used to monitor the film thickness during growth which becomes more severe for aperiodic structure growth, as we cannot calibrate the tool for all the thicknesses. However, within commercial systems such targets can be matched much more accurately. As such, this is not a fundamental limitation of our approach, but of the deposition tool used to grow these samples.

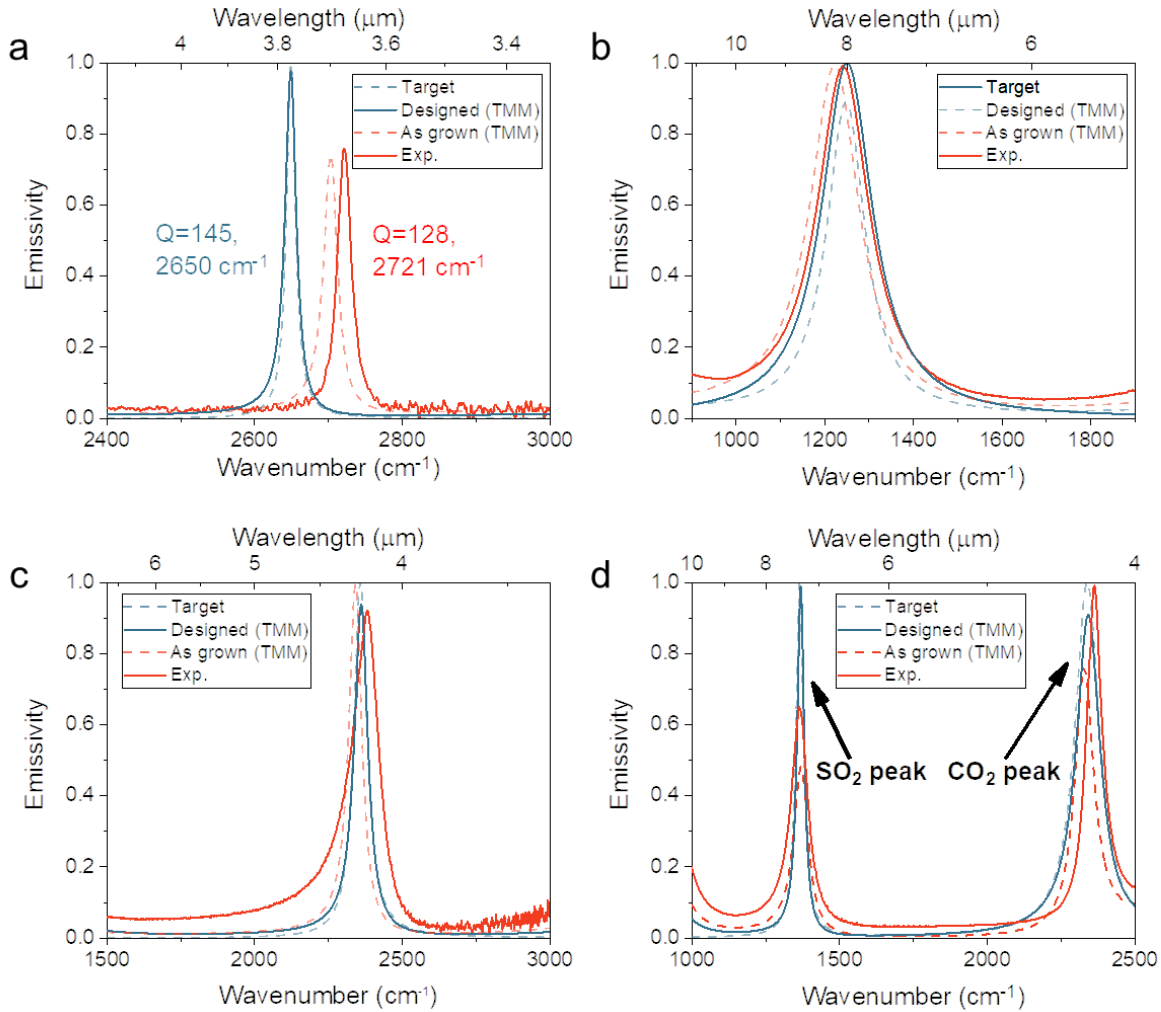


Figure 6.4: The inverse-design algorithm was employed to realize TMM-EM structures featuring a) single, high Q -factor emission in the MWIR, b) single emission mode in the LWIR, and resonant emission designed for NDIR sensing of c) CO_2 and d) N_2O . The target spectra are plotted as blue dashed lines, while the emissivity experimentally measured at 150°C is plotted as red lines. Blue and red dashed curves are calculated absorption spectra of inversely designed and as-grown thickness, respectively.

6.2.3 Advantages of CdO in Design of Tamm Plasmon Thermal Emitters

So far, we have demonstrated the remarkably high degree of freedom in designing the emissivity of TPP-WS-EM devices using inverse design. As was outlined in section 6.1.2, these structures owe their broad spectral tunability to two things: the aperiodicity of the DBR and the use of a doped semiconductor with a controllable dielectric function as the metal layer. The aperiodicity of the DBR allows for significant control over the photonic band structure, with the parameter space being limited only by the number of allowed layers of the DBR. Another reason is that the optical impedance of the CdO layer is not restricted by a fixed dielectric function as is

the case for a noble metal. This additional tuning knob allows for more advanced TPP-WS-EM designs to be realized, such as matching to complex absorption spectra. To illustrate this point, we used our SGD algorithm to design a CdO-based TPP-WS-EM that closely matches the absorption spectrum of the nerve agent DMMP (Figure 6.4a, black line). The parameters of this film can be found in Appendix A. We then attempt to match the absorption spectrum of DMMP by designing a TPP-WS-EM where gold is used in place of the CdO. In both cases the maximum number of DBR layers was set a 29. Also, here we replace the AlO_x with ZnSe ($n \approx 2.4$) as it is far less dispersive within this spectral range and therefore exhibits lower optical losses. Due to the differences in the metal layer optical impedances, the resultant DBR layer thicknesses ended up differing significantly. Our optimization technique was able to design a CdO-based emitter DBR that matched the absorption spectrum quite well (Figure 6.5a, red line). However, when the tunable CdO is replaced with gold, the matching of the complex vibrational spectra is severely diminished while using the same number of dielectric layers (Figure 6.5a, blue line). Since the only difference between the two systems is the metal layer (CdO vs. gold), we attribute the dramatically improved spectral control to the tunability of CdO plasma frequency, which can be tuned between $\sim 1200 \text{ cm}^{-1}$ to 7800 cm^{-1} (8.33 to $1.28 \mu\text{m}$) by controlling the dopant concentration.¹⁸⁴

The CdO plasma frequency also sets an upper limit on the frequency range where Tamm plasmons can be supported and can therefore be used as a low-pass filter for thermal radiation. Since the permittivity of the CdO becomes positive above the plasma frequency, the sign of the reflected phase is no longer $-\pi$, which is required to achieve phase matching at the DBR-CdO interface. Therefore, a Tamm plasmon would not be supported in the DBR photonic bandgaps above the CdO plasma frequency. A more detailed explanation of the conditions where Tamm plasmons are support is provided in section 6.1.2. In order to demonstrate the high-frequency filtering that is enabled by CdO, we grew two TPP-WS-EMs consisting of an identical DBR (in same growth) grown on two different CdO layers featuring different plasma frequencies, i.e., 2700 cm^{-1} (red curve) and 4300 cm^{-1} (blue curve) (Figure 6.5b). The plasma frequency of the low-doped film is denoted in the figure by a black dashed line. The emissivity spectra of the two TPP-WS-EM films differ in a number of different ways. First, both TPP-WS-EMs support highly-emissive Tamm plasmon modes within DBR photonic bandgap spanning from $\sim 1000 - 2000 \text{ cm}^{-1}$ (gray line in Figure 6.5b), however the peak position within the photonic bandgap blueshifts with increased CdO carrier density. Stronger absorption is observed at the photonic band edge at a lower energy.

Note that this is not a Tamm plasmon mode, however it is still observed as an absorptive/emissive feature in the reflectance/emission spectrum due to the losses within AlO_x . Finally, since Tamm plasmons are not supported above the plasma frequency of the CdO, an additional Tamm plasmon is observed at 3500 cm^{-1} in the emissivity spectrum of the high-doped CdO TPP-WS-EM that is not observed in the emissivity spectrum of the low-doped CdO TPP-WS-EM spectrum. Therefore, the carrier density of the CdO acts as a spectral filter, cutting off high-frequency Tamm plasmon resonances that would otherwise be supported if a metal with a higher carrier density were used.

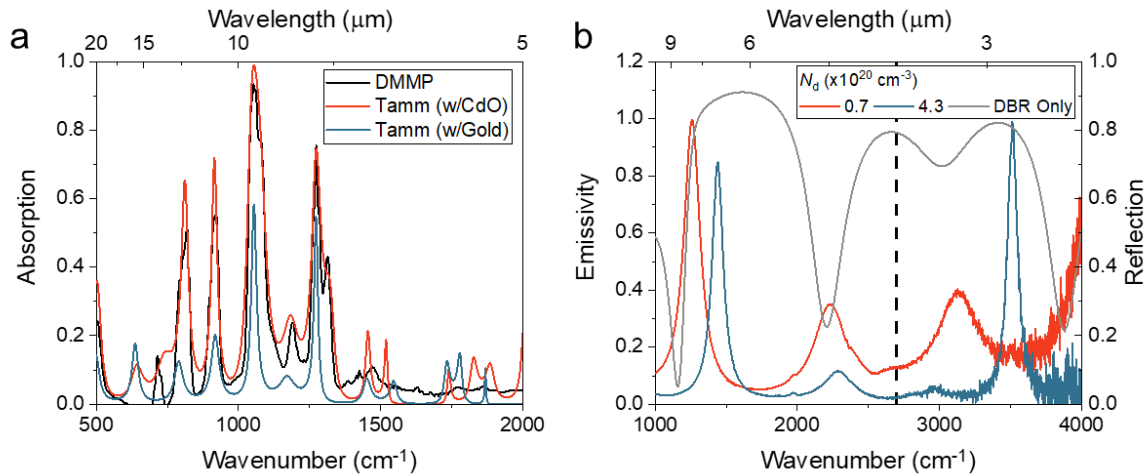


Figure 6.5: a) TPP-WS-EM designs targeting at DMMP spectra with CdO and gold as metal layers. b) The emissivity (reflectance) of the same DBR on CdO of different carrier densities (sapphire substrate). The plasma frequency of CdO with a carrier density of $7 \times 10^{19}\text{ cm}^{-3}$ ($4.3 \times 10^{20}\text{ cm}^{-3}$) is displayed by the vertical dashed line (above 4000 cm^{-1}).

6.2.4 NDIR Gas Sensing Using Tamm Plasmons

With the aforementioned TPP-WS-EM films, we are able to experimentally validate the potential for filterless NDIR applications. In such a set up the TPP-WS-EM only emits at the frequency where the gas has strong absorption, so the integrated transmitted power change measured by the broadband detector reflects the concentration of the gas of interest. Although we are not directly measuring this drop in integrated power from the broadband detector, FTIR allows us to determine the transmitted power at each frequency point in the absorption when the gas is introduced into the gas cell (see Appendix B for a description of gas cell measurements), and change in the integrated power can be calculated. With such a methodology, we first test the TPP-WS-EM designed for CO_2 sensing (Figure 6.4d). By integrating the emitted power between 1500

cm^{-1} and 3000 cm^{-1} we determine that the power change from 0 to 50 ppm of CO_2 is 0.3%. Note that the averaged absorption between 2232 and 2397 cm^{-1} , which is the absorption band of CO_2 , is 0.75%, and such an absorption rate comes from the gas cell optical length (15 cm) and gas concentration. Therefore, even with such a proof-of-concept sample, which only contains three-dielectric-layers, we are still able to approach the fundamental limit.

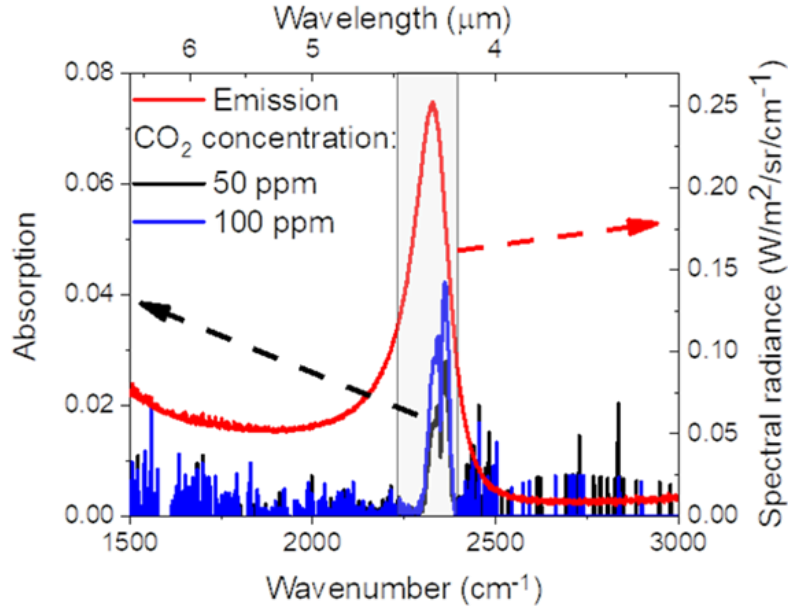


Figure 6.6: Measured absorption spectra of CO_2 at different concentration overlapped with the emission profile of TPP-WS-EM at 250°C . The shadowed region is the absorption band of CO_2 , determined from a NIST dataset.

6.3 Conclusions

Despite the limited precision of individual layer thicknesses during film growth and the material losses associated with the AlO_x , our experimental results demonstrate the power and potential of inversely designed TPP-WS-EMs, making them suitable for a variety of applications. In these demonstrations we have designed and grown samples with very few DBR layers (< 7). However, to demonstrate further the potential of the inverse design of TPP-WS-EMs, we expand the design capabilities by utilizing a Ge/ZnSe DBR with 29 layers on a bilayer of CdO. Therefore, the ‘metal’ layer becomes a bilayer film with a more tailorable optical impedance. This additional design freedom allows for the realization of Tamm plasmon modes supported at a single frequency with Q-factors varying from 26 to 10,127 (Figure 6.7a). Here, we not only calculate record high

Q-factors for Tamm plasmons but demonstrate that an extremely large range of Q-factors can be realized. We also illustrate a multi-peak design, exhibiting three emission peaks with significantly varying linewidths: one broad (Q-factor=25) peak and two sharp (Q-factor = 37 and 145) peaks. This sort of variable WS-EM designs can be of interest for free-space communication at several channels with different bandwidths, and spectral barcoding, yet has not been demonstrated or proposed presumably due to the significant design challenges this entails. Although the task is extremely challenging, the emissivity spectrum of our TPP-WS-EM can be matched to the target exceptionally well, with only minor discrepancies (Figure 6.7b). Again, owing to the widely tunable plasma frequency of CdO, a TPP-WS-EM with absorption peaks spanning from telecommunication to the LWIR can be realized. Here, we show a single design featuring three isolated emissivity peaks at LWIR (1200 cm^{-1}), MIR (2700 cm^{-1}) and telecommunication ($1.55\text{ }\mu\text{m}$) wavelengths simultaneously (Figure 6.7c), again demonstrating unprecedented spectral control. Finally, we emphasize the potential of TPP-WS-EMs in more advanced NDIR applications. As an example, we realize an inversely designed TPP-WS-EM that matches the absorption spectrum of the greenhouse gas NO (Figure 6.7d) with a great deal of accuracy. Note that exceptional matching is achieved to both the positions of the main features as well as the amplitudes, with undesirable features being greatly suppressed. Although we only provide a match to NO in the figure here, we employed the same approach to match the absorption spectra of other greenhouse gases such as CO, O₃, NH₃, and CH₄. The parameters of the designed films in figure 6.7 as well as the designs for the greenhouse gases listed above can be found in appendix A.

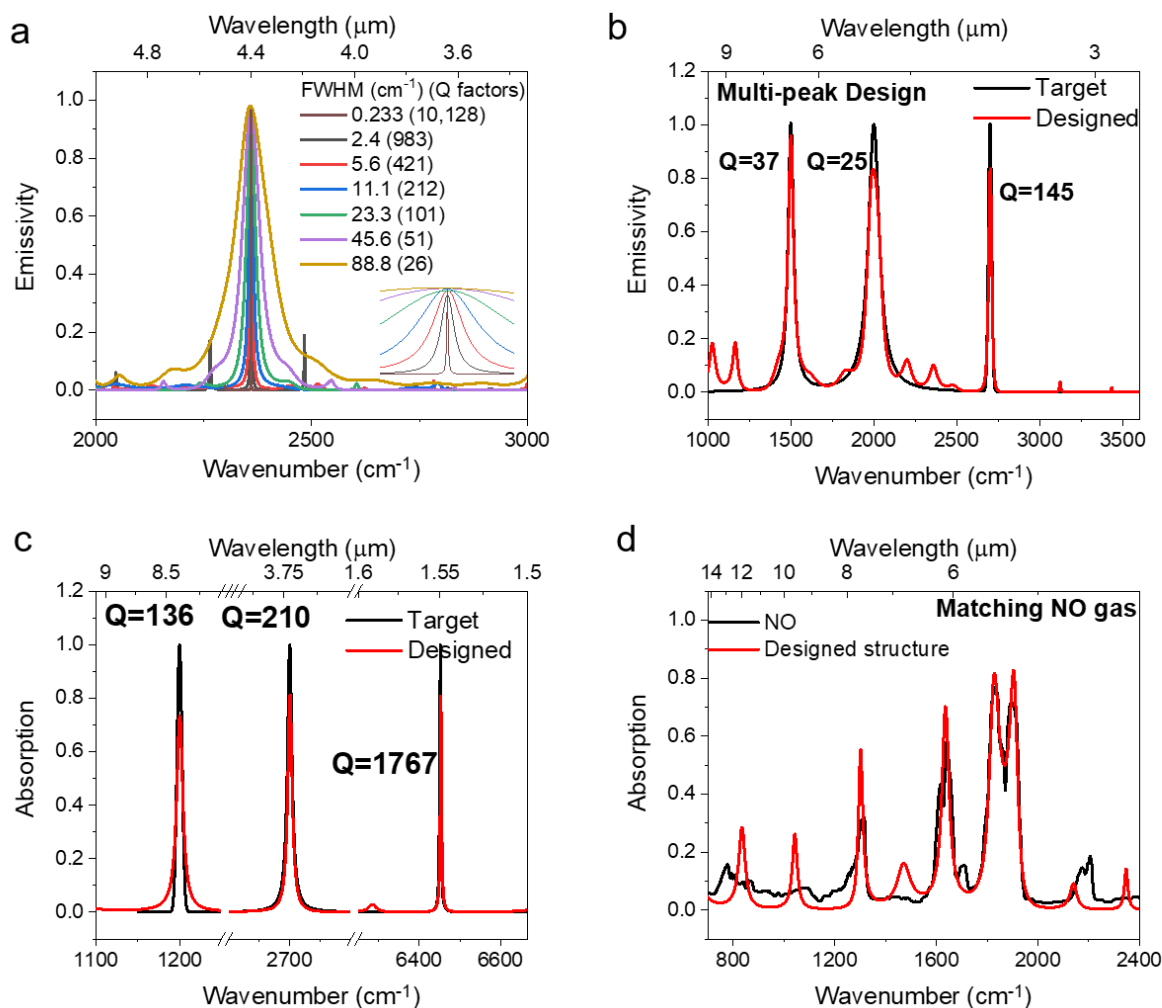


Figure 6.7: a) EMs targeting at single frequency with different Q-factors. b) multiple-peak TPP-WS-EM. c) One TPP-WS-EM featuring absorption at LWIR, MWIR and telecommunication simultaneously. d) Matching the absorption spectrum of NO gas for filterless NDIR.

In conclusion, we experimentally validate the broad functionality of TPP-WS-EMs enabled by the combination of inverse design and tunability of CdO plasmon frequency. With the SGD, the structure of the TPP-WS-EMs can be designed efficiently (minutes on a consumer-grade desktop) with high freedom. Equipped with the optimization method, we experimentally demonstrated TPP-WS-EMs for filterless NDIR of CO_2 and N_2O , free-space communication in the MIR (Q=128) and LWIR (Q=16), with excellent agreement between experiments and simulations. Further, we propose designs for numerous applications from the LWIR to telecommunication ($1.55 \mu\text{m}$) wavelengths, including single-peak emission with various Q-factors (from 28 to 10,000), multi-peak emission for free-space communication and NDIR for gas with

extremely complicated absorption spectra, demonstrating deterministic spectral control. Empowered by our algorithm and the tunability of CdO, the TPP-WS-EMs shows a singularly wide functionality, and they can be fabricated at low-cost at wafer-scale, providing a cost-effective, wafer-scale and lithography-free solution for numerous applications in the MIR. Future work will be focused on optimizing the material growth process in order to increase the precision of individual layer thicknesses and realize some of the more advanced designs provided in Figure 6.7. We will also investigate potential routes towards active tunability of these Tamm plasmon devices by incorporating phase change and ferroelectric materials into the DBR stack or by actively tuning the carrier density of the metal layer.

Chapter 7

7. Spectroscopic Investigation of Hyperbolic Resonances in Monolithic, Homoepitaxial CdO Superlattices

7.1 Introduction

One of the primary goals of nanophotonics is confining the free-space wavelength to dimensions far below the diffraction limit. Past work on dielectric metasurfaces has relied on high-index^{185–188} and dispersive materials¹⁶¹ in order to confine light sub-wavelength scale Mie resonators. However, here the wavelength, and therefore the resonator dimensions, is diffraction-limited as the wavevector ($k = 2\pi/\lambda$) is constrained by the closed isofrequency contour, with a maximum amplitude dictated by the real part of the permittivity $Re[\epsilon]$.

Alternatively, one could achieve further confinement of light by coupling to surface polariton modes in materials with a negative real permittivity. Examples include metals and doped semiconductors, which support both propagating and localized SPP modes at the material-air interface at frequencies less than the plasma frequency. However, the maximum SPP wavevector, and therefore optical confinement, is limited by the elevated imaginary permittivity of plasmonic materials. Polar dielectrics also exhibit a negative permittivity between the TO and LO phonon frequencies, a spectral region referred to as the Reststrahlen band. SPhPs are supported within this spectral range which exhibit narrower linewidths than SPPs due to the long scattering time of optic phonons. The optical field confinement (decreased mode volume) provided by SPP and SPhP-supporting films and structures have been used to increase the coupling strength to emitters and absorbers, enhancing emission/absorption rates and achieve modal strong coupling as was discussed in chapter 3.

In extremely anisotropic materials where the in- and out-of-plane components of the permittivity tensor are opposite in sign, the isofrequency contour becomes an unbounded hyperboloid (Fig. 7.1a and 7.1b) with a dispersion given by

$$\frac{k_z^2}{\epsilon_{x,y}(\omega)} + \frac{k_{x,y}^2}{\epsilon_z(\omega)} = k_o^2 \quad (1)$$

where $k_o = \frac{\omega}{c}$, $\epsilon_{x,y}(\omega)$ and $\epsilon_z(\omega)$ are the in- and out-of-plane components of the dielectric tensor, and $k_{x,y}$ and k_z are the propagation constants oriented in- and out-of-plane. For simplicity we assume uniaxial symmetry, therefore the in-plane dielectric tensor components are equivalent. Due to the shape of the isofrequency contour, these materials are referred to as hyperbolic, and sometimes as indefinite, materials. The hyperbolic modes supported by these materials exhibit extreme confinement of the optical field to the film volume, a result of the unbounded dispersion. The extreme confinement of light achieved using hyperbolic modes can opens the door to applications such as sub-diffraction and high-resolution imaging as well as sub-diffraction optical lithography. The magnitude of the wavevector is limited only by the optical losses (in natural hyperbolic materials), therefore if $Im[\epsilon] \rightarrow 0$, the magnitude of the wavevector $|k| \rightarrow \infty$.

There are two types of hyperbolic modes: Type I and Type II.³¹ Type I hyperbolic modes are supported when one tensor component is negative ($\epsilon_z(\omega) < 0$) and the other two are positive ($\epsilon_{x,y}(\omega) > 0$), whereas Type II hyperbolic modes are supported when two tensor components are negative ($\epsilon_{x,y}(\omega) < 0$) and one is positive ($\epsilon_z(\omega) > 0$). Unlike conventional materials that have elliptical isofrequency contours and therefore no restriction on propagation direction, hyperbolic modes propagate within the material at a fixed angle (see inset of Figure 1a). This is due to the electric \vec{E} and magnetic \vec{H} fields being tangential to the isofrequency surface (insets of 7.1a and 7.1b). The resultant Poynting vector \vec{S} and group velocity (v_g) are then oriented orthogonal to the isofrequency surface, and therefore are oriented at a fixed angle with respect to the z-axis.

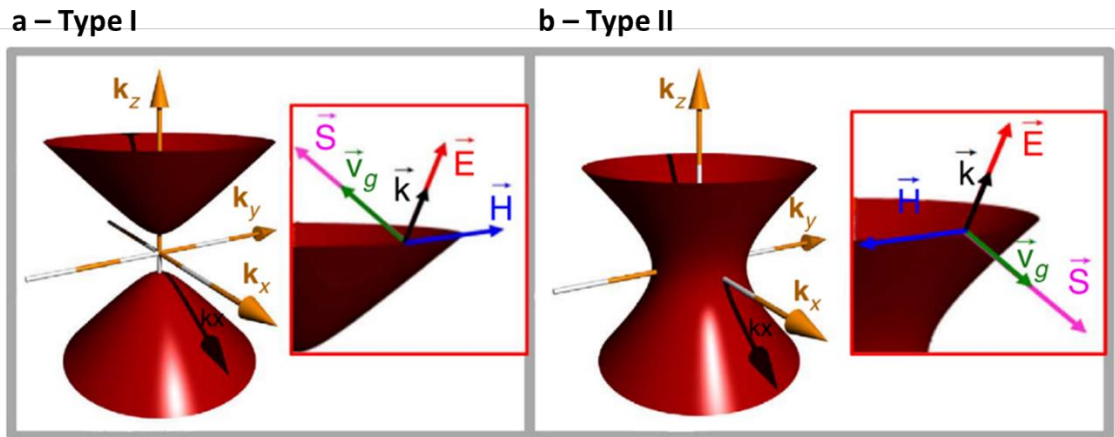


Figure 7.1: Isofrequency contour of a) Type I and b) Type II hyperbolic media. The arrows in the insets indicate the directions of the electric (E) and magnetic (H) fields, the Poynting vector (S), the momentum (k) and the group velocity (v_g) of the HP modes. Reprinted from [ref⁴¹].

In natural hyperbolic materials, the optical anisotropy is a result of a lack of symmetry in the crystal structure leading to phonon modes that are non-degenerate along different crystal axes. Therefore, the Reststrahlen bands along different crystal axes are offset from one another. Arguably the most widely studied natural hyperbolic materials is hBN, which has been studied using both near-^{189,190} and far-field¹⁰ techniques. Optical anisotropy can also be engineered through the fabrication of hyperbolic metamaterials (HMMs). There are two common HMM structures: 1) superlattices consisting of alternating dielectric and metallic layers¹⁹¹ and 2) dielectric matrices embedded with metallic rods¹⁹². In both cases the dimensions of the unit cell (layer thicknesses and rod geometry and periodicity, respectively) must be far smaller than the free space wavelength. Hyperbolic phenomena arise in these structures as a result of coupling between the SPPs at each metal film/structure interface, resulting in collective, propagative modes within the volume of the film.

The extreme anisotropy in these materials opens the door to demonstrating interesting optical phenomena such as negative refraction³², sub-diffraction imaging¹⁹⁰, waveguiding and focusing^{189,193}, and a large photonic density of states (PDOS) enhancement.^{194,195} This PDOS enhancement can be utilized to engineer the spontaneous emission of a quantum emitter, such as the emission from interband transitions supported by MQW structures.¹⁹⁶ It can also be used to engineer thermal emission. For example, theory has shown that HMMs are capable of achieving Super-Planckian thermal emission in the near-field^{197,198} which is attractive for enhancing the performance of thermophotovoltaic (TPV) devices. Further, an enhancement in the PDOS would also enhance the emission into the far-field which, if occurring within the atmospheric transparency bands (3 – 5 μm and 8 – 14 μm), could be useful for radiative cooling. In this chapter we demonstrate that monolithic, homoepitaxial (interfaceless) HMMs can be grown by modulating the carrier density of CdO during film growth.

7.2 CdO Hyperbolic Metamaterials

HMMs utilizing traditional metals are capable of supporting hyperbolic modes within the visible and NIR. However, due to the fixed, high carrier densities of these metals, the real permittivity (ϵ_m) becomes highly negative in the MIR. The large mismatch between $|\epsilon_m|$ and the permittivity of commonly used relatively non-dispersive dielectrics ($|\epsilon_d|$) leads to hyperbolic

resonances not being able to be supported in these metal-dielectric superlattices. In addition, the elevated imaginary permittivity of metals in the MIR results in high optical losses, diminishing their utility in this spectral range. In HMMs, these losses manifest as increased linewidths and a reduction of the maximum achievable in-plane wavevector (k_{\parallel}) in the hyperbolic dispersion.

Consequently, a lot of attention has been placed on finding alternatives to traditional metals for HMMs in the MIR to FIR. One option that has been proposed is to utilize polar dielectrics, such as SiC, which behave optically as a metal between the TO and LO phonon frequencies (the Reststrahlen band). The low optical losses of these materials allow for hyperbolic modes to be supported at large values of k_{\parallel} resulting in an extreme compression of the polaritonic wavelength and high PDOS. However, as is discussed in chapter 1, the TO and LO phonon frequencies are set by fundamental properties of the crystal lattice and exhibit little tunability. Further, TO and LO phonon frequencies occur in LWIR to FIR and are therefore inaccessible within the 3 – 5 μm atmospheric transparency band, which is important for potential radiative cooling applications. Further, SPhP-based HMMs would not be efficient for TPV applications which require high temperatures and thermal emission from $\sim 1 - 3 \mu\text{m}$.

Doped semiconductors have been investigated recently as another strong candidate for IR HMMs due to their relatively low optical losses and tunable IR plasma frequencies. One of the proposed advantages of semiconductor-based HMMs is that one could take advantage of the enhanced PDOS associated with HMMs by imbedding MQWs with ISTs (or other devices) within the hyperbolic bands of the HMMs resulting in a significant enhancement in the emission output.¹⁹⁶ To this date there have been several reports of HMMs that rely on the heteroepitaxial growth of doped (metal) and undoped (dielectric) semiconductor layers, including Si-doped binary and tertiary III-V semiconductors^{32,143}, as well as TCOs such as lattice-matched doped ITO and In_2O_3 .³³ However, in order to suppress scattering and strain-induced losses, the options for layer and substrate materials in these HMMs is limited to those that are lattice-matched, dramatically reducing the design flexibility. Further, due to the extremely small effective masses (and/or optical mobilities) of these materials, these structures often suffer from high Ohmic losses at elevated carrier densities.

The requirement of lattice matching between metal-dielectric layers can be relaxed by creating a single material HMM, where the superlattice consists of alternating doped/undoped

layers of the same material. This allows for greater potential design flexibility and wavelength coverage while also simplifying the growth process. In these single material HMMs the carrier confinement within as-grown layers is enabled by band bending at the doped/undoped layer ‘interfaces’. This is contrasted with the doped semiconductor HMM heterostructures where carrier confinement is ensured by sharp changes in the optical bandgap. Single material HMMs were first demonstrated using alternating layers of doped and undoped InAs.¹⁹⁹ However, due to constraints on the plasma wavelength of InAs (and other III-V semiconductors), these structures are not capable of supporting hyperbolic modes at wavelengths below $5.5 \mu\text{m}$ leaving a large portion of the MIR (including the $3 - 5 \mu\text{m}$ atmospheric transparency window) and NIR uncovered.⁴⁷ Further, Poisson calculations of these structures reveal high carrier diffusion between layers, with the carrier distribution deviating significantly from the ideal square wave distribution. Thus, the performance of the devices differed from what would be anticipated using effective medium theory (EMT).

Another exciting candidate for realizing single-material HMMs is n-doped CdO. For one, the plasma frequency of CdO has been shown to be tunable throughout the MIR and into the NIR ($2 - 9 \mu\text{m}$) through control over the carrier density during film growth^{40,184}, all while maintaining consistently high mobility values ($\mu_{Hall} = 300 \text{ cm}^2/\text{V} - \text{s}$) as is described in detail in chapter 2. Further, investigations of the thermal transport properties of CdO superlattices have revealed that despite the lack of interfaces, the thermal conductivity can be modelled assuming sharp interfaces between high and low doped layers.¹⁴⁰ These measurements (coupled with Poisson calculations) imply that the carrier confinement is extremely high in multilayer CdO films. For this reason, multilayer CdO films have shown to be a promising platform for realizing a number of exciting optical effects, such as SPP-ENZ strong coupling and multi-frequency thermal emission from multilayer ENZ-supporting CdO films. Finally, high-quality CdO film growth can be achieved through HIPIMS sputtering, with the optical properties surpassing those of MBE-grown CdO films.

In this chapter we demonstrate that monolithic, homoepitaxial CdO HMMs are a powerful platform for realizing tunable hyperbolic modes from the NIR through the MIR. By controlling the carrier densities and layer thicknesses during film growth we achieve a high degree of tunability over both Type I and Type II hyperbolic modes, and achieve significant compression of

the free-space wavelength. First, however, in the following section we discuss the EMT which, due to the high carrier confinement of these CdO HMMs, is successful in modelling the optical response of these structures.

7.2.1 Effective Medium Theory – 1D Metamaterials

A 1D metamaterial consisting of alternating, subwavelength thickness layers ($k_{x,y}, k_z \ll 1/t_{m,d}$) can be treated as a homogenous medium with a uniaxial dielectric tensor by employing an EMT. By controlling the layer thicknesses and individual layer properties (carrier density for doped semiconductors) the anisotropic optical response of these 1D metamaterials can be engineered. The effective in- and out-of-plane permittivity for an HMM with arbitrary number of layers (i) with unit cell fill fraction f_i and dielectric function $\varepsilon_i(\omega)$ is can be determined from the following expressions.²⁰⁰

$$\varepsilon_{x,y}(\omega) = \sum_i f_i \varepsilon_i(\omega) \quad (2)$$

$$\varepsilon_z^{-1}(\omega) = \sum_i f_i \varepsilon_i^{-1}(\omega) \quad (3)$$

It is most common for planar HMMs to utilize a simple two-material unit cell (metal and dielectric). For these systems the effective in and out-of-plane permittivity simplifies to

$$\varepsilon_{x,y}(\omega) = f \varepsilon_m(\omega) + (1 - f) \varepsilon_d(\omega) \quad (4)$$

$$\varepsilon_z(\omega) = \frac{\varepsilon_m(\omega) \varepsilon_d(\omega)}{f \varepsilon_d(\omega) + (1-f) \varepsilon_m(\omega)} \quad (5)$$

Where $f = t_m/(t_m + t_d)$ is the filling fraction of the metal layer. $\varepsilon_m(\omega)$ and $\varepsilon_d(\omega)$ are the dielectric functions of the metal and dielectric layers, respectively.

For the monolithic CdO HMMs, the layer with the higher plasma frequency (carrier density) acts as the ‘metal’ and the layer with the lower plasma frequency acts as the ‘dielectric’. Here it is assumed that the carrier distribution throughout the material follows a square wave function. The dielectric functions of the high and low doped layers are calculated using the Drude model along with previously reported values of the high frequency permittivity and effective mass. From the calculated effective dielectric functions, the resultant optical response can be divided into four different regions: effective metallic ($\varepsilon_{x,y}(\omega) \& \varepsilon_z(\omega) < 0$), effective dielectric ($\varepsilon_{x,y}(\omega) \& \varepsilon_z(\omega) > 0$), Type I ($\varepsilon_{x,y}(\omega) > 0 \& \varepsilon_z(\omega) < 0$), and Type II ($\varepsilon_{x,y}(\omega) < 0 \& \varepsilon_z(\omega) >$

0) hyperbolic. For a CdO HMM with a particular combination of carrier densities, at frequencies less than the low-doped layer plasma frequency, the effective permittivity is negative in all directions regardless of the filling fraction. In this effective metal regime, the CdO HMM is capable of supporting propagating SPP modes at the CdO-air interface. Conversely, at frequencies above the plasma frequency of the high-doped layer the effective dielectric function is always positive regardless of the filling fraction. However, between the two plasma frequencies the optical behavior is dependent on the fill fraction. When the high and low-doped layer thicknesses are equal ($f = 0.5$), the real part of the effective dielectric functions cross through zero (and therefore change signs) at the same frequency, resulting in no spectral separation between the Type I and II hyperbolic bands. If the low-doped layer is thicker than the high-doped layer ($f < 0.5$) a region of effective dielectric behavior opens up between the two hyperbolic bands. Alternatively, if the high-doped thickness is greater than the low-doped film thickness ($f > 0.5$) a similar spectral band of metallic behavior opens up between the hyperbolic bands. This is illustrated in effective dielectric functions and phase diagram provided in figure 7.2c.

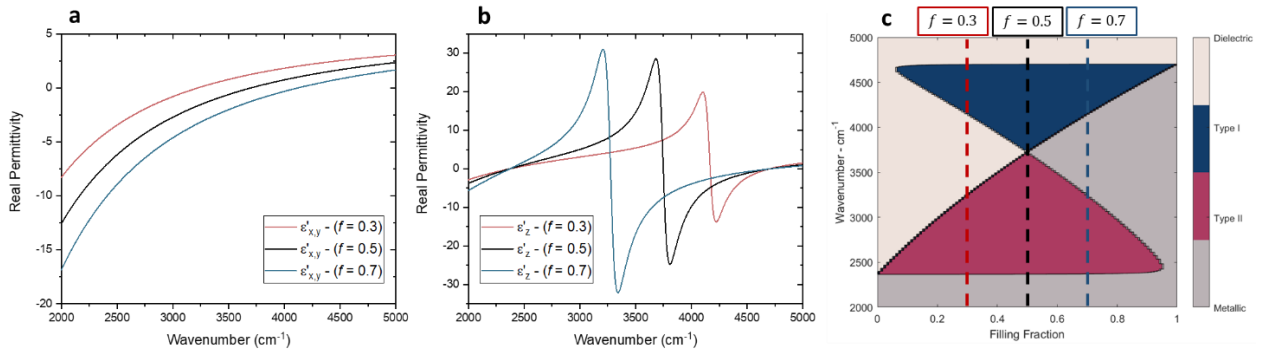


Figure 7.2: EMT-calculated in- ($\epsilon_{x,y}$) and out-of-plane (ϵ_z) real permittivity of CdO HMMs with $f = 0.3$ (red line), $f = 0.5$ (black line), and $f = 0.7$ (blue line) are displayed in a) and b), respectively. The carrier densities of the high and low-doped CdO layers are $N_d = 3 \times 10^{20} \text{ cm}^{-3}$ and $N_d = 3 \times 10^{19} \text{ cm}^{-3}$. c) Phase-diagram of a CdO HMM with the high and low-doped CdO layers of $N_d = 3 \times 10^{20} \text{ cm}^{-3}$ and $N_d = 3 \times 10^{19} \text{ cm}^{-3}$. The dashed lines are the filling fractions of the dielectric functions displayed in a) and b).

The accuracy of EMT is a reliant on the individual layer thicknesses being much thinner than the polaritonic wavelength. Therefore, in the absence of carrier diffusion, quantum, and nonlocal effects, the thinner the individual layers of the superlattice the less the optical response deviates from EMT. For example, the reflectivity map in figure 7.3a shows the dispersion of the

CdO HMM described in figure 7.2 with $f = 0.5$ calculate using EMT. Owing to the low optical losses of CdO, the hyperbolic modes extend to very large in-plane wavevectors (reciprocally to extremely small polaritonic wavelength). If the effective medium were replaced with an equivalent superlattice composed of 200 nm thick high and low doped CdO layers. Although the response at low in-plane momentum is equivalent to the calculated dispersion of the effective medium, as the dispersion extends to higher in-plane momentum (and polaritonic wavelength approaches the thickness of the individual layers) the response deviates from the dispersion calculated using EMT.

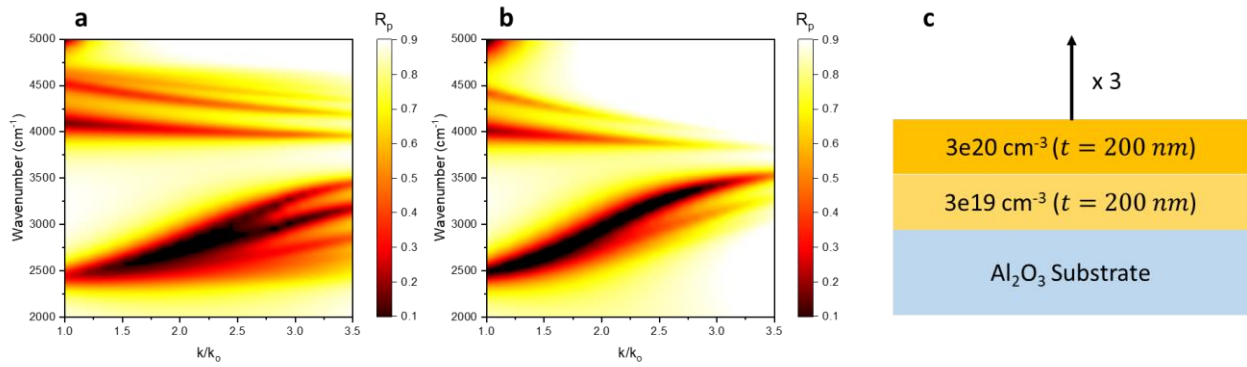


Figure 7.3: a) Calculated reflectance maps for the structure shown in c) using EMT. b) Calculated reflectance map of the structure in c) where $t = 200$ nm.

7.2.2 Attenuated Total Reflectance Measurements of CdO Hyperbolic Metamaterials

As is described in section 1.2.3, there are two configurations for ATR measurements: Kretschmann and Otto configuration. When using these techniques to excite surface polariton modes it is necessary that there be a metal-dielectric interface at which the mode is supported. In Kretschmann configuration the mode is launched on the film interface opposite the prism, whereas in the Otto configuration the mode is supported in a dielectric gap between the prism and the film. Of course, when taking into account films grown on substrates, which are often dielectric, a real measurement could be a combination of both techniques.

Hyperbolic modes, on the other hand, are supported in the film bulk rather than at the surface. For this reason, the evanescent extent of these modes is very small and coupling to hyperbolic modes using the Otto configuration can only be done in very close proximity to the HMM film surface. However, past work from our group has shown that hyperbolic polaritons in

hBN flakes can be observed by placing a prism directly in contact with the flake using a Pike ATR objective (Ge Prism).¹⁰ In the following sections we have taken a similar approach and measured the CdO HMMs with the film directly in contact with the prism. Further, by employing an angle-dependent ATR rig (Pike Veemax) equipped with multiple prisms, CaF₂ ($n \sim 1.4$ in MIR) and ZnSe ($n \sim 2.4$ in MIR), we were able to map the polaritonic dispersion from $k_{\parallel}/k_o = 1$ to 1.8.

Index matching liquid (IML) ($n = 1.78$ at $\lambda = 589 \text{ nm}$, Cargille) was used between the prism and the film in order to ensure that optical contact was met. The refractive index of the IML in the MIR can be calculated from the Cauchy dispersion formula $n = A + B/\lambda^2 + C/\lambda^4$, with the coefficients A, B , and C can be found in data sheets provided by Cargille. The IML consists of sulfur suspended in a diiodomethane solution. For this reason, there is polarization-insensitive IR absorption associated with the diiodomethane that overlaps with our experimental data. In some cases, these absorption features can be easily normalized out by taking the ratio R_p/R_s , such as what was done in chapter 3 when measuring the dispersion of SPP-ENZ hybrid films. This was allowed because no polaritonic response was expected in s -polarization and therefore the only absorption in s -polarization would be due to the IML. However, since at low filling fractions the HMM behaves as a dielectric, it is expected to support s -polarized waveguide-like modes that overlap in frequency with p -polarized modes. Therefore, we were not able to avoid these absorption features when plotting the dispersion for these hyperbolic films. Figure 7.4, shows a spectrum of the IML with sapphire and Au as the backplane.

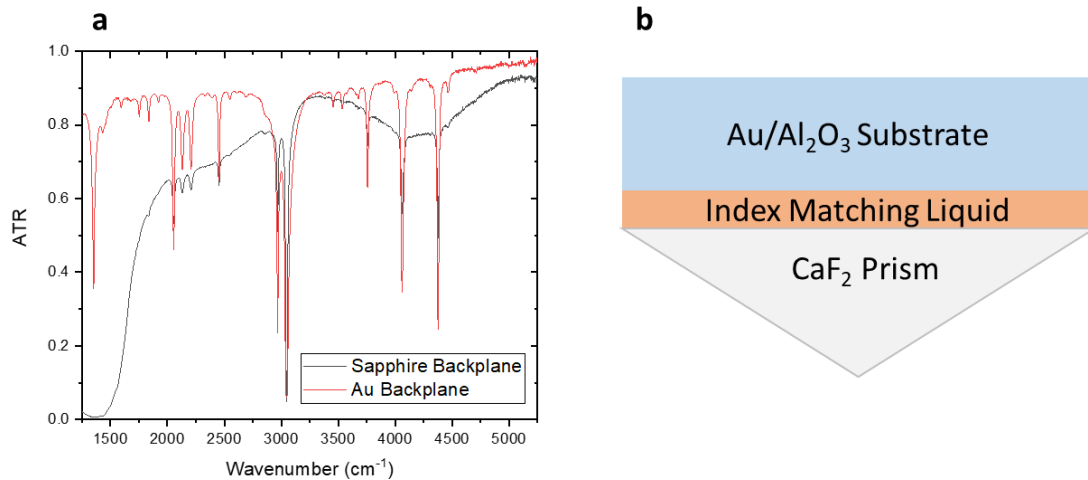


Figure 7.4: a) Kretschmann ATR measurement of the IML with a sapphire (black) and Au (red) backplane b) Diagram of measurement.

7.2.3 Role of CdO Hyperbolic Metamaterial Thickness

In order to determine the tunability of these CdO HMMs, several films of varying carrier densities, fill fractions, and overall thicknesses were grown and characterized using polarized ATR measurements as described in the previous section. The parameters of these films are summarized below in Table 7.1. The focus of this section will be on verifying the hyperbolic behavior within these CdO HMMs and discussing the role of the overall HMM thickness on the hyperbolic modes. In the sections that follow, we will demonstrate tunability through changes to the carrier densities and relative thicknesses of the low- and high-doped layers.

Table 7.1: Parameters of CdO HMM Films

Sample # (Dopant)	High – Doped N_d [cm^{-3}]	Low – Doped N_d [cm^{-3}]	High – Doped Thickness [nm]	Low – Doped Thickness [nm]	Filling Fraction	Overall Thickness [μm]
1 (Y)	2.4×10^{20}	9×10^{19}	50	50	0.5	1
2 (In)	3×10^{20}	3×10^{19}	100	100	0.5	1
3 (In)	3×10^{20}	3×10^{19}	100	100	0.5	1.5
4 (In)	3×10^{20}	3×10^{19}	140	60	0.7	1
5 (In)	3×10^{20}	3×10^{19}	60	140	0.3	1

The in- and out-of-plane dielectric functions of a CdO HMM stack with alternating $3 \times 10^{19} \text{ cm}^{-3}$ (low-doped) and $3 \times 10^{20} \text{ cm}^{-3}$ (high-doped) layers (2 and 3 from Table 7.1) and a fill fraction of $f = 0.5$ can be calculated using EMT (see figure 7.2). Note that the resultant dielectric function is significantly different than what would be expected if the carrier densities of the individual layers were simply averaged instead. Namely, if the optical properties of the homogenous film were an averaging of the contributions of the individual layers then the dielectric tensor would be isotropic with all components following the Drude dispersion, resulting in the film supporting an SPP mode alone. Instead, the engineered anisotropy results in Type II and Type I hyperbolic resonances being supported from 2450 cm^{-1} to 3750 cm^{-1} and 3750 cm^{-1} to 4600 cm^{-1} , respectively.

The hyperbolic behavior of these modes is evident from their polaritonic dispersion, which we have measured using angle-resolved ATR measurements (Figure 7.5a). Here, we again observe five modes. First, we see one Type II hyperbolic mode with a dispersion that blueshifts slightly at high in-plane momentum. If the dispersion were expended to even higher momentum, additional higher-order modes are expected to emerge similar to what is shown in Figure 7.3a of the previous section. Although we were able to observe the lowest order Type II mode begin to blue shift, we were unable provide sufficient auxiliary momentum to excite higher-order Type II hyperbolic modes in ATR measurements. However, by patterning these HMM films into arrays of resonators a further compression of the free-space wavelength and observation of high-order Type II modes can be observed. This will be the subject of future work. We also see four Type I modes, which disperse negatively with increased in-plane momentum.

Owing to the waveguide-like nature of hyperbolic modes, the propagation direction and frequency of hyperbolic modes are both tied to the thickness of the hyperbolic medium. Therefore, by changing the overall thickness of the CdO HMM, while keeping the fill fraction and carrier densities the same, the Type I and II modal locations are expected to shift within their respective bands. Indeed, this is what we observed in ATR measurements (Figure 7.5a) of a CdO HMM with an identical unit cell to the 1.5 μm film, but with an overall thickness of 1 μm (2 from Table 7.1). The direction that the Type I and Type II modes shifts with increased overall thickness is consistent with the group velocity of the different modes. Note that as the carrier densities of the constituent layers and fill fraction of these two films are the same, the phase diagrams (and ultimately the dielectric tensor) of these two films are identical. Therefore, the spectral locations and ranges of the Type II and Type I bands are not expected to change. In addition to the spectral shifts observed in the polaritonic dispersion, the thinner film is also shown to support one fewer Type I mode which is consistent with the thickness dependence calculated using TMM.

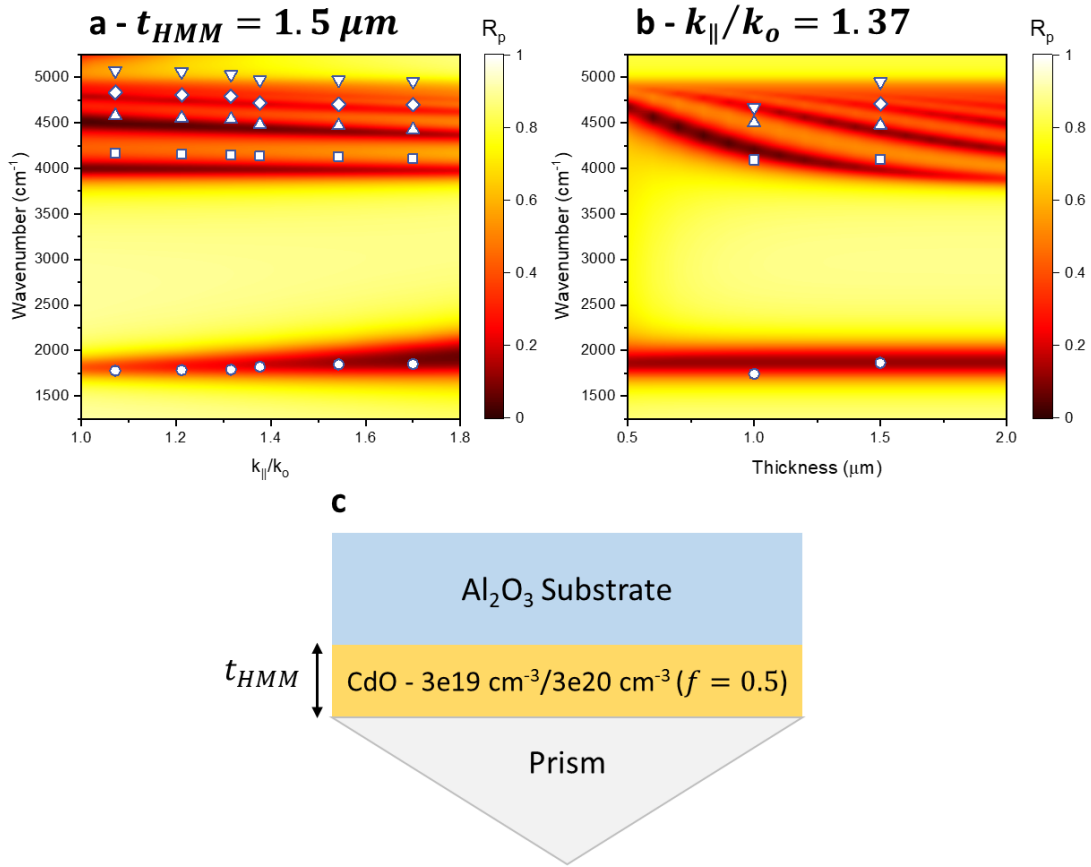


Figure 7.5: a) Dispersion of film in c) with $t_{HMM} = 1.5 \mu\text{m}$. b) Thickness dependence at constant angle ($k_{||}/k_o = 1.37$). The contour plots were calculated using TMM and the data points are from measurements.

7.2.4 Carrier Density Tunability of CdO Hyperbolic Metamaterials

In this section we will determine the role of the individual layer carrier densities in setting the ranges of the Type II and Type I hyperbolic bands. In order to explore the carrier density dependence on hyperbolic dispersion, two HMMs were grown (1 and 2 in Table 7.1) with identical overall thicknesses and fill fractions ($1 \mu\text{m}$, $f = 0.5$), but with varying individual layer carrier densities. The low- and high-doped layer carrier densities and thicknesses are defined in Table 7.1. Again, at this fill fraction the bandwidth of the Type II and Type I hyperbolic bands is maximized since there is no region of effective dielectric ($f < 0.5$) or metallic ($f > 0.5$) response between the bands.

In the limit as $f \rightarrow 0$, both the in- and out-of-plane components of the dielectric tensor will take on the dielectric function of the low-doped ('dielectric') layer alone $\varepsilon_{x,y}(\omega) = \varepsilon_z(\omega) = \varepsilon_d(\omega)$. Therefore, in this limit the film does not exhibit hyperbolic behavior and the metal-to-dielectric transition frequency is set by the plasma frequency of the low-doped layer. At non-zero fill fractions, the plasma frequency of the low-doped layer instead denotes the transition from the effective metal to the Type II hyperbolic regime (see Figures 7.6c and 7.6d). Therefore, by increasing (decreasing) the low-doped layer carrier density this transition will occur at a higher (lower) frequency. Note that this transition is set by the low-doped plasma frequency alone, and is therefore not impacted by the high-doped layer plasma frequency. The onset of Type II hyperbolic modes is identified by a highly absorptive feature in the spectral dispersion due to the large PDOS at the effective metal-Type II phase boundary (See reflectance maps in Figure 7.6a and 7.6b). As was discussed in the previous section, as k_{\parallel} is increased these modes will blue shift, a result of $v_g > 0$ for Type II modes, and higher-order modes will emerge in the polaritonic dispersion. As the carrier density is increased in the low-doped layer from $3 \times 10^{19} \text{ cm}^{-3}$ to $9 \times 10^{19} \text{ cm}^{-3}$, the transition from effective metal to Type II hyperbolic blueshifts from 1750 cm^{-1} to 3000 cm^{-1} .

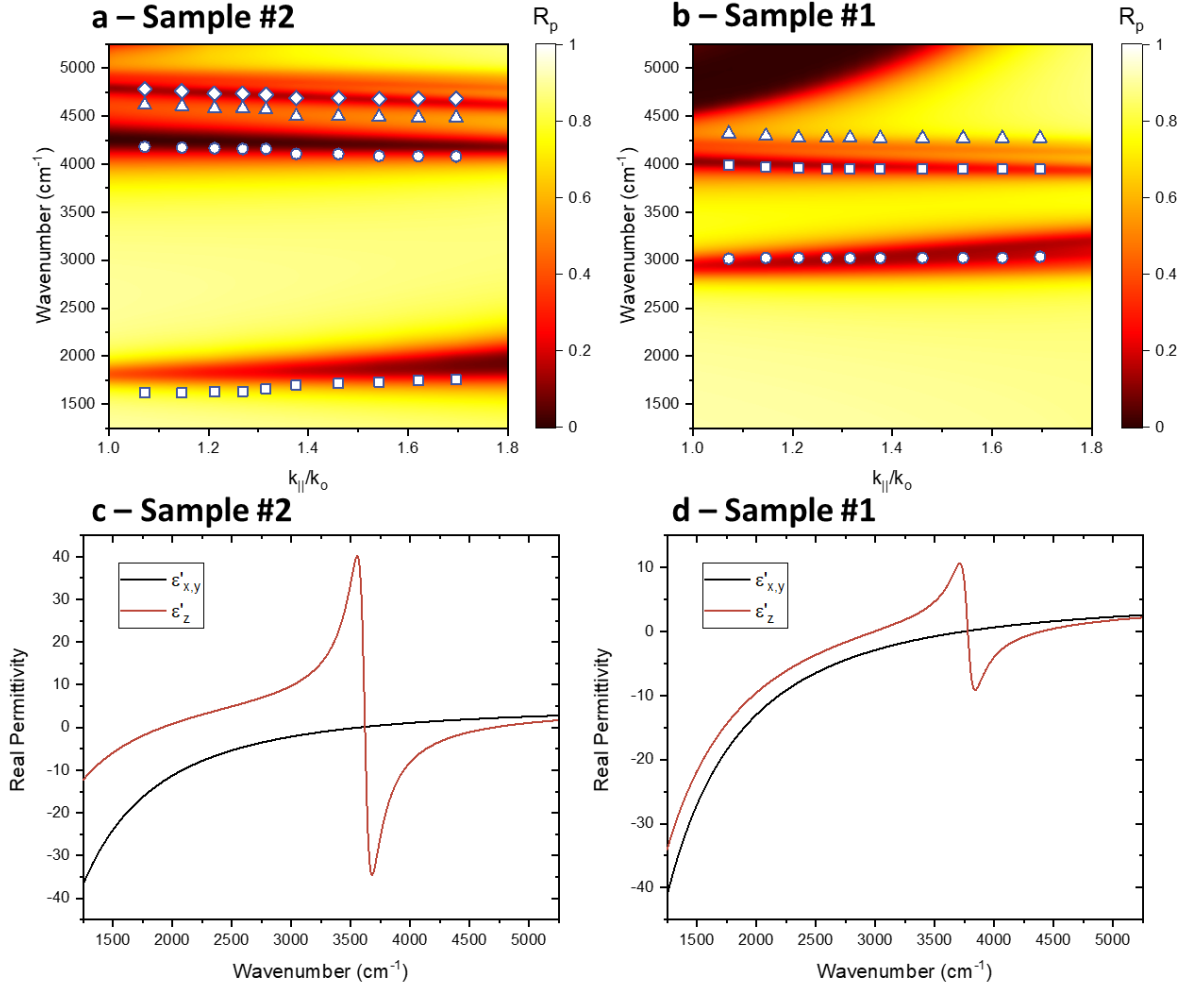


Figure 7.6: a) Dispersion relation of sample #2 from table 7.1 ($N = 3e19/3e20 \text{ cm}^{-3}$). a) Dispersion relation of sample #1 from table 7.1 ($N = 9e19/2.4e20 \text{ cm}^{-3}$). Contour plots are from TMM calculations and the measured values are included as data points overlaying the contour plots.

If instead $f \rightarrow 1$, all dielectric tensor components would converge to the high-doped layer dielectric function $\epsilon_{x,y}(\omega) = \epsilon_z(\omega) = \epsilon_m(\omega)$ and therefore the transition from metal to dielectric would occur at the high-doped layer plasma frequency (see phase diagram in Figure 7.2c). However, as the fill fraction is decreased the high doped layer plasma frequency would instead mark the transition from the Type I hyperbolic band to dielectric behavior. Therefore, the high frequency cut off of the Type I band is not impacted by the low-doped layer plasma frequency and can be controlled independently by changing the carrier density of the high-doped layer. This is verified in our ATR measurements where the upper bound of the Type I band is shows a strong

correlation to the high-doped layer carrier density, increasing from 4250 cm^{-1} for sample #1 (Figure 7.6b), to 4750 cm^{-1} for sample #2 (Figure 7.6a). Note that at large (small) fill fractions the outsized influence of the high (low)-doped layer results in Type II (Type I) hyperbolic modes not being supported.

For an HMM film with $f = 0.5$, the transition from Type II to Type I hyperbolic bands marks the frequency at which the in- and out-of-plane components of the dielectric tensor change in sign. Therefore, the frequency of this transition can easily be determined by calculating the frequency of the zero crossing of the in-plane dielectric function $\epsilon_{x,y}(\omega) = 0$. From equation 4, it is clear that this condition is met at an average of the low- and high-doped layer plasma frequencies $\omega_{p(x,y)} = 0.5[\omega_{p,d} + \omega_{p,m}]$. At fill fractions above and below $f = 0.5$, both hyperbolic bands contract giving way to an effective metal or effective dielectric band, respectively. These regions will be discussed further in the following section.

Finally, the individual layer thicknesses within all of the fabricated CdO HMMs are deeply subwavelength while also being much thicker than the carrier depletion/accumulation layer ($\sim 5 \text{ nm}$) that forms at the CdO interfaces. Therefore, the hyperbolic behavior of the CdO HMM films is not impacted by the change in layer thickness seen here. Samples #2 (Figure 7.6a) was grown with 10 individual layers with thicknesses of 100 nm , giving a total thickness of $1 \mu\text{m}$. Sample #1 (Figure 7.6b), on the other hand, had an overall thickness that was the same ($1 \mu\text{m}$) but consisted of 20 total layers with thicknesses of only 50 nm . In both cases, the measured dispersion agrees very well with TMM calculations of a CdO HMM with a dielectric function calculated using EMT. We discussed the breakdown in EMT as a result of increased layer thicknesses in section 7.2.1.

7.2.5 Filling Fraction Tunability of CdO Hyperbolic Metamaterials

In the previous section we demonstrated that broad spectral tunability of hyperbolic behavior can be achieved in CdO HMMs through changes to the individual layer carrier densities. Namely that the lower bound of the Type II and upper bound of the Type I hyperbolic bands can be controlled by tuning the low-doped and high-doped CdO layer carrier densities. Although the carrier densities differed between samples, the overall film thickness and the fill fraction were kept constant ($f = 0.5$). Therefore, as described in the previous section, there was a direct transition from Type II to Type I hyperbolic bands at the average plasma frequency of the two layers

($\omega_{p(x,y)} = 0.5[\omega_{p,d} + \omega_{p,m}]$). However, when the low- and high-doped layer thicknesses are not equal, a spectral range of anisotropic dielectric or anisotropic metallic behavior opens up within the dispersion of the HMM. In this section we discuss the properties of these two regions. Note that there is a cut off for Type II hyperbolic modes at high fill fractions ($f > 0.92$) and for Type I hyperbolic modes and low fill fractions ($f < 0.08$) which is due to optical losses within the HMM. In the absence of losses, both hyperbolic bands would extend across the phase diagram and therefore be supported for all fill fractions besides $f = 0$ and $f = 1$.

The out-of-plane dielectric function of a CdO HMM is represented by a single Lorentzian that manifests between the plasma frequencies of the two individual layers, very similar to the dispersive behavior near the optic phonons of polar dielectrics. The Type II hyperbolic band is a result of the increasing, positive region of $\epsilon_z(\omega)$ overlapping with a negative range of $\epsilon_{x,y}(\omega)$. When the low-doped layer thickness is greater than the thickness of the high-doped layer, the Lorentzian in $\epsilon_z(\omega)$ blueshifts whereas the zero crossing of $\epsilon_{x,y}(\omega)$ redshifts, resulting in the emergence of an effective anisotropic dielectric region. Within this region, the HMM film supports both *s*- and *p*-polarized slab waveguide modes. Further, frequency tunable Mie resonances can potentially be supported in subwavelength resonators fabricated using focused ion beam milling or a lithographic approach. Huygens modes could potentially be supported in these structures through careful control over the aspect ratio, resulting in near-unity absorption/emissivity as has been shown for 3C-SiC resonators in the highly dispersive spectral range just below the TO phonon.¹⁶¹

In order to confirm the expected dielectric behavior within CdO HMMs with $f < 0.5$, we grew a sample with a low-doped carrier density of $3 \times 10^{19} \text{ cm}^{-3}$ and thickness of 140 nm, and high-doped layer carrier density of $3 \times 10^{20} \text{ cm}^{-3}$ and thickness of 60 nm (Sample #5 from table 7.1). Therefore, the carrier densities of the individual layers and the overall HMM thickness is the same as sample 2, however the fill fraction is reduced to $f = 0.3$. We then collected the *s*- and *p*-polarized dispersion using ATR. In *p*-polarization, the absorption feature at the effective metal-Type II transition occurs at nominally the same frequency as what was seen in the $f = 0.5$ film, as expected. We also observe 1 Type I hyperbolic resonances, 1 fewer than the $f = 0.5$ due to the reduction in the bandwidth. In *s*-polarization, we observe one dielectric resonances within the

spectral range separating the hyperbolic bands. (Figure 7.7a) The hyperbolic and dielectric resonances are labelled on the figure.

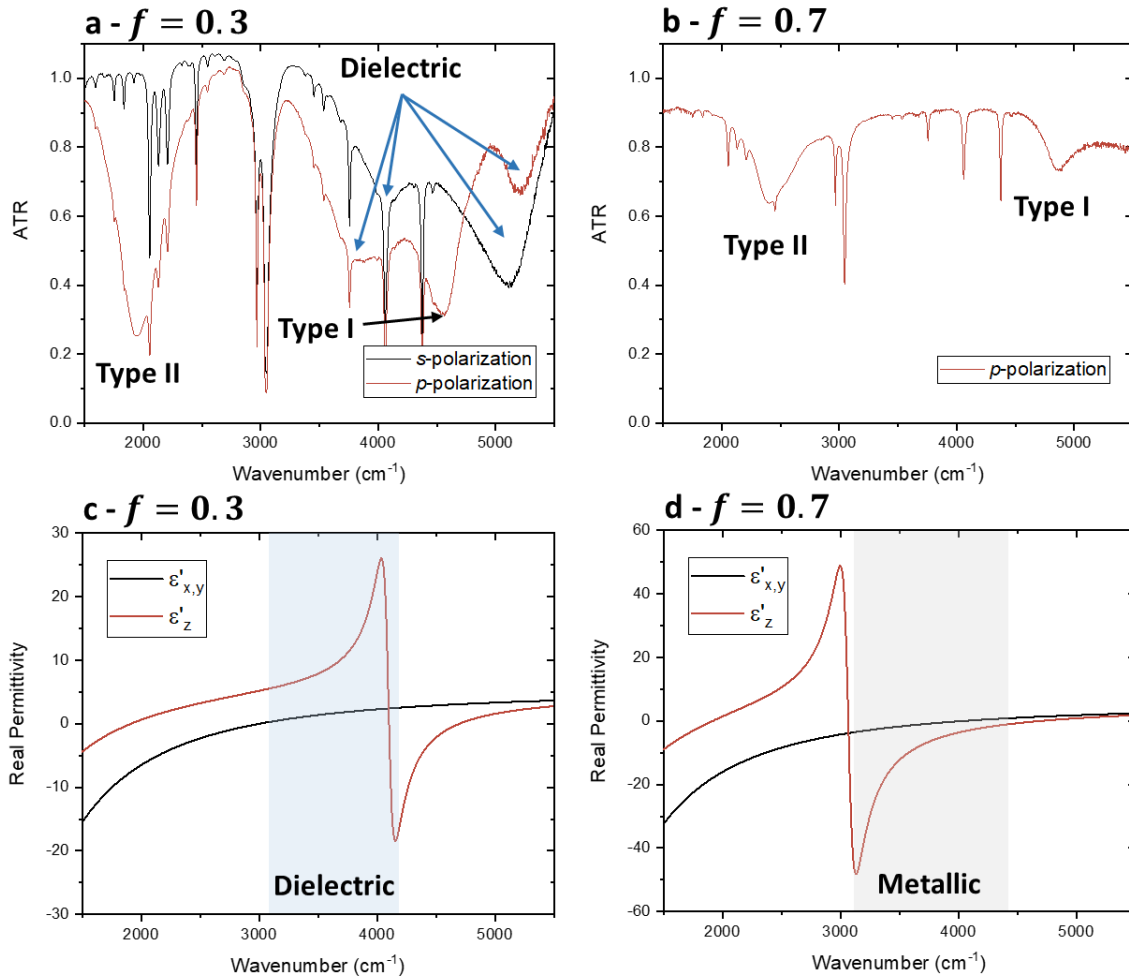


Figure 7.7: a) s- (black line) and p- (red line) polarized ATR measurements showing resonances supported in the dielectric regime of a CdO HMM with $f = 0.3$. The effective dielectric function of this film is displayed in c). b) p- (red line) polarized ATR measurements showing resonances of a CdO HMM with $f = 0.7$. The response between the Type II and Type I hyperbolic band is featureless (besides the absorption from the IML). The effective dielectric function of this film is displayed in d).

If instead the thickness of the high-doped layer were larger than the thickness of the low-doped layer, there would be a region within the dispersion of effective metallic behavior separating the Type II and Type I band. In this region, hyperbolic and dielectric resonances would not be supported. However, for sufficiently thin films ($t_{film} < 1 \mu m$), propagating SPP modes are supported at the HMM-air interface. These can be observed in ATR measurements where the

HMM film is face-up and the substrate is in contact with the prism (see section 7.2.6). If instead the film was measured with the HMM in contact with the prism, the effective metallic region of the dispersion would be featureless (Figure 7.7b). Here we measured an HMM with the same overall thickness ($1 \mu\text{m}$) and low- and high-doped layer carrier densities, but with a fill fraction of $f = 0.7$ (Sample #4 in table 7.1). The behavior within the Type II and Type I hyperbolic bands remains nominally the same as for the $f = 0.3$ film (See Figure 7.7a), however as was stated before the effective metal regime (spanning from 3100 cm^{-1} to 4450 cm^{-1}) is featureless.

7.2.6 Surface Plasmon Polariton – Hyperbolic Plasmon Polariton Strong Coupling

Throughout this chapter we have been measuring these CdO HMM films in Kretschmann configuration ATR measurements by placing the HMM directly in contact with the prism (substrate facing away from the prism). If instead the ATR measurements were performed with the substrate in contact with the prism (CdO facing away from prism, Figure 7.8d), an interesting change to the resultant dispersion is observed. Namely, in addition to supporting volume-confined hyperbolic modes the CdO HMM also supports an SPP mode at the HMM-air interface. In an isotropic system where $\varepsilon_x, \varepsilon_y, \varepsilon_z = \varepsilon_{\parallel}$, the dispersion of this mode would follow that expected of an SPP mode $k_{\parallel} = k_o \sqrt{\frac{\varepsilon_{\parallel}}{\varepsilon_{\parallel} + 1}}$. However, due to the anisotropy of the CdO HMM, strong coupling is observed between the SPP and Type II hyperbolic modes with an anticrossing emerging at the effective metal-Type II phase boundary (Figure 7.8). A similar interaction is expected in the ATR configuration used in the other sections of the chapter (prism-CdO HMM-substrate), however due to the decreased slope of the light line in the sapphire substrate the spectral overlap of the SPP mode with the hyperbolic modes would be decreased and the anticrossing would occur at much higher momentum.

We provide an example of SPP-Type II hyperbolic strong coupling in Figure 7.8, where an anticrossing is observed in the calculated polaritonic dispersion of a CdO HMM film with an overall thickness of 500 nm . For the films studied earlier in this chapter, the upper branch in the polaritonic dispersion (within the Type II band) is easily observed whereas the lower branch (in the effective metal regime) is weak. This is due to the bare SPP mode being difficult to excite in such a thick film ($> 1 \mu\text{m}$), therefore by decreasing the overall thickness of the film to 500 nm , both branches are easily discernable in the polaritonic dispersion (Fig. 7.8b).

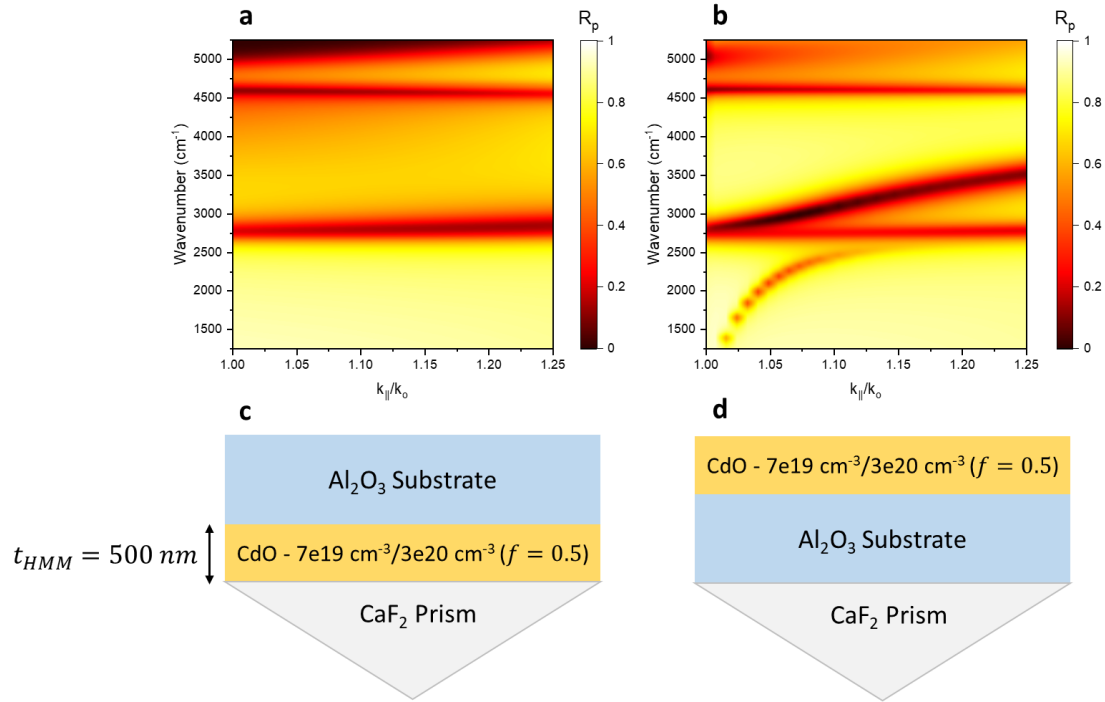


Figure 7.8: a) Dispersion calculated in face-down geometry (c). b) Calculated dispersion in the face up geometry (d).

7.3 Conclusions

In this chapter single-material, homoepitaxial CdO HMMs were grown and characterized using ATR measurements. These HMMs were shown to be highly tunable throughout the MIR through changes to the layer thicknesses and carrier densities. In the Kretschmann configuration measurements we employed to study these films, we are limited by the optical contact between the prism and the sample. Therefore, for the measured range of in-plane wavevectors only one Type II hyperbolic mode was observed. In order to extend the higher in-plane momentum, and therefore achieve additional compression of the free-space wavelength, confined hyperbolic modes in patterned HMMs will be investigated. Initial simulation and experimental results indicate that this would result in multiple higher-order Type II resonances being supported. A study of these 3D-confined modes in all-CdO HMMs is currently underway.

Chapter 8

8. Conclusions and Future Directions

8.1 Conclusions

The goal of this dissertation was to demonstrate novel approaches towards achieving both spectral and spatial control over thermal emission. My hope is that the work presented here can be used as a tool for future students working on similar projects. In Chapter 2, we outlined multiple methods of extracting the optical properties of materials that would be useful for polaritonic applications. More specifically, we utilized VASE and FTIR measurements to determine the carrier density-driven changes to the dielectric function and optical properties of n-doped CdO. We then used FTIR micro-spectroscopy to determine the dielectric function of HfS₂. This technique allowed us to restrict our collection area, therefore limiting the non-idealities that would be present in bench FTIR measurements. Determining accurate dielectric functions is incredibly important for modelling polaritonic structures making this analysis very useful for future students. In Chapter 3 we shift our focus to polaritonic strong coupling in multilayer films. Here, we demonstrate that by taking advantage of the high degree of carrier confinement in as-grown CdO multilayer films that an UID CdO layer can be used to provide spatial separation between an SPP-supporting CdO layer and an ENZ-supporting CdO layer. The UID layer can also be incorporated as a coating layer, perturbing the dielectric environment above a CdO bilayer film and increasing the ENZ absorption. This grants additional tunability over the SPP-ENZ dispersion which we outline in Chapter 3. We also provide a theoretical study of SPhP-ENP and SPP-ENZ-ENP strong coupling in InAs-GaSb and InAs-ALsB heterostructures and discuss the impacts of the InAs carrier density and GaSb/ALsB thickness on the hybrid dispersion. In Chapter 4, we provide a theoretical study of strong coupling between the monopole, ENZ, and ENP modes in InAs-ALsB nanostructure arrays. In this chapter we also determine the effects strong coupling has on the angle-resolved absorption, and therefore through Kirchhoff's law the angle-dependent thermal emission.

In Chapter 5, we characterized the angle-dependent thermal emission of a NIREM consisting of an ENZ-supporting CdO layer deposited onto a PSS. Here, we demonstrated that the PSS allows for the efficient outcoupling of the ENZ mode to free space, therefore enabling high, unpolarized and narrowband emission directed normal to the surface. The device was designed for

filterless NDIR sensing of CO₂, emitting at one of the molecular vibrational frequencies of CO₂. We then provide a proof-of-concept CO₂ detection experiment, demonstrating that our NIREM performs similarly to the conventional NDIR scheme (Blackbody plus filter). In Chapter 6, we used a stochastic gradient descent optimization technique to design aperiodic Tamm plasmon-supporting films with broadly tunable emissivity. Here, we experimentally demonstrate Tamm plasmon thermal emitters featuring single and multiple peak emission with significant control over the spectral positions and linewidths, even with DBR stacks with very few layers (≤ 7). We demonstrate that these emission peaks can be designed to overlap spectrally with peaks in the absorption spectra of gases such as CO₂ and N₂O, and can therefore be used for filterless NDIR demonstrations. Further, we explore more advanced designs which are capable of matching to non-trivial target spectra, such as achieving a strong match to the absorption spectra of a greenhouse gases, achieving extremely high Q-factors (> 10000), and multi-peak spectra with significantly different Q-factors. Finally, in Chapter 7 we investigated hyperbolic behavior in homoepitaxially grown CdO superlattices. We also demonstrated significant tunability over the hyperbolic modes through changes to the carrier densities of the CdO layers and the filling fraction. Using Kretschmann configuration ATR measurements we observed both types of hyperbolic modes as well as dielectric, waveguide-like modes in the dielectric regime of a CdO HMM with a low filling fraction. In all cases, the hyperbolic behavior agreed very well with EMT calculations.

8.2 Future Directions

In Chapter 3 (section 3.3), we provided a theoretical study of SPhP-ENP and SPP-ENZ-ENP strong coupling in InAs-AlSb and InAs-GaSb heterostructures. These calculations were performed in the Otto configuration at a constant air gap distance. However, as was stated in chapter 3, the evanescent extent of the hybrid modes is dependent on the in-plane wavevector being probed within the polaritonic dispersion. Put another way, the evanescent extent of the hybrid modes is tied to the mixing fractions (Hopfield coefficients) of the hybrid modes. Therefore, a multi-angle, gap-dependent study would be an interesting next step in understanding the character of the hybrid modes.

In Chapter 4, we provided a theoretical study of strong coupling between a monopole mode supported by an InAs pillar on an InAs substrate and the ENZ and ENP modes of a thin AlSb layer. Due to the angular dispersion of the monopole mode and the nominally non-dispersive behavior

of the ENP and ENZ modes, the strong coupling between the modes allows for control over the angular dispersion of the hybrid modes. The immediate next step would be to demonstrate this concept experimentally. Further, as was stated in the chapter 4, this analysis can be easily extended to other material systems such as SiC and AlN which have overlapping Reststrahlen bands, InAs and GaSb, and multilayer CdO films. Finally, InAs-AlSb and InAs-GaSb heterostructures have been used in the past to achieve multiple quantum wells. It is conceivable that these structures can be imbedded into the InAs pillar, taking the place of the single AlSb layer. Due to the large oscillator strength associated with intersubband transitions, strong coupling can potentially be achieved between the monopole and intersubband transitions granting control over the radiation pattern.

Finally, in Chapter 6 we realized a powerful approach of achieving lithography-free, widely tunable, narrowband thermal emitters through the inverse design of aperiodic Tamm plasmon films. Although we experimentally and theoretically realized significant control over the emissivity, we were only focused on emission directed normal from the film surface. In the future, we would like to extend our focus to engineering the full angular emission profile, allowing us to demonstrate control over the spatial coherent of the thermal emission from these structures. To this effort, we seek to utilize concepts from metasurface design in order to achieve additional control over the radiation pattern of thermal emission by structuring the metal film in the metal-on-top geometry. We will also investigate potential routes towards active tunability of these Tamm plasmon devices by incorporating phase change and ferroelectric materials into the DBR stack.

Appendix A

Parameters of Tamm Plasmon Films Designed Using Inverse Design

A.1 Matching the absorption spectra of O₃, CH₄, and NH₃

In chapter 6 we demonstrated TPP-EMs that matched the absorption spectra of N₂O, NO, and DMMP nerve agent. In those examples, we used the absorption spectrum itself as the target spectrum. However, in most cases matching to the exact shape of the absorption peaks adds unnecessary complexity and realizing an emitter with emission lobes at the absorption frequencies is sufficient. Further, in some cases the absorption features cannot be matched if the absorption spectrum is used as the target. For example, the absorption spectra of O₃ features a slope in the absorption and CH₄ and NH₃ feature numerous sharp peaks. However, if instead we use envelope spectra that encapsulates the sharp peaks or adjust for the slope in the absorption, we can match to the absorption peaks with great success. The parameters (film thicknesses and CdO carrier densities) of these films are provided in section A2.

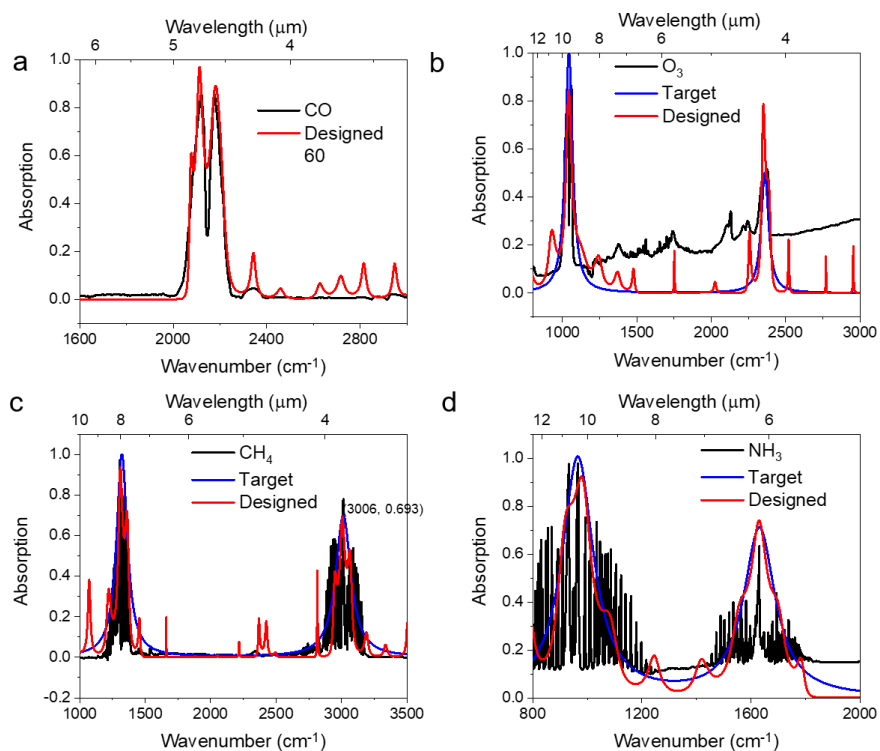


Figure A1: a) Matching CO. (b-d) Matching the envelope spectra of O₃, CH₄, and NH₃ respectively.

A.2 Parameters of Tamm Plasmon Emitters

Here we provide the parameters of the advanced TPP-EM designs from Figures 6.5, 6.7, and A1. As was described in chapter 6, these designs consisted of a 29 layer DBR deposited on a CdO bilayer. In all of the designs, the first and last layers in the DBR are Ge. The arrays below contain the thicknesses of all of the layers starting with the Ge top layer and ending with the top layer in the CdO film. The CdO carrier concentration is constrained between 0.2 and $12.0 \times 10^{20} \text{ cm}^{-3}$, which is the range that has been demonstrated in literature. The layer thickness is constrained between 3 nm and 2500 nm . The substrate is fixed to CdO with the carrier concentration of $12.0 \times 10^{20} \text{ cm}^{-3}$ (plasma frequency= 7800 cm^{-1}), so that we ensure there is no transmission.

High-Q in **Fig. 6.7a**:

[705 681 543 854 787 872 1073 1415 1491 1120 1133 1902 1702
2396 2563 2146 2051 2066 2447 2630 2141 1979 2351 2430 1945 2291
2308 2460 1920 2500 (C.C.= $1.02 \times 10^{20} \text{ cm}^{-3}$)]

Multi-peak in **Fig. 6.7b**:

[4 586 689 1 622 167 166 355 195 228 214 301 184
310 259 251 202 370 270 213 196 540 561 501 343 683
698 697 177 1213 (C.C.= $1.86 \times 10^{20} \text{ cm}^{-3}$)]

LWIR to telecommunication in **Fig. 6.7c**:

[476 345 258 261 455 399 297 176 458 447 355 407 286
467 433 332 447 316 286 360 395 250 283 290 366
326 454 307 437 324 (C.C.= 6.3 cm^{-3})]

Emissivity matching NO in **Fig. 6.7d**:

[855 197 218 19 378 68 186 476 118 198 60 156 193
454 313 100 312 230 285 314 311 537 170 457 464
52 28 669 153 906 (C.C.= 2.5 cm^{-3})]

Matching DMMP nerve agent in **Fig. 6.5a** with CdO:

[19 1385 270 411 770 351 603 111 553 759 583 206 480
 213 876 457 1095 289 459 754 224 359 722 491 200
 1009 898 1364 140 1713 (C.C.=0.29 cm⁻³)]

Matching DMMP nerve agent in **Fig. 6.5a** with gold (substrate is gold):

[244 394 402 314 300 421 359 404 324 284 434 591 495
 374 250 396 334 454 293 275 444 369 347 474 437
 491 106 442 574]

Matching CO in **Fig. A1a**:

[532 369 481 416 429 403 492 354 481 456 488 426 436
 343 464 365 509 342 451 399 516 453 461 362 301
 502 710 540 150 631 (C.C.=0.9 cm⁻³)]

Matching O₃ envelope in **Fig. A1b**:

[120 585 646 433 167 229 228 379 436 410 427 490 439
 441 362 445 465 528 245 343 371 174 267 676 582
 511 365 147 213 1313 (C.C.=1.4 cm⁻³)]

Matching CH₄ envelope in **Fig. A1c**:

[379 287 418 720 310 514 611 312 375 443 522 443 372
 394 590 236 408 432 245 278 454 467 460 649 196
 141 357 497 415 1116 (C.C.=2.1 cm⁻³)]

Matching NH₃ envelope in **Fig. A1d**:

[47 698 472 96 440 640 235 301 482 301 349 400 380
 274 421 381 323 365 399 254 439 174 567 739 626
 578 100 384 401 1582 (C.C.=0.48 cm⁻³)]

Appendix B

Angle Resolved Thermal Emission and Gas Cell Measurements

B.1 Angle Resolved Thermal Emission Measurements

Thermal emission was measured using a Bruker Vertex 70v FTIR along with a custom external thermal emission setup. An image of the thermal emission setup is included in the supporting information. The sample was mounted on a vertically-oriented hot plate equipped with a Venturi vacuum. Using a combination of micrometers and servo motors, this hot plate grants five degrees of freedom including xyz- position control as well as polar and azimuthal angle control. An aperture was placed in the beam path between the hot plate and a focusing parabolic mirror with the purpose of limiting the detected solid angle to an approximate 0.5 cm diameter spot size, limiting emission that could be from the hot plate. A schematic showing the beam path for the angle-dependent thermal emission measurements can be found in Fig. B1 of the supporting information. The emission from the sample was then guided and collected through a KBr window and into the FTIR internal beam path. For polarized thermal emission measurements, a Ge polarizer was placed in the beam path between the mirror and pinhole (location noted in Fig. B1) and measurements were conducted as is described for the unpolarized measurements. In this configuration the emitted signal passes through the interferometer block, taking the place of the spectrometer's internal broadband source which is turned off. The signal was measured using an IR labs mercury-cadmium-telluride (MCT) detector. In order to calculate angle-dependent emissivity, thermal emission measurements were taken at every 10° from 0° to 80° for the CdO devices at 250°C. These measurements were then compared to the thermal emission measured from an emissivity standard at the same temperature and angle of emission. We used 500 μm tall vertically aligned carbon nanotubes (VACNTs) grown on a Si substrate from an Fe-nanoparticle catalyst, grown by Nanotechlabs Inc., as an emissivity standard ($\epsilon \sim 0.97$). These VACNTs provide a high, consistent value for emissivity that is spectrally flat throughout the IR and stable with temperature. The signal collected by the MCT detector in these measurements contains the emission from both the sample as well as the internal optics of the FTIR.

$$M(T_{sample}, T_{ambient}, \lambda, \theta) = R(T_{ambient}, \lambda) [S(T_{sample}, \lambda, \theta) + G(T_{ambient}, \lambda)] \quad (1)$$

Here M is the total measured signal, R is a response function for the internal and external optics, S is the signal originating from the sample and G is the ‘background’ emission from the internal optics. Thus, in order to isolate the signal from the sample, a background measurement was taken by placing a gold mirror in the beam path in front of the hot plate. The resulting spectrum is a product of the response function R with the background emission G . Once the sample, emissivity standard and background emission have been measured we can rearrange equation (1).

$$R(T_{ambient}, \lambda)S_{sample}(T_{sample}, \lambda, \theta) = M_{sample}(T_{sample}, T_{ambient}, \lambda, \theta) - R(T_{ambient}, \lambda)G(T_{ambient}, \lambda) \quad (2)$$

$$R(T_{ambient}, \lambda)S_{standard}(T_{sample}, \lambda, \theta) = M_{standard}(T_{sample}, T_{ambient}, \lambda, \theta) - R(T_{ambient}, \lambda)G(T_{ambient}, \lambda) \quad (3)$$

The response function can be normalized out by taking the ratio of equation (2) to (3) and the emissivity relative to the standard can be determined.

$$\frac{R(T_{ambient}, \lambda)S_{sample}(T_{sample}, \lambda, \theta)}{R(T_{ambient}, \lambda)S_{standard}(T_{sample}, \lambda, \theta)} = \frac{S_{sample}(T_{sample}, \lambda, \theta)}{S_{standard}(T_{sample}, \lambda, \theta)} = \varepsilon(T_{sample}, \lambda, \theta) \quad (4)$$

Note that this technique is much quicker than the conventional approach to measuring emissivity using FTIR and allows for multiple background measurements to be taken throughout the day. Therefore, fluctuations in the ambient temperature can be accounted for readily.

B.2 Gas Cell Measurements

Transmission measurements of several concentrations of CO₂ were performed using a Bruker Vertex 70v FTIR along with a Pike short-path gas cell with KRS5 windows. Just as with the angle dependent thermal emission measurements, the CdO PSS NIREM or the VACNT blackbody standard was used in lieu of the globar source in the FTIR. The beam path for these measurements is shown in Fig. B1 of the supporting information. Here our sample is placed on a temperature controller located at a backport of the FTIR. The sample was heated to 250°C and the emission was directed into the FTIR at an angle normal from the sample surface. The gas cell was placed in the sample compartment of the FTIR which was under a constant N₂ purge. The remainder of the FTIR bench was also under a constant N₂ purge. The gas cell is equipped with 4 ports, 2 external ports for N₂ purging of the areas outside of the gas cell windows and 2 internal

(inlet and outlet) ports for supplying gas to the gas cell. The gas cell was initially purged with N_2 until the spectrum from the sample reached a steady state. The gas cell was then sealed (outlet valve shut) and a background transmission measurement was recorded under N_2 purge. We then opened the outlet valve and used CO_2/N_2 mixture calibration gases with varying CO_2 concentrations from GASCO to fill the gas cell. As with the background spectrum, we allowed the CO_2/N_2 calibration gas to flow until the spectrum reached a steady state and then closed the outlet valve and proceeded to collect our measurement.

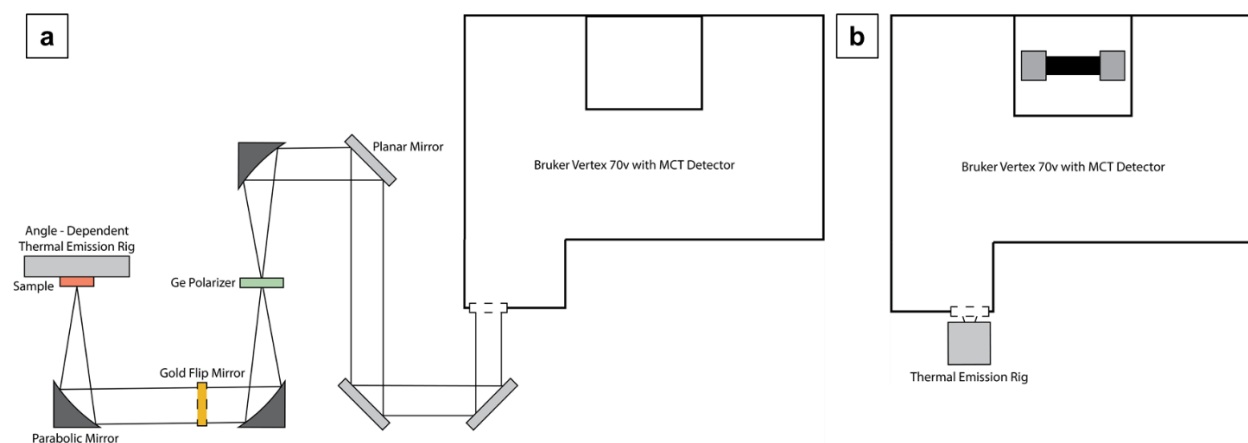


Figure B1: a) Experimental setup showing external, angle-dependent thermal emission rig. b) Backport for angular rig as well as external backport thermal emission device used for gas cell measurements. Both diagrams are not drawn to scale.

REFERENCES

- (1) Gupta, P. K.; Mehendale, S. C. Mid-Infrared Optically Pumped Molecular Lasers. *Hyperfine Interact.* **1987**, *37* (1–4), 243–273. <https://doi.org/10.1007/BF02395713>.
- (2) Faist, J.; Capasso, F.; Sivco, D. L.; Sirtori, C.; Hutchinson, A. L.; Cho, A. Y. Quantum Cascade Laser. *Science (80-.)*. **1994**, *264* (5158), 553–556. <https://doi.org/10.1126/science.264.5158.553>.
- (3) Lu, G.; Nolen, R. J.; Folland, T. G.; Tadjer, M.; Walker, D. G.; Caldwell, J. D. Narrowband Polaritonic Thermal Emitters Driven by Waste-Heat. *ACS Omega*.
- (4) Basov, D. N.; Fogler, M. M.; García De Abajo, F. J. Polaritons in van Der Waals Materials. *Science (80-.)*. **2016**, *354* (6309). <https://doi.org/10.1126/science.aag1992>.
- (5) Caldwell, J. D.; Lindsay, L.; Giannini, V.; Vurgaftman, I.; Reinecke, T. L.; Maier, S. A.; Glembocki, O. J. Low-Loss, Infrared and Terahertz Nanophotonics Using Surface Phonon Polaritons. *Nanophotonics*. 2015. <https://doi.org/10.1515/nanoph-2014-0003>.
- (6) Campione, S.; Brener, I.; Marquier, F. Theory of Epsilon-near-Zero Modes in Ultrathin Films. *Phys. Rev. B* **2015**, *91*, 121408. <https://doi.org/10.1103/PhysRevB.91.121408>.
- (7) Vassant, S.; Hugonin, J.-P.; Marquier, F.; Greffet, J.-J. Berreman Mode and Epsilon near Zero Mode. *Opt. Express* **2012**, *20* (21), 23971–23977.
- (8) Yang, Y.; Kelley, K.; Sachet, E.; Campione, S.; Luk, T. S.; Maria, J. P.; Sinclair, M. B.; Brener, I. Femtosecond Optical Polarization Switching Using a Cadmium Oxide-Based Perfect Absorber. *Nat. Photonics* **2017**, *11*, 390–396. <https://doi.org/10.1038/nphoton.2017.64>.
- (9) Runnerstrom, E. L.; Kelley, K. P.; Sachet, E.; Shelton, C. T.; Maria, J. P. Epsilon-near-Zero Modes and Surface Plasmon Resonance in Fluorine-Doped Cadmium Oxide Thin Films. *ACS Photonics* **2017**. <https://doi.org/10.1021/acsphotonics.7b00429>.
- (10) Folland, T. G.; Ma, T. W. W.; Matson, J. R.; Nolen, J. R.; Liu, S.; Watanabe, K.; Taniguchi, T.; Edgar, J. H.; Taubner, T.; Caldwell, J. D. Probing Hyperbolic Polaritons Using Infrared Attenuated Total Reflectance Micro-Spectroscopy. *MRS Commun.* **2018**, *8* (4), 1418–1425. <https://doi.org/10.1557/mrc.2018.205>.
- (11) Raether, H. *Surface Plasmons on Smooth and Rough Surfaces and on Gratings, Vol. 111 of Springer Tracts in Modern Physics*; 1988.
- (12) Passler, N. C.; Gubbin, C. R.; Folland, T. G.; Razdolski, I.; Katzer, D. S.; Storm, D. F.; Wolf, M.; De Liberato, S.; Caldwell, J. D.; Paarmann, A. Strong Coupling of Epsilon-Near-Zero Phonon Polaritons in Polar Dielectric Heterostructures. *Nano Lett.* **2018**, *18* (7), 4285–4292. <https://doi.org/10.1021/acs.nanolett.8b01273>.
- (13) Folland, T. G.; Nordin, L.; Wasserman, D.; Caldwell, J. D. Probing Polaritons in the Mid- to Far-Infrared. *J. Appl. Phys.* **2019**, *125* (19). <https://doi.org/10.1063/1.5090777>.
- (14) Adato, R.; Yanik, A. A.; Amsden, J. J.; Kaplan, D. L.; Omenetto, F. G.; Hong, M. K.; Erramilli, S.; Altug, H. Ultra-Sensitive Vibrational Spectroscopy of Protein Monolayers with Plasmonic Nanoantenna Arrays. *Proc. Natl. Acad. Sci.* **2009**, *106* (46), 19227–19232. <https://doi.org/10.1073/pnas.0907459106>.

- (15) Adato, R.; Altug, H. In-Situ Ultra-Sensitive Infrared Absorption Spectroscopy of Biomolecule Interactions in Real Time with Plasmonic Nanoantennas. *Nat. Commun.* **2013**, *4*, 1–10. <https://doi.org/10.1038/ncomms3154>.
- (16) Schuller, J. A.; Taubner, T.; Brongersma, M. L. Optical Antenna Thermal Emitters. *Nat. Photonics* **2009**, *3*, 658–661. <https://doi.org/10.1038/nphoton.2009.188>.
- (17) Wang, T.; Li, P.; Chigrin, D. N.; Giles, A. J.; Bezares, F. J.; Glembocki, O. J.; Caldwell, J. D.; Taubner, T. Phonon-Polaritonic Bowtie Nanoantennas: Controlling Infrared Thermal Radiation at the Nanoscale. *ACS Photonics* **2017**, *4*, 1753–1760. <https://doi.org/10.1021/acsp Photonics.7b00321>.
- (18) Planck, M. Ueber Das Gesetz. *Ann. Phys.* **1901**, *4* (October), 553–563.
- (19) Kirchhoff, G. Licht; Ff. *Ann. Phys. Chemie* **1860**, *109*, 275. <https://doi.org/10.1002/andp.18601850205>.
- (20) Mandel, L.; Wolf, E. Coherence Properties of Optical Fields. *Rev. Mod. Phys.* **1965**, *37* (2), 231–287. <https://doi.org/10.1103/RevModPhys.37.231>.
- (21) Greffet, J. J.; Carminati, R.; Joulain, K.; Mulet, J. P.; Mainguy, S.; Chen, Y. Coherent Emission of Light by Thermal Sources. *Nature* **2002**, *416* (6876), 61–64. <https://doi.org/10.1038/416061a>.
- (22) Kaliteevski, M.; Iorsh, I.; Brand, S.; Abram, R. A.; Chamberlain, J. M.; Kavokin, A. V; Shelykh, I. A. Tamm Plasmon-Polaritons: Possible Electromagnetic States at the Interface of a Metal and a Dielectric Bragg Mirror. **2007**, 1–5. <https://doi.org/10.1103/PhysRevB.76.165415>.
- (23) Chalabi, H.; Alù, A.; Brongersma, M. L. Focused Thermal Emission from a Nanostructured SiC Surface. *Phys. Rev. B* **2016**, *94* (9), 1–9. <https://doi.org/10.1103/PhysRevB.94.094307>.
- (24) Lu, G.; Gubbin, C. R.; Nolen, J. R.; Folland, T.; Tadjer, M. J.; De Liberato, S.; Caldwell, J. D. Engineering the Spectral and Spatial Dispersion of Thermal Emission via Polariton–Phonon Strong Coupling. *Nano Lett.* **2021**. <https://doi.org/10.1021/acs.nanolett.0c04767>.
- (25) Kelley, K. P.; Runnerstrom, E. L.; Sachet, E.; Shelton, C. T.; Grimley, E. D.; Klump, A.; Lebeau, J. M.; Sitar, Z.; Suen, J. Y.; Padilla, W. J.; Maria, J.-P. Multiple Epsilon-Near-Zero Resonances in Multilayered Cadmium Oxide: Designing Metamaterial-Like Optical Properties in Monolithic Materials. *ACS Photonics* **2019**, *6* (5), 1139–1145. <https://doi.org/10.1021/acsp Photonics.9b00367>.
- (26) Zhao, W.; Pan, J.; Fang, Y.; Che, X.; Wang, D.; Bu, K.; Huang, F. Metastable MoS₂: Crystal Structure, Electronic Band Structure, Synthetic Approach and Intriguing Physical Properties. *Chem. - A Eur. J.* **2018**, *24* (60), 15942–15954. <https://doi.org/10.1002/chem.201801018>.
- (27) Lucovsky, G.; White, R. M.; Benda, J. A.; Revelli, J. F. Infrared-Reflectance Spectra of Layered Group-IV and Group-VI Transition-Metal Dichalcogenides. *Phys. Rev. B* **1973**, *7* (8), 3859–3870. <https://doi.org/10.1103/PhysRevB.7.3859>.
- (28) Laturia, A.; Put, M. L. Van De. Dielectric Properties of Hexagonal Boron Nitride and Transition Metal Dichalcogenides : From Monolayer to Bulk. *npj 2D Mater. Appl.* **2018**, No. February, 1–7. <https://doi.org/10.1038/s41699-018-0050-x>.
- (29) Tiwald, T. E.; Woollam, J. A.; Zollner, S.; Christiansen, J.; Gregory, R. B.; Wetteroth, T.; Wilson, S. R.; Powell, A. Carrier Concentration and Lattice Absorption in Bulk and Epitaxial Silicon Carbide Determined Using Infrared Ellipsometry. *Phys. Rev. B - Condens. Matter Mater. Phys.* **1999**, *60*

- (16), 11464–11474. <https://doi.org/10.1103/PhysRevB.60.11464>.
- (30) Gubbin, C. R.; De Liberato, S. Theory of Four-Wave-Mixing in Phonon Polaritons. **2017**. <https://doi.org/10.1021/acsphotonics.7b00863>.
- (31) Shekhar, P.; Atkinson, J.; Jacob, Z. Hyperbolic Metamaterials: Fundamentals and Applications. *Nano Convergence*. 2014, pp 1–17. <https://doi.org/10.1186/s40580-014-0014-6>.
- (32) Hoffman, A. J.; Alekseyev, L.; Howard, S. S.; Franz, K. J.; Wasserman, D.; Podolskiy, V. A.; Narimanov, E. E.; Sivco, D. L.; Gmachl, C. Negative Refraction in Semiconductor Metamaterials. *Nat. Mater.* **2007**, *6* (12), 946–950. <https://doi.org/10.1038/nmat2033>.
- (33) Guo, P.; Diroll, B. T.; Huang, W.; Zeng, L.; Wang, B.; Bedzyk, M. J.; Facchetti, A.; Marks, T. J.; Chang, R. P. H.; Schaller, R. D. Low-Loss Near-Infrared Hyperbolic Metamaterials with Epitaxial ITO-In₂O₃ Multilayers. *ACS Photonics* **2018**, *5* (5), 2000–2007. <https://doi.org/10.1021/acsphotonics.7b01485>.
- (34) Álvarez-Pérez, G.; Folland, T. G.; Errea, I.; Taboada-Gutiérrez, J.; Duan, J.; Martín-Sánchez, J.; Tresguerres-Mata, A. I. F.; Matson, J. R.; Bylinkin, A.; He, M.; Ma, W.; Bao, Q.; Martín, J. I.; Caldwell, J. D.; Nikitin, A. Y.; Alonso-González, P. Infrared Permittivity of the Biaxial van Der Waals Semiconductor α -MoO₃ from Near- and Far-Field Correlative Studies. *Adv. Mater.* **2020**, *32* (29), 1–10. <https://doi.org/10.1002/adma.201908176>.
- (35) Sturm, C.; Furthmüller, J.; Bechstedt, F.; Schmidt-Grund, R.; Grundmann, M. Dielectric Tensor of Monoclinic Ga₂O₃ Single Crystals in the Spectral Range 0.5–8.5 eV. *APL Mater.* **2015**, *3* (10), 0–9. <https://doi.org/10.1063/1.4934705>.
- (36) Shubnic, A. A.; Polozkov, R. G.; Shelykh, I. A.; Iorsh, I. V. High Refractive Index and Extreme Biaxial Optical Anisotropy of Rhenium Diselenide for Applications in All-Dielectric Nanophotonics. *Nanophotonics* **2020**, *9* (16), 4737–4742. <https://doi.org/10.1515/nanoph-2020-0416>.
- (37) Zong, J. Q.; Zhang, S. F.; Ji, W. X.; Zhang, C. W.; Li, P.; Wang, P. J. Electric Structure and Optical Properties of ReS₂ Nanomaterials. *Superlattices Microstruct.* **2018**, *122* (June), 262–267. <https://doi.org/10.1016/j.spmi.2018.07.040>.
- (38) Echeverry, J. P.; Gerber, I. C. Theoretical Investigations of the Anisotropic Optical Properties of Distorted 1T ReS₂ and ReSe₂ Monolayers, Bilayers, and in the Bulk Limit. *Phys. Rev. B* **2018**, *97* (7). <https://doi.org/10.1103/PhysRevB.97.075123>.
- (39) Schubert, M. *Infrared Ellipsometry on Semiconductor Layer Structures Phonons, Plasmons, and Polaritons*; 2005; Vol. 209.
- (40) Nolen, J. R.; Runnerstrom, E. L.; Kelley, K. P.; Luk, T. S.; Folland, T. G.; Cleri, A.; Maria, J.-P.; Caldwell, J. D. Ultraviolet to Far-Infrared Dielectric Function of *n*-Doped Cadmium Oxide Thin Films. *Phys. Rev. Mater.* **2020**, *4* (2), 1–10. <https://doi.org/10.1103/physrevmaterials.4.025202>.
- (41) Caldwell, J. D.; Kretinin, A. V.; Chen, Y.; Giannini, V.; Fogler, M. M.; Francescato, Y.; Ellis, C. T.; Tischler, J. G.; Woods, C. R.; Giles, A. J.; Hong, M.; Watanabe, K.; Taniguchi, T.; Maier, S. A.; Novoselov, K. S. Sub-Diffractive Volume-Confined Polaritons in the Natural Hyperbolic Material Hexagonal Boron Nitride. *Nat. Commun.* **2014**, *5* (5221). <https://doi.org/10.1038/ncomms6221>.
- (42) Hofmann, T.; Herzinger, C. M.; Boosalis, A.; Tiwald, T. E.; Woollam, J. A.; Schubert, M. Variable-Wavelength Frequency-Domain Terahertz Ellipsometry. *Rev. Sci. Instrum.* **2010**, *81* (2).

<https://doi.org/10.1063/1.3297902>.

- (43) Báez-Chorro, M. A.; Vidal, B. Single Trace Terahertz Spectroscopic Ellipsometry. *Opt. Express* **2019**, *27* (24), 35468. <https://doi.org/10.1364/oe.27.035468>.
- (44) Yu, P.; Cardona, M. *Fundamentals of Semiconductors*; 2012.
- (45) Jellison, G. E.; Modine, F. A. Parameterization of the Optical Functions of Amorphous Materials in the Interband Region. *Appl. Phys. Lett.* **1996**, *69* (3), 371–373. <https://doi.org/10.1063/1.118064>.
- (46) Jellison, G. E.; Jr.; Merkulov, V. I.; Puretzky, A. A.; Geohegan, D. B.; Eresa, G.; Lowndes, D. H.; Caughman, J. B. Characterization of Thin-Film Amorphous Semiconductors Using Spectroscopic Ellipsometry. *Thin Solid Films* **2000**, 377–378, 68.
- (47) Law, S.; Adams, D. C.; Taylor, A. M.; Wasserman, D. Mid-Infrared Designer Metals. *2012 IEEE Photonics Conf. IPC 2012* **2012**, *20* (11), 786–787. <https://doi.org/10.1109/IPCon.2012.6358858>.
- (48) Yang, H. U.; D’Archangel, J.; Sundheimer, M. L.; Tucker, E.; Boreman, G. D.; Raschke, M. B. Optical Dielectric Function of Silver. *Phys. Rev. B* **2015**, *91* (235137). <https://doi.org/10.1103/PhysRevB.91.235137>.
- (49) Adachi, S. *Optical Properties of Crystalline and Amorphous Semiconductors: Materials and Fundamental Principles*; Springer: New York, 1999.
- (50) Hillenbrand, R.; Taubner, T.; Keilmann, F. Phonon-Enhanced Light – Matter Interaction at the Nanometre Scale. *Nature* **2002**, *418* (1984), 159–162.
- (51) Foteinopoulou, S.; Devarapu, G. C. R.; Subramania, G. S.; Krishna, S.; Wasserman, D. *Phonon-Polaritons: Enabling Powerful Capabilities for Infrared Photonics*; 2019. <https://doi.org/10.1515/nanoph-2019-0232>.
- (52) Howes, A.; Nolen, J. R.; Caldwell, J. D.; Valentine, J. Near-Unity and Narrow-Band Thermal Emissivity in Balanced Dielectric Metasurfaces. *Rev.*
- (53) Caldwell, J. D.; Lindsay, L.; Giannini, V.; Vurgaftman, I.; Reinecke, T. L.; Maier, S. A.; Glembocki, O. J. Low-Loss, Infrared and Terahertz Nanophotonics Using Surface Phonon Polaritons. *Nanophotonics* **2015**, *4*, 44–68. <https://doi.org/10.1515/nanoph-2014-0003>.
- (54) Caldwell, J. D.; Glembocki, O. J.; Francescato, Y.; Sharac, N.; Giannini, V.; Bezares, F. J.; Long, J. P.; Owrutsky, J. C.; Vurgaftman, I.; Tischler, J. G.; Wheeler, V. D.; Bassim, N. D.; Shirey, L. M.; Kasica, R.; Maier, S. A. Low-Loss, Extreme Subdiffraction Photon Confinement via Silicon Carbide Localized Surface Phonon Polariton Resonators. *Nano Lett.* **2013**, *13* (8), 3690–3697. <https://doi.org/10.1021/nl401590g>.
- (55) Schuller, J. A.; Zia, R.; Taubner, T.; Brongersma, M. L. Dielectric Metamaterials Based on Electric and Magnetic Resonances of Silicon Carbide Particles. *Phys. Rev. Lett.* **2007**, *99* (107401). <https://doi.org/10.1103/PhysRevLett.99.107401>.
- (56) Kim, J.; Dutta, A.; Naik, G. V.; Giles, A. J.; Bezares, F. J.; Ellis, C. T.; Tischler, J. G.; Mahmoud, A. M.; Caglayan, H.; Glembocki, O. J.; Kildishev, A. V.; Caldwell, J. D.; Boltasseva, A.; Engheta, N. Role of Epsilon-near-Zero Substrates in the Optical Response of Plasmonic Antennas. *Optica* **2016**, *3* (3), 339–346. <https://doi.org/10.1364/OPTICA.3.000339>.
- (57) Powell, A.; Christiansen, J.; Gregory, R. B.; Wetteroth, T.; Wilson, S. R. Carrier Concentration and

- Lattice Absorption in Bulk and Epitaxial Silicon Carbide Determined Using Infrared Ellipsometry. *Phys. Rev. B* **1999**, *60* (16), 464–474. <https://doi.org/10.1103/PhysRevB.60.11464>.
- (58) Marronnier, A.; Lee, H.; Geffroy, B.; Even, J.; Bonnassieux, Y.; Roma, G. Structural Instabilities Related to Highly Anharmonic Phonons in Halide Perovskites. *J. Phys. Chem. Lett.* **2017**, *8* (12), 2659–2665. <https://doi.org/10.1021/acs.jpcclett.7b00807>.
- (59) Barker, A. S.; Hopfield, J. J. Coupled-Optical-Phonon-Mode Theory of the Infrared Dispersion in BaTiO₃, SrTiO₃, and KTaO₃. *Phys. Rev.* **1964**, *135* (6A), 1732–1737. <https://doi.org/10.1103/PhysRev.135.A1732>.
- (60) Lockwood, D. J.; Yu, G.; Rowell, N. L. Oblique Incidence Infrared Reflectance Spectroscopy of Phonons in Cubic MgO, MnO, and NiO. *Infrared Phys. Technol.* **2020**, *109* (June), 103405. <https://doi.org/10.1016/j.infrared.2020.103405>.
- (61) Minami, T. Transparent Conducting Oxide Semiconductors for Transparent Electrodes. *Semicond. Sci. Technol.* **2005**, *20* (4). <https://doi.org/10.1088/0268-1242/20/4/004>.
- (62) Exarhos, G. J.; Zhou, X. D. Discovery-Based Design of Transparent Conducting Oxide Films. *Thin Solid Films* **2007**, *515* (18), 7025–7052. <https://doi.org/10.1016/j.tsf.2007.03.014>.
- (63) Sachet, E.; Shelton, C. T.; Harris, J. S.; Gaddy, B. E.; Irving, D. L.; Curtarolo, S.; Donovan, B. F.; Hopkins, P. E.; Sharma, P. A.; Sharma, A. L.; Ihlefeld, J.; Franzen, S.; Maria, J. P. Dysprosium-Doped Cadmium Oxide as a Gateway Material for Mid-Infrared Plasmonics. *Nat. Mater.* **2015**, *14* (4), 414–420. <https://doi.org/10.1038/nmat4203>.
- (64) Boltasseva, A.; Atwater, H. A. Low-Loss Plasmonic Metamaterials. *Science (80-.)*. **2011**, *331* (6015), 290–291. <https://doi.org/10.1126/science.1198258>.
- (65) Bädeker, K. Über Die Elektrische Leitfähigkeit Und Die Thermoelektrische Kraft Einiger Schwermetallverbindungen. *Ann. Phys.* **1907**, *327* (4), 749–766. <https://doi.org/10.1002/andp.19073270409>.
- (66) Wang, A.; Babcock, J. R.; Edleman, N. L.; Metz, A. W.; Lane, M. A.; Asahi, R.; David, V. P.; Kannewurf, C. R.; Freeman, A. J.; Marks, T. J. Indium-Cadmium-Oxide Films Having Exceptional Electrical Conductivity and Optical Transparency: Clues for Optimizing Transparent Conductors. *Proc. Natl. Acad. Sci.* **2002**, *98* (13), 7113–7116. <https://doi.org/10.1073/pnas.121188298>.
- (67) Kelley, K. P.; Sachet, E.; Shelton, C. T.; Maria, J. P. High Mobility Yttrium Doped Cadmium Oxide Thin Films. *APL Mater.* **2017**, *5* (7), 0–6. <https://doi.org/10.1063/1.4993799>.
- (68) Runnerstrom, E. L.; Kelley, K. P.; Sachet, E.; Shelton, C. T.; Maria, J. P. Epsilon-near-Zero Modes and Surface Plasmon Resonance in Fluorine-Doped Cadmium Oxide Thin Films. *ACS Photonics* **2017**, *4* (8), 1885–1892. <https://doi.org/10.1021/acsphotonics.7b00429>.
- (69) Gudmundsson, J. T.; Brenning, N.; Lundin, D.; Helmersson, U. High Power Impulse Magnetron Sputtering Discharge. *J. Vac. Sci. Technol. A Vacuum, Surfaces, Film.* **2012**, *30* (3), 030801. <https://doi.org/10.1116/1.3691832>.
- (70) Anders, A. Tutorial: Reactive High Power Impulse Magnetron Sputtering (R-HiPIMS). *J. Appl. Phys.* **2017**, *121* (17). <https://doi.org/10.1063/1.4978350>.
- (71) Larsson, E. M.; Alegret, J.; Käll, M.; Sutherland, D. S. Sensing Characteristics of NIR Localized

- Surface Plasmon Resonances in Gold Nanorings for Application as Ultrasensitive Biosensors. *Nano Lett.* **2007**, *7* (5), 1256–1263. <https://doi.org/10.1021/nl0701612>.
- (72) Bo, L.; Claes, N.; Ingemar, L. Surface Plasmon Resonance for Gas Detection and Biosensing. *Sensors and Actuators* **1983**, *4*, 299–304. [https://doi.org/10.1016/0250-6874\(83\)85036-7](https://doi.org/10.1016/0250-6874(83)85036-7).
- (73) Cleary, J.; Peale, R.; Shelton, D.; Boreman, G.; Soref, R.; Buchwald, W. Silicides for Infrared Surface Plasmon Resonance Biosensors. *MRS Proc.* **2008**, *1133*, 1133-AA10-03. <https://doi.org/10.1557/PROC-1133-AA10-03>.
- (74) Rieder, K. H.; Nie, S.; Emory, S. R. *Probing Single Molecules and Single Nanoparticles by Surface-Enhanced Raman Scattering Downloaded From*; Springer, 1994; Vol. 50.
- (75) Caldwell, J. D.; Glembocki, O.; Bezares, F. J.; Bassim, N. D.; Rendell, R. W.; Feygelson, M.; Ukaegbu, M.; Kasica, R.; Shirey, L.; Hosten, C. Plasmonic Nanopillar Arrays for Large-Area, High-Enhancement Surface-Enhanced Raman Scattering Sensors. *ACS Nano* **2011**, *5* (5), 4046–4055. <https://doi.org/10.1021/nn200636t>.
- (76) Caldwell, J. D.; Glembocki, O. J.; Bezares, F. J.; Kariniemi, M. I.; Niinistö, J. T.; Hatanpää, T. T.; Rendell, R. W.; Ukaegbu, M.; Ritala, M. K.; Prokes, S. M.; Hosten, C. M.; Leskelä, M. A.; Kasica, R.; Fleischmann, . M; Hendra, P. J.; Mcquillan, A. J.; Raman, ". Large-Area Plasmonic Hot-Spot Arrays: Sub-2 Nm Interparticle Separations with Plasma-Enhanced Atomic Layer Deposition of Ag on Periodic Arrays of Si Nanopillars. **2011**, *19* (160).
- (77) Yoo, D.; Mohr, D. A.; Vidal-Codina, F.; John-Herpin, A.; Jo, M.; Kim, S.; Matson, J.; Caldwell, J. D.; Jeon, H.; Nguyen, N. C.; Martin-Moreno, L.; Péraire, J.; Altug, H.; Oh, S. H. High-Contrast Infrared Absorption Spectroscopy via Mass-Produced Coaxial Zero-Mode Resonators with Sub-10 Nm Gaps. *Nano Lett.* **2018**, *18* (3), 1930–1936. <https://doi.org/10.1021/acs.nanolett.7b05295>.
- (78) Ni, X.; Emani, N. K.; Kildishev, A. V; Boltasseva, A.; Shalaev, V. M. Broadband Light Bending with Plasmonic Nanoantennas. *Science (80-.).* **2012**, *335* (6067), 427. <https://doi.org/10.1126/science.1210713>.
- (79) Aieta, F.; Genevet, P.; Kats, M. A.; Yu, N.; Blanchard, R.; Gaburro, Z.; Capasso, F. Aberration-Free Ultrathin Flat Lenses and Axicons at Telecom Wavelengths Based on Plasmonic Metasurfaces. *Nano Lett.* **2012**, *12* (9), 4932–4936. <https://doi.org/10.1021/nl302516v>.
- (80) Capasso, F.; Genevet, P.; Tétienne, J.-P.; Kats, M. A.; Gaburro, Z.; Yu, N.; Aieta, F. Light Propagation with Phase Discontinuities: Generalized Laws of Reflection and Refraction. *Science (80-.).* **2011**, *334* (6054), 333–337. <https://doi.org/10.1126/science.1210713>.
- (81) Naik, G. V.; Shalaev, V. M.; Boltasseva, A. Alternative Plasmonic Materials: Beyond Gold and Silver. *Adv. Mater.* **2013**, *25*, 3264–3294. <https://doi.org/10.1002/adma.201205076>.
- (82) Autore, M.; Li, P.; Dolado, I.; Alfaro-Mozaz, F. J.; Esteban, R.; Atxabal, A.; Casanova, F.; Hueso, L. E.; Alonso-González, P.; Aizpurua, J.; Nikitin, A. Y.; Vélez, S.; Hillenbrand, R. Boron Nitride Nanoresonators for Phonon-Enhanced Molecular Vibrational Spectroscopy at the Strong Coupling Limit. *Light Sci. Appl.* **2018**, *7* (4). <https://doi.org/10.1038/lsa.2017.172>.
- (83) Gu, Y.; Li, X.; Chen, J.; Zeng, H. Anomalous Plasmon Resonance from Confined Diffusive Charges: High Quality and Tunability from Mid to Far Infrared Wavebands. *Opt. Express* **2016**, *24* (26), 29908. <https://doi.org/10.1364/oe.24.029908>.

- (84) Sönnichsen, C.; Franzl, T.; Wilk, T.; von Plessen, G.; Feldmann, J.; Wilson, O.; Mulvaney, P. Drastic Reduction of Plasmon Damping in Gold Nanorods. *Phys. Rev. Lett.* **2002**, *88* (7), 774021–774024. <https://doi.org/10.1103/PhysRevLett.88.077402>.
- (85) Liu, C. P.; Foo, Y.; Kamruzzaman, M.; Ho, C. Y.; Zapien, J. A.; Zhu, W.; Li, Y. J.; Walukiewicz, W.; Yu, K. M. Effects of Free Carriers on the Optical Properties of Doped CdO for Full-Spectrum Photovoltaics. *Phys. Rev. Appl.* **2016**, *6* (6), 1–12. <https://doi.org/10.1103/PhysRevApplied.6.064018>.
- (86) Burbano, M.; Scanlon, D. O.; Watson, G. W. Sources of Conductivity and Doping Limits in CdO from Hybrid Density Functional Theory. *J. Am. Chem. Soc.* **2011**, *133* (38), 15065–15072. <https://doi.org/10.1021/ja204639y>.
- (87) Cleary, J. W.; Smith, E. M.; Leedy, K. D.; Grzybowski, G.; Guo, J. Optical and Electrical Properties of Ultra-Thin Indium Tin Oxide Nanofilms on Silicon for Infrared Photonics. *Opt. Mater. Express* **2018**, *8* (5), 1231–1245. <https://doi.org/10.1364/OME.8.001231>.
- (88) Burstein, E. Anomalous Optical Absorption Limit in InSb [4]. *Phys. Rev.* **1954**, *93* (3), 632–633. <https://doi.org/10.1103/PhysRev.93.632>.
- (89) Moss, T. S. The Interpretation of the Properties of Indium Antimonide. *Proc. Phys. Soc. Sect. B* **1954**, *67* (10), 775–782. <https://doi.org/10.1088/0370-1301/67/10/306>.
- (90) Moss, T. S. Relations between the Refractive Index and Energy Gap of Semiconductors. *Phys. Status Solidi* **1985**, *131* (2), 415–427. <https://doi.org/10.1002/pssb.2221310202>.
- (91) Pisarkiewicz, T.; Zakrzewska, K.; Leja, E. Scattering of Charge Carriers in Transparent and Conducting Thin Oxide Films with a Non-Parabolic Conduction Band. *Thin Solid Films* **1989**, *174*, 217–223. [https://doi.org/10.1016/0040-6090\(89\)90892-4](https://doi.org/10.1016/0040-6090(89)90892-4).
- (92) Pisarkiewicz, T.; Kolodziej, A. Nonparabolicity of the Conduction Band Structure in Degenerate Tin Dioxide. *Phys. Status Solidi* **1990**, *158*, 5–8.
- (93) Koida, T.; Kondo, M.; Tsutsumi, K.; Sakaguchi, A.; Suzuki, M.; Fujiwara, H. Hydrogen-Doped In₂O₃ Transparent Conducting Oxide Films Prepared by Solid-Phase Crystallization Method. *J. Appl. Phys.* **2010**, *107* (3). <https://doi.org/10.1063/1.3284960>.
- (94) Mendelsberg, R. J.; Zhu, Y.; Anders, A. Determining the Nonparabolicity Factor of the CdO Conduction Band Using Indium Doping and the Drude Theory. *J. Phys. D: Appl. Phys.* **2012**, *45* (42), 425302. <https://doi.org/10.1088/0022-3727/45/42/425302>.
- (95) Wang, F.; Shen, Y. R. General Properties of Local Plasmons in Metal Nanostructures. *Phys. Rev. Lett.* **2006**, *97* (206806). <https://doi.org/10.1103/PhysRevLett.97.206806>.
- (96) Khurgin, J. B.; Sun, G. In Search of the Elusive Lossless Metal. *Appl. Phys. Lett.* **2010**, *96* (181102). <https://doi.org/10.1063/1.3425890>.
- (97) Agrawal, A.; Singh, A.; Yazdi, S.; Singh, A.; Ong, G. K.; Bustillo, K.; Johns, R. W.; Ringe, E.; Milliron, D. J. Resonant Coupling between Molecular Vibrations and Localized Surface Plasmon Resonance of Faceted Metal Oxide Nanocrystals. *Nano Lett.* **2017**, *17* (4), 2611–2620. <https://doi.org/10.1021/acs.nanolett.7b00404>.
- (98) Chen, Y.; Francescato, Y.; Caldwell, J. D.; Giannini, V.; Ma, T. W. W.; Glembocki, O. J.; Bezares, F.

- J.; Taubner, T.; Kasica, R.; Hong, M.; Maier, S. A. Spectral Tuning of Localized Surface Phonon Polariton Resonators for Low-Loss Mid-IR Applications. *ACS Photonics* **2014**, *1* (8), 718–724. <https://doi.org/10.1021/ph500143u>.
- (99) Tamagnone, M.; Chaudhary, K.; Zhu, A.; Meretska, M.; Li, J.; Edgar, J. H.; Ambrosio, A.; Capasso, F. High Quality Factor Polariton Resonators Using van Der Waals Materials. **2019**, arXiv:1905.02177.
- (100) Bohren, C. F.; Huffman, D. R. *Absorption and Scattering of Light by Small Particles*, 6th ed.; Wiley: New York, 1983.
- (101) Malerba, M.; Alabastri, A.; Miele, E.; Zilio, P.; Patrini, M.; Bajoni, D.; Messina, G. C.; Dipalo, M.; Toma, A.; Zaccaria, R. P.; De Angelis, F. 3D Vertical Nanostructures for Enhanced Infrared Plasmonics. *Nat. Sci. Reports* **2015**, *5* (16436). <https://doi.org/10.1038/srep16436>.
- (102) Cornelius, S.; Vinnichenko, M.; Shevchenko, N.; Rogozin, A.; Kolitsch, A.; Möller, W. Achieving High Free Electron Mobility in ZnO:Al Thin Films Grown by Reactive Pulsed Magnetron Sputtering. *Appl. Phys. Lett.* **2009**, *94* (042103). <https://doi.org/10.1063/1.3074373>.
- (103) Chen, Z.; Zhuo, Y.; Tu, W.; Li, Z.; Ma, X.; Pei, Y.; Wang, G. High Mobility Indium Tin Oxide Thin Film and Its Application at Infrared Wavelengths: Model and Experiment. *Opt. Express* **2018**, *26* (17), 22123. <https://doi.org/10.1364/OE.26.022123>.
- (104) Ajimsha, R. S.; Das, A. K.; Misra, P.; Joshi, M. P.; Kukreja, L. M.; Kumar, R.; Sharma, T. K.; Oak, S. M. Observation of Low Resistivity and High Mobility in Ga Doped ZnO Thin Films Grown by Buffer Assisted Pulsed Laser Deposition. *J. Alloys Compd.* **2015**, *638*, 55–58. <https://doi.org/10.1016/j.jallcom.2015.02.162>.
- (105) Ray, S.; Banerjee, R.; Basu, N.; Batabyal, A. K.; Barua, A. K. Properties of Tin Doped Indium Oxide Thin Films Prepared by Magnetron Sputtering. *J. Appl. Phys.* **1983**, *54* (6), 3497–3501. <https://doi.org/10.1063/1.332415>.
- (106) Park, S. M.; Ikegami, T.; Ebihara, K. Effects of Substrate Temperature on the Properties of Ga-Doped ZnO by Pulsed Laser Deposition. *Thin Solid Films* **2006**, *513*, 90–94. <https://doi.org/10.1016/j.tsf.2006.01.051>.
- (107) Agura, H.; Suzuki, A.; Matsushita, T.; Aoki, T.; Okuda, M. Low Resistivity Transparent Conducting Al-Doped ZnO Films Prepared by Pulsed Laser Deposition. *Thin Solid Films* **2003**, *445* (2), 263–267. [https://doi.org/10.1016/S0040-6090\(03\)01158-1](https://doi.org/10.1016/S0040-6090(03)01158-1).
- (108) Fujiwara, H.; Kondo, M. Effects of Carrier Concentration on the Dielectric Function of ZnO:Ga and In 2O 3:Sn Studied by Spectroscopic Ellipsometry: Analysis of Free-Carrier and Band-Edge Absorption. *Phys. Rev. B* **2005**, *71* (07109). <https://doi.org/10.1103/PhysRevB.71.075109>.
- (109) Gordon, T. R.; Paik, T.; Klein, D. R.; Naik, G. V.; Caglayan, H.; Boltasseva, A.; Murray, C. B. Shape-Dependent Plasmonic Response and Directed Self-Assembly in a New Semiconductor Building Block, Indium-Doped Cadmium Oxide (ICO). *Nano Lett.* **2013**, *13* (6), 2857–2863. <https://doi.org/10.1021/nl4012003>.
- (110) Schubert, M.; Tiwald, T. E.; Herzinger, C. M. Infrared Dielectric Anisotropy and Phonon Modes of Sapphire. *J. Appl. Phys.* **1999**, *61* (12), 8187–8201. <https://doi.org/10.1063/1.4802715>.
- (111) Cuscó, R.; Ibáñez, J.; Domenech-Amador, N.; Artús, L.; Zúiga-Préz, J.; Muoz-Sanjoá, V. Raman

- Scattering of Cadmium Oxide Epilayers Grown by Metal-Organic Vapor Phase Epitaxy. *J. Appl. Phys.* **2010**, *107* (063519). <https://doi.org/10.1063/1.3357377>.
- (112) Finkenrath, H.; Uhle, N.; Waidelich, W. The Influence of Phonons and Polarons on the Infrared Absorption of Cadmium Oxide. *Solid State Commun.* **1969**, *7* (1), 11–14. [https://doi.org/10.1016/0038-1098\(69\)90681-4](https://doi.org/10.1016/0038-1098(69)90681-4).
- (113) Passler, N. C.; Paarmann, A. Generalized 4×4 Matrix Formalism for Light Propagation in Anisotropic Stratified Media: Study of Surface Phonon Polaritons in Polar Dielectric Heterostructures. *J. Opt. Soc. Am. B* **2017**, *34* (10), 2128–2139. <https://doi.org/10.1364/josab.34.002128>.
- (114) Cingolani, A.; Lugará, M.; Scamarcio, G.; Lévy, F. The Raman Scattering in Hafnium Disulfide. *Solid State Commun.* **1987**, *62* (2), 121–123. [https://doi.org/10.1016/0038-1098\(87\)91126-4](https://doi.org/10.1016/0038-1098(87)91126-4).
- (115) Zwick, A.; Renucci, M. A.; Kjekshus, A.; Rajalakshmi, M.; Sakuntala, T.; Arora, K.; Garg, A. K. Resonance Raman Scattering in HfSe₂ and HfS₂. **1988**.
- (116) Riede, V.; Sobotta, H. Two-Phonon Absorption Spectra and Lattice Vibration Anisotropy in HfS₂. *9*, 9–14.
- (117) Purcell, E. Spontaneous Emission Probabilities at Radio Frequencies. *Phys. Rev.* **1946**, *69*, 681. https://doi.org/https://doi.org/10.1007/978-1-4615-1963-8_40.
- (118) Kaluzny, Y.; Goy, P.; Gross, M.; Raimond, J. M.; Haroche, S. Observation of Self-Induced Rabi Oscillations in Two-Level Atoms Excited inside a Resonant Cavity: The Ringing Regime of Superradiance. *Phys. Rev. Lett.* **1983**, *51* (13), 1175–1178. <https://doi.org/10.1103/PhysRevLett.51.1175>.
- (119) Byrnes, T.; Kim, N. Y.; Yamamoto, Y. Exciton-Polariton Condensates. *Nat. Phys.* **2014**, *10* (11), 803–813. <https://doi.org/10.1038/nphys3143>.
- (120) Runnerstrom, E. L.; Kelley, K. P.; Folland, T. G.; Nolen, J. R.; Engheta, N.; Caldwell, J. D.; Maria, J. P. Polaritonic Hybrid-Epsilon-near-Zero Modes: Beating the Plasmonic Confinement vs Propagation-Length Trade-Off with Doped Cadmium Oxide Bilayers. *Nano Lett.* **2019**, *19* (2), 948–957. <https://doi.org/10.1021/acs.nanolett.8b04182>.
- (121) Gubbin, C. R.; Martini, F.; Politi, A.; Maier, S. A.; De Liberato, S. Strong and Coherent Coupling between Localized and Propagating Phonon Polaritons. *Phys. Rev. Lett.* **2016**, *116* (24). <https://doi.org/10.1103/PhysRevLett.116.246402>.
- (122) Niemczyk, T.; Deppe, F.; Huebl, H.; Menzel, E. P.; Hocke, F.; Schwarz, M. J.; Garcia-Ripoll, J. J.; Zueco, D.; Hümmer, T.; Solano, E.; Marx, A.; Gross, R. Circuit Quantum Electrodynamics in the Ultrastrong-Coupling Regime. *Nat. Phys.* **2010**, *6* (10), 772–776. <https://doi.org/10.1038/nphys1730>.
- (123) Benz, F.; Schmidt, M. K.; Dreismann, A.; Chikkaraddy, R.; Zhang, Y.; Demetriadou, A.; Carnegie, C.; Ohadi, H.; De Nijs, B.; Esteban, R.; Aizpurua, J.; Baumberg, J. J. Single-Molecule Optomechanics in “Picocavities.” *Science (80-.)*. **2016**, *354* (6313), 726–729. <https://doi.org/10.1126/science.aah5243>.
- (124) Peraca, N. M.; Baydin, A.; Gao, W.; Bamba, M.; Kono, J. *Ultrastrong Light–Matter Coupling in Semiconductors*, 1st ed.; Elsevier Inc., 2020; Vol. 105.

<https://doi.org/10.1016/bs.semsem.2020.10.002>.

- (125) Frisk Kockum, A.; Miranowicz, A.; De Liberato, S.; Savasta, S.; Nori, F. Ultrastrong Coupling between Light and Matter. *Nat. Rev. Phys.* <https://doi.org/10.1038/s42254-018-0006-2>.
- (126) Adato, R.; Artar, A.; Erramilli, S.; Altug, H. Engineered Absorption Enhancement and Induced Transparency in Coupled Molecular and Plasmonic Resonator Systems. **2013**. <https://doi.org/10.1021/nl400689q>.
- (127) Caldwell, J. D.; Glembocki, O.; Bezares, F. J.; Bassim, N. D.; Rendell, R. W.; Feygelson, M.; Ukaegbu, M.; Kasica, R.; Shirey, L.; Hosten, C. Plasmonic Nanopillar Arrays for Large-Area, High-Enhancement Surface-Enhanced Raman Scattering Sensors. **2011**. <https://doi.org/10.1021/nn200636t>.
- (128) Giannini, V.; Francescato, Y.; Amrania, H.; Phillips, C. C.; Maier, S. A. Fano Resonances in Nanoscale Plasmonic Systems: A Parameter-Free Modeling Approach. *Nano Lett.* **2011**, *11* (7), 2835–2840. <https://doi.org/10.1021/nl201207n>.
- (129) Törmö, P.; Barnes, W. L. Strong Coupling between Surface Plasmon Polaritons and Emitters: A Review. *Reports on Progress in Physics.* 2015. <https://doi.org/10.1088/0034-4885/78/1/013901>.
- (130) Xiang, B.; Ribeiro, R. F.; Dunkelberger, A. D.; Wang, J.; Li, Y.; Simpkins, B. S. Two-Dimensional Infrared Spectroscopy of Vibrational Polaritons. **2018**, No. 16. <https://doi.org/10.1073/pnas.1722063115>.
- (131) Ahn, W.; Vurgaftman, I.; Dunkelberger, A. D.; Owrutsky, C.; Simpkins, B. S. Molecules within the Optical Cavity. **2018**. <https://doi.org/10.1021/acsphotonics.7b00583>.
- (132) Dunkelberger, A. D.; Spann, B. T.; Fears, K. P.; Simpkins, B. S.; Owrutsky, J. C. Modified Relaxation Dynamics and Coherent Energy Exchange in Coupled Vibration-Cavity Polaritons. *Nat. Commun.* **2016**, *7*, 1–10. <https://doi.org/10.1038/ncomms13504>.
- (133) Coles, D. M.; Somaschi, N.; Michetti, P.; Clark, C.; Lagoudakis, P. G.; Savvidis, P. G.; Lidzey, D. G. Polariton-Mediated Energy Transfer between Organic Dyes in a Strongly Coupled Optical Microcavity. **2014**, *13* (July). <https://doi.org/10.1038/NMAT3950>.
- (134) Zhong, X.; Chervy, T.; Zhang, L.; Thomas, A.; George, J.; Genet, C.; Hutchison, J. A.; Ebbesen, T. W. Energy Transfer between Spatially Separated Entangled Molecules *Angewandte*. **2017**, 9034–9038. <https://doi.org/10.1002/anie.201703539>.
- (135) Zhong, X.; Chervy, T.; Wang, S.; George, J.; Thomas, A.; Hutchison, J. A.; Devaux, E.; Genet, C.; Ebbesen, T. W. Energy Transfer Hot Paper Non-Radiative Energy Transfer Mediated by Hybrid Light-Matter States. **2016**, 6202–6206. <https://doi.org/10.1002/anie.201600428>.
- (136) Wallraff, A.; Schuster, D. I.; Blais, A.; Frunzio, L.; Majer, J.; Kumar, S.; Girvin, S. M.; Schoelkopf, R. J. Strong Coupling of a Single Photon to a Superconducting Qubit Using Circuit Quantum Electrodynamics. **2004**, *431* (September), 0–5. <https://doi.org/10.1038/nature02831.1>.
- (137) Askenazi, B.; Vasanelli, A.; Todorov, Y.; Sakat, E.; Greffet, J.-J.; Beaudoin, goire; Sagnes, I.; Sirtori, C. Midinfrared Ultrastrong Light–Matter Coupling for THz Thermal Emission. **2017**. <https://doi.org/10.1021/acsphotonics.7b00838>.
- (138) Todorov, Y.; Andrews, A. M.; Colombelli, R.; De Liberato, S.; Ciuti, C.; Klang, P.; Strasser, G.;

- Sirtori, C. Ultrastrong Light-Matter Coupling Regime with Polariton Dots. *Phys. Rev. Lett.* **2010**, *105* (19), 1–4. <https://doi.org/10.1103/PhysRevLett.105.196402>.
- (139) Todorov, Y. Dipolar Quantum Electrodynamics Theory of the Three-Dimensional Electron Gas. *Phys. Rev. B - Condens. Matter Mater. Phys.* **2014**, *89* (7), 1–20. <https://doi.org/10.1103/PhysRevB.89.075115>.
- (140) Radue, E.; Runnerstrom, E. L.; Kelley, K. P.; Rost, C. M.; Donovan, B. F.; Grimley, E. D.; Lebeau, J. M.; Maria, J. P.; Hopkins, P. E. Charge Confinement and Thermal Transport Processes in Modulation-Doped Epitaxial Crystals Lacking Lattice Interfaces. *Phys. Rev. Mater.* **2019**, *3* (3), 1–9. <https://doi.org/10.1103/PhysRevMaterials.3.032201>.
- (141) Li, P.; Yang, X.; Maß, T. W. W.; Hanss, J.; Lewin, M.; Michel, A. U.; Wuttig, M.; Taubner, T. Reversible Optical Switching of Highly Confined Phonon–Polaritons with an Ultrathin Phase-Change Material. **2016**, No. May. <https://doi.org/10.1038/NMAT4649>.
- (142) Fiorentini, V.; Bernardini, F.; Sala, F. Della; Di Carlo, A.; Lugli, P. Effects of Macroscopic Polarization in III-V Nitride Multiple Quantum Wells. *Phys. Rev. B - Condens. Matter Mater. Phys.* **1999**, *60* (12), 8849–8858. <https://doi.org/10.1103/PhysRevB.60.8849>.
- (143) Sohr, P.; Wei, D.; Tomasulo, S.; Yakes, M. K.; Law, S. Simultaneous Large Mode Index and High Quality Factor in Infrared Hyperbolic Metamaterials. *ACS Photonics* **2018**, *5* (10), 4003–4008. <https://doi.org/10.1021/acsp Photonics.8b01097>.
- (144) Harima, H. Raman Scattering from Anisotropic LO- Phonon – Plasmon – Coupled Mode in n -Type 4H – and 6H – SiC LO-Phonon-Plasmon-Coupled. **2001**, *1996* (June 1998), 1995–2005.
- (145) Mooradian, A.; Wright, B. OBSERVATION OF THE INTERACTION OF PLASMONS WITH LONGITUDINAL OPTICAL PHONONS IN GaAs. *Phys. Rev. Lett.* **1966**, *16* (22), 999–1001.
- (146) Dunkelberger, A. D.; Ellis, C. T.; Ratchford, D. C.; Giles, A. J.; Kim, M.; Kim, C. S.; Spann, B. T.; Vurgaftman, I.; Tischler, J. G.; Long, J. P.; Glembocki, O. J.; Owrutsky, J. C.; Caldwell, J. D. Active Tuning of Surface Phonon Polariton Resonances via Carrier Photoinjection. *Nat. Photonics* **2018**, *12* (1), 50–56. <https://doi.org/10.1038/s41566-017-0069-0>.
- (147) Molesky, S.; Jacob, Z. High Temperature Epsilon-near-Zero and Epsilon-near-Pole Metamaterial Emitters for Thermophotovoltaics. *2013 Conf. Lasers Electro-Optics, CLEO 2013* **2013**, *21* (January), 549–554. https://doi.org/10.1364/cleo_qels.2013.qtu1a.6.
- (148) Hugall, J. T.; Singh, A.; Van Hulst, N. F. Plasmonic Cavity Coupling. *ACS Photonics* **2018**, *5* (1), 43–53. <https://doi.org/10.1021/acsp Photonics.7b01139>.
- (149) Etin, A. E.; Yanik, A. A.; Yilmaz, C.; Somu, S.; Busnaina, A.; Altug, H. Monopole Antenna Arrays for Optical Trapping, Spectroscopy, and Sensing. *Appl. Phys. Lett.* **2011**, *98* (11), 2009–2012. <https://doi.org/10.1063/1.3559620>.
- (150) Gubbin, C. R.; Maier, S. A.; De Liberato, S. Theoretical Investigation of Phonon Polaritons in SiC Micropillar Resonators. *Phys. Rev. B* **2017**, *95* (3), 35313. <https://doi.org/10.1103/PhysRevB.95.035313>.
- (151) Caldwell, J. D.; Glembocki, O. J.; Francescato, Y.; Sharac, N.; Giannini, V.; Bezares, F. J.; Long, J. P.; Owrutsky, J. C.; Vurgaftman, I.; Tischler, J. G.; Wheeler, V. D.; Bassim, N. D.; Shirey, L. M.; Kasica, R.; Maier, S. A. Low-Loss, Extreme Subdiffraction Photon Confinement via Silicon Carbide

- Localized Surface Phonon Polariton Resonators. *Nano Lett.* **2013**, *13* (8), 3690–3697. <https://doi.org/10.1021/nl401590g>.
- (152) Sberveglieri, G. ed. *Gas Sensors: Principles, Operation and Developments.*; Kluwer: Boston, 1992.
- (153) Meyer, J. R.; Vurgaftman, I.; Canedy, C. L.; Bewley, W. W.; Kim, C. S.; Merritt, C. D.; Warren, M. V.; Kim, M. In-Plane Resonant-Cavity Infrared Photodetectors with Fully-Depleted Absorbers, 2019.
- (154) Tan, X.; Zhang, H.; Li, J.; Wan, H.; Guo, Q.; Zhu, H.; Liu, H.; Yi, F. Non-Dispersive Infrared Multi-Gas Sensing via Nanoantenna Integrated Narrowband Detectors. *Nat. Commun.* **2020**, *11* (1), 1–9. <https://doi.org/10.1038/s41467-020-19085-1>.
- (155) Hodgkinson, J.; Tatam, R. P. A Review of Optical Gas Sensing Techniques. **2013**, *24* (1), 43.
- (156) Lochbaum, A.; Dorodnyy, A.; Koch, U.; Koepfli, S. M.; Volk, S.; Fedoryshyn, Y.; Wood, V.; Leuthold, J. Compact Mid-Infrared Gas Sensing Enabled by an All-Metamaterial Design. *Nano Lett.* **2020**, *20* (6), 4169–4176. <https://doi.org/10.1021/acs.nanolett.0c00483>.
- (157) Koppens, F. H. L.; Mueller, T.; Avouris, P.; Ferrari, A. C.; Vitiello, M. S.; Polini, M. Photodetectors Based on Graphene, Other Two-Dimensional Materials and Hybrid Systems. *Nat. Nanotechnol.* **2014**, *9* (10), 780–793. <https://doi.org/10.1038/nnano.2014.215>.
- (158) De Zoysa, M.; Asano, T.; Mochizuki, K.; Oskooi, A.; Inoue, T.; Noda, S. Conversion of Broadband to Narrowband Thermal Emission through Energy Recycling. *Nat. Photonics* **2012**, *6* (8), 535–539. <https://doi.org/10.1038/nphoton.2012.146>.
- (159) Laroche, M.; Carminati, R.; Greffet, J. Coherent Thermal Antenna Using a Photonic Crystal Slab. **2014**, No. May. <https://doi.org/10.1103/PhysRevLett.96.123903>.
- (160) Inoue, T.; Zoysa, M. De; Asano, T.; Noda, S. High- Q Mid-Infrared Thermal Emitters Operating with High Power-Utilization Efficiency. **2016**, *24* (13), 899–907. <https://doi.org/10.1364/OE.24.015101>.
- (161) Howes, A.; Nolen, J. R.; Caldwell, J. D.; Valentine, J. Near-Unity and Narrowband Thermal Emissivity in Balanced Dielectric Metasurfaces. *Adv. Opt. Mater.* **2020**, *8* (4), 1–8. <https://doi.org/10.1002/adom.201901470>.
- (162) Mason, J. A.; Smith, S.; Wasserman, D. Strong Absorption and Selective Thermal Emission from a Midinfrared Metamaterial. **2011**, *241105* (June), 15–18. <https://doi.org/10.1063/1.3600779>.
- (163) Baranov, D. G.; Xiao, Y.; Nechepurenko, I. A.; Krasnok, A.; Alù, A.; Kats, M. A. Nanophotonic Engineering of Far-Field Thermal Emitters. *Nat. Mater.* **2019**, *18* (9), 920–930. <https://doi.org/10.1038/s41563-019-0363-y>.
- (164) Liu, X.; Tyler, T.; Starr, T.; Starr, A. F.; Jokerst, N. M.; Padilla, W. J. Taming the Blackbody with Infrared Metamaterials as Selective Thermal Emitters. *Phys. Rev. Lett.* **2011**, *107* (4), 4–7. <https://doi.org/10.1103/PhysRevLett.107.045901>.
- (165) Landy, N. I.; Sajuyigbe, S.; Mock, J. J.; Smith, D. R.; Padilla, W. J. Perfect Metamaterial Absorber. **2008**. <https://doi.org/10.1103/PhysRevLett.100.207402>.
- (166) Lochbaum, A.; Fedoryshyn, Y.; Dorodnyy, A.; Koch, U.; Hafner, C.; Leuthold, J. On-Chip Narrowband Thermal Emitter for Mid-IR Optical Gas Sensing. *ACS Photonics* **2017**, *4* (6), 1371–

1380. <https://doi.org/10.1021/acsphotonics.6b01025>.
- (167) Chao, S. H.; Yeh, L. H.; Wu, R. T.; Kawagishi, K.; Hsu, S. C. Novel Patterned Sapphire Substrates for Enhancing the Efficiency of GaN-Based Light-Emitting Diodes. *RSC Adv.* **2020**, *10* (28), 16284–16290. <https://doi.org/10.1039/d0ra01900c>.
- (168) Nikitin, A. G.; Kabashin, A. V.; Dallaporta, H. Plasmonic Resonances in Diffractive Arrays of Gold Nanoantennas: Near and Far Field Effects. *Opt. Express* **2012**, *20* (25), 27941. <https://doi.org/10.1364/oe.20.027941>.
- (169) Kravets, V. G.; Schedin, F.; Grigorenko, A. N. Extremely Narrow Plasmon Resonances Based on Diffraction Coupling of Localized Plasmons in Arrays of Metallic Nanoparticles. **2008**, *087403* (August), 1–4. <https://doi.org/10.1103/PhysRevLett.101.087403>.
- (170) Giannini, V.; Francescato, Y.; Amrania, H.; Phillips, C. C.; Maier, S. A. Fano Resonances in Nanoscale Plasmonic Systems: A Parameter-Free Modeling Approach. *Nano Lett.* **2011**, *11* (7), 2835–2840. <https://doi.org/10.1021/nl201207n>.
- (171) Simpkins, B. S.; Long, J. P.; Glembocki, O. J.; Guo, J.; Caldwell, J. D. Pitch-Dependent Resonances and near-Field Coupling in Infrared Nanoantenna Arrays. **2012**, *20* (25), 18178–18188.
- (172) Linstrom, P. J.; Mallard, W. G.; (eds.). *NIST Chemistry WebBook, NIST Standard Reference Database Number 69*; National Institute of Standards and Technology: Gaithersburg MD.
- (173) Wang, Z.; Clark, J. K.; Ho, Y. L.; Volz, S.; Daiguji, H.; Delaunay, J. J.; Delaunay, J. J. Ultranarrow and Wavelength-Tunable Thermal Emission in a Hybrid Metal-Optical Tamm State Structure. *ACS Photonics* **2020**, *7* (6), 1569–1576. <https://doi.org/10.1021/acsphotonics.0c00439>.
- (174) Wang, Z.; Clark, J. K.; Ho, Y. L.; Vilquin, B.; Daiguji, H.; Delaunay, J. J. Narrowband Thermal Emission from Tamm Plasmons of a Modified Distributed Bragg Reflector. *Appl. Phys. Lett.* **2018**, *113* (16). <https://doi.org/10.1063/1.5048950>.
- (175) Mikhlin, V. S.; Kavokin, A. V.; Sasin, M. E.; Seisyan, R. P.; Kalitseevski, M. A.; Brand, S.; Abram, R. A. Tamm Plasmon Polaritons : Slow and Spatially Compact Light. **2013**, *251112* (May 2008), 1–4. <https://doi.org/10.1063/1.2952486>.
- (176) Kavokin, A. V.; Shelykh, I. A.; Malpuech, G. Lossless Interface Modes at the Boundary between Two Periodic Dielectric Structures. **2005**, 1–4. <https://doi.org/10.1103/PhysRevB.72.233102>.
- (177) Auguie, B.; Bruchhausen, A.; Fainstein, A. Critical Coupling to Tamm Plasmons. *J. Opt.* **2015**, *17* (3), 35003. <https://doi.org/10.1088/2040-8978/17/3/035003>.
- (178) Sakurai, A.; Yada, K.; Simomura, T.; Ju, S.; Kashiwagi, M.; Okada, H.; Nagao, T.; Tsuda, K.; Shiomi, J. Ultranarrow-Band Wavelength-Selective Thermal Emission with Aperiodic Multilayered Metamaterials Designed by Bayesian Optimization. *ACS Cent. Sci.* **2019**, *5* (2), 319–326. <https://doi.org/10.1021/acscentsci.8b00802>.
- (179) Reines, I. C.; Wood, M. G.; Luk, T. S.; Serkland, D. K.; Campione, S. Compact Epsilon-near-Zero Silicon Photonic Phase Modulators. *Opt. Express* **2018**, *26* (17), 21594. <https://doi.org/10.1364/oe.26.021594>.
- (180) Kingma, D. P.; Ba, J. L. Adam: A Method for Stochastic Optimization. In *3rd International Conference on Learning Representations, ICLR 2015 - Conference Track Proceedings*; 2015; pp 1–

15.

- (181) Robbins, H.; Monro, S. A Stochastic Approximation Method. *Ann. Math. Stat.* **1951**, *22* (3), 400–407. <https://doi.org/10.1214/aoms/1177729586>.
- (182) Bordes, A.; Bottou, L.; Gallinari, P. SGD-QN: Careful Quasi-Newton Stochastic Gradient Descent Antoine. *J. Mach. Learn. Res.* **2009**, *10*, 56.
- (183) Livingood, A.; Nolen, J. R.; Folland, T. G.; Potechin, L.; Lu, G.; Criswell, S.; Maria, J. P.; Shelton, C. T.; Sachet, E.; Caldwell, J. D. Filterless Nondispersive Infrared Sensing Using Narrowband Infrared Emitting Metamaterials. *ACS Photonics* **2021**. <https://doi.org/10.1021/acsp Photonics.0c01432>.
- (184) Cleri, A.; Tomko, J.; Quiambao-tomko, K.; Imperatore, M. V; Zhu, Y.; Nolen, J. R.; Nordlander, J.; Caldwell, J. D.; Mao, Z.; Giebink, N. C.; Kelley, K. P.; Runnerstrom, E. L.; Hopkins, P. E.; Maria, J. Mid-Wave to near-IR Optoelectronic Properties and Epsilon-near-Zero Behavior in Indium-Doped Cadmium Oxide. *Phys. Rev. Mater.* **2021**, *5* (3), 35202. <https://doi.org/10.1103/PhysRevMaterials.5.035202>.
- (185) Overvig, A. C.; Shrestha, S.; Malek, S. C.; Lu, M. Dielectric Metasurfaces for Complete and Independent Control of the Optical Amplitude and Phase. *Light Sci. Appl.* **2019**. <https://doi.org/10.1038/s41377-019-0201-7>.
- (186) Zhou, Y.; Zheng, H.; Kravchenko, I. I.; Valentine, J. Flat Optics for Image Differentiation. *Nat. Photonics*. <https://doi.org/10.1038/s41566-020-0591-3>.
- (187) Zhou, Y.; Kravchenko, I. I.; Wang, H.; Nolen, J. R.; Gu, G.; Valentine, J. G. Multilayer Non-Interacting Dielectric Metasurfaces For Multiwavelength Metaoptics. **2018**. <https://doi.org/10.1021/acs.nanolett.8b03017>.
- (188) Arbabi, A.; Horie, Y.; Bagheri, M.; Faraon, A. Dielectric Metasurfaces for Complete Control of Phase and Polarization with Subwavelength Spatial Resolution and High Transmission. 1–27.
- (189) Fali, A.; White, S. T.; Folland, T. G.; He, M.; Aghamiri, N. A. Refractive Index-Based Control of Hyperbolic Phonon-Polariton Propagation.
- (190) Li, P.; Lewin, M.; Kretinin, A. V.; Caldwell, J. D.; Novoselov, K. S.; Taniguchi, T.; Watanabe, K.; Gaussmann, F.; Taubner, T. Hyperbolic Phonon-Polaritons in Boron Nitride for near-Field Optical Imaging and Focusing. *Nat. Commun.* **2015**, *6*. <https://doi.org/10.1038/ncomms8507>.
- (191) Yang, X.; Yao, J.; Rho, J.; Yin, X.; Zhang, X. Experimental Realization of Three-Dimensional Indefinite Cavities at the Nanoscale with Anomalous Scaling Laws. *Nat. Photonics* **2012**, *6* (7), 450–454. <https://doi.org/10.1038/nphoton.2012.124>.
- (192) Yao, J.; Yang, X.; Yin, X.; Bartal, G.; Zhang, X. Three-Dimensional Nanometer-Scale Optical Cavities of Indefinite Medium. *Proc. Natl. Acad. Sci. U. S. A.* **2011**, *108* (28), 11327–11331. <https://doi.org/10.1073/pnas.1104418108>.
- (193) He, M.; Halimi, S. I.; Folland, T. G.; Sunku, S. S.; Liu, S.; Edgar, J. H.; Basov, D. N.; Weiss, S. M.; Caldwell, J. D. Guided Mid-IR and Near-IR Light within a Hybrid Hyperbolic-Material/Silicon Waveguide Heterostructure. *Adv. Mater.* **2021**, 1–19. <https://doi.org/10.1002/adma.202004305>.
- (194) Jacob, Z.; Smolyaninov, I. I.; Narimanov, E. E. Broadband Purcell Effect: Radiative Decay Engineering with Metamaterials. *Appl. Phys. Lett.* **2012**, *100* (18).

<https://doi.org/10.1063/1.4710548>.

- (195) Iorsh, I.; Poddubny, A.; Orlov, A.; Belov, P.; Kivshar, Y. S. Spontaneous Emission Enhancement in Metal-Dielectric Metamaterials. *Phys. Lett. Sect. A Gen. At. Solid State Phys.* **2012**, *376* (3), 185–187. <https://doi.org/10.1016/j.physleta.2011.11.001>.
- (196) Shekhar, P.; Jacob, Z. Strong Coupling in Hyperbolic Metamaterials. *Phys. Rev. B - Condens. Matter Mater. Phys.* **2014**, *90* (4), 1–11. <https://doi.org/10.1103/PhysRevB.90.045313>.
- (197) Guo, Y.; Jacob, Z. Broadband Super-Planckian Thermal Emission from Hyperbolic Metamaterials; 2013; Vol. 131106. https://doi.org/10.1364/cleo_qels.2013.qtu3a.4.
- (198) Biehs, S. A.; Tschikin, M.; Ben-Abdallah, P. Hyperbolic Metamaterials as an Analog of a Blackbody in the near Field. *Phys. Rev. Lett.* **2012**, *109* (10), 1–5. <https://doi.org/10.1103/PhysRevLett.109.104301>.
- (199) Wei, D.; Harris, C.; Bomberger, C. C.; Zhang, J.; Zide, J.; Law, S. Single-Material Semiconductor Hyperbolic Metamaterials. *Opt. Express* **2016**, *24* (8), 8735. <https://doi.org/10.1364/oe.24.008735>.
- (200) Lalanne, P.; Lemercier-Lalanne, D. On the Effective Medium Theory of Subwavelength Periodic Structures. *J. Mod. Opt.* **1996**, *43* (10), 2063–2085.